NORTHWESTERN UNIVERSITY

Scope, Mechanism, and Applications of High Temperature Entrenchment of Metal Nanoparticles on Amorphous Silicon Oxide Supports

A DISSERTATION

SUBMITTED TO THE GRADUATE SCHOOL IN PARTIAL FULFILLMENT OF THE REQUIREMENTS

for the degree

DOCTOR OF PHILOSOPHY

Field of Chemical and Biological Engineering

By

Abha Anand Gosavi

EVANSTON, ILLINOIS

September 2019

Abstract

Metal nanoparticles supported on oxides are versatile systems. Ordered arrays of multimetallic nanoparticles of different sizes and surface densities can be synthesized using block copolymer-mediated nanolithography techniques. Metal nanoparticles on planar supports like silica can be utilized for catalyst discovery. Under reaction conditions and at high temperatures, the changing surface energy equilibria at the metal-oxide interface causes a rearrangement of the metal nanoparticles and/or the supporting oxide. This often leads to catalyst deactivation by sintering where metal nanoparticle may migrate along the surface and coalesce or atoms from the nanoparticles migrate to other nanoparticles to form larger and fewer nanoparticles.

Partially embedding uniform arrays of nanoparticles within the support can prevent their sintering. When some metal nanoparticles, supported on amorphous silica, are heated to temperatures above 1000 ºC under inert conditions, nanopores are formed in the silica surface. This behavior is observed for gold, silver, copper, palladium, and platinum nanoparticles but not cobalt or nickel nanoparticles. Furthermore, nanopore formation is unique to planar, amorphous silica and does not occur on planar quartz, hafnia, titania, and alumina as well as on nanoscale spherical silica.

The mechanism that governs this behavior relies heavily on the diffusion of metal ions into the supporting silica at elevated temperatures. The dissolution of metal ions in the amorphous silica matrix lowers its glass transition temperature (T_g). At temperatures above the T_g (~1000 ºC), the supporting silica exhibits viscoelastic behavior and allows the nanoparticles. Crystalline oxide supports that do not undergo glass transition (like quartz and alumina) prevent nanopore formation. Moreover, metals with very low diffusivities in amorphous silica (like nickel and cobalt) do not form nanopores at 1040 ºC while silver, that has a very high diffusivity in silica forms nanopores readily even at 800 ºC. The shape of the supporting silica also plays a crucial role in nanopore formation. Spherical geometries have high internal stresses that hamper diffusive processes at the surface. On such supports, since metal ion diffusion into the support is significantly lowered, no nanopore formation is observed at high temperatures.

The selective nature of nanopore formation is applied to design and fabricate modified tri-layer supports consisting of silica on alumina on silicon wafers. The thin layers of silica allow nanopore formation while the alumina layer acts as a barrier to this behavior. On these tri-layer supports, the depth to which nanoparticles (of sizes 10-15 nm) will entrench can be controlled between 3-5 nm. The partially embedded nanoparticles are location stabilized and could have potential applications as sinter-resistant catalysts.

Nanopore formation by thermal entrenchment of metal nanoparticles occurs above a specific minimum temperature which depends on the composition of metal nanoparticles. While Au and Pd nanoparticles form nanopores above 1000 ºC, Ag nanoparticles entrench above 800 ºC. Additionally, the ramp rates employed to attain these high temperatures also control nanopore formation. Lower ramp rates (<1 ºC/s) cause partial embedding and nanoparticle encapsulation whereas higher ramp rates (>1 ºC/s) lead to formation of clear nanopores. Thermal entrenchment competes with other surface phenomena, including nanoparticle agglomeration, diffusion, and encapsulation, which also occur at high temperatures. The dominant behavior, amongst these many competing phenomena arising at the metal-oxide interface, depends on the initial surface distribution of the nanoparticles. While well-spaced, large nanoparticles will each form a nanopores of comparable diameters, densely packed, small nanoparticles will agglomerate to form larger nanoparticles before entrenchment. There are also some distributions, where nanoparticle mobility is not favored, for which encapsulation of nanoparticles within the silica support is observed.

Nanopore formation in silica supports is accompanied by the formation of oxide ridges around the nanopores. These are caused by oxide transport along the metal-oxide interface as the system attains to equilibrate at the high temperatures. The height of these oxide ridges depends on the nanoparticle composition as well as on the size. Silver nanoparticles form the tallest oxide ridges when compared to those created by gold and palladium nanoparticles of similar sizes. Moreover, highly mobile nanoparticles that aggregate before nanopore formation create very short oxide ridges as the metal-oxide interface is not stationary. Thus, nanopore with tunable diameters and oxide ridges can be generated by controlling the size and surface density of metal nanoparticles. These nanopores may be potentially used in separations and sensing applications.

Acknowledgments

These five years at Northwestern University have been the most eventful, educational, and inspired ones in my life. I came to a new country, far away from everything familiar and comfortable. This bold step was the best decision I have ever made. Northwestern has enriched me beyond chemical engineering. I have found my community here. The brilliant, creative, kind, and inspiring people I have met here will be builders of our society's future, and I am humbled to have met them.

I am greatly indebted to my advisors, Profs. Chad Mirkin and Justin Notestein. Their distinct, yet complementary styles have helped me grow as a researcher and as a person. Chad's vision and passion for nanoscience is truly inspiring. Justin's depth of knowledge and intuition in catalysis continues to amaze me. I am truly grateful for their support in tackling a new research direction for both groups. I also thank my committee members Profs. Linda Broadbelt and Vinayak Dravid for their valuable feedback. Furthermore, I thank Justin for appointing me as the lab safety designate which led to me find my cause and calling. Research safety has been an issue close to my heart throughout graduate school. I am forever indebted to Dr. Michael Blayney, for he, although the Executive Director of Research Safety at Northwestern University, replied to the email of a second-year graduate student seeking to learn more about laboratory safety. I cannot possibly thank Michael enough for his mentorship, encouragement, and most importantly, friendship.

My interest in chemical engineering started in school. I am thankful to my middle school teachers, Minal Deo and Sadhana Kamerkar, who went beyond the textbooks and kindled an enthusiasm for math and science in our young, impressionable minds. I am especially grateful to my favorite teacher, Vinitha Nair, who pushed me out of my comfort zone and showed me the wonders that await one when they stop being afraid. I am truly indebted to Prof. Dev Jha, who believed in me when no one else did. I am also thankful to Prof. Amol Kulkarni, of the National Chemical Laboratory, for giving me my first research opportunity in his lab.

When I first joined the Mirkin and Notestein labs, I had so much to learn about nanolithography and catalysis. I am grateful to all my mentors, Dr. Natalia Chernyak, Prof. Keith Brown, Dr. Peng-Cheng Chen, Dr. James Hedrick, and Dr. Nicholas Thornburg for everything they have taught me. I am also thankful to Dr. Brian Meckes, who spent hours teaching me how to use the atomic force microscope, the one instrument that I have used almost every day of my graduate life. I am also grateful to Dr. Gajendra Shekhawat for his assistance in my atomic force microscopy experiments. I have had the honor and joy of working with some of the most creative mentees. I am grateful to Ryan Frank, Eric Taw, and Nikhita Ahuja for their patience and enthusiasm. I am thankful to Dr. James Griffin, Ryan Paull, Zachary Mansley, Kacper Skakuj, and Andrea D'Aquino for showing me that collaborations make better science.

Over the years, I have had the joy of sharing office and lab spaces with some of the smartest and kindest people. Being part of two groups means you have twice as many friends. I am grateful to Dr. Corinna Raimondo, Dr. Chieh-Chao Yang, Dr. Todd Eaton, Dr. Scott Nauert, Dr. Chao Liu, Dr. Zhenyu Bo, Dr. Rachel Watson, Dr. Alexander Ardagh, Dr. Sol Ahn, Mihir Bhagat, Emily Cheng, Andrew Rosen, Charmaine Bennett, Christian Contreras, Joshua Kirkham, Andrew Wolek, Kenton Hicks, and Qining Wang for creating a happy and productive work environment in the Notestein student office. I also thank the Mirkin folks, Dr. Maria Cabezas, Dr. Andrey Ivankin, Dr. Anindita Das, Dr. Pavlo Gordiichuk, Edward Kluender, Jingshan Du, Jinghan Zhu, Kent Miao, Eun Bi Oh, Bo Shen, Liban Jibril, and Namrata Ramani, with whom it has been a joy to share lab spaces. I am also thankful to the Mirkin office staff, Elizabeth Forest, Dr. Tanushri Sengupta, Dr. Sara Rupich, and Pamela Watson for keeping the group organized and safe.

The friendship and love that I have received throughout the last five years has been truly overwhelming. Thank you, Dr. Sara Yacob for being a source of inspiration and a good friend. Thank you, Lin Sun for being a good listener and a constant partner in trying new restaurants. I am grateful to Tejaswinee Sohoni, Allan Valsaraj, Aakash Mishra, and Ritwik Ummalaneni for always keeping my spirits up and cheering me on. I thank Rustin Golnabi and Liliang Huang for their friendship, commiseration, and those endless chats in the lab. I thank Dr. Louisa Savereide for her kindness, sense of humor, and company

for all the little walks around campus. I will not thank Dr. Lauren McCullough, for our friendship goes beyond that. I am grateful to have met a colleague, a friend, a mentor, and a sister in her.

I am greatly indebted to my family whose love and encouragement over the years have helped me get to where I am. My parents, Anand and Kanchan Gosavi, were my first math and science teachers. Staying so far away from them for the last five years has brought us closer. Thank you for believing in me and supporting me. I am also grateful for the support of my grandmothers and hope that I have made my late grandfathers proud. I am also thankful to have the love and support of my parents-in-law Ravindernath and Veneeta Siram. Finally, I thank my fiancé and partner, Susheel Siram, without whom none of this would be possible. Thank you Susheel, for keeping me sane for the past five years. Thank you for the late-night dinners brought to the office, the constant critique on my slides, and for your unwavering presence by my side.

For my father Anand Gosavi, because if there is anyone who will read this thesis from end to end, it is him. Baba, thank you for everything.

Table of Contents

List of Figures and Schemes

Chapter Two

Chapter Six

Chapter Seven

Chapter Eight

Supplementary Information

List of Tables

Supplementary Information

Chapter One: Stabilizing Metal Nanoparticles on Planar Supports for Applications in Catalysis

1.1 Introduction

Metal nanoparticles of different geometries, distributions, composition, and sizes have a wide range of applications.[1–3] These nanoparticles can exist in colloidal solutions where they have many optical and catalytic applications.[1,2] The nanoparticles can also be immobilized on oxides supports or polymeric matrices where they gain heterogeneity without completely losing their function. Metal nanoparticles supported on a wide range of porous, oxide supports have been used as heterogeneous catalysts for decades.[3,4] Supported metal nanoparticles are used as heterogeneous catalysts for a wide range of industrially important reactions.[5–7] Similarly, metal nanoparticles supported on planar substrates (Si wafer, quartz, graphene oxide) are especially important for their plasmonic and opto-electronic properties.[8,9] These are, moreover, crucial precursors for nanowire growth and have applications in the microelectronics industry.[10] Well-ordered arrays of nanoparticles on planar supports might also serve as a platform for catalyst discovery[11] and a model to study various interfacial surface phenomena.[12]

In this work, we have tried to understand some of the various behaviors at the metal-oxide interface for metal nanoparticles on planar SiO_2 supports and their implication in catalysis. Our goal was to stabilize the metal nanoparticles, synthesized by nanolithography, against catalyst deactivation by sintering or detachment, under liquid-phase reaction conditions. We explored the Suzuki-Miyaura cross-coupling reaction as a model to probe the stability of these nanoparticle catalysts. Having learnt that this reaction has mechanistic limitation that prevents the heterogeneity of the catalyst, we moved on to exploring thermal entrenchment of metal nanoparticles into the SiO_2 support as a novel way to stabilize the nanoparticles. In the latter part of this thesis we have endeavored to understand and expand the scope, limitations, mechanism, and application of nanopore formation by rapid thermal processing of metal nanoparticles on amorphous SiO_2 supports.

1.2 Objectives

The primary objective of this thesis is to develop stable and robust supported nanoparticle arrays on planar SiO_2 supports for application as a catalyst screening platform. To achieve this, we explore the Suzuki-Miyaura cross-coupling reaction[13] as a model reaction to test the efficacy and stability of such nanoparticles under reaction conditions.

Our next objective is to establish the scope and mechanism of thermal entrenchment[14] of metal nanoparticle within SiO_2 supports and to employ this phenomenon to design stable heterogeneous catalysts. The nanopore formation by thermal entrenchment of Au nanostructures on fused SiO_2 at 1050 ºC was first reported in 2015.[14] Our first goal is to expand the library of materials that undergo this transformation to other transition metal nanoparticles and different supporting oxides. To this end, we examine the behavior of Au, Ag, Cu, Pd, and Pt nanoparticles on SiO_2 planar supports. This behavior is also tested on other planar oxide supports (Al_2O_3, HfO_2, TiO_2, quartz). Using insights from these preliminary tests, we aim to understand the mechanism that governs nanopore formation. Our next objective is to control the depth to which nanoparticles entrench so that partially embedded nanoparticles may be used as sinter-resistant catalysts. We develop modified Si-wafer supports with thin layers of Al_2O_3 and SiO_2 that allow only partial embedding of nanoparticles which could still be catalytically active in reaction conditions.

While we could explain how the nanopore formation proceeds, there was little understanding of how this behavior was favored over other behaviors that arise out of metal-metal and metal-oxide interactions at high temperatures. Thus, our next objective is to study how the nanopore formation competes with the sintering, agglomeration, diffusion, and encapsulation pathways that are also available to metal nanoparticles at these high temperatures. For this, using Pd/SiO_2 as the model system, we study the behaviors of metal nanoparticles of a wide range of sizes and surface densities at various heating conditions. We also use this model system to achieve nanopores of a range of different nanopores by tuning the initial Pd nanoparticle size and surface density. In order to gain further insight into the mechanism of nanopore formation, we study in further detail the outlying metal nanoparticles that either do not form nanopores (Co, Ni) or form nanopores at significantly lower temperatures (Ag).

Our final objective is to extend the nanopore formation on planar supports to three-dimensional spherical supports with the aim to design to industrially relevant sinter-resistant catalysts. In order to achieve this, we explore the behavior of Au and Pd metal nanoparticles on Stober SiO_2 spheres at high temperatures.

1.3 Background

1.3.1 Synthesis of metal nanoparticles on planar oxide supports

Uniformly distributed metal nanoparticles on planar supports like Si-wafers, have been traditionally synthesized by three major routes- 1) ordered deposition of pre-synthesized nanoparticles *via* printing techniques,[15,16] 2) deposition of thin films of pure metal, with or without photolithographic masks, and ensuring nanoparticle formation by dewetting,[17–24] and finally, 3) deposition of controlled amounts of metal precursor-laden polymeric solutions in an ordered array followed by a reduction procedure to ensure nanoparticle formation.[25–37] In ink-jet printing, uniform suspensions of metal nanoparticles are used as the "ink" for the ink-jet printer to obtain uniquely patterned surfaces. The nanoparticles are then sintered to create continuous patterns that have potential applications in the development of electronic devices.[15] Micro-contact printing is soft-lithography technique that transfers nanoparticles in unique patterns onto a surface using a polydimethylsiloxane (PDMS) master. The master acts as a stamp and can be used over large areas.[38,39] However, it difficult to achieve sub-50 nm resolution with these techniques reproducibly.[16]

Uniform metal nanoparticles of different compositions are also obtained depositing thin films of metals on substrates followed by dewetting of the films to form nanoparticles. Multiple metals can be co-sputtered to obtain concentration gradients or photo-lithographic masks can be used to deposit these thin films in various patterns.[40] Mask-less methods like electron beam lithography are used to achieve very high (sub-10 nm) resolutions.[18] The dewetting of the metallic thin films can be achieved by thermal annealing[17] or by electron beam[20] and lasers.[19] The alignment of nanoparticles on the surface can also be directed by using templated or modified supports.[21,22] These techniques rely on the nucleation and growth of voids in the thin films to control the final size and spacing of the nanoparticles, usually leading to formation of faceted

nanoparticles. If no photoresist is used this approach can be used to generate nanoparticles free from any organic contaminants.

One of the easiest ways to achieve uniform arrays of nanoparticles without complex instrumentation is block copolymer micelle lithography.[27,29,41,42] When metal salts coordinate with block copolymer micelles, they get incorporated in the micelle core.[29] Thin films of these micelles are transferred onto substrates, upon which they assemble in uniform hexagonal patterns.[27,41] These thin films can be deposited either by high rotation spin-coating or by dip-coating.[42] Depending on the chain lengths of the various blocks in the polymer and the amount of metal coordinated to them, the size and spacing of the micelles can be tuned.[29,43] The nanoparticles are reduced within the micelle by a reducing agent like $NaBH_4$.[44] Alternately, the block copolymer can be removed by employing oxidizing or reducing plasma to obtain uniform nanoparticle arrays.[36,41] Polystyrene-b-polyvinyl pyridine (PS-*b*-P2VP) is the most commonly studied block copolymer and is to synthesize Au, Pd, and Pt nanoparticles of uniform distributions for a variety of applications from catalysis[45] to carbon nanotube growth.[46] Using block copolymer lithography enables one to synthesize metal, metal oxides, metal sulfides, as well as multi-metallic nanoparticles, while other techniques are limited to only certain metals or compositions.[29] Additionally, with block copolymer lithography, the shape and the spatial arrangements of the nanoparticles can be controlled. Core-shell, hollow, and anisotropic nanoparticles can be generated by this technique in the minimum number of steps.[29]

Scanning probe block copolymer lithography (SPBCL) is another way to achieve uniform arrays of metal nanoparticles with a wide range of sizes and composition.[11,25,26,30,32–35] This technique also relies on block copolymer-based metal precursor solutions to generate nanoparticles. Aqueous solutions of polyethylene oxide-*b*-polyvinyl pyridine (PEO-*b*-P2VP) block copolymer coordinated with metal salts are used as inks. In this technique, attoliter volumes of the ink are transferred onto planar hydrophobic substrates, usually hexamethyldisilazane (HMDS)-modified Si wafer, using a sharp atomic force microscopy (AFM) probe in ordered arrays.[25,32,33] This may be scaled up significantly by polymer pen lithography (PPL) that uses the same ink on PDMS tip arrays to transfer the ink to the planar supports.[34] By using multimetallic polymer solutions or a dual-spray system, one can achieve an array of multimetallic

nanoparticles or a compositional gradient.[11,26] By approaching the surface at a tilt, the PPL tip arrays can be used to create nanoparticle arrays with size gradients.[47] Using SiO_2-modified PDMS tips, a greater resolution maybe achieved.[30] Together, these techniques provide tremendous control over the size, composition and location of the nanoparticles. Nanoparticles thus synthesized can be used for applications in catalyst discovery.[11] While SPBCL is very precise in both the location and the size and composition of the nanoparticle, it requires special instrumentation and is suitable only for a small scale.

For the scope of this work, we have heavily relied on block copolymer lithography using PEO-*b*-P2VP block copolymers and optimized the synthesis conditions to suit our requirements of metal nanoparticle size, spacing, and composition.

1.3.2 The Suzuki-Miyaura cross-coupling reaction

The Suzuki-Miyaura reaction, for which its researchers have been awarded a Nobel Prize in 2010, has been used extensively in chemical research and industry for to achieve cross-coupling across two aliphatic or aromatic groups using simple starting reactants.[13,48–51] This extremely powerful reaction opens a gateway to synthesizing a multitude of complex organic compounds that are of particular significance in the pharmaceutical industry.[13] The cross-coupling reaction enables aryl halides to react with organoboron compounds in the presence of trace palladium catalyst to form functionalized biaryls that act as precursors to important pharmaceutical products like *valsartan* (used to treat hypertension) and *boscalid* (anti-fungal agent) among many others.[52] The reaction is also widely used in industry in the later stages in the synthesis of complex molecules (*Pleuromutilin, Epothilone*), pharmaceuticals (*Caparratriene* for leukemia treatment) and fine chemicals.[53] The popularity of the reaction in the pharmaceutical industry can be attributed to the high efficiency of the Pd catalyst even in aqueous conditions and low toxicity of the boronic side products. A side reaction, usually undesirable, occurs when the individual reactants couple with themselves to form homocoupling products. This side reaction can be avoided by use of appropriate catalysts and cocatalyst.[13,54]

Since its first introduction in 1979, a wide range of Pd species have been used to catalyze the Suzuki reaction. Homogeneous catalysis was attained using Pd(II) complexes with phosphorous ligands.

With the advancements in nanotechnology, nanoparticle catalysts were developed for Suzuki reactions. Phosphine ligands were used as co-catalysts for this reaction in styrene or toluene as reaction media[13,50,55]. With a rising demand for environmentally-friendly or *green* chemistry, ligand-free nanoparticle catalysts that can be used in aqueous media have been developed.[53] In recent years, Ni, Cu, and Rh have been used along with Pd to achieve a synergistic improvement in its catalytic activity.[53,56,57]

Transition metal nanoparticles supported on metal oxides have emerged as versatile catalysts for the Suzuki-Miyaura cross-coupling reaction.[51] There has also been an increasing motivation towards developing "*green catalysts"* that discourage the use of environmentally detrimental solvents (like benzene and THF) and ligands (like phosphine).[58] Nanoparticle catalysts that remain active in ligand-free and aqueous reaction conditions are proving to be effective and green alternatives to their homogeneous counterparts[3,59].

The mechanism of this reaction is fairly well understood in the homogenous reaction medium catalyzed by a Pd(0) complex. The reaction begins with the oxidative addition of the aryl halide to the Pd(0) to form a Pd(II) complex. The hydroxide, alkoxide, or carbonate from the base then replaces the halide on the Pd complex. Another hydroxide, alkoxide, or carbonate from the base adds to the organoboron compound to form a borate reagent. The addition of this base makes the aryl group in the organoboron compound more nucleophilic. Transmetalation of the Pd complex with the borate then occurs causing the aryl group from the organoboron to replace the anion from the base on the Pd complex. Reductive elimination of the cross-coupled biaryls generates the Pd(0) catalyst and the reaction cycle continues.[48]

Over the past few decades, a staggering number of heterogenous nanoparticle catalysts have been developed for the Suzuki-Miyaura cross-coupling reaction.[60–65] Many of these studies claim heterogeneity of the catalyst by several reuse cycles or by employing hot-filtration steps. The *true* heterogeneity of these catalysts has been the subject of much debate. The exceptional reactivity of heterogeneous Pd combined with other studies that do show a steady loss in rate provide a counterclaim that the system leaches active Pd. The latter hypothesis has been supported by several studies using conventional supported Pd nanoparticles.[66–70] The mechanism of the reaction requires a continuous cycle between Pd(0) and Pd(II)

states. The Pd(II) that complexes with the reactants enters the solution phase and thus, does not remain heterogenous. This steady loss of Pd, although very small, leads to leaching of the catalyst and its eventual deactivation. Moreover, this raises the bigger question of the utility of the heterogenous catalyst if the atomic leaching is inevitable. While regeneration of catalyst is possible *via* redeposition of Pd on the support, the Suzuki-Miyaura cross-coupling is not a suitable model reaction to study heterogenous catalysts.

1.3.3 Nanopore formation in SiO_2 supports at high temperatures

Nanopore formation in Si wafers is conventionally achieved by using HF-H_2O_2 as etchants, catalyzed by metal particles[71–76]. Recently, there have been a few reports of nanopore formation in fused SiO_2 surfaces by heating of Au nanostructures to temperatures above 1000 ºC. de Vreede et al., have demonstrated the entrenchment of 1 μm Au discs in fused SiO_2 and silicon nitride substrates at 1050 ºC in air over 10 hours.[14] The authors hypothesize that the nanopore formation is driven by simultaneous melting and evaporation of the metal nanoparticles and partial melting of oxide support. The proposed mechanism extends the scope of nanoparticle material beyond Au. Thus, in principle, the entrenchment of metal nanoparticles, mainly discussed for gold, can be applied to any metal. The thermodynamic instability of small metal clusters on oxide supports leading to “sinking” was first observed in 1989 where gold nanoparticles were reported to be burrowing in MgO smoke particles on being subjected to electron beam irradiation.[77] The have also been other reports of gold[77–82] and copper[83,84] particles exhibiting some extent of entrenchment in the supporting oxide layers, although without nanopore formation, when subjected to temperatures above 900 ºC, without etchants or promoters.

Many literature reports in this field observe that metal entrenchment in oxide supports is accompanied by an oxide ridge-formation around the particle.[14,79,81–83,85–87] Small metal particles experience preferential melting at temperatures below their bulk melting temperature. It is hypothesized that due to a lowered surface energy, the metal oxide in contact with the small metal particle undergoes partial melting. This leads to formation of a triple line at the interface of the metal, gas (air, or inert gas) and oxide boundary.

To seek a configuration corresponding to the minimum energy, the supporting metal oxide gets transported along the triple line, forming an oxide ridge. This behavior is typically observed during high temperature dewetting of thin metal films.[86,87] However, for metal nanoparticles, simultaneous surface evaporation occurs along with nanoparticle melting, including the metal vapor now in the equilibrating system. As the metal evaporates, the triple line is constantly replenished. It is thus hypothesized that, there is a continuous metal oxide transport along the triple line that drives the nanoparticle inside the support layers causing the nanopore formation.[14] In principle, the nanopore formation will continue without reaching equilibrium until the nanoparticle reaches the underlying Si layer[14], the metal particle completely evaporates[81], or the particle burrows completely through the SiO_2 layer.[79] It is however unclear, in this proposed mechanism, how the oxide would undergo partial melting in presence of the metal nanoparticle at temperatures way below its melting point. Additionally, this hypothesized mechanism implies that nanopore formation would be possible in all oxides. However, this behavior has only been reported for SiO_2 supports. Thus, there might be a few missing pieces in the proposed mechanism.

While no nanopore formation is observed, local excavation of SiO_2 layers is observed when Au nanoparticles supported on thin films of SiO_2 on Si wafers are heated to high temperatures (> 1000 ºC).[80] It is hypothesized that this behavior arises from the reaction of the Au nanoparticles with the SiO_2 to cause desorption of SiO_2. While some metals are known to react with crystalline oxides to form nanopores by the reverse-vapor-liquid-solid mechanism,[88] no such reaction is known for Au on SiO_2. SiO_2 is inert towards most metals and no silicide formation is observed outside of reducing conditions for most noble metals (with the exception of Cu).[89,90] While Au will not react with SiO_2 under most conditions, it is reported to diffuse through SiO_2.[91] Since the thickness of SiO_2 is very small, the Au from the nanoparticles in this case can diffuse to the underlying Si layer and react with it to form AuSi. AuSi is known to cause decomposition of SiO_2, thus forming pits in the SiO_2 surface.[78] Although slightly different from the nanopore formation observed in amorphous SiO_2, the reaction of AuSi gives a new insight into the possible mechanism of nanopore formation.

1.3.4 The behaviors of metal nanoparticles on oxide supports at high temperatures

Metal-oxide and metal-metal interactions, especially at high temperatures, are of critical importance in catalysis[92–95] and electronics.[96,97] The metal-oxide interface is a catalytically active site for many industrially important reactions. At high temperatures, catalyst deactivation can occur *via* sintering or encapsulation due to surface rearrangement at the metal-oxide interface.[98–102] Similarly, thin films of metals deposited on oxide layers are used for the fabrication of electronic devices where the metal-semiconductor interface is of significance.[103,104] At high temperatures, the stability of these films is reduced by dewetting mechanisms.[85,86,105,106] Thus, studying the metal-oxide interactions at high temperatures is important for designing stable catalysts and electronic devices. To this end, these interactions have been studied for a wide range of metals (Au, Pd, Pt, Cu) and oxides (TiO_2, SiO_2, Al_2O_3) across different temperature ranges.[12,91,98–100,107–110]

The most commonly reported behavior arising out of simultaneously metal-metal and metal-support interactions is nanoparticle sintering. Nanoparticle sintering is characterized by a reduction in the number density of nanoparticles, accompanied by an increase in the nanoparticle size when the metal nanoparticles are heated at elevated temperatures (usually above 600 ºC).[12,98,107] The sintering of nanoparticles can occur by two pathways-1) particle migration and coalesce or 2) atomic migration (also known as Ostwald ripening).[12] There are many studies that have tried to elucidate how the two pathways dominate at different heating conditions or nanoparticle sizes. Datye et al., have performed *in situ* electron microscopy studies to understand this mechanism better.[111,112] Particle mobility begins at temperatures above the metal Tamman temperature (half of the melting temperature in Kelvin).[113] Literature in this field has shown that particle sintering *via* migration and coalescence mainly occurs for nanoparticles smaller than 6 nm[98] while Ostwald ripening that is most commonly observed for metal nanoparticles 1-10 nm in size and at temperature as low as 500 ºC.[110] [12,98,111,112,114] Overall, it is generally agreed upon that sintering occurs as a combination of both these processes, but Ostwald ripening is the dominant of the two processes.[12]

Sintering usually occurs when the metal-metal interactions are stronger than the metal-support interactions. However, in cases where the metal-support interactions are stronger, increasing temperatures lead to the encapsulation, partial or complete, of metal nanoparticle encapsulation on the supporting oxides

via strong metal surface interactions (SMSI).[100,101] This behavior is commonly observed for reducible oxides like TiO_2. Amongst the commonly used oxide supports the tendency of most metal nanoparticles to be encapsulated by the oxide is TiO_2> Al_2O_3> SiO_2.[101]

At high temperatures, due to increased mobility, metal ions also tend to diffuse into SiO_2 supports.[91,115–119] The diffusivities depend on the ionic radius of the metals as well as on the temperature of operation.[118] Literature reports have shown that Ag and Cu have much higher diffusivities than Pd, Au, and Pt.[91] The reported diffusivities of Ni and Co are even lower.[117,118] The diffusion of metals into SiO_2 is usually non-reactive and work done in this field has shown that under inert conditions, no silicide formation is observed for most metal nanoparticles.[89] The exception in this case is Cu. While there are literature reports showing that no copper silicide formation is observed when thin films of Cu deposited on SiO_2 are heated to 800 ºC for extended periods of time under vacuum,[89] there is also evidence of Cu reacting with SiO_2 to form mixed oxide as well as silicides.[120]

There also are instances in literature where, in the absence of all other behaviors, nanoparticle evaporation is observed at high temperatures in air or under vacuum. On extended annealing at 950 ºC in air, Au nanoparticles supported on sapphire are observed to undergo evaporation only on certain facets that are in contact with the support. It is hypothesized that the Au atoms from the side facets diffuse into the supporting sapphire and undergo evaporation from there.[121] In another report, photolithographically deposited patterns of Au supported on crystalline Al_2O_3 are observed to evaporate between 800- 950 ºC under vacuum. The authors show that under these conditions the diffusivity of the metal into the support is negligibly low compared to the evaporation.[122] Thus, there are many mechanisms, in addition to nanopore formation, that occur simultaneously or competitively at high temperatures due to the various interactions at the metal-oxide-vapor interface.

1.4 References

(1) Liz-Marzán, L. M. Tailoring Surface Plasmons through the Morphology and Assembly of Metal Nanoparticles. *Langmuir* **2006**, *22* (1), 32–41.

(2) Sevonkaev, I.; Privman, V.; Goia, D. Synthesis of Dispersed Metal Particles for Applications in

Photovoltaics, Catalysis, and Electronics. *J. Solid State Electrochem.* **2013**, *17* (2), 279–297.

(3) Astruc, D. *Transition - Metal Nanoparticles in Catalysis : From Historical Background to the State - of - the Art*; 2008.

(4) Astruc, D.; Lu, F.; Aranzaes, J. R. Nanoparticles as Recyclable Catalysts: The Frontier between Homogeneous and Heterogeneous Catalysis. *Angew. Chemie - Int. Ed.* **2005**, *44* (48), 7852–7872.

(5) Blanckenberg, A.; Malgas-Enus, R. Olefin Epoxidation with Metal-Based Nanocatalysts. *Catal. Rev. - Sci. Eng.* **2019**, *61* (1), 27–83.

(6) Rodriguez, J. A. Gold-Based Catalysts for the Water-Gas Shift Reaction: Active Sites and Reaction Mechanism. *Catal. Today* **2011**, *160* (1), 3–10.

(7) Hussain, M. A.; Joseph, N.; Kang, O.; Cho, Y. H.; Um, B. H.; Kim, J. W. Supported Metal Nanoparticles: Their Catalytic Applications to Selective Alcohol Oxidation. *Appl. Chem. Eng.* **2016**, *27* (3), 227–238.

(8) Baffou, G.; Quidant, R. Nanoplasmonics for Chemistry. *Chem. Soc. Rev.* **2014**, *43* (11), 3898–3907.

(9) Noguez, C. Optical Properties of Isolated and Supported Metal Nanoparticles. *Opt. Mater. (Amst).* **2005**, *27* (7), 1204–1211.

(10) Lu, J. Q.; Yi, S. S. Uniformly Sized Gold Nanoparticles Derived from PS-b-P2VP Block Copolymer Templates for the Controllable Synthesis of Si Nanowires. *Langmuir* **2006**, *22* (9), 3951–3954.

(11) Kluender, E. J.; Hedrick, J. L.; Brown, K. A.; Rao, R.; Meckes, B.; Du, J. S.; Moreau, L. M.; Maruyama, B.; Mirkin, C. A. Catalyst Discovery through Megalibraries of Nanomaterials. *Proc. Natl. Acad. Sci.* **2019**, *116* (1), 40–45.

(12) Goeke, R. S.; Datye, A. K. Model Oxide Supports for Studies of Catalyst Sintering at Elevated Temperatures. *Top. Catal.* **2007**, *46* (1–2), 3–9.

(13) Miyaura, N.; Suzuki, A. Palladium-Catalyzed Cross-Coupling Reactions of Organoboron Compounds. *Chem. Rev.* **1995**, *95* (7), 2457–2483.

(14) de Vreede, L. J.; Van Den Berg, A.; Eijkel, J. C. T. Nanopore Fabrication by Heating Au Particles on Ceramic Substrates. *Nano Lett.* **2015**, *15*, 727–731.

(15) Kamyshny, A.; Ben-Moshe, M.; Aviezer, S.; Magdassi, S. Ink-Jet Printing of Metallic Nanoparticles and Microemulsions. *Macromol. Rapid Commun.* **2005**, *26* (4), 281–288.

(16) Han, S. T.; Zhou, Y.; Xu, Z. X.; Huang, L. B.; Yang, X. B.; Roy, V. A. L. Microcontact Printing of

Ultrahigh Density Gold Nanoparticle Monolayer for Flexible Flash Memories. *Advanced Materials*. 2012, pp 3556–3561.

(17) Niekiel, F.; Schweizer, P.; Kraschewski, S. M.; Butz, B.; Spiecker, E. The Process of Solid-State Dewetting of Au Thin Films Studied by in Situ Scanning Transmission Electron Microscopy. *Acta Mater.* **2015**, *90*, 118–132.

(18) Corbierre, M. K.; Beerens, J.; Lennox, R. B. Gold Nanoparticles Generated by Electron Beam Lithography of Gold(I)-Thiolate Thin Films. *Chem. Mater.* **2005**, *17* (23), 5774–5779.

(19) Wu, Y.; Fowlkes, J. D.; Rack, P. D. The Optical Properties of Cu-Ni Nanoparticles Produced via Pulsed Laser Dewetting of Ultrathin Films: The Effect of Nanoparticle Size and Composition on the Plasmon Response. *J. Mater. Res.* **2011**, *26* (2), 277–287.

(20) Kojima, Y.; Kato, T. Nanoparticle Formation in Au Thin Films by Electron-Beam-Induced Dewetting. *Nanotechnology* **2008**, *19* (25).

(21) Ye, J.; Thompson, C. V. Templated Solid-State Dewetting to Controllably Produce Complex Patterns. *Adv. Mater.* **2011**, *23* (13), 1567–1571.

(22) Giermann, A. L.; Thompson, C. V. Solid-State Dewetting for Ordered Arrays of Crystallographically Oriented Metal Particles. *Appl. Phys. Lett.* **2005**, *86* (12), 1–3.

(23) Kwon, S. H.; Han, D. H.; Choe, H. J.; Lee, J. J. Synthesis of Copper Nanoparticles by Solid-State Plasma-Induced Dewetting. *Nanotechnology* **2011**, *22* (24).

(24) Feng, T.; Ding, L.; Chen, L.; Di, J. Deposition of Gold Nanoparticles upon Bare and Indium Tin Oxide Film Coated Glass Based on Annealing Process. *J. Exp. Nanosci.* **2019**, *14* (1), 13–22.

(25) Chen, P. C.; Liu, G.; Zhou, Y.; Brown, K. A.; Chernyak, N.; Hedrick, J. L.; He, S.; Xie, Z.; Lin, Q. Y.; Dravid, V. P.; et al. Tip-Directed Synthesis of Multimetallic Nanoparticles. *J. Am. Chem. Soc.* **2015**, *137* (28), 9167–9173.

(26) Mirkin, C. A.; Chen, P.-C.; Liu, X.; Hedrick, J. L.; Xie, Z.; Wang, S.; Lin, Y.; Hersam, M. C.; Dravid, V. P. Polyelemental Nanoparticle Libraries. *Science (80-.).* **2016**, *352* (June), 1565–1569.

(27) Spatz, J. P.; Roescher, A.; Moller, M. Gold Nanoparticles in Micellar Poly(Styrene)-b-Poly(Ethylene Oxide) Films-Size and Interparticle Distance Control in Monoparticulate Films. *Adv. Mater.* **1996**, *8* (4), 337–340.

(28) Aizawa, M.; Buriak, J. M. Block Copolymer Templated Chemistry for the Formation of Metallic Nanoparticle Arrays on Semiconductor Surfaces. *Chem. Mater.* **2007**, *19* (21), 5090–5101.

(29) Li, X.; Iocozzia, J.; Chen, Y.; Zhao, S.; Cui, X.; Wang, W.; Yu, H.; Lin, S.; Lin, Z. From Precision Synthesis of Block Copolymers to Properties and Applications of Nanoparticles. *Angew. Chemie - Int. Ed.* **2018**, *57* (8), 2046–2070.

(30) Hedrick, J. L.; Brown, K. A.; Kluender, E. J.; Cabezas, M. D.; Chen, P. C.; Mirkin, C. A. Hard Transparent Arrays for Polymer Pen Lithography. *ACS Nano* **2016**, *10* (3), 3144–3148.

(31) Saha, S. K.; Culpepper, M. L. A Surface Diffusion Model for Dip Pen Nanolithography Line Writing. *Appl. Phys. Lett.* **2010**, *96* (24), 1–3.

(32) Liu, G.; Eichelsdoerfer, D. J.; Rasin, B.; Zhou, Y.; Brown, K. A.; Liao, X.; Mirkin, C. A. Delineating the Pathways for the Site-Directed Synthesis of Individual Nanoparticles on Surfaces. *Proc. Natl. Acad. Sci. U. S. A.* **2013**, *110* (3), 887–891.

(33) Chai, J.; Huo, F.; Zheng, Z.; Giam, L. R.; Shim, W.; Mirkin, C. A. Scanning Probe Block Copolymer Lithography. *Proc. Natl. Acad. Sci.* **2010**, *107* (47), 20202–20206.

(34) Huo, F.; Zheng, Z.; Zheng, G.; Giam, L. R.; Zhang, H.; Mirkin, C. A. Polymer Pen Lithography. *Science (80-.).* **2008**, *321* (5896), 1658–1660.

(35) Piner, R. D.; Zhu, J.; Xu, F.; Hong, S. “Dip-Pen” Nanolithography. *Science (80-.).* **1999**, *283* (January), 661–663.

(36) Spatz, J. P.; Mößmer, S.; Möller, M. Mineralization of Gold Nanoparticles in a Block Copolymer Microemulsion. *Chem. - A Eur. J.* **1996**, *2* (12), 1552–1555.

(37) Bronstein, L. M.; Sidorov, S. N.; Valetsky, P. M.; Hartmann, J.; Cölfen, H.; Antonietti, M. Induced Micellization by Interaction of Poly(2-Vinylpyridine)- Block -Poly(Ethylene Oxide) with Metal Compounds. Micelle Characteristics and Metal Nanoparticle Formation . *Langmuir* **2002**, *15* (19), 6256–6262.

(38) Perl, A.; Reinhoudt, D. N.; Huskens, J. Microcontact Printing: Limitations and Achievements. *Adv. Mater.* **2009**, *21* (22), 2257–2268.

(39) Santhanam, V.; Andres, R. P. Microcontact Printing of Uniform Nanoparticle Arrays. *Nano Lett.* **2004**, *4* (1), 41–44.

(40) Cong, P.; Doolen, R. D.; Fan, Q.; Giaquinta, D. M.; Guan, S.; Mcfarland, E. W.; Poojary, D. M.; Self, K.; Turner, H. W.; Weinberg, W. H. High-Throughput Synthesis and Screening of Combinatorial Heterogeneous Catalyst Libraries. *Angew. Chemie* **1999**, *38* (4), 483–488.

(41) Spatz, J. P.; Mössmer, S.; Hartmann, C.; Möller, M.; Herzog, T.; Krieger, M.; Boyen, H. G.; Ziemann,

P.; Kabius, B. Ordered Deposition of Inorganic Clusters from Micellar Block Copolymer Films. *Langmuir* **2000**, *16* (2), 407–415.

(42) Krishnamoorthy, S.; Hinderling, C.; Heinzelmann, H. Nanoscale Patterning with Block Copolymers. *Mater. Today* **2006**, *9* (9), 40–47.

(43) Krishnamoorthy, S.; Pugin, R.; Brugger, J.; Heinzelmann, H.; Hinderling, C. Tuning the Dimensions and Periodicities of Nanostructures Starting from the Same Polystyrene-Block-Poly(2-Vinylpyridine) Diblock Copolymer. *Adv. Funct. Mater.* **2006**, *16* (11), 1469–1475.

(44) Lo Celso, F.; Triolo, A.; Bronstein, L.; Zwanziger, J.; Strunz, P.; Lin, J. S.; Crapanzano, L.; Triolo, R. Investigating Self-Assembly and Metal Nanoclusters in Aqueous Di-Block Copolymers Solutions. *Appl. Phys. A Mater. Sci. Process.* **2002**, *74* (SUPPL.I), 540–542.

(45) Behafarid, F.; Roldan Cuenya, B. Towards the Understanding of Sintering Phenomena at the Nanoscale: Geometric and Environmental Effects. *Top. Catal.* **2013**, *56* (15–17), 1542–1559.

(46) Bhaviripudi, S.; Reina, A.; Qi, J.; Kong, J.; Belcher, A. M. Block-Copolymer Assisted Synthesis of Arrays of Metal Nanoparticles and Their Catalytic Activities for the Growth of SWNTs. *Nanotechnology* **2006**, *17* (20), 5080–5086.

(47) Giam, L. R.; Massich, M. D.; Hao, L.; Shin Wong, L.; Mader, C. C.; Mirkin, C. A. Scanning Probe-Enabled Nanocombinatorics Define the Relationship between Fibronectin Feature Size and Stem Cell Fate. *Proc. Natl. Acad. Sci.* **2012**, *109* (12), 4377–4382.

(48) Miyaura, N.; Yamada, K.; Suzuki, A. A New Stereospecific Cross-Coupling by the Palladium-Catalyzed Reaction of 1-Alkenylboranes with 1-Alkenyl or 1-Alkynyl Halides. *Tetrahedron Lett.* **1979**, *20* (36), 3437–3440.

(49) Colacot, T. J.; Matthey, J. The 2010 Nobel Prize in Chemistry: Palladium-Catalysed Cross-Coupling the Importance of Carbon-Carbon Coupling for Real World Applications. *Platin. Met. Rev.* **2011**, *55* (2), 84–90.

(50) Colacot, T. J.; Seechurn, J. C.; Deangelis, A. *Introduction to New Trends in Cross-Coupling*; 2015.

(51) Astruc, D. Palladium Nanoparticles as Efficient Green Homogeneous and Heterogeneous C-C Coumplex Precatalysis: A Unifying View. *Inorganic Chemistry.* 2007, p 1884.

(52) Rouhi, A. M. Fine Chemicals. *Chem. Eng. News* **2003**, *82* (36), 37–49.

(53) Handa, S.; Smith, J.; Hageman, M.; Gonzalez, M.; Lipshutz, B. H. Synergistic and Selectrive Copper/Ppm Pd-Catalyzed Suzuki-Miyaura Couplings: In Water, Mild Conditions, with Recycling.

ACS Catal. **2016**, *6* (6), 8179–8183.

(54) Suzuki, A. Recent Advances in the Cross-Coupling Reactions of Organoboron Derivatives with Organic Electrophiles, 1995–1998. *J. Organomet. Chem.* **1999**, *576* (1–2), 147–168.

(55) Phan, N. T. S.; Van Der Sluys, M.; Jones, C. W. On the Nature of the Active Species in Palladium Catalyzed Mizoroki-Heck and Suzuki-Miyaura Couplings - Homogeneous or Heterogeneous Catalysis, a Critical Review. *Adv. Synth. Catal.* **2006**, *348* (6), 609–679.

(56) Handa, S.; Slack, E. D.; Lipshutz, B. H. Nanonickel-Catalyzed Suzuki-Miyaura Cross-Couplings in Water. *Angew. Chemie - Int. Ed.* **2015**, *54* (41), 11994–11998.

(57) Wang, S.; Zhu, W.; Ke, J.; Lin, M.; Zhang, Y. Pd − Rh Nanocrystals with Tunable Morphologies and Compositions as E Ffi Cient Catalysts toward Suzuki Cross-Coupling Reactions. *ACS Catal.* **2014**, *4*, 2298–2306.

(58) Constable, D. J. C.; Dunn, P. J.; Hayler, J. D.; Humphrey, G. R.; Leazer, Jr., J. L.; Linderman, R. J.; Lorenz, K.; Manley, J.; Pearlman, B. a.; Wells, A.; et al. Key Green Chemistry Research Areas: A Perspective from Pharmaceutical Manufacturers. *Green Chem.* **2007**, *9* (5), 411–420.

(59) de Vries, J. G. A Unifying Mechanism for All High-Temperature Heck Reactions. The Role of Palladium Colloids and Anionic Species. *Dalton Trans.* **2006**, No. 3, 421–429.

(60) Niembro, S.; Shafir, A.; Vallribera, A. Catalytically Active Palladium Nanoparticles Embedded in an Organic-Inorganic Fluorinated Hybrid Material. *Arkivoc* **2010**, *2010* (3), 181–190.

(61) Narayanan, R.; El-sayed, M. A. Effect of Catalysis on the Stability of Metallic Nanoparticles : Suzuki Reaction Catalyzed by PVP-Palladium Nanoparticles. **2003**, 8340–8347.

(62) Pröckl, S. S.; Kleist, W.; Gruber, M. A.; Köhler, K. In Situ Generation of Highly Active Dissolved Palladium Species from Solid Catalysts—A Concept for the Activation of Aryl Chlorides in the Heck Reaction. *Angew. Chemie - Int. Ed.* **2004**, *43*, 1881–1882.

(63) Mandali, P. K.; Chand, D. K. Palladium Nanoparticles Catalyzed Suzuki Cross-Coupling Reactions in Ambient Conditions. *Catal. Commun.* **2013**, *31*, 16–20.

(64) Hooshmand, S. E.; Heidari, B.; Sedghi, R.; Varma, R. S. Recent Advances in the Suzuki-Miyaura Cross-Coupling Reaction Using Efficient Catalysts in Eco-Friendly Media. *Green Chem.* **2019**, *21* (3), 381–405.

(65) Dell'Anna, M. M.; Mali, M.; Mastrorilli, P.; Rizzuti, A.; Ponzoni, C.; Leonelli, C. Suzuki-Miyaura Coupling under Air in Water Promoted by Polymer Supported Palladium Nanoparticles. *J. Mol.*

Catal. A Chem. **2013**, *366*, 186–194.

(66) Thathagar, M. B.; Elshof, J. E.; Rothenberg, G. Pd Nanoclusters in C-C Coupling Reactions: Proof of Leaching. *Angew. Chemie - Int. Ed.* **2006**, *45*, 2886–2890.

(67) Kohler, K.; Heidenreich, R. G.; Krauter, J. G. E.; Pietsch, J. Highly Active Palladium / Activated Carbon Catalysts for Heck Reactions : Correlation of Activity, Catalyst Properties, and Pd Leaching. *Chem. - A Eur. J.* **2002**, *8* (3), 622–631.

(68) Mcglacken, G. P. Pd (0) Nanoparticles (NPs) as Catalysts in Cross-Coupling Reactions and the Homogeneous vs . Heterogeneous Debate. *Organomet. Chem.* **2016**, *40* (0), 33–53.

(69) Niu, Z.; Peng, Q.; Zhuang, Z.; He, W.; Li, Y. Evidence of an Oxidative-Addition-Promoted Pd-Leaching Mechanism in the Suzuki Reaction by Using a Pd-Nanostructure Design. *Chem. - A Eur. J.* **2012**, *18* (32), 9813–9817.

(70) Gaikwad, A. V.; Holuigue, A.; Thathagar, M. B.; Ten Elshof, J. E.; Rothenberg, G. Ion- and Atom-Leaching Mechanisms from Palladium Nanoparticles in Cross-Coupling Reactions. *Chem. - A Eur. J.* **2007**, *13* (24), 6908–6913.

(71) James, T.; Kalinin, Y. V.; Chan, C. C.; Randhawa, J. S.; Gaevski, M.; Gracias, D. H. Voltage-Gated Ion Transport through Semiconducting Conical Nanopores Formed by Metal Nanoparticle-Assisted Plasma Etching. *Nano Lett.* **2012**, *12* (7), 3437–3442.

(72) Scheeler, S. P.; Ullrich, S.; Kudera, S.; Pacholski, C. Fabrication of Porous Silicon by Metal-Assisted Etching Using Highly Ordered Gold Nanoparticle Arrays. *Nanoscale Res. Lett.* **2012**, *7* (1), 450.

(73) Tsujino, K.; Matsumura, M. Boring Deep Cylindrical Nanoholes in Silicon Using Silver Nanoparticles as a Catalyst. *Adv. Mater.* **2005**, *17* (8), 1045–1047.

(74) Tsujino, K.; Matsumura, M. Morphology of Nanoholes Formed in Silicon by Wet Etching in Solutions Containing HF and H2O2 at Different Concentrations Using Silver Nanoparticles as Catalysts. *Electrochim. Acta* **2007**, *53* (1), 28–34.

(75) Nikoobakht, B.; Herzing, A.; Muramoto, S.; Tersoff, J. Vapor-Liquid-Solid Etch of Semiconductor Surface Channels by Running Gold Nanodroplets. *Nano Lett.* **2015**, *15* (12), 8360–8364.

(76) Chartier, C.; Bastide, S.; Lévy-Clément, C. Metal-Assisted Chemical Etching of Silicon in HF-H2O2. *Electrochim. Acta* **2008**, *53* (17), 5509–5516.

(77) Ajayan, P. M.; Makrs, L. D. Evidence for Sinking of Small Particles into Substrates and Implications for Heterogeneous Catalysis. *Nature* **1989**, *338*, 139–141.

(78) Babor, P.; Duda, R.; Polcak, J.; Prusa, S.; Potocek, M.; Varga, P.; Chechal, J.; Sikola, T. Real-Time Observation of Self-Limiting SiO2/Si Decomposition Catalysed by Gold Silicide Droplets. *RSC Adv.* **2015**, *5*, 101726–101731.

(79) de Vreede, L. J.; Schmidt Muniz, M.; Van Den Berg, A.; Eijkel, J. C. T. Nanopore Fabrication in Silicon Oxynitride Membranes by Heating Au-Particles. *J. Micromechanics Microengineering* **2016**, *26*, 37001–37006.

(80) Ono, L. K.; Behafarid, F.; Cuenya, B. R. Nano-Gold Diggers: Au-Assisted SiO2-Decomposition and Desorption in Supported Nanocatalysts. *ACS Nano* **2013**, *7* (11), 10327–10334.

(81) Sui, M.; Pandey, P.; Li, M. Y.; Zhang, Q.; Kunwar, S.; Lee, J. Au-Assisted Fabrication of Nano-Holes on c-Plane Sapphire via Thermal Treatment Guided by Au Nanoparticles as Catalysts. *Appl. Surf. Sci.* **2017**, *393*, 23–29.

(82) Ilkiv, I.; Kotlyar, K.; Amel'chuk, D.; Lebedev, S.; Cirlin, G.; Bouravleuv, A. Thermal Penetration of Gold Nanoparticles into Silicon Dioxide. *Acta Phys. Pol. A* **2017**, *132* (2), 366–368.

(83) Curiotto, S.; Chien, H.; Meltzman, H.; Labat, S.; Wynblatt, P.; Rohrer, G. S.; Kaplan, W. D.; Chatain, D. Copper Crystals on the (1120) Sapphire Plane: Orientation Relationships, Triple Line Ridges and Interface Shape Equilibrium. *J. Mater. Sci.* **2013**, *48* (7), 3013–3026.

(84) Ghetta, V.; Chatain, D. Morphologies Adopted by Al2O3 Single-Crystal Surfaces in Contact with Cu Droplets. *J. Am. Ceram. Soc.* **2004**, *85* (4), 961–964.

(85) Kunwar, S.; Pandey, P.; Sui, M.; Zhang, Q.; Li, M. Y.; Lee, J. Effect of Systematic Control of Pd Thickness and Annealing Temperature on the Fabrication and Evolution of Palladium Nanostructures on Si (111) via the Solid State Dewetting. *Nanoscale Res. Lett.* **2017**, *12* (1), 364–378.

(86) Saiz, E.; Tomsia, a. P.; Cannon, R. M. Ridging Effects on Wetting and Spreading of Liquids on Solids. *Acta Mater.* **1998**, *46* (7), 2349–2361.

(87) Saiz, E.; Tomsia, A. P.; Cannon, R. M. Triple Line Ridging and Attachment in High-Temperature Wetting. *Scr. Mater.* **2001**, *44* (1), 159–164.

(88) Yu, L.; Riddle, A. J.; Wang, S.; Sundararajan, A.; Thompson, J.; Chang, Y. J.; Park, M. E.; Seo, S. S. A.; Guiton, B. S. Solid-Liquid-Vapor Synthesis of Negative Metal Oxide Nanowire Arrays. *Chem. Mater.* **2016**, *28* (24), 8924–8929.

(89) Pretorius, R.; Harris, J. M.; Nicolet, M. A. Reaction of Thin Metal Films with SiO2 Substrates. *Solid State Electron.* **1978**, *21* (4), 667–675.

(90) Van Den Oetelaar, L. C. A.; Van Den Oetelaar, R. J. A.; Partridge, A.; Flipse, C. F. J.; Brongersma, H. H. Reaction of Nanometer-Sized Cu Particles with a SiO2substrate. *Appl. Phys. Lett.* **1999**, *74* (20), 2954–2956.

(91) McBrayer, J. D. Diffusion of Metals in Silicon Dioxide. *J. Electrochem. Soc.* **1986**, *133* (6), 1242.

(92) Flynn, P. C. The Sintering of Supported Metal Catalysts. *Catal. Rev.* **1975**, *12* (1), 93–135.

(93) Wynblatt, P. Particle Growth in Model Supported Comparison of Experiment. *Acta Met.* **1976**, *24*, 1175--1182.

(94) Schauermann, S.; Nilius, N.; Shaikhutdinov, S.; Freund, H. J. Nanoparticles for Heterogeneous Catalysis: New Mechanistic Insights. *Acc. Chem. Res.* **2013**, *46* (8), 1673–1681.

(95) Coq, B. Structure – Activity Relationships in Catalysis by Metals : Some Aspects of Particle Size , Bimetallic and Supports Effects. *Coord. Chem. Rev.* **1998**, *180*, 1753–1783.

(96) Zhou, Y.; Ramanathan, S. Correlated Electron Materials and Field Effect Transistors for Logic: A Review. *Crit. Rev. Solid State Mater. Sci.* **2013**, *38* (4), 286–317.

(97) Dieny, B.; Chshiev, M. Perpendicular Magnetic Anisotropy at Transition Metal/Oxide Interfaces and Applications. *Rev. Mod. Phys.* **2017**, *89* (2).

(98) Hansen, T. W.; Delariva, A. T.; Challa, S. R.; Datye, A. K. Sintering of Catalytic Nanoparticles: Particle Migration or Ostwald Ripening? *Acc. Chem. Res.* **2013**, *46* (8), 1720–1730.

(99) Powell, B. R.; Whittington, S. E. Encapsulation: A New Mechanism of Catalyst Deactivation. *J. Catal.* **1983**, *81* (2), 382–393.

(100) Tauster, S. J.; Fung, S. C.; Garten, R. L. Strong Metal-Support Interactions. Group 8 Noble Metals Supported on TiO2. *J. Am. Chem. Soc.* **1978**, *100* (1), 170–175.

(101) Pan, C. J.; Tsai, M. C.; Su, W. N.; Rick, J.; Akalework, N. G.; Agegnehu, A. K.; Cheng, S. Y.; Hwang, B. J. Tuning/Exploiting Strong Metal-Support Interaction (SMSI) in Heterogeneous Catalysis. *J. Taiwan Inst. Chem. Eng.* **2017**, *74*, 154–186.

(102) Panpranot, J.; Phandinthong, K.; Sirikajorn, T.; Arai, M.; Praserthdam, P. Impact of Palladium Silicide Formation on the Catalytic Properties of Pd/SiO2catalysts in Liquid-Phase Semihydrogenation of Phenylacetylene. *J. Mol. Catal. A Chem.* **2007**, *261* (1), 29–35.

(103) Fu, Q.; Wagner, T. Interaction of Nanostructured Metal Overlayers with Oxide Surfaces. *Surf. Sci. Rep.* **2007**, *62* (11), 431–498.

(104) Anton, R. Interaction of Gold, Palladium and Au-Pd Alloy Deposits with Oxidized Si(100) Substrates. *Thin Solid Films* **1984**, *120* (4), 293–311.

(105) Karakouz, T.; Tesler, A. B.; Sannomiya, T.; Feldman, Y.; Vaskevich, A.; Rubinstein, I. Mechanism of Morphology Transformation during Annealing of Nanostructured Gold Films on Glass. *Phys. Chem. Chem. Phys.* **2013**, *15* (13), 4656–4665.

(106) Harrisp, J. M.; Pretorius, R.; Nicole. Reaction of Thin Metal Films with SiO2 Substrates. *Solid-State Electrotronics* **1978**, *21* (1), 667–675.

(107) Helveg, S.; Chorkendorff, I.; Skoglundh, M.; Simonsen, S. B.; Dahl, S. Coarsening of Pd Nanoparticles in an Oxidizing Atmosphere Studied by in Situ TEM. *Surf. Sci.* **2015**, *648* (June), 278–283.

(108) Levy, D.; Grob, A.; Grob, J. J.; Ponpon, J. P. Formation of Palladium Silicide by Rapid Thermal Annealing. *Appl. Phys. A Solids Surfaces* **1984**, *35* (3), 141–144.

(109) Tromp, R.; Rubloff, G. W.; Balk, P.; LeGoues, F. K.; Van Loenen, E. J. High-Temperature SiO2 Decomposition at the SiO2/Si Interface. *Phys. Rev. Lett.* **1985**, *55* (21), 2332–2335.

(110) Min, B. K.; Santra, A. K.; Goodman, D. W. Understanding Silica-Supported Metal Catalysts: Pd/Silica as a Case Study. *Catal. Today* **2003**, *85* (2–4), 113–124.

(111) Delariva, A. T.; Hansen, T. W.; Challa, S. R.; Datye, A. K. In Situ Transmission Electron Microscopy of Catalyst Sintering. *J. Catal.* **2013**, *308*, 291–305.

(112) Benavidez, A. D.; Kovarik, L.; Genc, A.; Agrawal, N.; Larsson, E. M.; Hansen, T. W.; Karim, A. M.; Datye, A. K. Environmental Transmission Electron Microscopy Study of the Origins of Anomalous Particle Size Distributions in Supported Metal Catalysts. *ACS Catal.* **2012**, *2* (11), 2349–2356.

(113) Baker, R. T. K. The Relationship between Particle Motion on a Graphite Surface and Tammann Temperature. *J. Catal.* **1982**, *78* (2), 473–476.

(114) Xu, Q.; Kharas, K. C.; Croley, B. J.; Datye, A. K. The Sintering of Supported Pd Automotive Catalysts. *ChemCatChem* **2011**, *3* (6), 1004–1014.

(115) Sears, W. M.; Love, D. A. Rapid Migration of Silver on Roughened Glass Surfaces in a Methanol/Air Mixture near 500°C. *J. Appl. Phys.* **1995**, *77* (6), 2407–2414.

(116) Kato, H.; Oizumi, Y.; Umetani, S.; Yamada, K.; Hashimoto, I.; Homma, Y. Thermal Behavior of Metal Layers Sandwiched by Silicon Dioxide Layers. *Jpn. J. Appl. Phys.* **2015**, *54* (8), 2–5.

(117) Ghoshtagore, R. N. Diffusion of Nickel in Amorphous Silicon Dioxide and Silicon Nitride Films. *J.*

Appl. Phys. **1969**, *40* (11), 4374–4376.

(118) Baten, J.; Offenberg, M.; Emmerichs, U.; Balk, P.; Grunthaner, P. J.; Ewert, S. Diffusion of Cobalt and Titanium in SiO2. *Appl. Surf. Sci.* **1989**, *39* (1–4), 266–272.

(119) Atkinson, A.; Gardner, J. W. The Diffusion of Fe3+ in Amorphous SiO2 and the Protective Properties of SiO2 Layers. *Corros. Sci.* **1981**, *21* (1), 49–58.

(120) van den Oetelaar, L. C. A.; van den Oetelaar, R. J. A.; Partridge, A.; Flipse, C. F. J.; Brongersma, H. H. Reaction of Nanometer-Sized Cu Particles with a SiO2 Substrate. *Appl. Phys. Lett.* **1999**, *74* (20), 2954–2956.

(121) Malyi, O.; Rabkin, E. The Effect of Evaporation on Size and Shape Evolution of Faceted Gold Nanoparticles on Sapphire. *Acta Mater.* **2012**, *60* (1), 261–268.

(122) Meng, G.; Yanagida, T.; Kanai, M.; Suzuki, M.; Nagashima, K.; Xu, B.; Zhuge, F.; Klamchuen, A.; He, Y.; Rahong, S.; et al. Pressure-Induced Evaporation Dynamics of Gold Nanoparticles on Oxide Substrate. *Phys. Rev. E - Stat. Nonlinear, Soft Matter Phys.* **2013**, *87*.

Chapter Two: Metal Nanoparticle Synthesis by Block Copolymer Micelle Lithography

Abha Gosavi, Justin Notestein, Chad Mirkin

2.1 Introduction

Evenly distributed and uniformly sized metal nanoparticles supported on planar substrates (Si wafer, quartz, sapphire, and ITO) serve as model platforms to study various phenomena like sintering,[1] catalytic activity,[2] photochemical activity,[3,4] and electronic properties.[5] These nanoparticles can be synthesized by a range of different techniques, like ink-jet printing,[6] micro-contact printing,[7] atomic layer deposition (ALD),[8] solid-state dewetting of thin films,[9–12] block copolymer micelle lithography,[13–29] scanning probe block copolymer lithography (SPBCL),[30–32] and electron beam lithography.[33,34] Each of these routes offer different levels of controls over the nanoparticle size, uniformity, location, and composition. Many of these techniques are fast and involve fewer steps (for example, block copolymer lithography, dewetting of thin films) but enable limited control over the uniformity of nanoparticle size and spacing. Other techniques, like SPBCL, electron beam lithography, and microcontact printing involve multiple steps but generate nanoparticles of very uniform sizes with precise location control.

The different compositions of nanoparticles that can be accessed using a specific technique is also of some consequence. Using block copolymer lithography enables one to synthesize metal, metal oxides, metal sulfides, as well as multi-metallic nanoparticles, while other techniques are limited to only certain metals or compositions.[24] Additionally, with block copolymer lithography, the shape and the spatial arrangements of the nanoparticles can be controlled. Core-shell, hollow, and anisotropic nanoparticles can be generated by this technique in the minimum number of steps.[24]

Another important consideration while choosing the appropriate method for nanoparticle synthesis is the potential contaminants that may be left on the surface from the process. Block copolymer-mediated methods involve a polymer removal by oxidation or reduction using plasma[17,29] and high temperature

decomposition.[35] Incomplete removal of block copolymer may result in organic or carbon residue that can cause poisoning of catalytic activity of the nanoparticles. Similarly, contamination from inefficient removal of photoresist and developer, can introduce contamination in the nanoparticles. On the other hand, metal nanoparticles with no contaminants can be achieved by using ALD and templated evaporation-deposition, especially if carried out under clean-room conditions.

In this work, we explore the versatility of block copolymer micelle lithography in obtaining well dispersed metal nanoparticles on Si wafers with a thermal oxide layer. Two block copolymer systems were investigated- PS-*b*-P2VP and PEO-*b*-P2VP. PS-*b*-P2VP is soluble in organic solvents (toluene, THF, etc.) while PEO-*b*-P2VP is water soluble. We use varying chain lengths of each of the block copolymer and study the nanoparticle formation at different metal loadings, P2VP:metal ratios, and different dilutions. In both cases, the metal precursors are known to coordinate with the pyridine in the P2VP block.[24] The control over nanoparticle size, uniformity, arrangement, and composition for the two systems were compared. We also investigated two different methods of polymer removal. Block copolymer removal, either with O_2 or H_2 plasma is usually used for obtained metal nanoparticles from the micelles.[15,17,29] However, we observe that using plasma causes the supporting SiO_2 surface to coarsen. In previous our previous work, we have shown that a two-step annealing process in Ar and H_2 is effective in not only removing the block copolymer from SPBCL patterned polymer nano-reactors but also in forming single nanoparticles per spot.[31,35] In this chapter, we extend this two-step annealing method to remove the block copolymer from assembled metal-polymer micelles and observe that we see uniformly distributed metal nanoparticles instead of the commonly observed raspberry-like arrangement of metal nanoparticles.[24] Thus, we present an alternate way to remove the block copolymer to obtain uniform arrays of solid metal nanoparticles by two-step annealing.

We observed that while metal nanoparticles synthesized by using PS-*b*-P2VP exhibit the desired hexagonal spatial arrangement and uniform feature sizes, there is residual polymer is not completely removed even after extensive annealing at temperatures above the thermal decomposition temperature of the polymer The nanoparticles synthesized using PEO-*b*-P2VP, on the other hand, are randomly spatially

distributed but have uniform sizes. The two-step annealing process used for polymer removal is successful and no polymer residue is observed. Using PEO-*b*-P2VP block copolymer of different chain lengths and by varying the M: P2VP ratio, we can achieve a variety of metal nanoparticles (Pd, Au, Pt, Cu, Co, Ni, Ag) of different sizes and surface densities. Despite the lack of uniform spatial arrangement, the metal nanoparticles synthesis using PEO-*b*-P2VP micelle lithography is highly controllable and versatile. The variety of metal nanoparticles thus produced serve as model systems to study the stabilization of nanoparticle catalysts on modified Si wafers.

2.2 Methods

2.2.1 Synthesis of metal-block copolymer micelles

Aqueous solutions of metal-block copolymer micelles were synthesized by combining the diblock copolymer, polyethylene oxide-*b*-polyvinyl pyridine (PEO-*b*-P2VP) of varying chain lengths (PEO(1.8K)-*b*-P2VP(1.0K), PEO(2.8K)-*b*-P2VP(1.5K), PEO(14K)-*b*-P2VP(2.5K), PEO(7K)-*b*-P2VP(3.5K), PEO(21K)-*b*-P2VP(13.5K)) (Polymer Source, Inc.) and water soluble metal precursors (Na_2PdCl_4, $HAuCl_4$, H_2PtCl_6, $CuNO_3$, $Co(NO_3)_2$ $Ni(NO_3)_2$, $AgNO_3$) (Sigma Aldrich) at different pyridyl: M ratios (64:1, 32:1, 16:1, 8:1, 4:1, 2:1, 1:1, and 0.5:1) in nanopore water. The pH of the inks was maintained between 4-5 by adding dilute HCl and these were shaken for 16 h to allow micelle formation.

Organic solutions of metal-block copolymer micelle solutions were similarly synthesized by mixing polystyrene-polyvinyl pyridine (PS-*b*-P2VP) of different chain lengths (PS(32.5K)-*b*-P2VP(12K), PS(185K)-*b*-P2VP(32K), PS(110K)-*b*-P2VP(52K), PS(43K)-*b*-P2VP(69K)) (Polymer Source, Inc.) and metal precursors ($Pd(Ac)_2$, $HAuCl_4$, H_2PtCl_6) (Sigma Aldrich) and different pyridyl: M ratios (64:1, 32:1, 16:1, 4:1, 2:1, and 0.5:1) in toluene. These solutions were shaken for 16 h to allow micelle formation.

2.2.2 Nanoparticle assembly on Si wafer

Thin films of the M-micelle solution were spin-cast on Si wafers (NOVA Electronic Materials, 285 nm thermal oxide) at different rotation speeds (1000 RPM for aqueous solutions and 4000 RPM for toluene solutions). Two different methods of block copolymer removal were investigated.[18,35] First, the samples

were treated with oxygen plasma at 100 W for 20 min (Southbay, P2000C) to decompose the block copolymer, followed by annealing in H_2 flow (195 mL/min) at 500 ºC for 8 h to reduce the oxidized nanoparticles. In the other method, for PEO-*b*-P2VP-Au, PEO-*b*-P2VP-Ag, PEO-*b*-P2VP-Cu and PEO-*b*-P2VP-Pt, mild plasma treatment (60 W for 2 min) was used to break the continuous film of the block copolymer micelle solution. Next, the M-micelles were reduced to nanoparticles by thermal annealing in a tube furnace (ThermoScientific Blue) under flowing Ar (195 mL/min) for 10 hours at 150 ºC and then for 10 hours at 500 ºC under H_2 flow (195 mL/min) to ensure complete thermal degradation of the block copolymer.

2.2.3 Characterization

The nanoparticle height and spatial distribution was characterized by atomic force microscopy (AFM) (Bruker FastScan using FastScan C probes). AFM image analysis and quantitative measurements were performed using Nanoscope Analysis software (Bruker). Scanning electron microscopy (SEM) the nanoparticles was done using a Hitachi SU-8030 scanning electron microscope at an accelerating voltage of 5 kV and 10 µA current. The changes in the oxidation state of the Pd precursor and the pyridyl component of the P2VP were tracked after each annealing/ O_2 plasma step using X-ray photo-electron spectroscopy (XPS) equipped with an Al-source with a spot size of 500 µm (ThermoScientific, Escalab 250 Xi).

2.3 Results and Discussion

2.3.1 Different methods of block copolymer removal

The metal ions in the precursor coordinate with the pyridyl end of the block copolymer and after shaking for 16 h, micelles with a metal core are formed.[24] On being transferred onto a surface by spin-casting a thin layer, the PS-*b*-P2VP micelles assemble into a hexagonal pattern on the surface. The polymer can be removed in two ways- using O_2 plasma or by thermal decomposition of the block copolymer. Both these methods were investigated for PS-*b*-P2VP (Figure 2.1). It was observed that while the O_2 plasma (100 W, 20 min) is successful in removing the block copolymer and forming uniform Pd nanoparticles, the Pd nanoparticles are present in their oxide form as shown by a major peak at 337.8 (PdO_2) and a small peak at 338.9 ($PdAc_2$) in the XPS spectra (Figure 2.1A). However, the aggressive O_2 plasma also causes

some coarsening of the SiO_2 surface. In order to obtain Pd metal nanoparticles, the O_2 plasma treated material were reduced under H_2 gas at 500 ºC. While the Pd nanoparticles are fully reduced and have a major peak at 335.9 (Pd metal) and a minor peak at 338.97 ($PdAc_2$) (Figure 2.1Bii), the SiO_2 surface undergoes severe coarsening making the nanoparticles nearly indistinguishable from the support (Figure 2.1Bi).

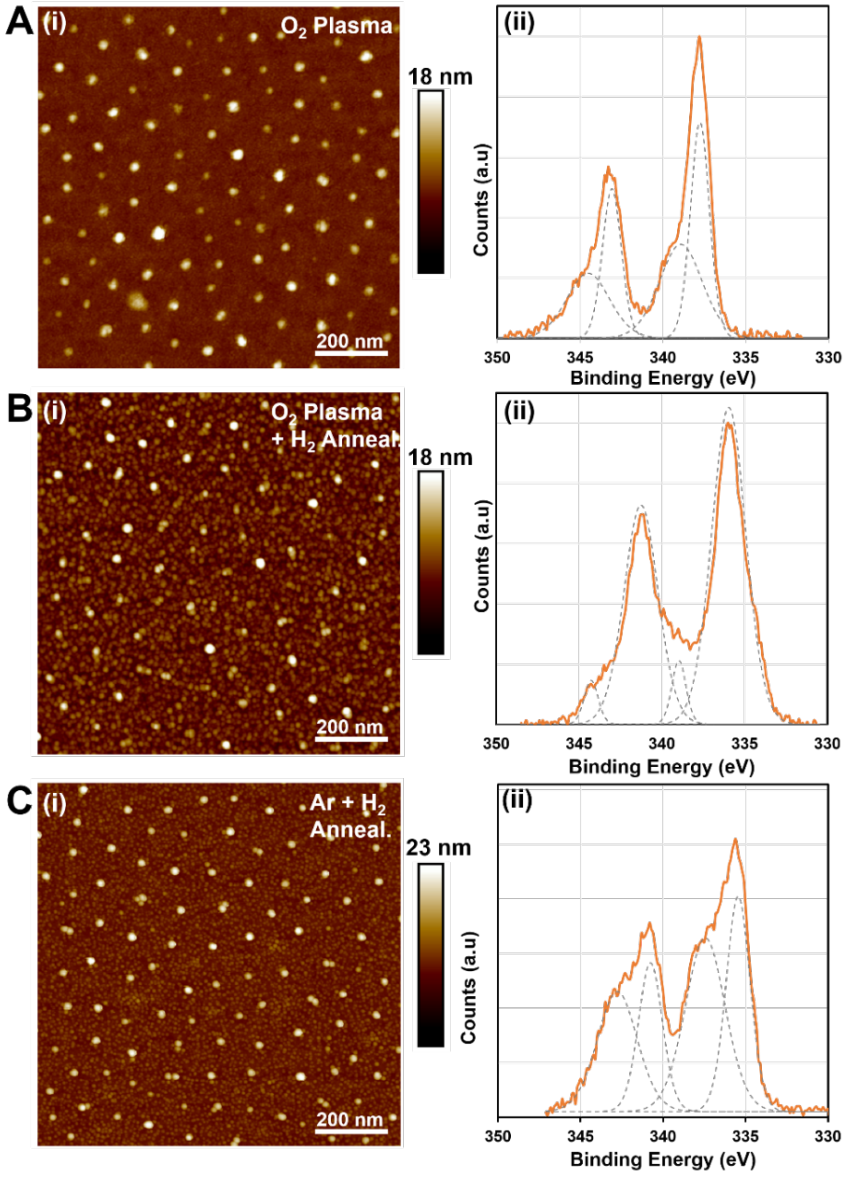

Figure 2.1 (i) AFM images and (ii) Pd 3d XPS spectra of Pd nanoparticles obtained after removal of PS(110K)-b-P2VP(52K) by A) O_2 plasma treatment at 100 W for 20 min, B) O_2 plasma treatment at 100 W for 20 min followed by

reduction under H_2 at 500 ºC, and C) annealing under Ar at 150 ºC for 10 h followed by annealing under H_2 at 500 ºC for 10 h.

The method of thermal annealing on the other hand is more successful in both the polymer removal and maintaining the uniformity of the SiO_2 surface. Most PS-*b*-P2VP block copolymers have been reported to undergo complete thermal degradation between 420-450 ºC. We followed a two-step annealing process- first, annealing under Ar at 150 ºC for 10 h followed by annealing under H_2 at 500 ºC for 10 h. The first step ensures that the Pd ions coordinated to P2VP aggregate within the micelle to form a single nanoparticle within the micelle to avoid raspberry-like nanostructures. In the second step, the block copolymer is removed by thermal degradation and the Pd nanoparticles are fully reduced to its metal state.[35] In this case, the metal nanoparticles are obtained in a uniform hexagonal arrangement and the major Pd peak in the XPS spectra obtained at 335.5 indicates that the nanoparticles are fully reduced. A shoulder obtained at 337.4 could mean that a thin oxide shell is present around the nanoparticles due to atmospheric exposure (Figure 2.1 C). This method of removal is used for all subsequent syntheses.

2.3.1 Dependence of nanoparticle size on P2VP chain length

Previous work done with P2VP-based block copolymers has shown that the size of the eventual metal nanoparticle increases with increasing length of the P2VP block chain length.[36] While optimizing the nanoparticle size and spacing for Au nanoparticles, we used PS-*b*-P2VP block copolymers of increasing P2VP chain lengths so that the increasing core size would accommodate more metal and form larger nanoparticles. We found that, for PS-*b*-P2VP (Figure 2.2), the size of the metal nanoparticle increases with a corresponding decrease in the surface density of nanoparticles so long as the PS block is longer than the P2VP block. The exact relationship between the size of the micelle core and the size of the nanoparticle isn't well understood, but it can be hypothesized that increasing P2VP chain length allows for a large core diameter to coordinate to the metal precursor.[24,36] A long PS chain ensures that the micelles assemble well apart from each other along with contributing to the large micelle diameter. A short PS chain, however, will increase the packing density of the micelle as well as reduce the micelle diameter. Thus, in the case of PS(42K)-*b*-P2VP(69K), even though the P2VP chain length is the greatest, the nanoparticle surface density

is higher than PS(110K)-*b*-P2VP(52K). In this case the nanoparticle within the same range for these two block copolymers (Figure 2.2 A).

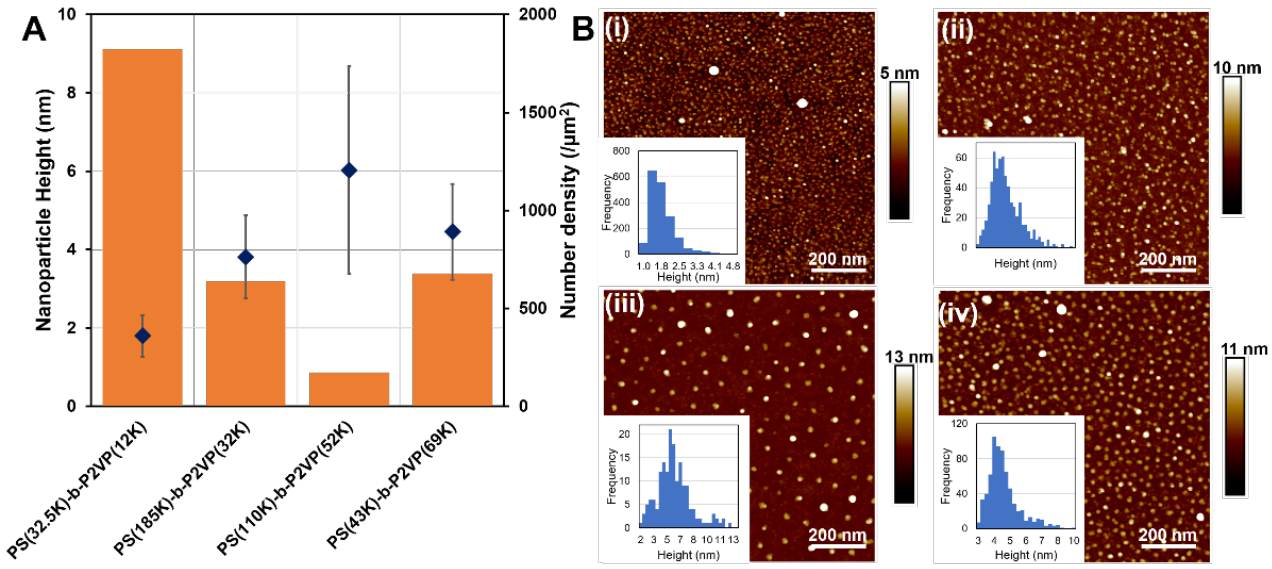

Figure 2.2 A) Au nanoparticle height and surface density as a function of P2VP chain length. B) AFM images and nanoparticle height distributions of Au nanoparticles synthesized using i) PS(32.5K)-*b*-P2VP(12K), ii) PS(185K)-*b*-P2VP(32K), iii) PS(110K)-*b*-P2VP(52K), and iv) PS(43K)-*b*-P2VP(69K) with the metal:P2VP loading at 1:16. The blue diamonds and error bars indicate the average nanoparticle height and the standard deviation (left axis) and the orange bars indicate the surface density (right axis)

Au nanoparticles are desired as a model for both PS-*b*-P2VP and PEO-*b*-P2VP block copolymers since the same precursor can be used for both ($HAuCl_4$). However, due to the very high mobility of Au on SiO_2 surface within the block copolymer film, uniform well dispersed Au nanoparticles are obtained only after employing mild O_2 plasma to break the continuous film (Figure 2.3). This makes it harder to decouple the effects of changing the block copolymer parameters from the effect of O_2 plasma in obtaining different nanoparticle distributions. Thus, for the PEO-*b*-P2VP system, we use Pd as the model since it readily forms uniform nanoparticles without plasma owing to its low mobility.[35]

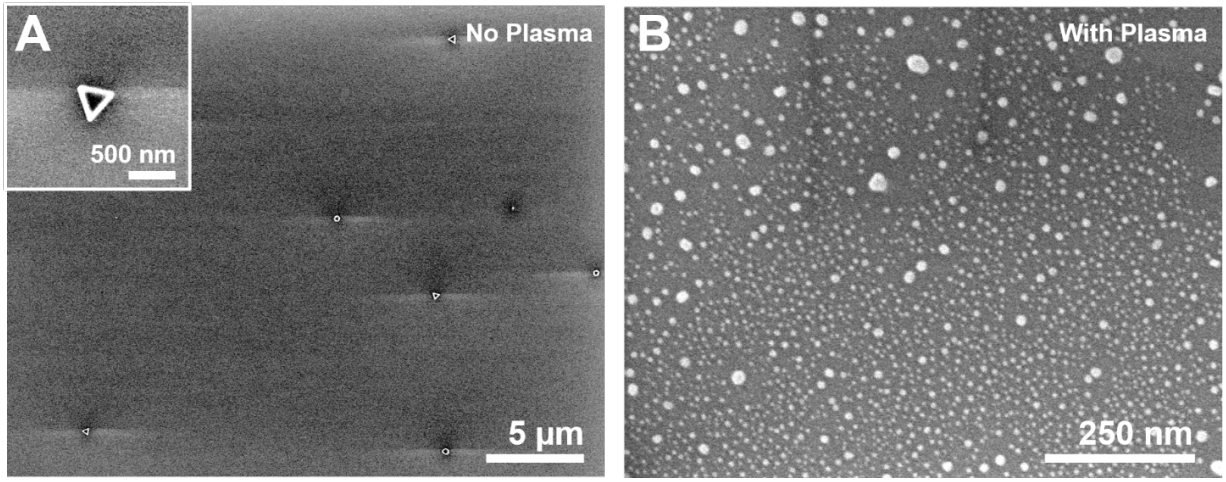

Figure 2.3 SEM images of Au nanoparticles formed after the two-step thermal annealing of Au-block copolymer micelles synthesized using PEO(2.8K)-*b*-P2VP(1.5K) A) without plasma treatment and B) with prior O_2 plasma treatment

For the PEO-*b*-P2VP system, we observed the exact opposite trend as PS-*b*-P2VP. With increasing P2VP (and PEO) chain lengths, the nanoparticle size decreases accompanied with an increase in the nanoparticle surface density (Figure 2.4). Colloidal studies done comparing two PEO-*b*-P2VP-$HAuCl_4$ micelles have shown that block copolymer with larger cores (P2VP) form smaller micelles than those with shorter P2VP chains since the latter form more loosely associated micelles.[14] However, has been no previous work done towards a complete understanding of the size dependence of the nanoparticles on the micelle formation and surface assembly for PEO-*b*-P2VP block copolymers. The micelles formed in the solution, may undergo rearrangement on the surface if they aren't present in uniform hexagonal packing. This could lead to some aggregation during the annealing steps changing the distribution from the solution to the surface. Additionally, the P2VP chain lengths in all the PEO-*b*-P2VP block copolymers we have used are much smaller than those used for PS-*b*-P2VP. Although there is no known correlation between the size dependence and the minimum P2VP chain length needed to observe it, most trends are seen within specific ranges of nanoparticle size.[24]

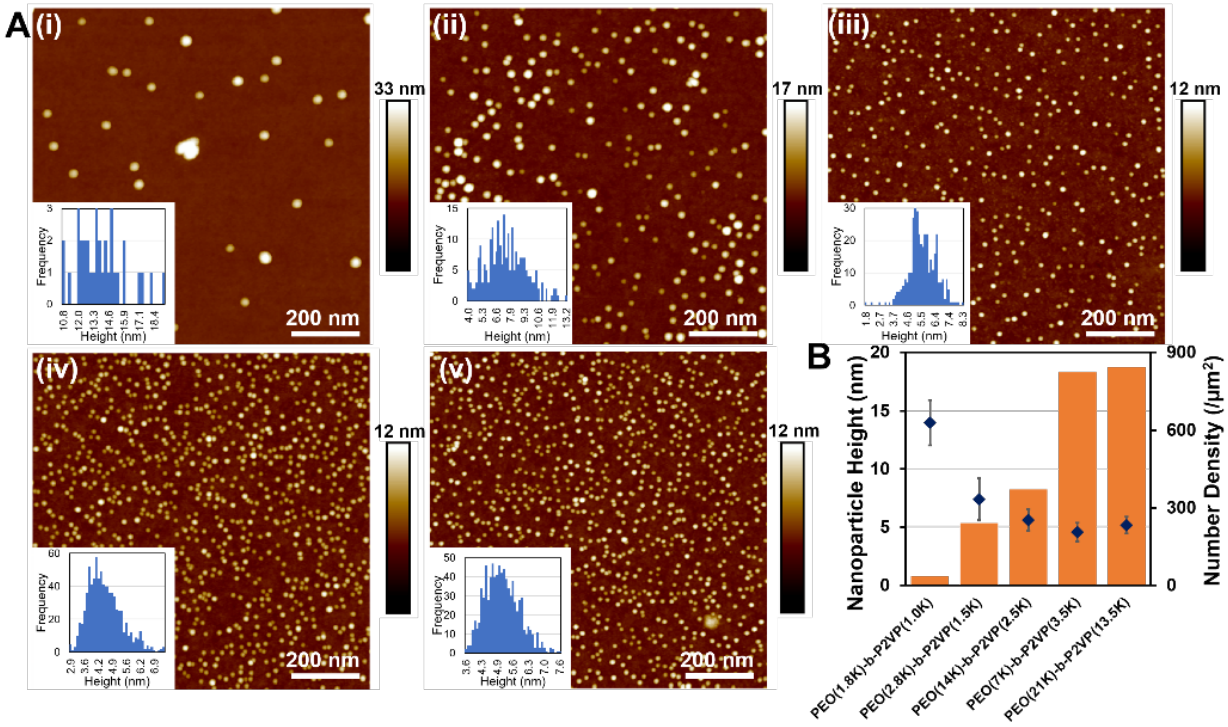

Figure 2.4 A) AFM images and nanoparticle height distributions of Pd nanoparticles synthesized using i) PEO(1.8K)-*b*-P2VP(1.0K), ii) PEO(2.8K)-*b*-P2VP(1.5K), iii) PEO(14K)-*b*-P2VP(2.5K), iv) PEO(7K)-*b*-P2VP(3.5K), v) PEO(21K)-*b*-P2VP(13.5K) with the metal:P2VP loading at 1:4. B) Pd nanoparticle height and surface density as a function of P2VP chain length. The blue diamonds and error bars indicate the average nanoparticle height and the standard deviation (left axis) and the orange bars indicate the surface density (right axis)

2.3.3 Nanoparticle distribution controlled by M: P2VP ratio

A way to obtain a higher nanoparticle size with the same block copolymer is to increase the molar metal: P2VP ratio.[17] Above a ratio of 1:1, not all the metal ions will be coordinated to a P2VP block, resulting in non-uniformity of nanoparticle size and spacing. We observed that for PS-*b*-P2VP the nanoparticle size increased slightly with increasing metal loading of Au precursors along with a significant increase in the surface density nanoparticles (Figure 2.5). However, when the Au: P2VP ratio is 2:1, the not only is the nanoparticle size non-uniform, but the surface arrangement is also random. At this high metal loading, the surface micelle density is high and the during the annealing process, some of the neighboring nanoparticles can agglomerate to form larger nanoparticles which accounts for the disparity in the nanoparticle size and density.

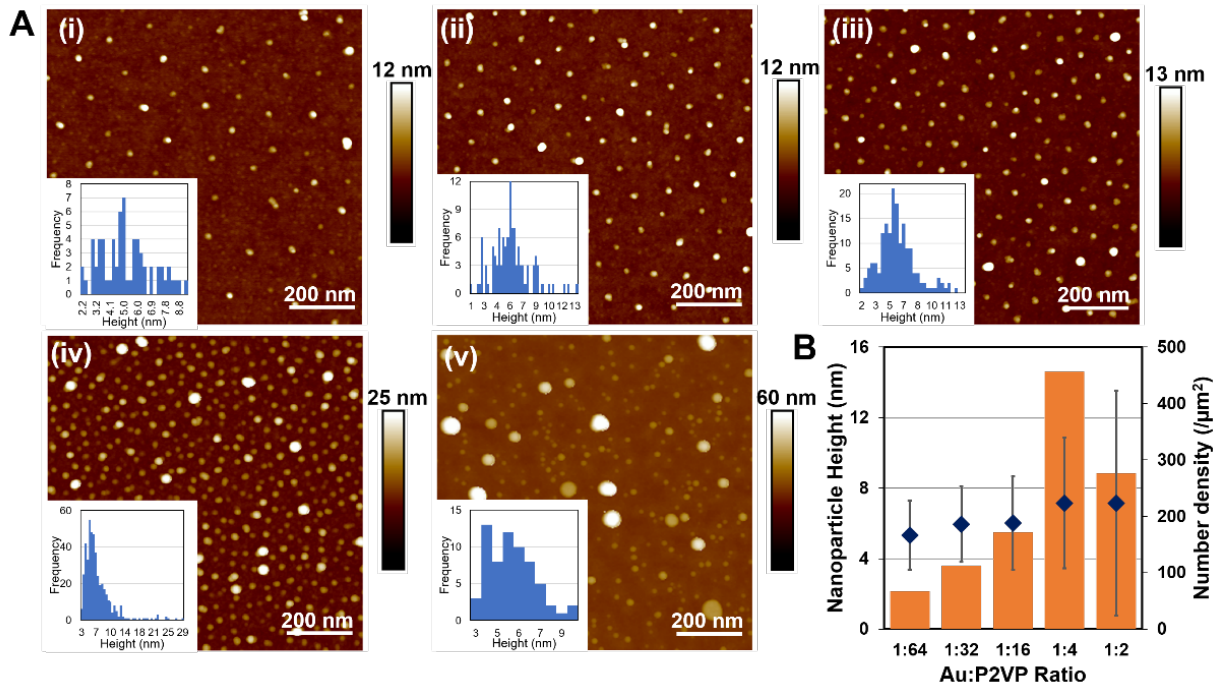

Figure 2.5 A) AFM images and size distributions of Au nanoparticles synthesized using PS(110K)-*b*-P2VP(52K), at the Au:P2VP loadings of i)1:64, ii) 1:32, iii) 1:16, iv) 1:4, and v) 1:2. B) Au nanoparticle height and surface density as a function of the Au: P2VP ratio. The blue diamonds and error bars indicate the average nanoparticle height and the standard deviation (left axis) and the orange bars indicate the surface density (right axis)

For this parameter again, the trends observed for PEO-*b*-P2VP are the reverse of those observed and expected of PS-*b*-P2VP (Figure 2.6). We observe that the nanoparticle size and surface density for the Pd: P2VP ratios of 1:64, 1:32 and 1:16 is the same (~12 nm, ~10 nanoparticles/μm^2). With increasing ratio to 1:4, the nanoparticle size abruptly decreases, and the nanoparticle density increases correspondingly. For the Pd: P2VP ratios of 1:4, 1:2, 1:1 and 1:0.5, the nanoparticle size remains the same (~6 nm) while the nanoparticle surface density increases with increasing metal loading. As would be expected, the nanoparticle size and surface arrangement for Pd: P2VP ratios of 1:1 and 1:0.5 is highly non-uniform due to the agglomeration of some of the closely spaced nanoparticles.

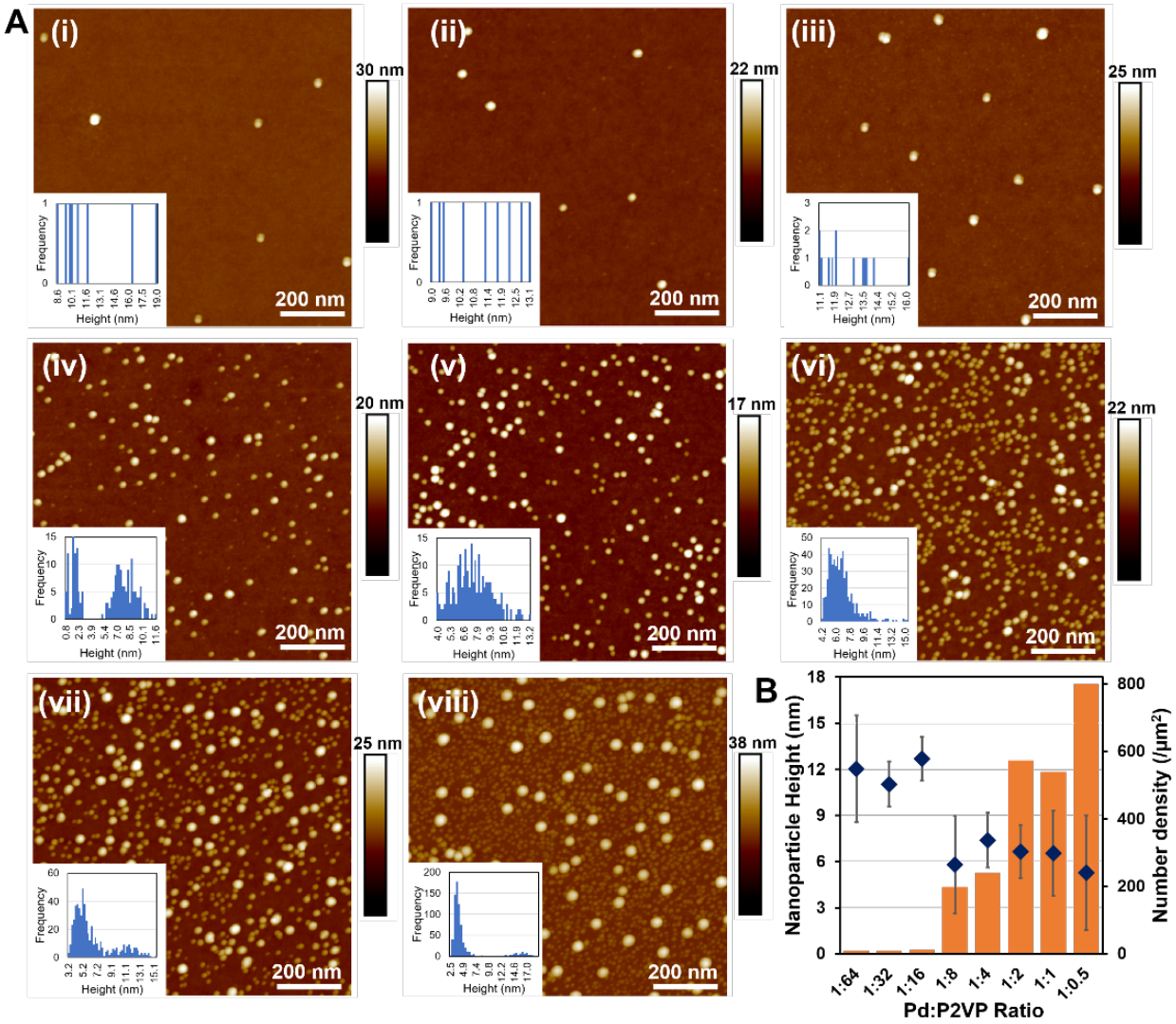

Figure 2.6 A) AFM images and size distributions of Pd nanoparticles synthesized using PEO(2.8K)-*b*-P2VP(1.5K), at the Pd:P2VP loadings of i)1:64, ii) 1:32, iii) 1:16, iv) 1:8, v) 1:4, vi) 1:2, vii) 1:1, and viii) 1:0.5, respectively. B) Pd nanoparticle height and surface density as a function of the Pd: P2VP ratio. The blue and error bars indicate the average nanoparticle height and the standard deviation (left axis) and the orange bars indicate the surface density (right axis)

2.3.3 Diluting the micelle solution to control the surface feature density

So far, in all the synthesis techniques used to obtain different distributions of Au and Pd nanoparticles, the size and surface density of the nanoparticles changes simultaneously, either in reverse or direct proportion. However, nanoparticles of the same size but different spacings may be obtained by diluting the M: block copolymer micelle solution after the complete micelle formation. The micelle solutions

are diluted just before spin-coating on the surface to prevent redistribution within the micelles. By this modification, the nanoparticles assemble farther apart from each other when diluted, without alteration in the nanoparticle size. For PS(110K)-b-P2VP(52K)-Au micelles with an initial molar metal:P2VP ratio of 1:4, dilution to 4 times and 16 times the concentration led to the decrease in the number of nanoparticle density by 50 % each time, while the nanoparticle size remained steady at 8 nm (Figure 2.7).

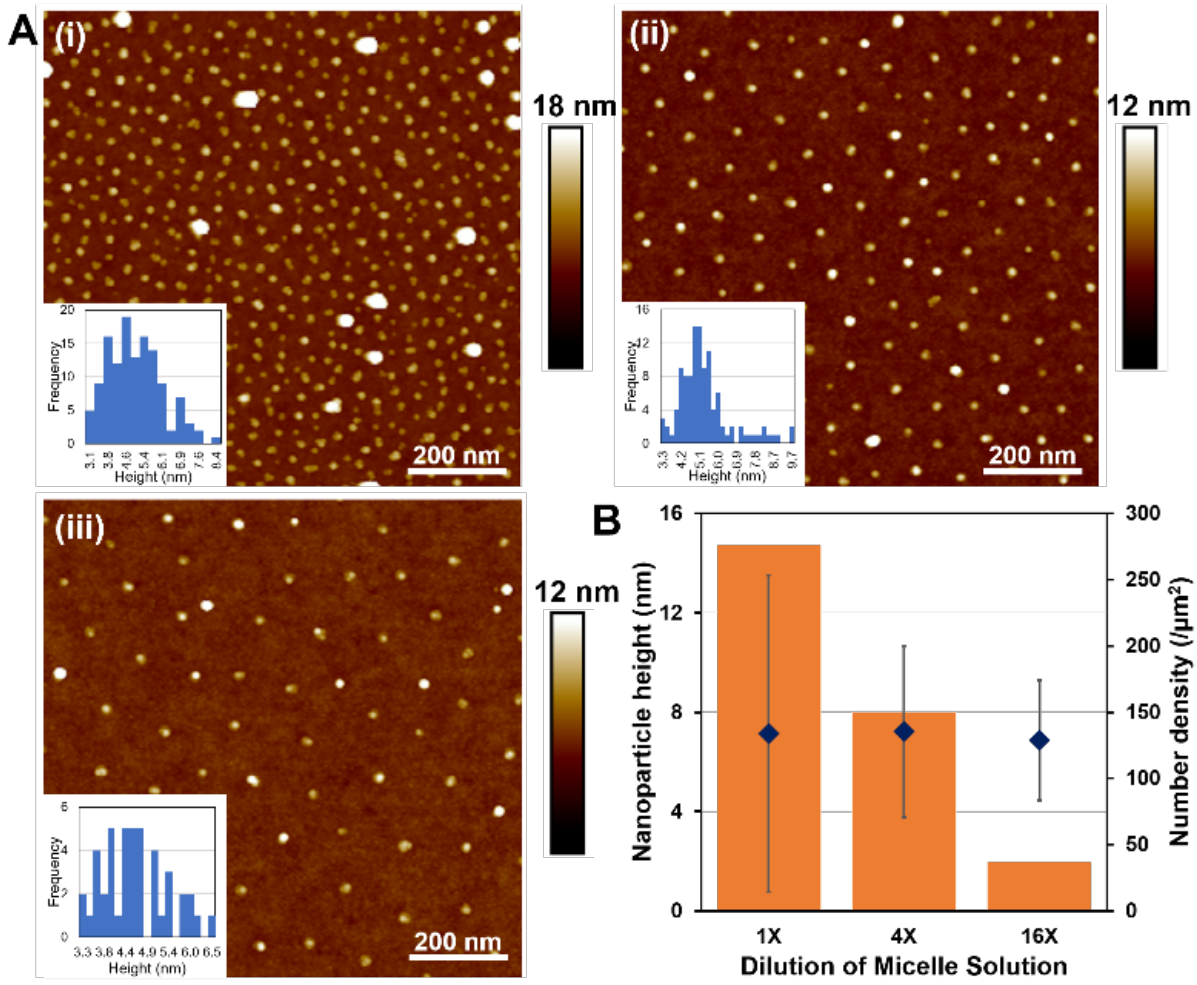

Figure 2.7 A) AFM images and size distributions of Au nanoparticles synthesized using PS(110K)-*b*-P2VP(52K), with initial Au:P2VP loading of 1:4 with i) no dilution, ii) dilution to 4 times, and iii) dilution to 16 times. B) Au nanoparticle height and surface density as a function of the dilutions. The blue diamonds and error bars indicate the average nanoparticle height and the standard deviation (left axis) and the orange bars indicate the surface density (right axis)

Pd nanoparticles synthesized using PEO-*b*-P2VP follow the same trend (Figure 2.8). With sequential dilution, the nanoparticle density decreases while the nanoparticle size remains the same. However, the nanoparticles synthesized from the solution before any dilution (Figure 2.8Ai), due to the high density of the micelles, the nanoparticles agglomerate to form fewer, larger nanoparticles during the annealing process.

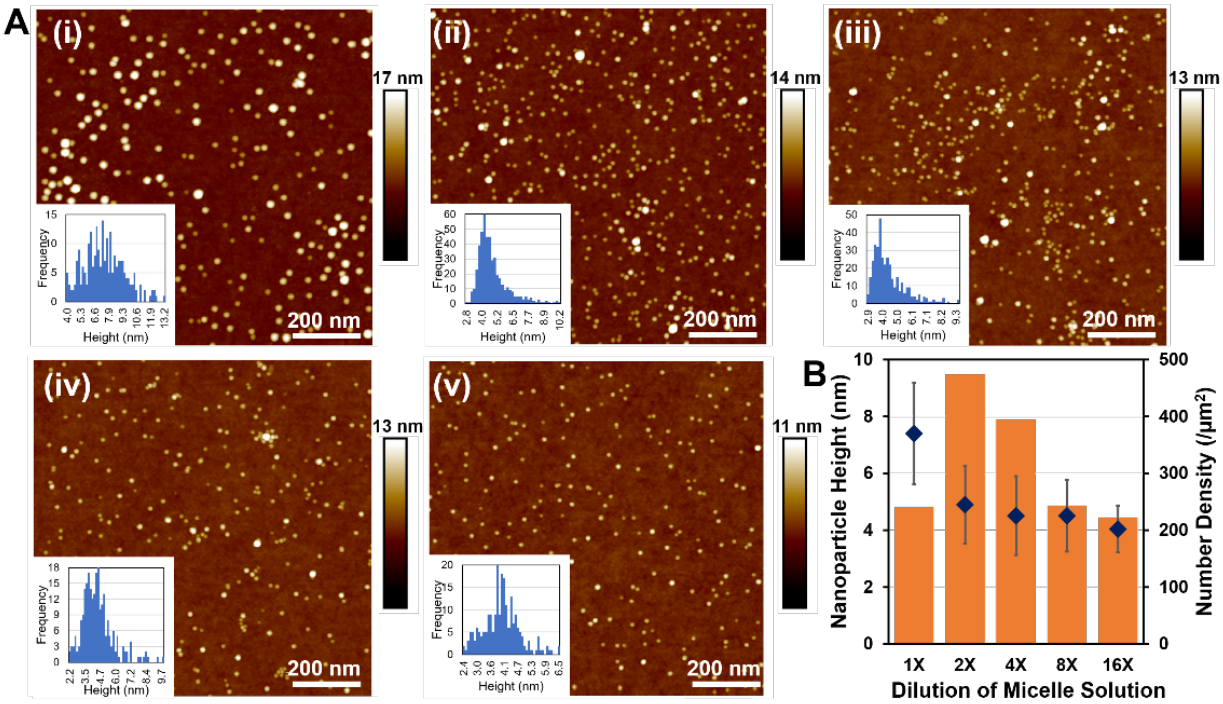

Figure 2.8 A) AFM images and size distributions of Pd nanoparticles synthesized using PEO(2.8K)-*b*-P2VP(1.5K), with initial Pd:P2VP loading of 1:4 with i) no dilution, ii) dilution to 2 times, iii) dilution to 4 times, iv) dilution to 8 times, and v) dilution to 16 times. B) Pd nanoparticle height and surface density as a function of the dilutions. The blue diamonds and error bars indicate the average nanoparticle height and standard deviation (left axis) and the orange bars indicate the surface density (right axis)

2.3.4 A detailed XPS analysis to understand the polymer removal process

Au nanoparticles are easily reducible, even in the absence of a reducing agent. In order to ensure that the annealing process is successful in reducing nanoparticles that are not as easy to reduce and may exist in many oxidation states, Pd nanoparticles were chosen to study the polymer removal and annealing

process. The preliminary Pd 3d XPS spectra of nanoparticles synthesized using PS-*b*-P2VP revealed that a two-step annealing process was successful in reducing the Pd micelles to metal nanoparticles. However, we have no handle over the extent of polymer removal. In order to understand how the Pd and the block copolymer undergoes the transformation from micelles to nanoparticles with each annealing step, we examined the XPS Pd and N spectra at every step. The pyridine in the P2VP block has a peak between 399.6-400.0 which can be used as an indicator of the presence of polymer residue on the metal nanoparticles. An additional step of oxidation in O_2 at 600 ºC was added before the reduction step to ensure complete combustion of any organic matter on the surface.

We observed that for Pd nanoparticles synthesized using PS-*b*-P2VP, the spatial arrangement of the final nanoparticles is the same as the initial micelles (Figure 2.9 A). From the Pd XPS spectra, we observe that the Pd within the micelles is present in its acetate form with a peak at 337.9. After annealing at 150 ºC, a major peak corresponding to PdO_2 (337.5) and minor peak corresponding to Pd metal (335.6) are obtained. When annealed under O_2 at 600 ºC, only one Pd peak corresponding to PdO_2 is obtained. After the final reduction step, majority of the Pd comes back to its metal state with a small PdO_2 peak, probably arising from the oxide shell formed on the surface after exposure to air and humidity. The N spectra, on the other hand, showed a consistent peak between 399.6-400.1 corresponding to pyridine from the P2VP block. The intensity of the N peak is lost during the oxidation step and the data seems noisy (Figure 2.9 Ciii). However, looking just at the raw counts, we observe very low-intensity peaks at 399 and 406 eV corresponding to pyridine and nitrates respectively showing that the pyridine has been oxidized (Figure S1). The pyridine peak is clearly visible again after the reduction step in H_2 (Figure 2.9 Civ). These results indicate that even though fully reduced Pd nanoparticles are obtained by stepwise thermal annealing of PS-*b*-P2VP block copolymer micelles, the polymer removal isn't complete and as such will be present as an impurity around the nanoparticles. High temperature annealing of these metal nanoparticles lead to carbon nanowire growth at 1000 ºC in completely inert atmosphere (Figure S2). Similar annealing of Au nanoparticles synthesized in this way showed complete thermal stability and the hexagonal arrangement of the metal nanoparticles was maintained (Figure S3). Additional steps, like washing in toluene, might be

needed to ensure complete polymer removal, but such steps risk rearranging the nanoparticles on the surface.

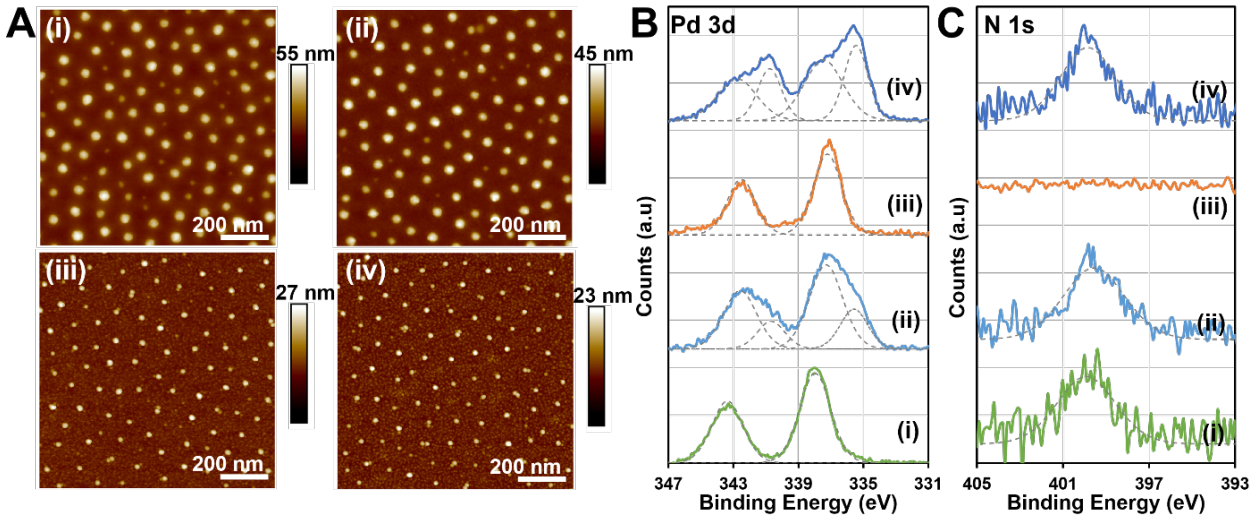

Figure 2.9 A) AFM images, B) Pd 3d XPS spectra, and C) N 1s XPS spectra of PS-*b*-P2VP-Pd micelles synthesized using PS(110K)-*b*-P2VP(52K), with initial Pd:P2VP loading of 1:2 after 8 times dilution after i) spin-coating, ii) annealing at 150 ºC under Ar for 10 h, iii) annealing at 150 ºC under Ar for 10 h followed by O_2 at 600 ºC for 3h, and iv) annealing at 150 ºC under Ar for 10 h and at 600 ºC under O_2 for 3h, followed by reduction at 500 ºC under H_2 for 10 h.

Pd nanoparticles that were generated using PEO-*b*-P2VP showed a different trend in the spatial arrangement after annealing (Figure 2.10 A). The micelles deposited by spin coating have no hexagonal spatial arrangement on the surface and this arrangement is maintained after the first annealing step (150 ºC, Ar, 10h). After the oxidation step (600 ºC. O_2, 3 h), the small, densely packed nanoparticles aggregate to form uniformly sized, if not uniformly arranged nanoparticles. This arrangement is maintained after the reduction step. This shows that the nanoparticles synthesized using PEO(2.8K)-*b*-P2VP(1.5K) does not proceed through the self-arrangement of micelles and eventual removal of polymer, but through agglomeration of smaller nanoparticles to form larger aggregates. This behavior could be explained by the especially low chain lengths of the P2VP block in this polymer compares to the PS(110K)-b-P2VP(52K), resulting in the formation of much smaller and densely packed micelles.

The Pd 3d XPS spectra, shows that after spin-coating on the surface the Pd within the PEO-*b*-P2VP micelles is present in its coordinated form with a peak at 337.5 (corresponding to Na_2PdCl_4) with a minor peak corresponding to Pd metal (335.5). After annealing at 150 ºC, two peaks corresponding to PdO_2 (337.8) and Pd metal (335.3) are obtained. When annealed under O_2 at 600 ºC, only one Pd peak corresponding to PdO_2 is obtained. After the final reduction step, majority of the Pd comes back to its metal state with a small PdO_2 peak, probably arising from the oxide shell formed on the surface after exposure to air and humidity, like the one obtained with PS-*b*-P2VP (Figure 2.10 B). The N spectra, on the other hand, showed a peak between 399.6-400.1 corresponding to pyridine from the P2VP block after spin casting and the first annealing step (Figure 2.10 C). The peak intensity is lowered to the level of noise after the oxidation step and completely absent after reduction in H_2. These results show that the removal of PEO(2.8K)-*b*-P2VP(1.5K) is complete and no polymer residue is left on the surface. The low molecular weight of the polymer could be the reason for this.

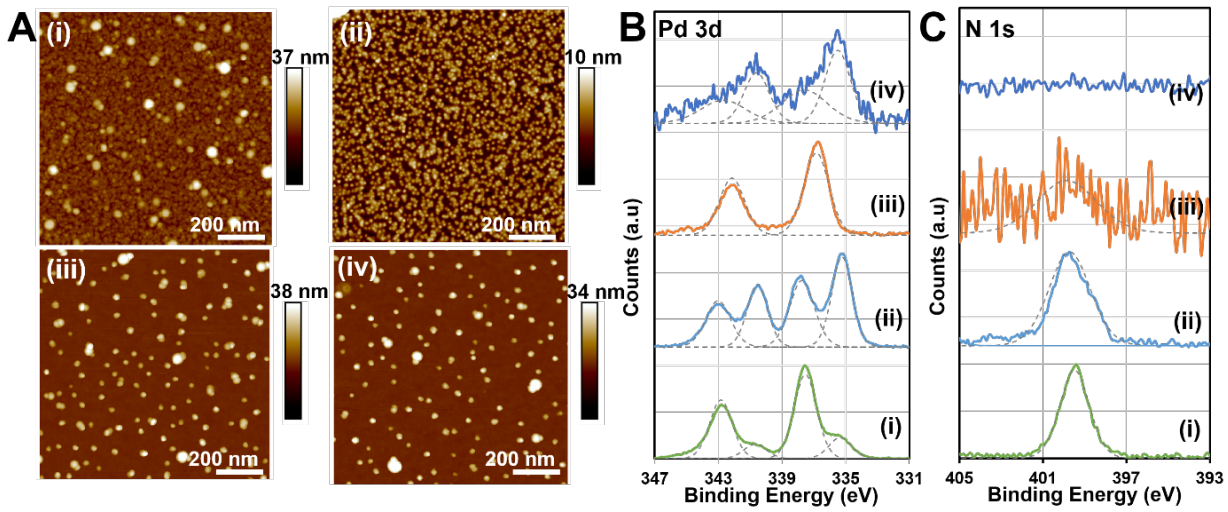

Figure 2.10 A) AFM images, B) Pd 3d XPS spectra, and C) N 1s XPS spectra of PEO-b-P2VP-Pd micelles synthesized using PE(2.8K)-b-P2VP(1.5K), with initial Pd:P2VP loading of 1:2 after 8 times dilution after i) spin-coating, ii) annealing at 150 ºC under Ar for 10 h, iii) annealing at 150 ºC under Ar for 10 h followed by O_2 at 600 ºC for 3h, and iv) annealing at 150 ºC under Ar for 10 h and at 600 ºC under O_2 for 3h, followed by reduction at 500 ºC under H_2 for 10 h.

2.3.5 Other metal nanoparticles synthesized

A wide range of metal nanoparticles can be synthesized using block copolymer micelle lithography, using either of PS-*b*-P2VP or PEO-*b*-P2VP. Depending on the application, a different level of spatial arrangement, uniformity in size, and impurities may be desired. Using PS-*b*-P2VP, apart from Au and Pd, we synthesized uniformly distributed Pt nanoparticles (Figure 2.11). Obtaining metal precursors, that are soluble in organic as well as aqueous solvents, is the limiting factor in the types of nanoparticles that can be synthesized using PS-*b*-P2VP.

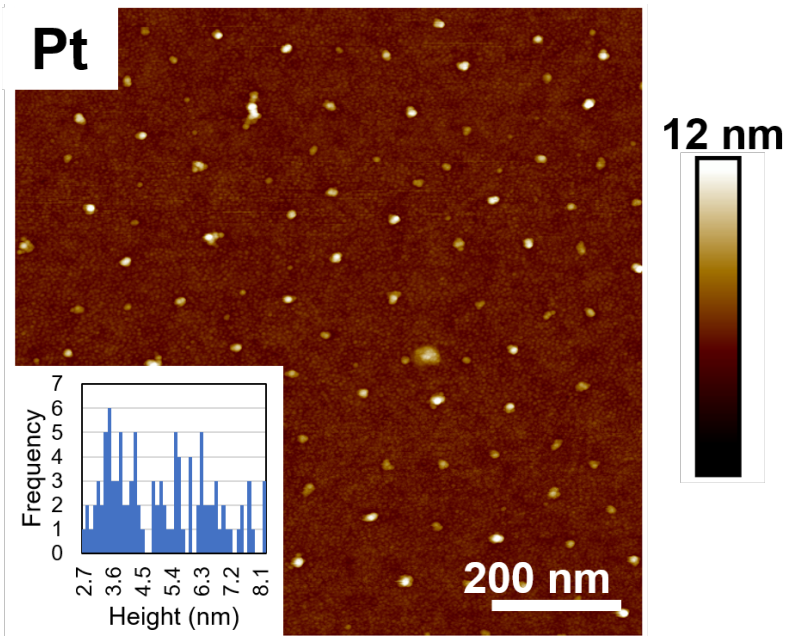

Figure 2.11 AFM image and particle size distribution of Pt nanoparticles synthesized using PS(110K)-*b*-P2VP(52K), with initial Pt:P2VP loading of 1:4 after annealing at 150 ºC under Ar for 10 h followed by reduction at 500 ºC under H_2 for 10 h

On the other hand, given the ready solubility of most metal salts in water, block copolymer-metal micelles using PEO-*b*-P2VP can be easily obtained. Apart from Pd, Co, Ni, Co, Au, Ag, and Pt nanoparticles can be synthesized and potentially many others (Figure 2.12). Multi-metallic nanoparticles can also be similarly synthesized. As we have seen previously, for the synthesis of Au, Ag and Cu nanoparticles, mild O_2 plasma treatment is necessary to break the continuous block copolymer film to avoid the formation of very large aggregates due to the high mobility of these metals.

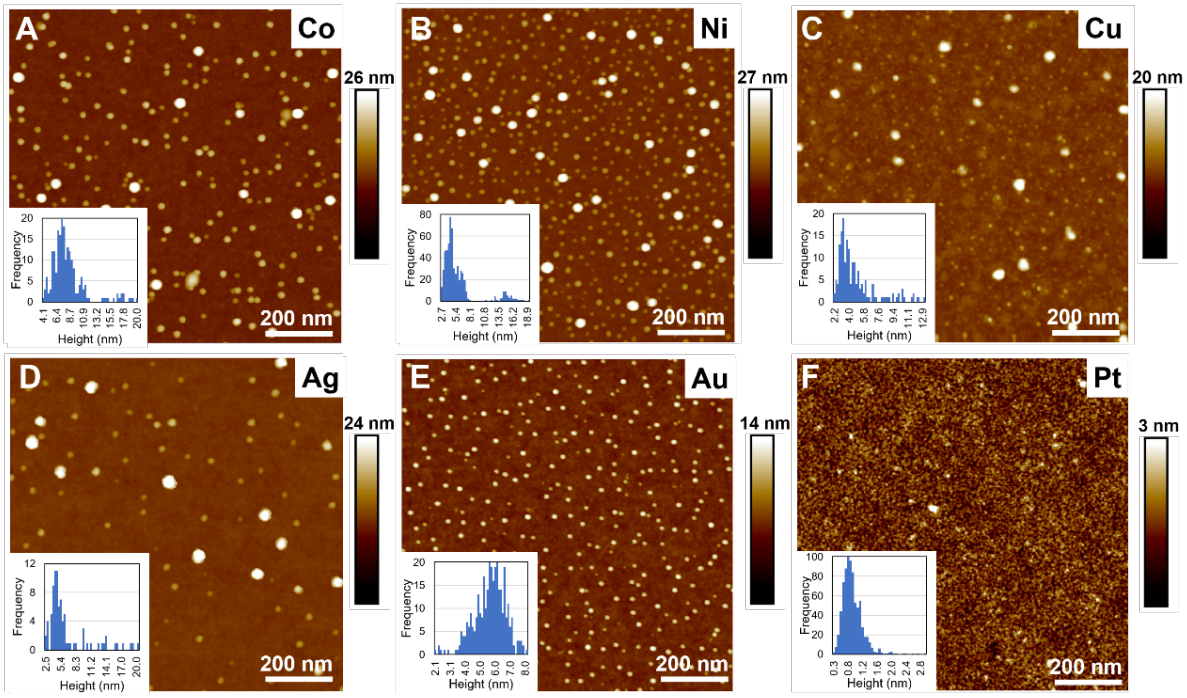

Figure 2.12 AFM images and particle size distributions of A) Co, B) Ni, C) Cu, D) Ag, E) Au, and F) Pt nanoparticles synthesized using PEO(2.8K)-*b*-P2VP(51.5K), with initial M:P2VP loading of 1:4 after annealing at 150 ºC under Ar for 10 h followed by reduction at 500 ºC under H_2 for 10 h. The Ag, Au, and Cu micelles are treated with mild plasma (60 W, 2 min) before annealing.

2.4 Conclusions

In this work, we have demonstrated two ways of obtaining uniform metal nanoparticles of a variety of sizes, surface densities, and composition using block copolymer micelle lithography using two types of block copolymers. Nanoparticles synthesized using PEO-*b*-P2VP can be made from a wide range of water-soluble metal salts that are readily available. Additionally, a simple two step annealing at temperatures above the thermal decomposition temperature of the polymers ensures complete polymer removal. PS-*b*-P2VP on the other hand is soluble only in organic solvents and there are limited number of metal compositions that can be accessed using this block copolymer. The Au and Pd nanoparticles synthesized using PS-*b*-P2VP are however very uniform in size and surface arrangement. They assemble in ordered hexagonal arrays with highly tunable size and spacing. The two-step annealing process is not successful

in completely removing the polymer and the O_2 plasma treatment causes coarsening of the supporting SiO_2. Both block copolymers give uniformly sized nanoparticles.

Even after high temperatures annealing to temperatures above 1000 ºC, the Au nanoparticles maintain their hexagonal arrangement instead of forming nanopores in the SiO_2 surface, as is observed at these temperatures.[37] Thus, based on the intended application, a suitable block copolymer, metal precursor, metal loading, dilution, and polymer removal method may be selected. For optical studies, where contamination from residual block copolymer will not be an issue, closely packed and highly ordered arrays of metal nanoparticles synthesized using PS-*b*-P2VP will be suitable. On the other hand, for applications in catalysis, where the spatial arrangement of the nanoparticles is not as important as the absence of organic contaminants, uniform metal nanoparticles synthesized using PEO-*b*-P2VP are desirable.

Acknowledgments

This material is based upon work supported by the Sherman Fairchild Foundation, Inc. and the Air Force Office of Scientific Research under Award number FA9550-16-1-0150. This work made use of the EPIC and SPID facilities of Northwestern University's NUANCE Center, which has received support from the Soft and Hybrid Nanotechnology Experimental (SHyNE) Resource (NSF ECCS-1542205); the MRSEC program (NSF DMR-1121262) at the Materials Research Center; the International Institute for Nanotechnology (IIN); the Keck Foundation; and the State of Illinois, through the IIN.

2.5 References

(1) Delariva, A. T.; Hansen, T. W.; Challa, S. R.; Datye, A. K. In Situ Transmission Electron Microscopy of Catalyst Sintering. *J. Catal.* **2013**, *308*, 291–305.

(2) Cong, P.; Doolen, R. D.; Fan, Q.; Giaquinta, D. M.; Guan, S.; Mcfarland, E. W.; Poojary, D. M.; Self, K.; Turner, H. W.; Weinberg, W. H. High-Throughput Synthesis and Screening of Combinatorial Heterogeneous Catalyst Libraries. *Angew. Chemie* **1999**, *38* (4), 483–488.

(3) McGinn, P. J. Combinatorial Electrochemistry – Processing and Characterization for Materials Discovery. *Mater. Discov.* **2015**, *1*, 38–53.

(4) Baeck, S. H.; Jaramillo, T. F.; Kleiman-Shwarsctein, A.; McFarland, E. W. Automated

Electrochemical Synthesis and Characterization of TiO 2 Supported Au Nanoparticle Electrocatalysts. *Meas. Sci. Technol.* **2005**, *16* (1), 54–59.

(5) Han, S. T.; Zhou, Y.; Xu, Z. X.; Huang, L. B.; Yang, X. B.; Roy, V. A. L. Microcontact Printing of Ultrahigh Density Gold Nanoparticle Monolayer for Flexible Flash Memories. *Advanced Materials*. 2012, pp 3556–3561.

(6) Kamyshny, A.; Ben-Moshe, M.; Aviezer, S.; Magdassi, S. Ink-Jet Printing of Metallic Nanoparticles and Microemulsions. *Macromol. Rapid Commun.* **2005**, *26* (4), 281–288.

(7) Santhanam, V.; Andres, R. P. Microcontact Printing of Uniform Nanoparticle Arrays. *Nano Lett.* **2004**, *4* (1), 41–44.

(8) Liu, R.; Han, L.; Huang, Z.; Ferrer, I. M.; Smets, A. H. M.; Zeman, M.; Brunschwig, B. S.; Lewis, N. S. A Low-Temperature Synthesis of Electrochemical Active Pt Nanoparticles and Thin Films by Atomic Layer Deposition on Si(111) and Glassy Carbon Surfaces. *Thin Solid Films* **2015**, *586*, 28–34.

(9) Niekiel, F.; Schweizer, P.; Kraschewski, S. M.; Butz, B.; Spiecker, E. The Process of Solid-State Dewetting of Au Thin Films Studied by in Situ Scanning Transmission Electron Microscopy. *Acta Mater.* **2015**, *90*, 118–132.

(10) Kwon, S. H.; Han, D. H.; Choe, H. J.; Lee, J. J. Synthesis of Copper Nanoparticles by Solid-State Plasma-Induced Dewetting. *Nanotechnology* **2011**, *22* (24).

(11) Thompson, C. V. Solid-State Dewetting of Thin Films. *Annu. Rev. Mater. Res.* **2012**, *42* (1), 399–434.

(12) Feng, T.; Ding, L.; Chen, L.; Di, J. Deposition of Gold Nanoparticles upon Bare and Indium Tin Oxide Film Coated Glass Based on Annealing Process. *J. Exp. Nanosci.* **2019**, *14* (1), 13–22.

(13) Liao, J.; Li, X.; Wang, Y.; Zhang, C.; Sun, J.; Duan, C.; Chen, Q.; Peng, L. Patterned Close-Packed Nanoparticle Arrays with Controllable Dimensions and Precise Locations. *Small*. 2012, pp 991–996.

(14) Bronstein, L. M.; Sidorov, S. N.; Valetsky, P. M.; Hartmann, J.; Cölfen, H.; Antonietti, M. Induced Micellization by Interaction of Poly(2-Vinylpyridine)- Block -Poly(Ethylene Oxide) with Metal Compounds. Micelle Characteristics and Metal Nanoparticle Formation . *Langmuir* **2002**, *15* (19), 6256–6262.

(15) Lu, J. Q.; Yi, S. S. Uniformly Sized Gold Nanoparticles Derived from PS-b-P2VP Block Copolymer Templates for the Controllable Synthesis of Si Nanowires. *Langmuir* **2006**, *22* (9), 3951–3954.

(16) Bhaviripudi, S.; Reina, A.; Qi, J.; Kong, J.; Belcher, A. M. Block-Copolymer Assisted Synthesis of Arrays of Metal Nanoparticles and Their Catalytic Activities for the Growth of SWNTs. *Nanotechnology* **2006**, *17* (20), 5080–5086.

(17) Spatz, J. P.; Roescher, A.; Moller, M. Gold Nanoparticles in Micellar Poly(Styrene)-b-Poly(Ethylene Oxide) Films-Size and Interparticle Distance Control in Monoparticulate Films. *Adv. Mater.* **1996**, *8* (4), 337–340.

(18) Spatz, J. P.; Mössmer, S.; Hartmann, C.; Möller, M.; Herzog, T.; Krieger, M.; Boyen, H. G.; Ziemann, P.; Kabius, B. Ordered Deposition of Inorganic Clusters from Micellar Block Copolymer Films. *Langmuir* **2000**, *16* (2), 407–415.

(19) Hawker, C. J.; Russell, T. P. Block Copolymer Lithography: Merging “Bottom-Up” with “Top-Down” Processes. *MRS Bull.* **2005**, *30* (12), 952–966.

(20) Nunns, A.; Gwyther, J.; Manners, I. Inorganic Block Copolymer Lithography. *Polym. (United Kingdom)* **2013**, *54* (4), 1269–1284.

(21) Bates, C. M.; Maher, M. J.; Janes, D. W.; Ellison, C. J.; Willson, C. G. Block Copolymer Lithography. *Macromolecules* **2014**, *47* (1), 2–12.

(22) Mayer, A. B. R.; Mark, J. E. Transition Metal Nanoparticles Protected by Amphiphilic Block Copolymers as Tailored Catalyst Systems. *Colloid Polym. Sci.* **1997**, *275* (4), 333–340.

(23) Aizawa, M.; Buriak, J. M. Block Copolymer Templated Chemistry for the Formation of Metallic Nanoparticle Arrays on Semiconductor Surfaces. *Chem. Mater.* **2007**, *19* (21), 5090–5101.

(24) Li, X.; Iocozzia, J.; Chen, Y.; Zhao, S.; Cui, X.; Wang, W.; Yu, H.; Lin, S.; Lin, Z. From Precision Synthesis of Block Copolymers to Properties and Applications of Nanoparticles. *Angew. Chemie - Int. Ed.* **2018**, *57* (8), 2046–2070.

(25) Lo Celso, F.; Triolo, A.; Bronstein, L.; Zwanziger, J.; Strunz, P.; Lin, J. S.; Crapanzano, L.; Triolo, R. Investigating Self-Assembly and Metal Nanoclusters in Aqueous Di-Block Copolymers Solutions. *Appl. Phys. A Mater. Sci. Process.* **2002**, *74* (SUPPL.I), 540–542.

(26) Pan, D.; Fu, Q.; Lu, J. Nanolithography through Mixture of Block Copolymer Micelles. *Nanotechnology* **2012**, *23* (30).

(27) Sarrazin, A.; Gontier, A.; Plaud, A.; Béal, J.; Yockell-Lelièvre, H.; Bijeon, J.-L.; Plain, J.; Adam, P.-M.; Maurer, T. Single Step Synthesis and Organization of Gold Colloids Assisted by Copolymer Templates. **2014**.

(28) Pan, D.; Fu, Q.; Lu, J. Nanolithography through Mixture of Block Copolymer Micelles. *Nanotechnology* **2012**, *23* (30), 305302.

(29) Spatz, J. P.; Mößmer, S.; Möller, M. Mineralization of Gold Nanoparticles in a Block Copolymer Microemulsion. *Chem. - A Eur. J.* **1996**, *2* (12), 1552–1555.

(30) Chai, J.; Huo, F.; Zheng, Z.; Giam, L. R.; Shim, W.; Mirkin, C. A. Scanning Probe Block Copolymer Lithography. *Proc. Natl. Acad. Sci.* **2010**, *107* (47), 20202–20206.

(31) Chen, P. C.; Liu, G.; Zhou, Y.; Brown, K. A.; Chernyak, N.; Hedrick, J. L.; He, S.; Xie, Z.; Lin, Q. Y.; Dravid, V. P.; et al. Tip-Directed Synthesis of Multimetallic Nanoparticles. *J. Am. Chem. Soc.* **2015**, *137* (28), 9167–9173.

(32) Mirkin, C. A.; Chen, P.-C.; Liu, X.; Hedrick, J. L.; Xie, Z.; Wang, S.; Lin, Y.; Hersam, M. C.; Dravid, V. P. Polyelemental Nanoparticle Libraries. *Science (80-.).* **2016**, *352* (June), 1565–1569.

(33) Le-The, H.; Berenshot, E.; Tiggelaar, R.; Tas, N.; Van Den Berg, A.; Eijkel, J. C. T. Large-Scale Fabrication of Highly Ordered Sub-20 Nm Noble Metal Nanaoparticles Om Silica Substrates without Metallic Adhesion Layers. *Microsystems Nanoeng.* **2018**, *4* (4).

(34) Clément, N.; Patriarche, G.; Smaali, K.; Vaurette, F.; Nishiguchi, K.; Troadec, D.; Fujiwara, A.; Vuillaume, D. Large Array of Sub-10-Nm Single-Grain Au Nanodots for Use in Nanotechnology. *Small* **2011**, *7* (18), 2607–2613.

(35) Liu, G.; Eichelsdoerfer, D. J.; Rasin, B.; Zhou, Y.; Brown, K. A.; Liao, X.; Mirkin, C. A. Delineating the Pathways for the Site-Directed Synthesis of Individual Nanoparticles on Surfaces. *Proc. Natl. Acad. Sci. U. S. A.* **2013**, *110* (3), 887–891.

(36) Antonietti, M.; Wenz, E.; Bronstein, L.; Seregina, M. Synthesis and Characterization of Noble Metal Colloids in Block Copolymer Micelles. *Adv. Mater.* **1995**, *7* (12), 1000–1005.

(37) de Vreede, L. J.; Van Den Berg, A.; Eijkel, J. C. T. Nanopore Fabrication by Heating Au Particles on Ceramic Substrates. *Nano Lett.* **2015**, *15*, 727–731.

Chapter Three: Understanding the Nature of Heterogeneous Pd Catalyzed Suzuki-Miyaura Cross-coupling Reaction

Abha A Gosavi, Natalia Chernyak, Justin Notestein, Chad Mirkin

3.1 Introduction

Finding the perfect catalyst for a chemical process is often an arduous process that requires several iterations and complex lab-scale reactors which are capable of testing only a handful of catalysts at once. Combinatorial catalysis enables methodical synthesis and testing of a range of chemically and physically distinct materials in a high throughput fashion.[1] One way to achieve speed up this process is by miniaturization using nanolithography. Nanolithography is a novel way of synthesizing metallic nanoparticles with atomic precision. Using polymer pen lithography (PPL)[2,3] and scanning probe block co-polymer lithography (SPBCL),[4–6] the size, composition and location can be precisely controlled to achieve highly ordered, uniform arrays of multi-metallic nanoparticles. Large area patterns of multi-metallic nanoparticles with systematic size and composition gradients can be used to build screening platforms for combinatorial catalysis.[7]

The Suzuki-Miyaura reaction enables cross-coupling between an alkyl or aryl halide and an organoboron compound catalyzed by Pd(0) species in the presence of a base.[8] This reaction could be used as a model for catalyst optimization since it can be catalyzed by even trace Pd. Typically catalyzed by Pd complexes,[8–10] a wide range of heterogenous Pd nanoparticle catalysts have been shown to be effective in facilitating this reaction.[11] Additionally, traces of Cu and Ni have been reported to promote the catalytic activity of Pd nanoparticles towards the Suzuki-Miyaura cross-coupling reaction.[12,13] Designing multi-metallic nanoparticles that would maximize the conversion and selectivity of the reaction with the least amount of precious metal nanoparticles is desirable. The Pd nanoparticle size and composition, that gives the highest conversion and selectivity for the Suzuki-Miyaura cross-coupling reaction, can be optimized using multimetallic (Pd-Cu, Pd-Ni) nanoparticle arrays synthesized using SPBCL and block copolymer micelle lithography. These can then be scaled up using solution-phase synthesis techniques.

In the past 20 years, there have been numerous studies on the development of Suzuki-Miyaura catalysts based on immobilized Pd nanoparticles.[14–19] Many of these claim that the catalyst is truly heterogeneous because little Pd is lost into solution or because the solid catalyst can be recycled effectively However, the exceptional reactivity of homogeneous Pd combined with other studies that do show a steady loss in rate provide a counter-claim that the system leaches active Pd. The latter hypothesis has been supported by several studies using conventional supported Pd nanoparticles. [20–24] The mechanism of the molecular catalyst is known and involves Pd(0) - Pd(II) cycles when the aryl halide undergoes oxidative addition to the Pd(0).[25,26] For immobilized Pd nanoparticles, it might be possible for oxidative addition to occur without complete loss of Pd atoms into solution, but this was not unambiguously known.

In this chapter, we initially discuss the various reaction conditions used to study the Suzuki-Miyaura reaction catalyzed by Pd nanoparticles supported on planar Si wafers. Despite remarkable conversion and selectivity, we observed that there was trace Pd in the reaction mixture despite the initial heterogeneity of the catalytic nanoparticles. We used several approaches to investigate the source of the Pd and explored different routes to immobilize the nanoparticles on the support. We observe that the Pd atoms leach into the reaction mixture under any conditions, with all modifications. We thus conclude that the Suzuki-Miyaura cross-coupling reaction, even when provided with solid-immobilized metal nanoparticles, proceeds by pathways in the solution phase. As such, it is unsuitable as a model reaction to study catalyst optimization by nanocombinatorial arrays, even if it may be practically possible to reduce leaching and improve metal recovery to arbitrarily high levels.[14,27–29]

3.2 Methods

Densely packed Pd nanoparticles, with random spatial arrangement, were synthesized using block copolymer micelle lithography. Aqueous solutions of Pd micelles were synthesized by combining the diblock copolymer, polyethylene oxide-b-polyvinyl pyridine (PEO (1500) -*b*-P2VP (2800)) (Polymer Source, Inc.) and Na_2PdCl_4 at 4:1 pyridyl: Pd ratios and allowing them to shake overnight. The pH of the inks was maintained between 3-4 by adding dilute HCl. Thin films of the Pd micelle solution were spin-cast on Si wafers (NOVA Electronic Materials, 500 nm thermal oxide) at 1000 RPM rotation speed for 60 s. The

samples were treated with oxygen plasma (60 W, 5 min) and subsequently annealed in a tube furnace (ThermoScientific Blue) under flowing argon gas (195 mL/min) for 10 hours at 150 ºC using a ramp-rate of 4 ºC/minute and then for 10 hours at 500 ºC under hydrogen gas (195 mL/min) using ramp-rate of 11 ºC/minute. All catalytic reactions were carried out in glass vials with a ~1 cm^2 catalyst chip at the bottom. For most of the reactions, of 0.05 mmol haloarene was allowed to react with 0.075 mmol boronic acid in the presence of a range of different bases and solvents at different temperatures (Tables 3.1 and 3.2). The reaction products were analyzed in Shimadzu GCMS- QC2010 SE fitted with a ZB 624 polar column. 100 µL of 200 mM dodecane was mixed with 1 mL of reaction mixture and used as the internal standard during the GC-MS analysis. The oven temperature was programmed from 120ºC to 180ºC and 15 min methods were run. Thermo iCAP Q Inductively Coupled Plasma Mass Spectrometry (ICP-MS) was used to determine Pd metal presence in the reaction mixtures.

3.3 Results and Discussion

3.3.1 Optimization of solvent, co-catalyst and reaction temperature

Optimization of reaction conditions was carried out to increase the conversion of iodobenzene by changing the reaction conditions, reaction media and base (co-catalyst) (Table 3.1). A sample GC-MS chromatogram of the cross-coupling reaction is shown in Figure S4. The best selectivity and conversion were observed when iodobenzene reacted with 50% excess of 4-methoxyphenyl boronic acid for 6 hours at 60 ºC using K_2CO_3 as the base in a methanol-acetonitrile-water (1:1:1) medium. This solvent composition ensures a homogenous reaction medium that eliminates the necessity of agitation during the reaction.

Table 3.1 The yield and selectivity of Pd catalyst as a function of solvents, base (co-catalyst), temperature reaction time. For each condition, 0.05 mmol iodobenzene and 0.075 mmol of 4-methoxy phenyl boronic acid were reacted in a total reaction volume of 4 ml.

Solvent	Base	Temperature	Agitation	Time	Yield	Side Reaction
EtOH-Toluene-H_2O	$NaHCO_3$	85ºC	None	15 h	<5%	None
MeOH-MeCN- H_2O	K_2CO_3	RT (~27ºC)	Mild	2 h	37%	None
MeOH-MeCN- H_2O	K_2CO_3	60ºC	None	6 h	56%	None
MeOH-MeCN- H_2O	K_2CO_3	70ºC	None	6 h	18%	50% Homocoupling
MeOH-MeCN- H_2O	K_2CO_3	80ºC	None	6 h	24%	>50% Homocoupling

3.3.2 Investigating loss of elemental Pd during the reaction

The similarly high yields and selectivity observed in both heterogenous and homogenous reaction conditions have often been an indication of Pd leaching in literature.[25,26,30] To examine if the high yields observed at our optimized reaction conditions also result from atomic loss of Pd, we performed elemental analysis of the reaction mixture and observed that Pd was present in very low concentrations (< 1 ppb). A set of control experiments (Scheme 3.1) were designed to further investigate the source of the Pd in the reaction mixture. In four identical vials, equal amounts of 0.1 mmol K_2CO_3 in 600 μl solvent (MeCN-MeOH-H_2O) were taken. In vials 1, 2, 3 and 4, catalyst wafers that had ~70 ng of elemental Pd, were placed at the base of the vials. Vials 1 and 2 had the complete reaction mixture (0.05 mmol iodobenzene, 0.075 mmol 4-methoxyphenyl boronic acid). Vial 3 had only 0.075 mmol 4-methoxyphenyl boronic acid while vial 4 had neither of the reactants. Vial 5 had the complete reaction mixture (0.05 mmol iodobenzene, 0.075 mmol 4-methoxyphenyl boronic acid) but no catalyst. The vials were tightly capped and placed in an aluminum bead bath at 60 ºC for 12 hours. The catalyst wafers in vials 2, 3 and 4 were removed and the reaction mixtures in vials 3 and 4 were completed by adding 0.05 mmol iodobenzene to vial 3 and 0.05 mmol iodobenzene and 0.075 mmol 4-methoxyphenyl boronic acid to vial 4. Vials 1 and 5 were left untampered. The entire set

was subjected to 12 more hours at 60 ºC after which the contents of each of the vials were analyzed using GC-MS and ICP-MS (Table 3.2).

Scheme 3.1 Control experiments designed to determine the source of Pd metal loss detected. In vial 1, the catalyst wafer was left in reaction mixture through both reaction cycles. In vials 2, 3 and 4, the catalyst wafer was removed after the first 12-hour reaction cycle. In vial 5, the reaction was carried out in the absence of any catalyst.

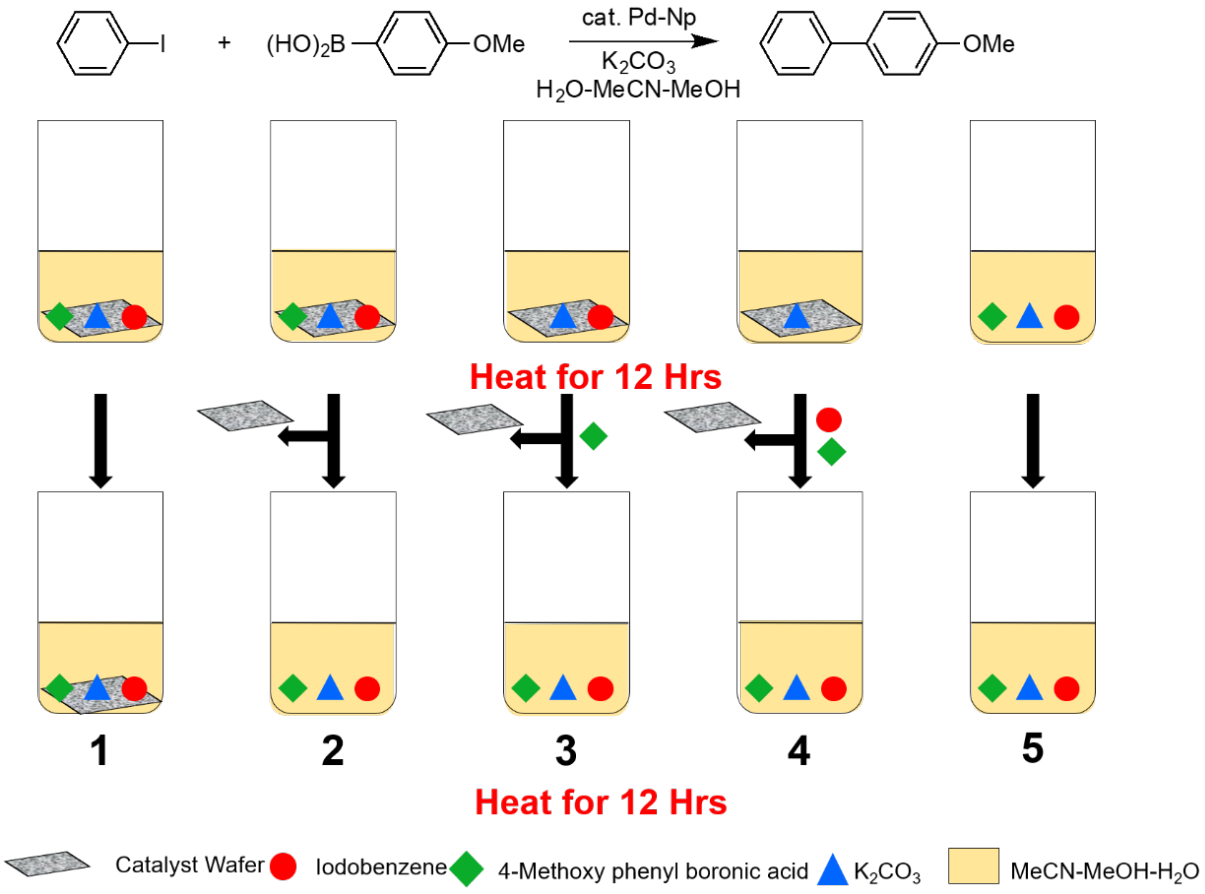

ICP-MS analysis of the different reaction mixtures revealed that significant amounts of Pd metal is present in each of the vials 1-4. The GC-MS spectra of the contents of vial 3 showed a significant yield of desired product as well as a homocoupling side product, indicating leaching of Pd metal from the catalyst wafer during the 1st heating cycle.

Table 3.2 Summary of reaction conditions, yields, amount of Pd present, and side-products of control experiments outlined in Scheme 3.1. For each condition, 0.05 mmol iodobenzene and 0.075 mmol of 4-methoxy phenyl boronic acid were reacted in a total reaction volume of 4 ml.

Vial	Catalyst Presence	Iodobenzene	4-Methoxyphenyl boronic acid	Base	Yield (%)	Pd (ppb)	Side-product
1	Present for 24 h	Present	Present	Present	50	0.44	None
2	Present for 12 h	Present	Present	Present	48.2	0.46	None
2	Removed after 12 h	Present	Present	Present	48.4	0.49	None
3	Present for first 12 h	Present	Added after 12 h	Added after 12 h	28.2	1.29	Biphenyl
4	Present for first 12 h	Added after 12 h	Added after 12 h	Present	<5	0.21	None
5	Absent	Present	Present	Present	~0	0	None

Reaction mixtures in vials 1 and 2 showed nearly equal conversion, selectivity and Pd content. Contents of vial 5 showed almost zero conversion and Pd concentration. The analysis of the reaction carried out in vial 3 yielded the most peculiar results. The complete reaction mixture and catalyst were never simultaneously present in the vial during the 24-hour duration. Despite this, there is significant yield of the desired cross-coupling product, 4-methoxy biphenyl, indicating a presence of leached Pd in the reaction mixture after the catalyst wafer was removed. The distinct side-product product of biphenyl may have formed in the first 12 hours from the homocoupling of iodobenzene. The Pd content in this vial was also significantly higher than the others. Reaction mixture in vial 4 showed a very low yield, no side product and a lower Pd content. This indicates that the Pd loss during the first 12 hours in the presence of K_2CO_3 is not significant.

This set of control experiments confirms the Pd leaching reported in literature. It can be concluded that the loss is most notable in the presence of just the aryl halide when the homocoupling reaction is favored. Without further investigation, it would be speculative to claim the source of this Pd loss. The two most likely explanations to account for the presence of Pd in the reaction mixture are that the 1) Pd nanoparticles supported on planar Si wafers are dislocated from the support under harsh reaction conditions, or 2) individual Pd atoms/ions leach into the reaction medium as a part of the reaction mechanism. While the former can be avoided by using milder reaction conditions and immobilizing the Pd nanoparticles on the support, the latter cannot be controlled without sacrificing reactivity. In order to minimize Pd loss, we explored various reactants and co-catalysts and attempted to immobilize the Pd nanoparticles using TiO_2 supports as well as porous Al_2O_3 overcoats.

3.3.3 Exploring benign conditions for Suzuki-Miyaura reaction

The SiO_2 top layer on the Si wafers is very sensitive to strong bases and reagents. Corrosion of this top layer can dislodge the nanoparticles that it supports. With an aim to find the combination of mildest, yet most effective combination of reactants, several permutations of aryl halides and aryl boronic acids were screened. The conversion, yield, and Pd loss for each of these conditions were monitored. We quantified the total amount of Pd present on a standard catalyst chip and used that to monitor the percent Pd loss. Amongst all the haloarene-boronic acid permutations studied, iodobenzene and 4-methoxyphenyl boronic acid (which were already being used as model reactants) resulted in the highest conversion and the lowest Pd loss (Table 3.3). While the use of chlorobenzene causes the greatest Pd loss, the yields obtained are < 5%. Overall, iodoarenes are more reactive than bromoarenes due to its lowest electronegativity. Literature reports have shown that even trace amounts of Pd can catalyze the cross-coupling reactions of iodobenzene with boronic acids.[30] Presence of electron donating groups at the ortho- or para- positions can increase the catalytic activity of aryl-halides but bulky functional groups can also cause steric hinderance.[31,32] We observe that bromobenzene and iodobenzene gave the highest yields when coupled with 4- methoxyphenyl boronic acid. Addition of bulky ligands to the boronic acid also gave low product yields.

Table 3.3 Summary of different combinations of aryl halides and boronic acids tested in reaction conditions (K_3PO_4, dioxane-water, 60 ºC, 12 hours).

Aryl Halide	Boronic Acid	Yield (%)	Pd Loss	Side Reactions
4-bromotoluene	4-methoxyphenyl boronic acid	<5	12.80%	Homocoupling
4-bromo acetophenone	4-methoxyphenyl boronic acid	<5	15.90%	Homocoupling
4-bromo acetophenone	para tolyl boronic acid	<5	8.80%	Homocoupling
4-bromoanisole	para tolyl boronic acid	40.5	5.10%	Homocoupling
bromobenzene	para tolyl boronic acid	51.2	25.70%	None
bromobenzene	4-methoxyphenyl boronic acid	44.4	5.40%	None
4-iodoanisole	para tolyl boronic acid	46.5	4.30%	Homocoupling
2-iodoanisole	para tolyl boronic acid	43.9	4.50%	Homocoupling
iodobenzene	4-methoxyphenyl boronic acid	60.7	7.20%	None
iodobenzene	para tolyl boronic acid	<5	7.00%	Homocoupling
chlorobenzene	4-methoxyphenyl boronic acid	<5	30.20%	None
chlorobenzene	para tolyl boronic acid	<5	47.00%	None

3.3.4 Increasing the stability of Pd nanoparticles on modified supports

One hypothesis for the loss of Pd is that weak metal-oxide interactions between Pd nanoparticles and supporting planar SiO_2 layer on the Si wafers make it easier for nanoparticles to become dislodged from the support surface. Pd metal has stronger interactions with TiO_2 surfaces and is thus more stable on

it.[33] An attempt was made to stabilize Pd nanoparticles on the wafers by depositing a thin TiO_2 layer (7 nm) using ALD before synthesizing the nanoparticles by block copolymer lithography (Scheme 3.2 A). The strong metal surface interactions (SMSI) between Pd and SiO_2 are expected to increase the stability of the nanoparticles on the surface. While the TiO_2 pre-layer reduces the Pd loss, a lower yield of the product was observed under the same reaction conditions (Table 3.4). The reactivity and the loss of Pd appear to be correlated. The Pd nanoparticles are more stable on TiO_2, making it harder for the Pd species to leach into the solution, reducing the overall yield.

Scheme 3.2 Proposed modifications for improving the stability of Pd nanoparticles on the SiO_2 support by A) TiO_2 pre-layer and B) Al_2O_3 porous over-layer.

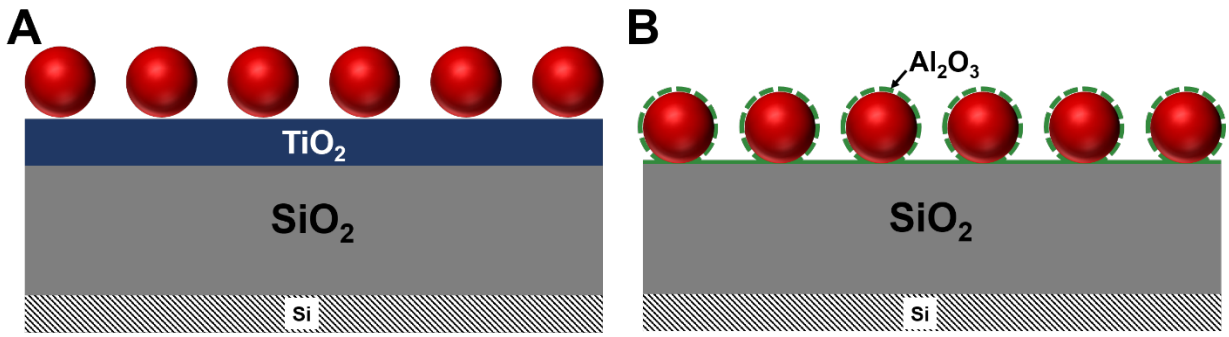

Table 3.4 Yield and Pd loss for reactions catalyzed by Pd nanoparticles on SiO_2 and TiO_2 supports. For each support, 0.05 mmol iodobenzene and 0.075 mmol of 4-methoxy phenyl boronic acid were reacted in a total reaction volume of 4 ml.

Support	Yield	Pd Loss
Si-SiO_2 (500 nm)	49 %	26 %
Si-SiO_2 (500 nm)- TiO_2 (10nm)	39 %	14 %

Since increasing the strength of the metal-oxide interaction was unable to prevent loss of Pd, steps were taken to immobilize the nanoparticles with a porous overlayer of Al_2O_3 (Scheme 3.2 B). A thin layer of Al_2O_3 deposited using atomic layer deposition (ALD) has been shown to be effective in immobilizing Pd

nanoparticles and preventing them from sintering. Due to the self-poisoning of Pd, the Al_2O_3 overcoat on the nanoparticles is porous while that over the SiO_2 support is dense.[34] The same principle was used to immobilize Pd nanoparticles. The porous overcoat has been shown to stabilize Pd nanoparticles without compromising the catalytic activity.[34] However, the elemental analysis of the reaction mixtures catalyzed by these modified catalysts showed that the porous Al_2O_3 overcoat did nothing to mitigate the observed Pd loss and the yields are identical with and without the overcoat (Table 3.5).

With both the methods used to stabilize the Pd nanoparticles on the surface, we observed similar loss of Pd. Since we have ensured that the Pd nanoparticles are immobilized on the surface, either by strong metal-surface interaction or by porous overcoats, the loss of the Pd must be from the atomic dissolution of the Pd species into the reaction mixture during the reaction.

Table 3.5 Yield and Pd loss for reactions catalyzed by Pd nanoparticles supported on SiO_2 with and without porous Al_2O_3 overcoat. For each catalyst, 0.05 mmol iodobenzene and 0.075 mmol of 4-methoxy phenyl boronic acid were reacted in a total reaction volume of 4 ml.

Porous Al_2O_3 Overcoat	**Yield**	**Pd Loss**
Absent	74 %	6 %
Present	75 %	7 %

3.3.5 Mechanism of Suzuki-Miyaura cross-coupling reaction on Pd nanoparticles

The true nature of the catalytic species in the Suzuki-Miyaura reaction has been a topic of debate for quite some time[16,20–24,30]. There is a vast body of literature that maintains that the nature of the reaction over solid catalysts is purely heterogeneous and no significant loss of palladium is observed over several reuse cycles[17,19,35]. There are other instances where the lost Pd species are re-captured and net-heterogeneity of the catalyst is maintained[23]. Efforts have also been made to isolate the real catalytic form of palladium using selectively permeable membranes[20,24,30]. The work done in this field has concluded that

the ionic species Pd(II) is the active species while Pd(0) on Pd precursors and nanoparticles merely acts as the pre-catalyst.[25,26,30]

Scheme 3.3 Mechanism of the Suzuki-Miyaura cross-coupling reaction[10]

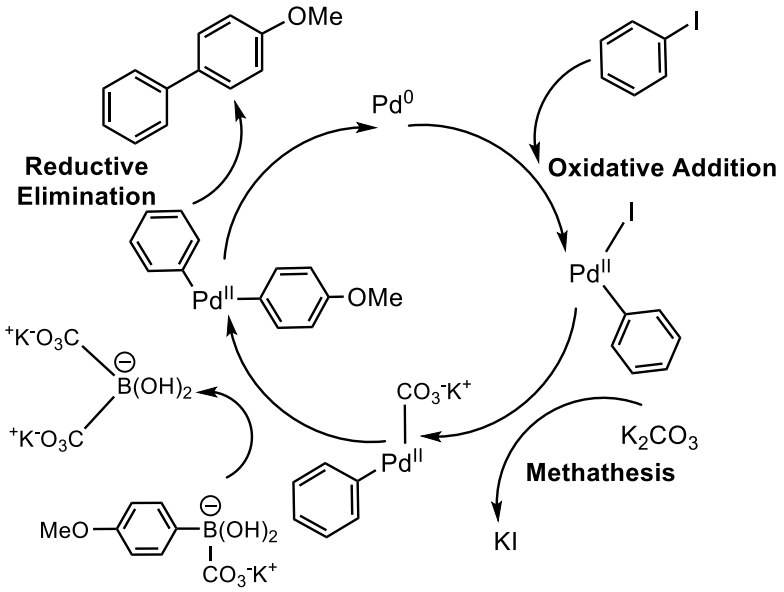

Against this controversial background, the experiments described in the preceding sections lead to the conclusion that the real catalytic species in the reaction are not the Pd(0) on the nanoparticles. The control experiments described in the previous sections prove that the reaction moves ahead without the heterogenous catalyst wafer present if the Pd(II)-haloaryl complex is already formed. The Pd loss registered per reaction vial, each starting with 0.05 mmol of haloarene, is observed to be nearly unchanged irrespective of the reaction conditions (Table 3.6). The consistent loss of Pd in every different reaction condition shows that this loss depends on the intrinsic nature of the reaction and not the reaction conditions. This can be used indirectly to conclude that the ionic Pd(II) species, formed as a result of oxidative addition of the aryl halide to Pd(0) (Scheme 3.3), is the true active species.

Table 2.6 Summary of amount of Pd lost per each reaction cycle as a function of reaction conditions. For each catalyst, 0.05 mmol iodobenzene and 0.075 mmol of 4-methoxy phenyl boronic acid were reacted in a total reaction volume of 4 ml.

Reaction Conditions	Amount of Pd Lost (ng)
Pd nanoparticles/SiO_2 in MeOH-MeCN-H_2O	1.5
Pd nanoparticles/SiO_2 in Dioxane-H_2O	1.2
Pd nanoparticles/TiO_2 in Dioxane-H_2O	6.7
Pd nanoparticles with Al_2O_3 overcoat in Dioxane-H_2O	1.2

3.4 Conclusions

In attempting to explore Suzuki-Miyaura cross-coupling reaction as a model for catalyst optimization on a catalytic screening platform developed using PPL and SPBCL, we investigated the true homogeneous nature of the reaction. The consistent Pd loss observed, despite several efforts to immobilize and stabilize Pd nanoparticles, proved that atomic dissolution of Pd into the reaction mixture is intrinsic to the reaction. This section demonstrates that using supported Pd as heterogenous catalysts in the Suzuki-Miyaura cross-coupling reaction will involve some leaching of Pd species into the solution, despite a large body of research asserting otherwise. Our findings corroborate the evidence provided by a growing literature that the Suzuki-Miyaura reaction occurs in solution even though the Pd species initially started out as heterogenous catalyst.[21,23–26,30]

However, we must exercise great caution before making any conclusions about the nature of the catalytically active species. The instrument used to measure the amount of elemental Pd, employing the ICP-MS technique, has a sensitivity limit of 1 ppb. Owing to the initial low metal loading on the block copolymer synthesized catalyst wafers, most of the Pd concentrations detected by the ICP-MS are in the range of 1-5 ppb. This introduces a significant amount of uncertainty in the data. Moreover, constant leaching-deposition cycles that occur near the surface of the Pd nanoparticles make it harder to trace the ionic species present *during* the reaction. Although the exact amount of leached Pd is uncertain due to the small amounts involved, those small amounts are enough to catalyze the reaction. Despite the controversy

over the true nature of the catalytic species, the Suzuki-Miyaura cross-coupling is an industrially pivotal reaction. Thus, the focus of academic and industrial research in this field should be on removal of Pd from the final product instead of developing new heterogeneous Pd catalysts. For the purposes of developing combinatorial screening platforms using PPL and SPBCL, reactions like N-alkylation of amines[36] or hydrogen evolution reaction,[37,38] that do not lead to atomic dissolution of the catalyst, will be more suitable.

Acknowledgments

This work is based upon work supported by the GlaxoSmithKline LLC Agreement 100037477. Metal analysis was performed at the Northwestern University Quantitative Bio-element Imaging Center generously supported by NASA Ames Research Center NNA06CB93G.

3.5 References

(1) Senkan, S. Combinatorial Heterogeneous Catalysis - A New Path in an Old Field. *Angew. Chemie - Int. Ed.* **2001**, *40* (2), 312–329.

(2) Huo, F.; Zheng, Z.; Zheng, G.; Giam, L. R.; Zhang, H.; Mirkin, C. A. Polymer Pen Lithography. *Science (80-.).* **2008**, *321* (5896), 1658–1660.

(3) Giam, L. R.; Massich, M. D.; Hao, L.; Shin Wong, L.; Mader, C. C.; Mirkin, C. A. Scanning Probe-Enabled Nanocombinatorics Define the Relationship between Fibronectin Feature Size and Stem Cell Fate. *Proc. Natl. Acad. Sci.* **2012**, *109* (12), 4377–4382.

(4) Chai, J.; Huo, F.; Zheng, Z.; Giam, L. R.; Shim, W.; Mirkin, C. A. Scanning Probe Block Copolymer Lithography. *Proc. Natl. Acad. Sci.* **2010**, *107* (47), 20202–20206.

(5) Liu, G.; Eichelsdoerfer, D. J.; Rasin, B.; Zhou, Y.; Brown, K. A.; Liao, X.; Mirkin, C. A. Delineating the Pathways for the Site-Directed Synthesis of Individual Nanoparticles on Surfaces. *Proc. Natl. Acad. Sci. U. S. A.* **2013**, *110* (3), 887–891.

(6) Chen, P. C.; Liu, G.; Zhou, Y.; Brown, K. A.; Chernyak, N.; Hedrick, J. L.; He, S.; Xie, Z.; Lin, Q. Y.; Dravid, V. P.; et al. Tip-Directed Synthesis of Multimetallic Nanoparticles. *J. Am. Chem. Soc.* **2015**, *137* (28), 9167–9173.

(7) Kluender, E. J.; Hedrick, J. L.; Brown, K. A.; Rao, R.; Meckes, B.; Du, J. S.; Moreau, L. M.; Maruyama, B.; Mirkin, C. A. Catalyst Discovery through Megalibraries of Nanomaterials. *Proc. Natl. Acad. Sci.* **2019**, *116* (1), 40–45.

(8) Miyaura, N.; Suzuki, A. Palladium-Catalyzed Cross-Coupling Reactions of Organoboron Compounds. *Chem. Rev.* **1995**, *95* (7), 2457–2483.

(9) Suzuki, A. Recent Advances in the Cross-Coupling Reactions of Organoboron Derivatives with Organic Electrophiles, 1995–1998. *J. Organomet. Chem.* **1999**, *576* (1–2), 147–168.

(10) Miyaura, N.; Yamada, K.; Suzuki, A. A New Stereospecific Cross-Coupling by the Palladium-Catalyzed Reaction of 1-Alkenylboranes with 1-Alkenyl or 1-Alkynyl Halides. *Tetrahedron Lett.* **1979**, *20* (36), 3437–3440.

(11) Li, Y.; Hong, X.; Collard, D.; El-sayed, M. A. Suzuki Cross-Coupling Reactions Catalyzed by Palladium Nanoparticles in Aquoes Solutions. *Org. Lett.* **2000**, *2* (15), 2385–2388.

(12) Handa, S.; Slack, E. D.; Lipshutz, B. H. Nanonickel-Catalyzed Suzuki-Miyaura Cross-Couplings in Water. *Angew. Chemie - Int. Ed.* **2015**, *54* (41), 11994–11998.

(13) Handa, S.; Smith, J.; Hageman, M.; Gonzalez, M.; Lipshutz, B. H. Synergistic and Selectrive Copper/Ppm Pd-Catalyzed Suzuki-Miyaura Couplings: In Water, Mild Conditions, with Recycling. *ACS Catal.* **2016**, *6* (6), 8179–8183.

(14) Niembro, S.; Shafir, A.; Vallribera, A. Catalytically Active Palladium Nanoparticles Embedded in an Organic-Inorganic Fluorinated Hybrid Material. *Arkivoc* **2010**, *2010* (3), 181–190.

(15) Narayanan, R.; El-sayed, M. A. Effect of Catalysis on the Stability of Metallic Nanoparticles : Suzuki Reaction Catalyzed by PVP-Palladium Nanoparticles. **2003**, 8340–8347.

(16) Pröckl, S. S.; Kleist, W.; Gruber, M. A.; Köhler, K. In Situ Generation of Highly Active Dissolved Palladium Species from Solid Catalysts—A Concept for the Activation of Aryl Chlorides in the Heck Reaction. *Angew. Chemie - Int. Ed.* **2004**, *43*, 1881–1882.

(17) Mandali, P. K.; Chand, D. K. Palladium Nanoparticles Catalyzed Suzuki Cross-Coupling Reactions in Ambient Conditions. *Catal. Commun.* **2013**, *31*, 16–20.

(18) Hooshmand, S. E.; Heidari, B.; Sedghi, R.; Varma, R. S. Recent Advances in the Suzuki-Miyaura Cross-Coupling Reaction Using Efficient Catalysts in Eco-Friendly Media. *Green Chem.* **2019**, *21* (3), 381–405.

(19) Dell'Anna, M. M.; Mali, M.; Mastrorilli, P.; Rizzuti, A.; Ponzoni, C.; Leonelli, C. Suzuki-Miyaura Coupling under Air in Water Promoted by Polymer Supported Palladium Nanoparticles. *J. Mol. Catal. A Chem.* **2013**, *366*, 186–194.

(20) Thathagar, M. B.; Elshof, J. E.; Rothenberg, G. Pd Nanoclusters in C-C Coupling Reactions: Proof

of Leaching. *Angew. Chemie - Int. Ed.* **2006**, *45*, 2886–2890.

(21) Kohler, K.; Heidenreich, R. G.; Krauter, J. G. E.; Pietsch, J. Highly Active Palladium / Activated Carbon Catalysts for Heck Reactions : Correlation of Activity, Catalyst Properties, and Pd Leaching. *Chem. - A Eur. J.* **2002**, *8* (3), 622–631.

(22) Mcglacken, G. P. Pd (0) Nanoparticles (NPs) as Catalysts in Cross-Coupling Reactions and the Homogeneous vs . Heterogeneous Debate. *Organomet. Chem.* **2016**, *40* (0), 33–53.

(23) Niu, Z.; Peng, Q.; Zhuang, Z.; He, W.; Li, Y. Evidence of an Oxidative-Addition-Promoted Pd-Leaching Mechanism in the Suzuki Reaction by Using a Pd-Nanostructure Design. *Chem. - A Eur. J.* **2012**, *18* (32), 9813–9817.

(24) Gaikwad, A. V.; Holuigue, A.; Thathagar, M. B.; Ten Elshof, J. E.; Rothenberg, G. Ion- and Atom-Leaching Mechanisms from Palladium Nanoparticles in Cross-Coupling Reactions. *Chem. - A Eur. J.* **2007**, *13* (24), 6908–6913.

(25) Astruc, D. Palladium Nanoparticles as Efficient Green Homogeneous and Heterogeneous C-C Coumplex Precatalysis: A Unifying View. *Inorganic Chemistry.* 2007, p 1884.

(26) Bourouina, A.; Meille, V.; de Bellefon, C. About Solid Phase vs. Liquid Phase in Suzuki-Miyaura Reaction. *Catalysts* **2019**, *9* (1), 60.

(27) Gogoi, N.; Bora, U.; Borah, G.; Gogoi, P. K. Nanosilica-Anchored Pd(II)-Schiff Base Complex as Efficient Heterogeneous Catalyst for Activation of Aryl Halides in Suzuki–Miyaura Cross-Coupling Reaction in Water. *Appl. Organomet. Chem.* **2017**, *31* (9), 1–8.

(28) Li, Y.; Mao, F.; Chen, T.; Zhou, Z.; Wang, Y.; Huang, J. In Situ Trapped and Immobilized Palladium Nanoparticles as Active and Clean Catalysts for Suzuki-Miyaura Reaction. *Adv. Synth. Catal.* **2015**, *357* (13), 2827–2832.

(29) Kim, S. W.; Kim, M.; Lee, W. Y.; Hyeon, T. Fabrication of Hollow Palladium Spheres and Their Successful Application to the Recyclable Heterogeneous Catalyst for Suzuki Coupling Reactions. *J. Am. Chem. Soc.* **2002**, *124* (26), 7642–7643.

(30) Phan, N. T. S.; Van Der Sluys, M.; Jones, C. W. On the Nature of the Active Species in Palladium Catalyzed Mizoroki-Heck and Suzuki-Miyaura Couplings - Homogeneous or Heterogeneous Catalysis, a Critical Review. *Adv. Synth. Catal.* **2006**, *348* (6), 609–679.

(31) Zhou, W. J.; Wang, K. H.; Wang, J. X.; Gao, Z. R. Ligand-Free, Atom-Efficient Suzuki-Miyaura Type Cross-Coupling Reactions at Room Temperature. *Tetrahedron* **2010**, *66* (38), 7633–7641.

(32) Hussain, I.; Capricho, J.; Yawer, M. A. Synthesis of Biaryls via Ligand-Free Suzuki–Miyaura Cross-Coupling Reactions: A Review of Homogeneous and Heterogeneous Catalytic Developments. *Adv. Synth. Catal.* **2016**, *358* (21), 3320–3349.

(33) Li, Y.; Fan, Y.; Yang, H.; Xu, B.; Feng, L.; Yang, M.; Chen, Y. Strong Metal-Support Interaction and Catalytic Properties of Anatase and Rutile Supported Palladium Catalyst Pd/TiO2. *Chem. Phys. Lett.* **2003**, *372* (1–2), 160–165.

(34) Lu, J.; Liu, B.; Greeley, J. P.; Feng, Z.; Libera, J. A.; Lei, Y.; Bedzyk, M. J.; Stair, P. C.; Elam, J. W. Porous Alumina Protective Coatings on Palladium Nanoparticles by Self-Poisoned Atomic Layer Deposition. *Chem. Mater.* **2012**, *24* (11), 2047–2055.

(35) Crudden, C. M.; Sateesh, M.; Lewis, R. Mercaptopropyl-Modified Mesoporous Silica: A Remarkable Support for the Preparation of a Reusable, Heterogeneous Palladium Catalyst for Coupling Reactions. *J. Am. Chem. Soc.* **2005**, *127* (28), 10045–10050.

(36) Shimizu, K.; Nishimura, M.; Satsuma, A. γ-Alumina-Supported Silver Cluster for N-Benzylation of Anilines with Alcohols. *ChemCatChem* **2009**, *1* (4), 497–503.

(37) Baeck, S. H.; Jaramillo, T. F.; Kleiman-Shwarsctein, A.; McFarland, E. W. Automated Electrochemical Synthesis and Characterization of TiO 2 Supported Au Nanoparticle Electrocatalysts. *Meas. Sci. Technol.* **2005**, *16* (1), 54–59.

(38) Jayaraman, S.; Hillier, A. C. Electrochemical Synthesis and Reactivity Screening of a Ternary Composition Gradient for Combinatorial Discovery of Fuel Cell Catalysts. *Measurement Science and Technology*. 2005, pp 5–13.

Chapter Four: Scope, Mechanism, and Control of Nanopore Formation in SiO_2 *via* High Temperature Entrenchment of Metal Nanoparticles

Abha Gosavi, James Hedrick, Peng-Cheng Chen, Justin Notestein, and Chad Mirkin

4.1 Introduction

At high temperatures, metal nanoparticles cause local excavation and/or subsequent pore formation on oxide supports.[1–9] Nanopore formation is observed when Au discs, 1 μm in diameter, are heated on fused SiO_2 to 1050 ºC over 10 h.[6,7] While no nanopore formation is observed, heating of Au and Cu particles on sapphire supports exhibit nanoparticle embedding and oxide ridge formation.[1,4,5] For both plasmonic and catalytic applications, a diversity of particles that can effect such processes would be desirable. Indeed, being able to use smaller particles with a greater diversity of compositions, while simultaneously having control over the extent of entrenchment, would be attractive. This could lead to arrays of site-isolated particles immobilized on a support but exposed for subsequent use, or to arrays of pores of controlled depth. In this chapter, we show that under rapid heating to temperatures of around 1000 ºC, metal nanoparticles (Au, Ag, Cu, Pd, and Pt) less than 15 nm in size will entrench in the SiO_2 layer on a silicon wafer to create pores as deep as 250 nm.

Recognizing that this process may be useful for creating arrays of immobilized nanoparticles where the nanoparticles are fixed in position but still exposed above the surface, we designed a novel tri-layer structure consisting of a layer of SiO_2 on Al_2O_3, on a silicon wafer. After fast heating to temperatures above 1000 ºC, we show that sub 15 nm diameter Au nanoparticles entrench on such substrates, yielding structures that can be partially buried into pits 3-5 nm deep. The depth of the pits is tuned based on the thickness of the top SiO_2 layer, because the Al_2O_3 layer acts as barrier layer for both further entrenchment and reaction with the Si layer underneath. Moreover, the exact mechanism that leads to selective nanopore formation on SiO_2 without total particle encapsulation is not well understood in previous literature. In this work, we identify that diffusion of metal in SiO_2 at high temperatures lowers the glass transition temperature

(T_g) of SiO_2. The viscoelastic behavior of SiO_2 above its T_g leads to the nanopore formation. This behavior is thus selective only to amorphous oxide supports.[10]

4.2 Methods

4.2.1 Support fabrication

Silicon wafers (NOVA Electronic Materials, 285 nm thermal oxide) were used as received. Al_2O_3, TiO_2 and HfO_2 layers were deposited by atomic layer deposition (ALD). ALD of Al_2O_3 was carried out at 300 ºC under conditions that give 1 Å/cycle. 100 alternating cycles of H2O and $Al(CH_3)_3$ were deposited to obtain a thickness of 10 nm. 10 nm layers of HfO_2 and TiO_2 were obtained by ALD using $Hf(N(CH_3)_2)_4$ (150 ºC, 1.04 Å /cycle) and $Ti(N(CH_3)_2)_4$ (150 ºC, 0.4 Å /cycle) as the precursors, respectively. All ALD was carried out using a Savannah S100 ALD system under cleanroom conditions using optimized preset recipes. SiO_2 was deposited using Lesker E-Beam evaporation of SiO_2 onto the wafers at 0.05 nm/sec under 8x10-8 mmHg pressure.

4.2.2 Nanoparticle synthesis and deposition

Metal precursor inks were synthesized by combining the diblock copolymer, PEO-*b*-P2VP (2800-b-1500) (Polymer Source, Inc.) and metal precursors ($HAuCl_4$, $AgNO_3$, Na_2PdCl_4, H_2PtCl_6, $CuNO_3$) at a 4:1 pyridyl: metal molar ratio in water and shaking overnight. The pH of the inks was maintained between 4-5 by adding dilute HCl. The ink solution was spin-coated on wafers (2000 rpm, 1 min) and the samples were treated with oxygen plasma (60 W, 5 min). To convert the polymer features into nanoparticles, the coated wafer was thermally annealed in a tube furnace under Ar (195 mL/min) for 10 h at 150 ºC and then under H_2 (195 mL/min) for 10 h at 500 ºC.

4.2.3 Rapid thermal processing

Metal nanoparticles were subsequently entrenched by heating in Ar flow (100 mL/min) in a rapid thermal processing (RTP) furnace (OTF-1200X-4-RTP-UL, MTI Corporation) with a fast ramp rate of 3.3 ºC/sec to the targeted temperature (900-1020 ºC) and held for 40 minutes in four intervals of 10 minutes each. The samples were taken out and AFM imaged between each interval before heating again. The

samples were passively cooled to room temperature under Ar flow (25 ml/min). The furnace cools down from 1000 ºC to 480 ºC in less than a minute, 480 ºC to room temperature takes 2 hours.

4.2.4 Characterization

Scanning electron microscopy (SEM) of the cross-sections of entrenched nanoparticles was done after coating the fractured samples with a 5 nm layer of gold using a Hitachi SU-8030 scanning electron microscope at an accelerating voltage of 3 kV and 10 μA current. Atomic force microscopy (AFM) measurements were performed on a FastScan (Bruker) using FastScan C probes to study the 3D topography of the samples. AFM image analysis and quantitative measurements were done using Nanoscope Analysis software (Bruker). Figure 4.1 shows how the particle height, apparent pore depth, and ridge height is measured.

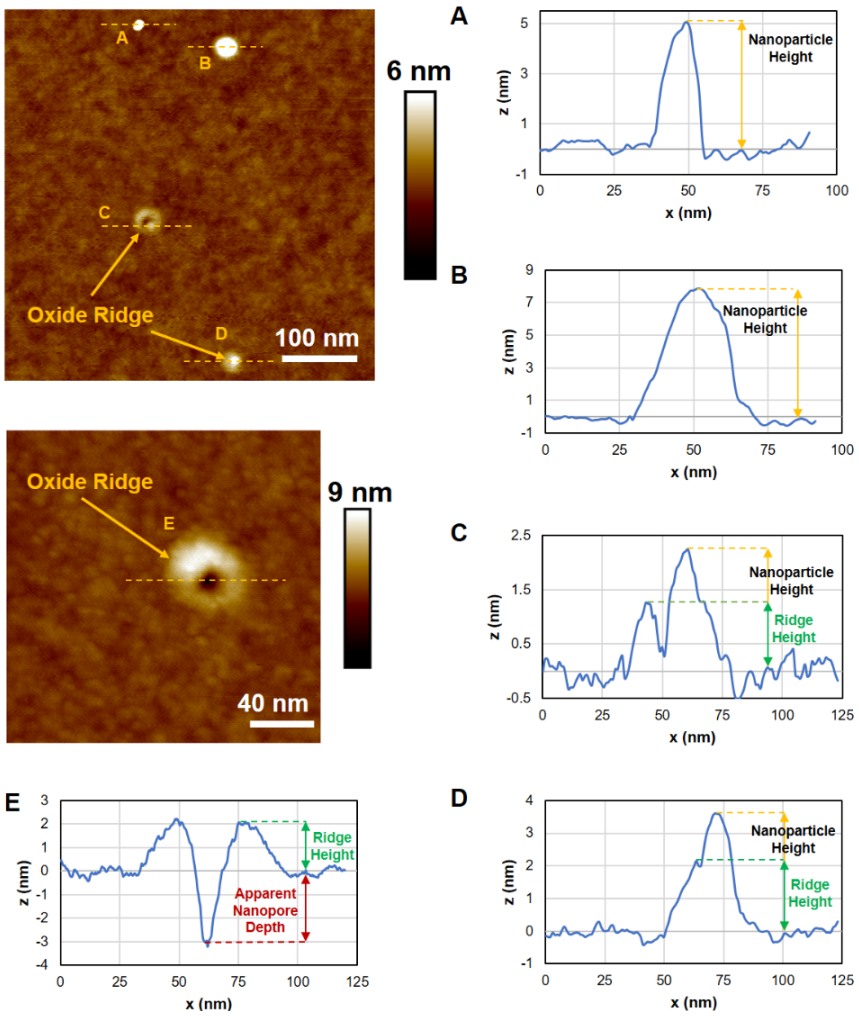

Figure 4.1 AFM images and line sections show how nanoparticle height and apparent nanopore depth are defined. For A & B) nanoparticles with no oxide ridges, C) a partially entrenched nanoparticle with oxide ridge, D) a nanoparticle with oxide ridge, and E) a nanopore with oxide ridge.

4.3 Results and Discussion

4.3.1 Total entrenchment of Au, Ag, Cu, Pd, and Pt nanoparticles

Supported nanoparticles (2.5-10 nm, depending on the metal) of Au, Ag, Cu, Pd, and Pt were synthesized by block copolymer micelle lithography (Figure 4.2, left).[11] These nanoparticles completely entrench into the 285 nm thermal oxide layer of a silicon wafer when heated for 40 minutes at 900 ºC (Ag) or 1020 ºC (other metals). The lower melting temperature of Ag and its higher diffusivity in SiO_2[12] is

presumed to be responsible for allowing entrenchment to proceed at a lower temperature for that metal. During the entrenchment process, the original supported nanoparticles are transformed into nanopores surrounded by oxide ridges that have similar diameters as the nanoparticles (Figure 4.2, center column). The nanopores thus formed, extend through the thermal oxide layer (Figure 4.2, right column), but stop at the underlying silicon surface. While all metals tested are entrenched completely, the resulting surface morphology is distinct for each metal (Figure S5). Pt nanoparticles entrench without forming significant ridges, while the entrenchment of Au and Pd nanoparticles is accompanied by slight (~ 1-2 nm high) ridge formation. Cu and Ag nanoparticles, on the other hand, cause the formation of larger ridges (~3-4 nm for Cu and 10-15 nm for Ag) in the SiO_2 surface. The ridges in Ag nearly close off the pores on the surface (Figure 4.2B inset). The trends in the sizes of the ridges observed are in agreement with the trends in solubility for the metals in SiO_2 at 1000 ºC (Ag>Cu>Pd>Au>Pt).[12]

While the small size of these nanoparticles does not readily permit scanning electron microscopy (SEM) to address whether the nanoparticles are still present at the base of the nanopores, similar imaging done on 1 μm particles by de Vreede et al.[6] suggests that the nanoparticles retain their crystallinity and structure at the bottom of the nanopores. The diagonal tracks of the pores (as observed for Au and Ag) have been previously reported in cases where fast ramp rates were employed.[6]

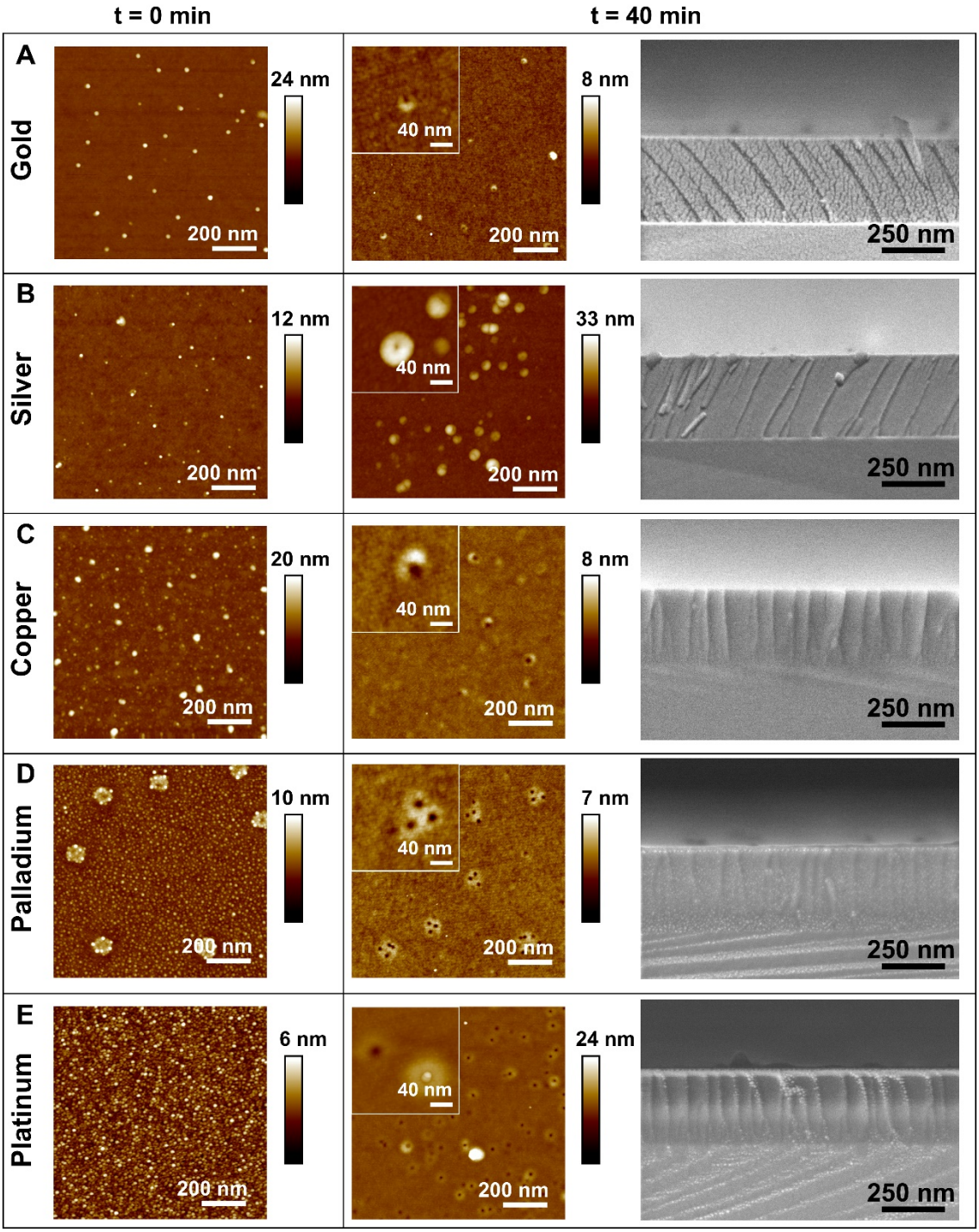

Figure 4.2 AFM images of different metal nanoparticles before and after heating to 1000 ºC (Ag- 900 ºC) A) Au nanoparticles (average height 14.0 nm ± 7.5 nm), B) Ag nanoparticles (average height 3.7 nm ± 1.8 nm), C) Cu nanoparticles (average height 9.2 nm ± 2.2 nm) as synthesized. D) Pd nanoparticles (average height 2.2 nm ± 0.6 nm),

E) Pt nanoparticles (average height 2.5 nm ± 0.5 nm). The insets show zoomed AFM images of the nanopore surface. The rightmost column shows scanning electron microscopy images of cross sections of surfaces after Au, Ag, Cu, Pd, and Pt nanoparticle entrenchment, respectively. The nanopores terminate at the interface of the SiO_2 and silicon layers.

4.3.2 Temperature dependence

Complete entrenchment of Au nanoparticles is observed upon heating for 40 minutes (in intervals of 10 minutes) only at 1000 ºC and above. Heating between 600 ºC - 800 ºC for 40 minutes shows no significant change in particle height or surface morphology (Figure 4.3 A-D). At 900 ºC, there is a slight decrease in the average nanoparticle height and ridge formation is observed around the nanoparticle after 10 min of heating, but no nanopore formation is seen at extended heating times of 40 min (Figure 4.4). This shows that nanopore formation is a kinetically driven phenomenon and requires a minimum temperature for initiation. Although manipulation of heating times and temperatures could enable one to control the depth to which nanoparticles entrench, these parameters would need to be laboriously optimized for different sizes and compositions of nanoparticles. Moreover, given that the process of entrenchment occurs rapidly at high temperatures, it may be extremely difficult to achieve reproducible, nanometer-level control of the extent of entrenchment.

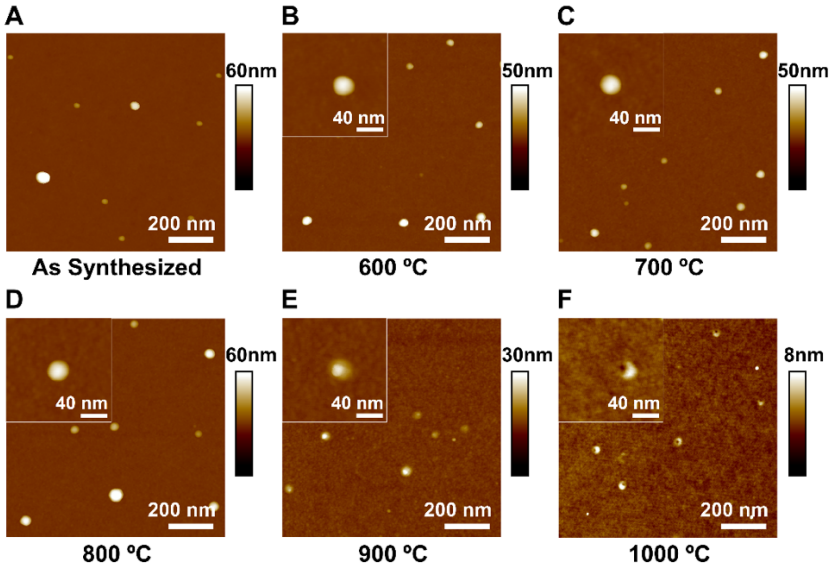

Figure 4.3 AFM images of Au nanoparticles supported on a silicon wafer with 285 nm thermal oxide layer, A) as synthesized, and heated to increasing temperatures, B) 600 ºC, C) 700 ºC, D) 800 ºC, E) 900 ºC, and F) 1000 ºC for

40 minutes each (in four intervals of 10 minutes each). The insets show zoomed AFM images of the nanopore or nanoparticle surface.

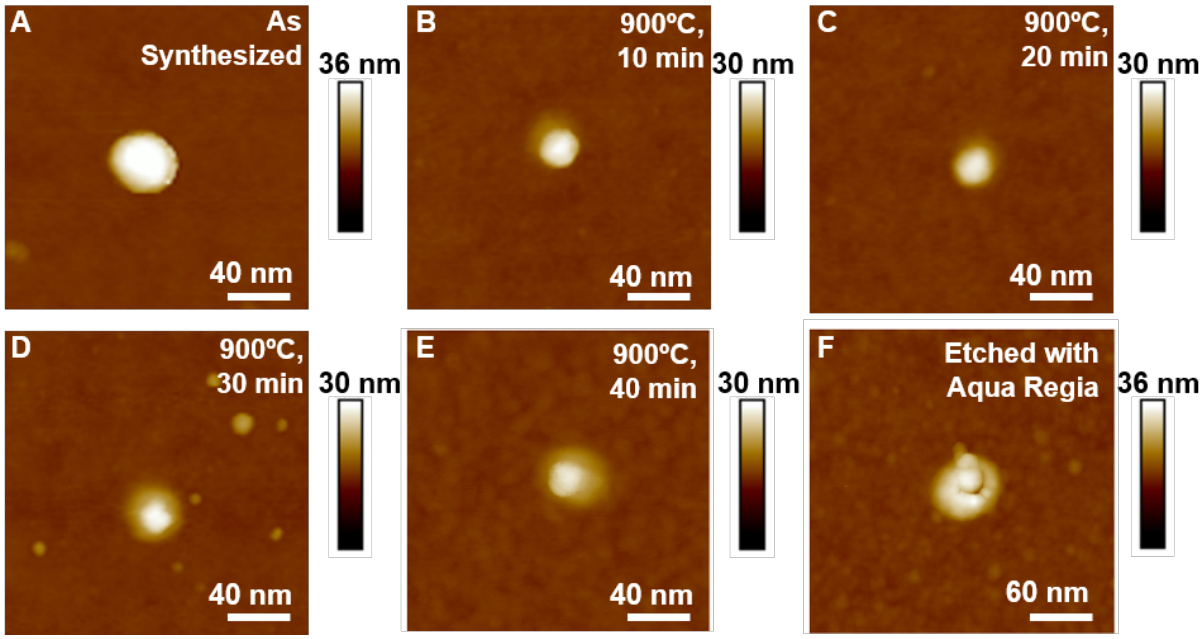

Figure 4.4 AFM images of an Au nanoparticle on SiO_2 surface A) as synthesized and heated at 900 ºC for B) 10 min, C) 20 min, D) 30 min, and E) 40 min followed by F) etching with aqua regia to remove the Au nanoparticle

4.3.3 Oxide support dependence

We next examined the behavior of Au nanoparticles on several common oxide layers consisting of 10 nm-thick layers of Al_2O_3, TiO_2, and HfO_2 on a silicon wafer and compared that to the nanopore formation observed on SiO2 surfaces. Materials were heated at 1020 ºC to understand the dependence of entrenchment behavior on the support material and to assess whether this could provide control over the process. Comparable Au nanoparticle distributions were obtained on the each of SiO_2, Al_2O_3, TiO_2, and HfO_2 layers on the silicon wafer. Au nanoparticles completely disappear into a 285 nm-thick thermal oxide (SiO_2) layer over 40 minutes at 1020 ºC, accompanied by pore formation (Figure 4.5 A). The height profile shows that most of the particles have entrenched below the surface within the first 10 minutes. The 10 nm Al_2O_3 layer is impervious to nanoparticle entrenchment at the same heating duration and temperature (Figure 4.5 B). The TiO_2 layer showed significant structural rearrangement after heating to 1020 ºC, which

is expected due to the transformation of anatase to rutile, but the Au nanoparticles also showed significant agglomeration during the heat treatment and some ridge formation is observed (Figure 4.5 C). The sample with Au nanoparticles on 10 nm HfO_2 showed coarsening of the support without nanoparticle entrenchment (Figure 4.5 D).

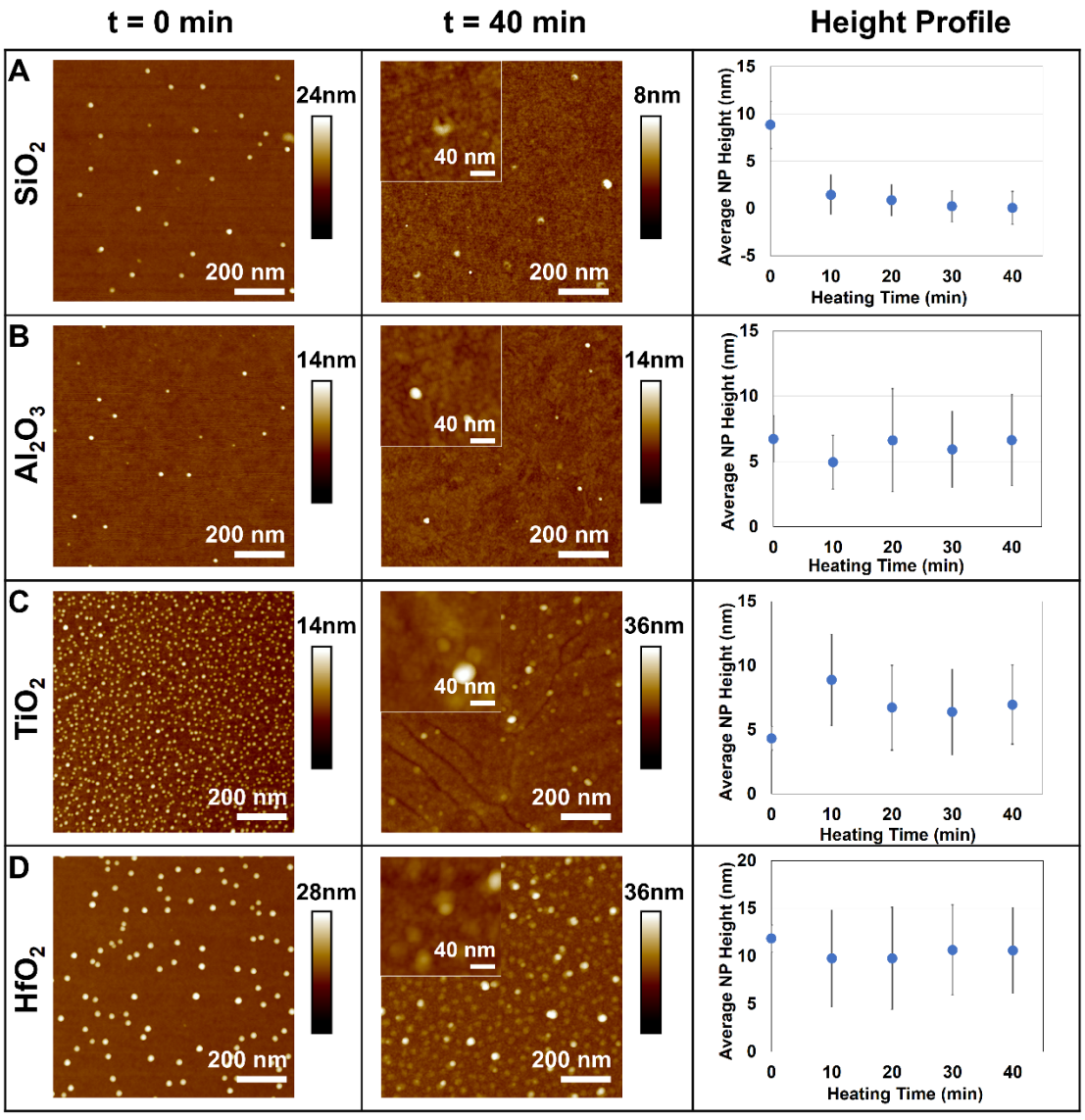

Figure 4.5 AFM images and height profiles of Au nanoparticles supported on modified silicon wafers with different terminal oxide layers - A) SiO_2, B) Al_2O_3, C) TiO_2, and D) HfO_2, after heating at to 1020 ºC for 40 minutes in four intervals of 10 minutes each.

TiO_2-supported catalysts are well known to engulf metal nanoparticles under reducing conditions through the strong-metal-support-interaction (SMSI) effect,[13,14] and these two processes (SMSI and entrenchment) may not be readily disentangled over reducible oxide surfaces. On the other hand, the Al_2O_3 film was structurally stable at these conditions and did not permit Au nanoparticle entrenchment. While there have been reports of Au[2] and Cu[1,4] particles showing structural rearrangements and ridge formation on sapphire wafers when exposed to high temperatures (780 ºC - 1100 ºC) for longer durations (~45 min-20 hours), nanopore formation does not appear to be possible in Al_2O_3 layers (Figure S6 A) under conditions that readily lead to nanopore formation in SiO_2. Thus, we establish that the process of nanopore formation is especially selective towards SiO_2 and does not occur to a significant extent on other oxide layers studied here.

4.3.4 Tri-layer supports for controlled entrenchment

As an application of the observations described above, we use a layer of Al_2O_3 as a barrier to entrenchment by adopting a tri-layer architecture (Scheme 4.1). Al_2O_3 is chosen among other impervious oxides since the surface is very stable under the high temperature and it is not reactive with Au. In principle, the Si layer on the wafer also acts as a barrier to entrenchment and can be used to control its extent. However, Au is known to alloy with Si at high temperatures[9] which can significantly alter its properties, such as catalytic activity.[15] The top layer is constructed by depositing uniform layers of SiO_2 on top of the Al_2O_3 layer. The thickness of the final SiO_2 layer controls the extent of nanoparticle entrenchment. Thus, an array of nanoparticles of varying sizes and compositions can be made to entrench, for example, only 3 nm into the support or be allowed to form pores of exactly uniform lengths. This makes the partially entrenched nanoparticles and nanopores of controlled lengths useful in a wide range of applications from catalysis to sensing to molecular separations.

Scheme 4.1 Construction of the 'tri-layer' supports for controlled nanoparticle entrenchment.

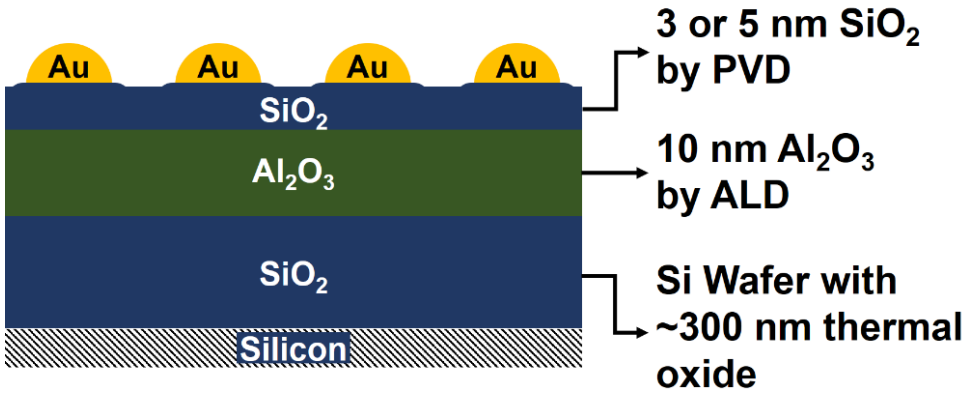

For tri-layer supports with a 3 nm SiO_2 entrenchment layer, the average height of Au nanoparticles decreases by 2.7 nm after heating for 40 minutes (in steps of 10 minutes) at 1020 ºC (Figure 4.6 A). Under the same conditions, the use of a 5 nm SiO_2 entrenchment layer in the tri-layer architecture results in an average Au nanoparticle height decrease of 4.2 nm after heating (Figure 4.6 B). Line sections from AFM (Figure S5 J and K) show a central mound corresponding to the partially entrenched Au nanoparticle, confirming the concept illustrated in Scheme 4.1. Cross-section SEM imaging (Figure S6 B) shows that no nanopore formation is observed on the tri-layer supports. In this way, the combination of tri-layer thicknesses and operating conditions could allow the partial entrenchment of many metallic nanoparticles.

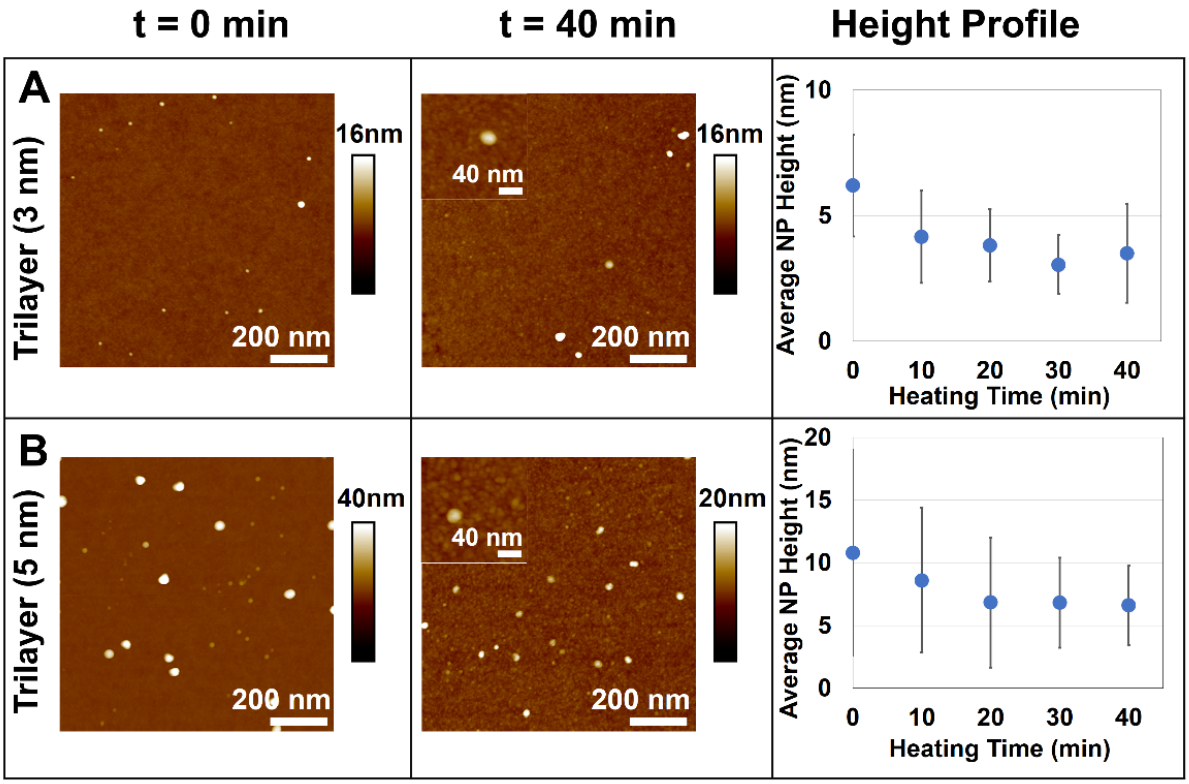

Figure 4.6 AFM images and height profiles of Au nanoparticles supported on A) tri-layer support with 3 nm SiO_2 on 10 nm Al_2O_3 on the wafer and B) tri-layer support with 5 nm SiO_2 on 10 nm Al_2O_3 on the wafer after being subjected for 40 minutes in four intervals of 10 minutes each at 1020 ºC. The insets show zoomed AFM images of the nanoparticle surface

4.3.5 Proposed mechanism of nanopore formation

In most of the literature reports so far, metal entrenchment in oxide supports is explained by oxide transport occurring at the metal-oxide interface.[1,4,6,7] Supported small metal particles (<70 nm) experience preferential melting along certain crystal planes at temperatures near their bulk melting points[16] while others (for example, Au (111)) remain solid.[17] Ridge formation occurs at high temperature around metals supported on oxides by surface transport of the oxide along the metal-oxide/air interface.[1,4,18–20] The continuous evaporation of the metal nanoparticles at the surface however prevents the ridge formation from reaching its equilibrium as the triple-line gets constantly renewed. The continued oxide transport has been proposed to cause the formation nanopores on SiO_2.[6] This explanation, however, does not justify the

formation of nanopores in SiO_2 and the absence of nanopores in Al_2O_3, TiO_2, and HfO_2. Likewise, ridge formation occurring in the absence of pore formation at lower temperatures (e.g. in Au/SiO_2 at 900 ºC and with extended heating times) cannot be satisfactorily explained. Other mechanisms proposed for the depletion of the SiO_2 layer include reactions that cause desorption of oxygen from the surface[5] and AuSi catalyzed SiO_2 decomposition[9] but these do not seem likely here as all the metals studied here do not react readily with SiO_2 to form silicides.[21] Alternately, Karakouz et al. have previously shown that Au crystals deform the surface of borosilicate glass substrates at temperatures above the glass transition temperature (T_g) of the substrate (~550ºC in that case).[22–24] Therefore, we propose that metal nanoparticle-induced changes to the glass transition temperature of SiO_2 above 900 ºC - 1000 ºC may be responsible for nanopore formation.

At high temperatures, above 900 ºC, nanoparticle evaporation[25–27] and oxide transport along the triple line (metal-vapor-oxide) leads to ridge formation[1,4,18–20] (Scheme 4.2 A). As the triple line (metal-oxide-gas) is constantly renewed due to evaporation, the oxide transport leads to further ridge formation (Scheme 4.2 B).[6] Simultaneously, at these temperatures, the solubility of metals in SiO_2 increases,[12] and the diffusion of the metals into the SiO_2 matrix causes a depression in the glass transition temperature of the thermal SiO_2, dropping it below its bulk T_g of 1197 ºC.[28–30] Because of the relatively slow diffusion of the metal through the glass, this T_g depression would only occur in the immediate vicinity of the nanoparticles, causing local changes in the SiO_2. At temperatures above the T_g, the SiO_2 behaves like a viscous liquid[31,32] allowing the metal nanoparticles to completely entrench through, generating nanopores (Scheme 4.2 C). The constant evaporation of Au could be the reason the nanoparticles are not completely engulfed in the SiO_2 layer closing the pores off. Because the nanopore formation process is mediated by T_g depression, it works for amorphous SiO_2, but on crystalline SiO_2 materials such as quartz, Au nanoparticles only undergo severe agglomeration upon heating with no entrenchment (Figure S7). Likewise, crystalline Al_2O_3, TiO_2, and HfO_2 are impervious to the pore formation, but can show ridge formation.

Scheme 4.2 Mechanism of nanopore formation in amorphous SiO_2 layer. A spherical supported metal nanoparticle is generated using block copolymer micelle lithography. A) At temperatures around 900 °C, surface evaporation from the metal nanoparticles occurs with simultaneous oxide transport along the triple line to form ridges. B) On further heating, the ridge formation continues and the solubility of the metal in the SiO_2 matrix increases. C) The diffusion of the metals into the SiO_2 matrix causes a depression in the glass transition temperature (T_g) of the neighboring thermal SiO_2. At temperatures above the T_g, the SiO_2 behaves like a viscous liquid allowing the metal nanoparticles to completely entrench through, generating nanopores.

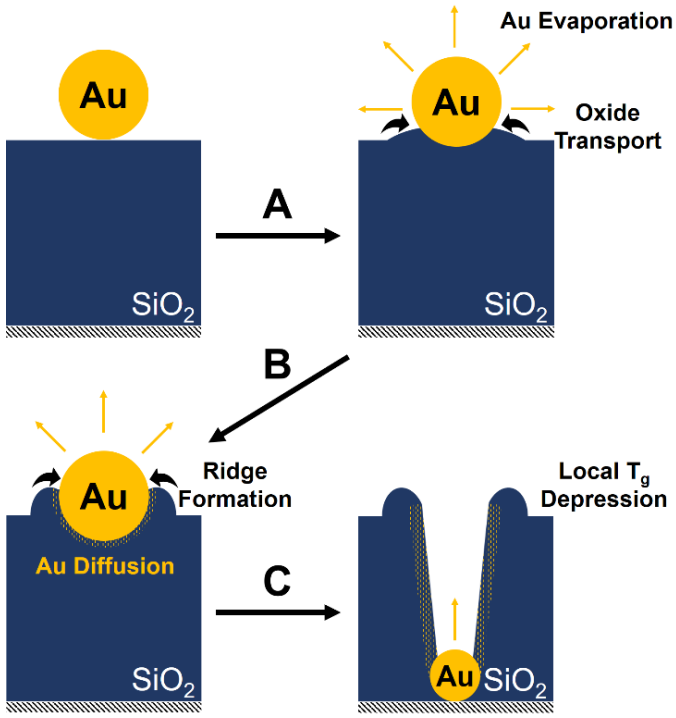

4.4 Conclusions

In this chapter, we have discovered that high temperature treatment of metallic nanoparticles leads to the formation of deep and narrow pores in thick thermal SiO_2 layers, using sub-15 nm nanoparticles of Au, Ag, Cu, Pd, and Pt. These findings thus expand and generalize the reported scope of this phenomenon to include the metals and nanoparticle sizes most relevant to applications including sensing and catalysis.[33–36] We have also established that nanopore formation is selective towards SiO_2 and occurs above a certain minimum temperature. Using the different behavior of Au nanoparticles on two common oxide supports (entrenchment in SiO_2, stability on Al_2O_3), we designed and prepared novel tri-layer supports for the

controlled, partial entrenchment of nanoparticles. We also provide evidence that nanopore formation is driven by dissolution of the metal into glassy oxides like SiO_2 but not quartz or Al_2O_3, which decreases the oxide T_g.

This innovation demonstrated results in robust, immobilized metal nanoparticles on modified Si wafer supports that would be stable under reaction conditions along with being structurally sound. These could be further extended to nanoparticles synthesized by techniques such as scanning probe block-copolymer lithography,[37–40] and polymer pen lithography.[41,42] The resulting controllably entrenched nanoparticles, with an exact control over the surfaces exposed to reaction conditions, could serve as location-stabilized catalysts or plasmonically active materials under reaction conditions that would otherwise lead to instability of the nanoparticles on planar supports. These instabilities include sintering, agglomeration, and other deactivation processes.[43–46] While the immobilized nanoparticles can be used for catalysis, the nanopores that are subsequently formed could have a wide range of applications on their own. The linear, high-aspect ratio nanopores formed in this process have diameters comparable to those of the starting nanoparticles (<15 nm) and are 100's of nanometers long. The resulting porous, planar materials could have applications in separation of large molecules.[47] The main advantage of using high temperature nanoparticle entrenchment to make nanopores in oxides is that the pores are highly oriented, linear, and have a high-aspect ratio which is crucial for sensing applications.[48,49] This would be difficult to achieve with other block copolymer-based techniques.[50] Pores derived from <15-nm nanoparticles would have advantages over the larger pores formed by other techniques,[51] and this method avoids the use of problematic etchants.[52–54] Some of these applications are currently being explored.

Acknowledgments

This material is based upon work supported by the Sherman Fairchild Foundation, Inc. and the Air Force Office of Scientific Research under Award number FA9550-16-1-0150. J.L.H. was supported by the Department of Defense (DoD) through the National Defense Science & Engineering Graduate Fellowship (NDSEG). P.-C.C. acknowledges support from the Cabell Terminal Year Fellowship from Northwestern University. This work made use of the EPIC and SPID facilities of Northwestern University's NUANCE

Center, which has received support from the Soft and Hybrid Nanotechnology Experimental (SHyNE) Resource (NSF ECCS-1542205); the MRSEC program (NSF DMR-1121262) at the Materials Research Center; the International Institute for Nanotechnology (IIN); the Keck Foundation; and the State of Illinois, through the IIN. This work utilized Northwestern University Micro/Nano Fabrication Facility (NUFAB), which is partially supported by Soft and Hybrid Nanotechnology Experimental (SHyNE) Resource (NSF ECCS-1542205), the Materials Research Science and Engineering Center (DMR-1720139), the State of Illinois, and Northwestern University.

4.5 References

(1) Curiotto, S.; Chien, H.; Meltzman, H.; Labat, S.; Wynblatt, P.; Rohrer, G. S.; Kaplan, W. D.; Chatain, D. Copper Crystals on the (1120) Sapphire Plane: Orientation Relationships, Triple Line Ridges and Interface Shape Equilibrium. *J. Mater. Sci.* **2013**, *48* (7), 3013–3026.

(2) Sui, M.; Pandey, P.; Li, M. Y.; Zhang, Q.; Kunwar, S.; Lee, J. Au-Assisted Fabrication of Nano-Holes on c-Plane Sapphire via Thermal Treatment Guided by Au Nanoparticles as Catalysts. *Appl. Surf. Sci.* **2017**, *393*, 23–29.

(3) Ajayan, P. M.; Makrs, L. D. Evidence for Sinking of Small Particles into Substrates and Implications for Heterogeneous Catalysis. *Nature* **1989**, *338*, 139–141.

(4) Ghetta, V.; Chatain, D. Morphologies Adopted by Al2O3 Single-Crystal Surfaces in Contact with Cu Droplets. *J. Am. Ceram. Soc.* **2004**, *85* (4), 961–964.

(5) Ono, L. K.; Behafarid, F.; Cuenya, B. R. Nano-Gold Diggers: Au-Assisted SiO2-Decomposition and Desorption in Supported Nanocatalysts. *ACS Nano* **2013**, *7* (11), 10327–10334.

(6) de Vreede, L. J.; Van Den Berg, A.; Eijkel, J. C. T. Nanopore Fabrication by Heating Au Particles on Ceramic Substrates. *Nano Lett.* **2015**, *15*, 727–731.

(7) de Vreede, L. J.; Schmidt Muniz, M.; Van Den Berg, A.; Eijkel, J. C. T. Nanopore Fabrication in Silicon Oxynitride Membranes by Heating Au-Particles. *J. Micromechanics Microengineering* **2016**, *26*, 37001–37006.

(8) Ilkiv, I.; Kotlyar, K.; Amel'chuk, D.; Lebedev, S.; Cirlin, G.; Bouravleuv, A. Thermal Penetration of Gold Nanoparticles into Silicon Dioxide. *Acta Phys. Pol. A* **2017**, *132* (2), 366–368.

(9) Babor, P.; Duda, R.; Polcak, J.; Prusa, S.; Potocek, M.; Varga, P.; Chechal, J.; Sikola, T. Real-Time Observation of Self-Limiting SiO2/Si Decomposition Catalysed by Gold Silicide Droplets. *RSC Adv.*

2015, *5*, 101726–101731.

(10) Gosavi, A. A.; Hedrick, J. L.; Chen, P.-C.; Notestein, J. M.; Mirkin, C. A. A Tri-Layer Approach to Controlling Nanopore Formation in Oxide Supports. *Nano Res.* **2019**, *12* (1), 1–6.

(11) Spatz, J. P.; Mößmer, S.; Möller, M. Mineralization of Gold Nanoparticles in a Block Copolymer Microemulsion. *Chem. - A Eur. J.* **1996**, *2* (12), 1552–1555.

(12) McBrayer, J. D. Diffusion of Metals in Silicon Dioxide. *J. Electrochem. Soc.* **1986**, *133* (6), 1242.

(13) Tauster, S. J.; Fung, S. C.; Garten, R. L. Strong Metal-Support Interactions. Group 8 Noble Metals Supported on TiO2. *J. Am. Chem. Soc.* **1978**, *100* (1), 170–175.

(14) Pesty, F.; Steinrück, H. P.; Madey, T. E. Thermal Stability of Pt Films on TiO2(110): Evidence for Encapsulation. *Surf. Sci.* **1995**, *339* (1–2), 83–95.

(15) Schleich, B.; Schmeisser, D.; Göpel, W. Structure and Reactivity of the System Si/Sio2/Pd: A Combined XPS, UPS and HREELS Study. *Surf. Sci.* **1987**, *191* (3), 367–384.

(16) Mei, Q. S.; Lu, K. Melting and Superheating of Crystalline Solids: From Bulk to Nanocrystals. *Prog. Mater. Sci.* **2007**, *52* (8), 1175–1262.

(17) Carnevali, P.; Ercolessi, F.; Tosatti, E. Melting and Nonmelting Behavior of the Au(111) Surface. *Phys. Rev. B* **1987**, *36* (12), 6701–6704.

(18) Chatain, D.; Curiotto, S.; Wynblatt, P.; Meltzman, H.; Kaplan, W. D.; Rohrer, G. S. Orientation Relationships of Copper Crystals on Sapphire (1 0 1^{-} 0) m-Plane and (1 0 1^{-} 2) r-Plane Substrates. *J. Cryst. Growth* **2015**, *418* (13), 57–63.

(19) Saiz, E.; Cannon, R. M.; Tomsia, A. P. Reactive Spreading in Ceramic/Metal Systems. *Oil Gas Sci. Technol.* **2001**, *56* (1), 89–96.

(20) Saiz, E.; Tomsia, a. P.; Cannon, R. M. Ridging Effects on Wetting and Spreading of Liquids on Solids. *Acta Mater.* **1998**, *46* (7), 2349–2361.

(21) Pretorius, R.; Harris, J. M.; Nicolet, M. A. Reaction of Thin Metal Films with SiO2 Substrates. *Solid State Electron.* **1978**, *21* (4), 667–675.

(22) Karakouz, T.; Tesler, A. B.; Sannomiya, T.; Feldman, Y.; Vaskevich, A.; Rubinstein, I. Mechanism of Morphology Transformation during Annealing of Nanostructured Gold Films on Glass. *Phys. Chem. Chem. Phys.* **2013**, *15* (13), 4656–4665.

(23) Karakouz, T.; Tesler, A. B.; Bendikov, T. A.; Vaskevich, A.; Rubinstein, I. Highly Stable Localized

Plasmon Transducers Obtained by Thermal Embedding of Gold Island Films on Glass. *Adv. Mater.* **2008**, *20* (20), 3893–3899.

(24) Karakouz, T.; Maoz, B. M.; Lando, G.; Vaskevich, A.; Rubinstein, I. Stabilization of Gold Nanoparticle Films on Glass by Thermal Embedding. *ACS Appl. Mater. Interfaces* **2011**, *3* (4), 978–987.

(25) Malyi, O.; Klinger, L.; Srolovitz, D. J.; Rabkin, E. Size and Shape Evolution of Faceted Bicrystal Nanoparticles of Gold on Sapphire. *Acta Mater.* **2011**, *59* (7), 2872–2881.

(26) Meng, G.; Yanagida, T.; Kanai, M.; Suzuki, M.; Nagashima, K.; Xu, B.; Zhuge, F.; Klamchuen, A.; He, Y.; Rahong, S.; et al. Pressure-Induced Evaporation Dynamics of Gold Nanoparticles on Oxide Substrate. *Phys. Rev. E - Stat. Nonlinear, Soft Matter Phys.* **2013**, *87*.

(27) Lee, J.; Pandey, P.; Sui, M.; Li, M. Y.; Zhang, Q.; Kunwar, S. Evolution of Self-Assembled Au NPs by Controlling Annealing Temperature and Dwelling Time on Sapphire (0001). *Nanoscale Res. Lett.* **2015**, *10* (1), 1–11.

(28) Johnson, L. E.; Sushko, P. V.; Tomota, Y.; Hosono, H. Electron Anions and the Glass Transition Temperature. *Proc. Natl. Acad. Sci.* **2016**, *113* (36), 10007–10012.

(29) Luis, M.; Dutra, E. Di Ff Usion Processes in Vitreous Silica Revisited. **2007**, 1–2.

(30) Ojovan, M. I. Configurons: Thermodynamic Parameters and Symmetry Changes at Glass Transition. *Entropy* **2008**, *10* (3), 334–364.

(31) Perez, J.; Duperray, B.; Lefevre, D. Viscoelastic Behaviour of an Oxide Glass near the Glass Transition Temperature. *J. Non. Cryst. Solids* **1981**, *44* (1), 113–136.

(32) Rouxel, T.; Sanglebœuf, J. C. The Brittle to Ductile Transition in a Soda-Lime-Silica Glass. *J. Non. Cryst. Solids* **2000**, *271* (3), 224–235.

(33) Kiyonaga, T.; Jin, Q.; Kobayashi, H.; Tada, H. Size-Dependence of Catalytic Activity of Gold Nanoparticles Loaded on Titanium (IV) Dioxide for Hydrogen Peroxide Decomposition. *ChemPhysChem* **2009**, *10* (17), 2935–2938.

(34) Overbury, S. H.; Schwartz, V.; Mullins, D. R.; Yan, W.; Dai, S. Evaluation of the Au Size Effect: CO Oxidation Catalyzed by Au/TiO2. *J. Catal.* **2006**, *241* (1), 56–65.

(35) Reske, R.; Mistry, H.; Behafarid, F.; Roldan Cuenya, B.; Strasser, P. Particle Size Effects in the Catalytic Electroreduction of CO2 on Cu Nanoparticles. *J. Am. Chem. Soc.* **2014**, *136* (19), 6978–6986.

(36) Beck, I. E.; Bukhtiyarov, V. I.; Pakharukov, I. Y.; Zaikovsky, V. I.; Kriventsov, V. V.; Parmon, V. N. Platinum Nanoparticles on Al2O3: Correlation between the Particle Size and Activity in Total Methane Oxidation. *J. Catal.* **2009**, *268* (1), 60–67.

(37) Liu, G.; Eichelsdoerfer, D. J.; Rasin, B.; Zhou, Y.; Brown, K. A.; Liao, X.; Mirkin, C. A. Delineating the Pathways for the Site-Directed Synthesis of Individual Nanoparticles on Surfaces. *Proc. Natl. Acad. Sci. U. S. A.* **2013**, *110* (3), 887–891.

(38) Chai, J.; Huo, F.; Zheng, Z.; Giam, L. R.; Shim, W.; Mirkin, C. A. Scanning Probe Block Copolymer Lithography. *Proc. Natl. Acad. Sci.* **2010**, *107* (47), 20202–20206.

(39) Chen, P. C.; Liu, G.; Zhou, Y.; Brown, K. A.; Chernyak, N.; Hedrick, J. L.; He, S.; Xie, Z.; Lin, Q. Y.; Dravid, V. P.; et al. Tip-Directed Synthesis of Multimetallic Nanoparticles. *J. Am. Chem. Soc.* **2015**, *137* (28), 9167–9173.

(40) Mirkin, C. A.; Chen, P.-C.; Liu, X.; Hedrick, J. L.; Xie, Z.; Wang, S.; Lin, Y.; Hersam, M. C.; Dravid, V. P. Polyelemental Nanoparticle Libraries. *Science (80-.).* **2016**, *352* (June), 1565–1569.

(41) Hedrick, J. L.; Brown, K. A.; Kluender, E. J.; Cabezas, M. D.; Chen, P. C.; Mirkin, C. A. Hard Transparent Arrays for Polymer Pen Lithography. *ACS Nano* **2016**, *10* (3), 3144–3148.

(42) Huo, F.; Zheng, Z.; Zheng, G.; Giam, L. R.; Zhang, H.; Mirkin, C. A. Polymer Pen Lithography. *Science (80-.).* **2008**, *321* (5896), 1658–1660.

(43) Behafarid, F.; Roldan Cuenya, B. Towards the Understanding of Sintering Phenomena at the Nanoscale: Geometric and Environmental Effects. *Top. Catal.* **2013**, *56* (15–17), 1542–1559.

(44) Liao, J.; Zhang, Y.; Yu, W.; Xu, L.; Ge, C.; Liu, J.; Gu, N. Linear Aggregation of Gold Nanoparticles in Ethanol. *Colloids Surfaces A Physicochem. Eng. Asp.* **2003**, *223* (1–3), 177–183.

(45) Jochem, A. R.; Ankah, G. N.; Meyer, L. A.; Elsenberg, S.; Johann, C.; Kraus, T. Colloidal Mechanisms of Gold Nanoparticle Loss in Asymmetric Flow Field-Flow Fractionation. *Anal. Chem.* **2016**, *88* (20), 10065–10073.

(46) Huang, N.; Xu, Y.; Jiang, D. High-Performance Heterogeneous Catalysis with Surface-Exposed Stable Metal Nanoparticles. *Sci. Rep.* **2014**, *4*, 7228–7236.

(47) Striemer, C. C.; Gaborski, T. R.; McGrath, J. L.; Fauchet, P. M. Charge- and Size-Based Separation of Macromolecules Using Ultrathin Silicon Membranes. *Nature* **2007**, *445* (7129), 749–753.

(48) Howorka, S.; Siwy, Z. Nanopore Analytics: Sensing of Single Molecules. *Chem. Soc. Rev.* **2009**, *38* (8), 2360.

(49) Shendure, J.; Ji, H. Next-Generation DNA Sequencing. *Nat. Biotechnol.* **2008**, *26* (10), 1135–1145.

(50) Li, Y.; Bastakoti, B. P.; Imura, M.; Hwang, S. M.; Sun, Z.; Kim, J. H.; Dou, S. X.; Yamauchi, Y. Synthesis of Mesoporous TiO2/SiO2 Hybrid Films as an Efficient Photocatalyst by Polymeric Micelle Assembly. *Chem. - A Eur. J.* **2014**, *20* (20), 6027–6032.

(51) Spinney, P. S.; Howitt, D. G.; Smith, R. L.; Collins, S. D. Nanopore Formation by Low-Energy Focused Electron Beam Machining. *Nanotechnology* **2010**, *21* (37), 375301–375308.

(52) Chartier, C.; Bastide, S.; Lévy-Clément, C. Metal-Assisted Chemical Etching of Silicon in HF-H2O2. *Electrochim. Acta* **2008**, *53* (17), 5509–5516.

(53) Tsujino, K.; Matsumura, M. Morphology of Nanoholes Formed in Silicon by Wet Etching in Solutions Containing HF and H2O2 at Different Concentrations Using Silver Nanoparticles as Catalysts. *Electrochim. Acta* **2007**, *53* (1), 28–34.

(54) Tsujino, K.; Matsumura, M. Boring Deep Cylindrical Nanoholes in Silicon Using Silver Nanoparticles as a Catalyst. *Adv. Mater.* **2005**, *17* (8), 1045–1047.

Chapter Five: Mapping the Thermal Entrenchment Behavior of Pd Nanoparticles on Planar SiO_2 Supports

Abha Gosavi, Justin Notestein, Chad Mirkin

5.1 Introduction

Metal-oxide and metal-metal interactions, especially at high temperatures, are of critical importance in catalysis[1–4] and electronics.[5,6] The metal-oxide interface is a catalytically active site for many industrially important reactions. At high temperatures, catalyst deactivation can occur via sintering or encapsulation due to surface rearrangement at the metal-oxide interface.[7–11] Similarly, thin films of metals deposited on oxide layers are used for the fabrication of electronic devices where the metal-semiconductor interface is of significance.[12,13] At high temperatures, the stability of these films is reduced by dewetting.[14–17] Thus, the understanding of metal-oxide interactions at high temperatures is important for designing stable catalysts and electronic devices. To this end, these interactions have been studied in literature for a wide range of metals (Au, Pd, Pt, Cu) and oxides (TiO_2, SiO_2, Al_2O_3) across different temperature ranges. At elevated temperatures (above 600 ºC) metal-oxide interactions, especially for metal nanoparticles, lead to a wide range of behaviors including agglomeration[7,18], Ostwald ripening[7,19], diffusion[20,21], reaction[11,22], encapsulation[9,23], and in some instances, nanopore formation.[24–27] The observation of one or more of these behaviors depends on the size and composition of the metal nanoparticles, the nature of the oxide, and the heating conditions.

Nanopore formation, predominantly observed for metal nanoparticles on amorphous SiO_2, occurs at very high temperatures (>1000 ºC).[24–27] This behavior is also described here as nanoparticle entrenchment since metal nanoparticles persist at the bottom of the pores.[26] Nanopores and embedded nanoparticles formed in this manner can be used in separations, catalysis, and electronics.[24,28–30] In this work, we have used Pd/SiO_2 as a model system to study nanopore formation and entrenchment behavior as a function of different heating conditions (temperature, time, and ramp-rate) and surface distributions (size and surface density). Out of all the metals that have exhibited nanopore formation (Au, Ag, Cu, Pd,

Pt), Pd nanoparticles entrench the most rapidly (within 10 minutes of heating) and form the most linear nanopores.[24] Moreover, the Pd/SiO_2 system has been thoroughly studied for different behaviors at high temperatures owing to its relevance to the field of catalysis.[31–34] Additionally, the low solubility of Pd in the SiO_2 matrix[21] minimizes potential Pd loss by diffusion into the SiO_2, thus allowing entrenchment to be studied in isolation.

In the previous chapter, we had proposed a mechanism for nanopore formation. When metal nanoparticles supported on amorphous SiO_2 are heated to temperatures above 1000 ºC. At high temperatures (above 900 ºC) the solubility of metals in the SiO_2 matrix is significant. When metal atoms diffuse into SiO_2, they lower its glass transition temperature (T_g). At temperatures above the T_g (~1000 ºC), the SiO_2 exhibits viscoelastic behavior due to partial melting, allowing the nanoparticles to form nanopores.[24] It has also been proposed, in other works, that the slow evaporation of the metal nanoparticles at their surface causes the continuous renewal of the metal- SiO_2-vapor interface and prevents the total encapsulation of the metal nanoparticle within the SiO_2 matrix. Even within the nanopore, the Au (111) plane of the nanoparticle is expected to not melt, which pins the nanopore and prevents its closing/pinching.[26]

When metal nanoparticles entrench within the SiO_2 surface at high temperatures, they form nanopores that extend though the entire thickness of the SiO_2 layer. We had previously shown that formation of nanopores occurs only above a certain minimum temperature (1000 ºC for Au nanoparticles).[24] The nanoparticles, depending on their composition and size, need different temperatures and heating times to entrench.[24] The two features that characterize a nanopore are the pore diameter and the height of the oxide ridge. The oxide ridge surrounding the nanopore is formed as a result of oxide transport occurring due to the shifting surface energy equilibrium at the metal-oxide-gas triple line.[17,26] Understanding how pathways such as agglomeration, diffusion, and encapsulation, also occurring at these temperatures, compete with nanopore and oxide ridge formation will provide a fundamental understanding of the metal-oxide interactions that lead to nanopore formation at these high temperatures. Moreover, this will also help us define synthesis conditions for nanopores of desired dimensions. Here, we examine Pd nanoparticles

of different sizes (1.5– 25 nm) and surface densities (5– 7000 nanoparticles/μm^2) and establish how the surface distribution of the nanoparticles define the final size and surface density of the nanopores, if entrenchment is observed.

We observe that nanoparticle surface densities that lead to agglomeration at a lower temperature[7], will form nanopores after they agglomerate to a certain size rather than in parallel or alternatively. To understand the role of the thermal processing in nanopore formation, the Pd on SiO_2 system was further studied under different heating conditions (temperature, hold time, and ramp rate) at two distinct sizes and surface densities- one that proceeds via agglomeration and one that does not. We observe that the nature of surface features after heating (1040 ºC, 10 minutes, 3.3 ºC/s) depends on the initial size and surface densities of nanoparticles. The features observed after heating include nanopores, partially embedded nanoparticles, agglomerated nanoparticles, and nanoparticles encapsulated in SiO_2. We also show that by tuning the initial size and surface density of Pd nanoparticles on SiO_2, we can control the nanopore diameter as well as the height of the surrounding oxide ridge. Initially the number of nanopores increases linearly with an increase in the number of nanoparticles, but above 20% surface coverage of nanoparticles, agglomeration becomes more important and the final number of nanopores are much less than the initial number of nanoparticles on the surface. This limits the maximum surface density of nanopores to ~150 nanopores/μm^2 but allows for a range of nanopore sizes (5-25 nm) by choosing the initial particle size distribution.

5.2 Methods

5.2.1 Nanoparticle synthesis

Randomly distributed Pd nanoparticles on SiO_2 surfaces were synthesized by using block co-polymer micelle lithography.[35–37] Aqueous solutions of Pd micelles were synthesized by combining the diblock copolymer, polyethylene oxide-b-polyvinyl pyridine (PEO-*b*-P2VP) of varying chain lengths (Table S1) (Polymer Source, Inc.) and Na_2PdCl_4 at different pyridyl: Pd molar ratios (32:1, 16:1, 8:1, 4:1, 2:1, 1:1, and 0.5:1) and allowing them to shake overnight. The pH of the solutions was maintained between 3-4 by adding dilute HCl. Thin films of the Pd micelle solution were spin-cast on Si wafers (NOVA Electronic

Materials, 285 nm thermal oxide) at different rotation speeds (1000 RPM, 2000 RPM, 3000 RPM, and 4000 RPM). Some of the samples were treated with oxygen plasma for different intervals (1 min, 2 min, 3min, and 5 min) (Plasma Etch Inc., PE 50XL, 30 W) to control the surface densities of Pd nanoparticles. The Pd-block co-polymer micelles were then reduced to nanoparticles by thermal annealing in a tube furnace (ThermoScientific Blue) under flowing argon gas (195 mL/min) for 10 hours at 150 ºC using a ramp-rate of 4 ºC/minute and then for 10 hours at 500 ºC under hydrogen gas (195 mL/min) using ramp-rate of 11 ºC/minute. The Pd nanoparticles synthesized have sizes ranging from 1.5- 25 nm and surface densities from 5-7000 nanoparticles/μm^2. A detailed description of the initial Pd nanoparticle size and distribution changes as a function of synthesis conditions is included in the supplementary materials and illustrated in Figure S8.

5.2.2 Rapid thermal processing

Thermal processing of the Pd nanoparticles on SiO_2 was performed under steady Ar flow (100 mL/min) in a rapid thermal processing (RTP) furnace (MTI Corporation, OTF-1200X-4-RTP-UL). Most of the samples were treated at 1040 ºC using a ramp rate of 3.3 ºC/s for 10 minutes. However, other operating conditions included ramp rates between 0.33 -3.3 ºC/s, temperatures between 850- 1040 ºC, and hold time between 1.5- 20 min. The samples were passively cooled to room temperature under Ar flow (25 mL/min). The furnace cools down from ~1000 ºC to 480 ºC in less than 5 min, while 480 ºC to room temperature takes 2 h.

5.2.3 Surface features and composition characterization

Atomic force microscopy (AFM) measurements were performed on a FastScan (Bruker) using FastScan C probes to study the 3D topography of the samples. AFM image analysis and quantitative measurements were performed using Nanoscope Analysis software (Bruker). The height of the nanoparticles detected by the software is defined as the standard nanoparticle size to avoid errors introduced due to tip convolution effects in the AFM. However, for certain surface configurations where there is great disparity between the nanoparticle height and diameter, both measurements are considered

and are specified clearly. The nanopore diameter is defined as the standard nanopore size since the exact depth of the nanopore cannot be detected using AFM.

The surface coverage of the Pd nanoparticles is defined as the percentage of the SiO_2 surface that is in contact with the Pd nanoparticles (as imaged from AFM), and is calculated via image processing in Image J. The surface composition of the SiO_2-supported Pd nanoparticles was analyzed before and after rapid thermal processing using X-ray photo-electron spectroscopy (XPS) equipped with an Al-source with a spot size of 500 μm (ThermoScientific, Escalab 250 Xi). To study the surface profile of the oxide ridges around the partially embedded nanoparticles, Pd nanoparticles were etched using an etchant solution (Transene, Pd Etchant) before imaging the surface via AFM.

5.3 Results and Discussion

5.3.1 Different behaviors observed at high temperatures

On subjecting the library of SiO_2 surfaces covered with Pd nanoparticles to rapid thermal processing (1040 ºC for 10 min using a ramp rate of 3.3 ºC/s), we observe a wide variety of resulting surface features. These include nanopores of various diameters, larger nanoparticles (due to agglomeration), smaller nanoparticles (possibly due to Ostwald ripening or evaporation and/or diffusion into the surface), and the formation of surface features that could not be removed by metal etching. These latter features indicate encapsulation of the Pd nanoparticle by SiO_2 that has become mobile at these temperatures. These behaviors were quantitatively defined using two non-dimensional values: pore fraction (f_{Pore}) and extent of agglomeration (E_{Agg}) (Equations 5.1 and 5.2, respectively).

$$f_{Pore} = 100 \times \left(\frac{Number\ of\ nanopores\ \ /\mu m^2}{Total\ number\ of\ features\ (nanopores + nanoparticles)\ /\mu m^2} \right) \tag{5.1}$$

$$E_{Agg} = 100 \times \left(1 - \frac{Final\ number\ of\ features (nanopores + nanoparticles)\ \ per\ \mu m^2}{Initial\ number\ of\ nanoparticles\ per\ \mu m^2} \right) \tag{5.2}$$

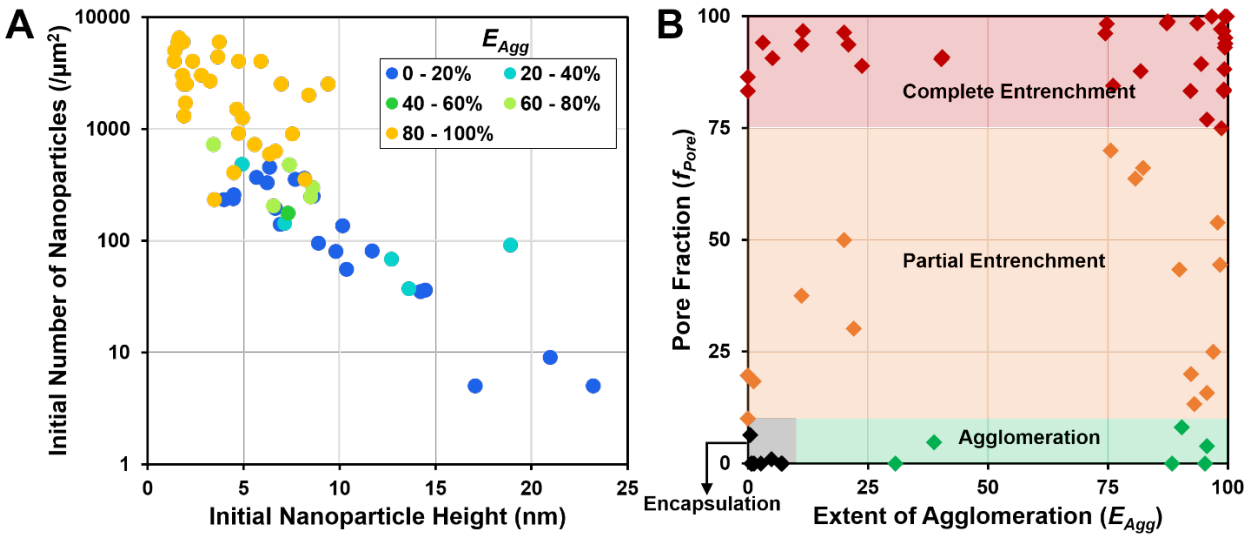

Figure 5.1 A) Tendencies to agglomerate (either with or without nanopore formation) across different distributions after being heated to 1040 ºC for 10 min using a ramp rate of 3.3 ºC/s. B) Defining different behaviors based different ranges of pore fraction (f_{Pore}) and extent of agglomeration (E_{Agg}).

For very small nanoparticles with low surface densities (size < 2 nm, surface density < 150 nanoparticles/μm^2), the surface features after heating are indistinguishable from the surface roughness (±1 nm) of the planar SiO_2 layer (Figure S9), and the nanoparticles may either be diffusing into the surface[21] or evaporating.[38] On the extreme end of the spectrum, after heating large nanoparticles with high surface densities where the nanoparticles tend to stack in a multi-layered arrangement (size ~ 7 nm, surface density ~ 4000 nanoparticles/μm^2), the SiO_2 surface becomes extremely porous indicating that overlapping nanopores are formed (Figure S10). These two distributions are excluded from consideration. In some other cases however, a decrease in the number density of the features (E_{Agg} > 0) is accompanied by an increase in the size of the remaining features. For cases where no nanopores are formed in the first 10 min of heating, the total amount of Pd is approximately conserved after heat treatment, confirming that, in most cases studied here, agglomeration of small particles into larger particles is the primary pathway for loss of nanoparticle number density (Table S2). The tendency of different nanoparticle distributions to agglomerate, either with or without nanopore formation, when heating to a temperature of 1040 ºC for 10 min using a ramp rate of 3.3 ºC/s is shown in Figure 5.1 A. Four different behaviors were quantitatively

identified across the entire range: 1) complete entrenchment, 2) partial entrenchment, 3) agglomeration, and 4) encapsulation. The different ranges of E_{Agg} and f_{Pore} used to define these behaviors are illustrated in Figure 5.1 B. These behaviors are observed across the entire range of nanoparticle size and surface densities considered (Figure S11).

Since the heating conditions employed here have shown nanopore formation previously, complete nanoparticle entrenchment is the most frequently observed outcome.[24,26] The complete entrenchment behavior is characterized by the presence of mostly nanopores on the surface (f_{Pore} > 75% and all ranges of E_{Agg}) and is accompanied by the formation of oxide ridges around the nanopores. The final surface density of these nanopores depends on whether the nanoparticles agglomerate before entrenchment. Thus, when extreme agglomeration occurs (E_{Agg} > 80%), the number of nanopores is only a small fraction of the initial number of nanopores. Even though the depth of the nanopore cannot be detected using AFM due the tip-size limitations, we have previously shown, via cross-section electron microcopy, that under these heating conditions, most nanopores extend through the entire thickness of the SiO_2 layer (285 nm in this case).[24] Partial entrenchment is defined as the behavior when not all the initial nanoparticles form nanopores upon heating. Under such circumstances, many particles remain on the surface (10% <f_{Pore} < 75% and all ranges of E_{Agg}). In this case, either nanoparticles are entrenched to a certain extent but do not form nanopores or a significant number of nanopores formed without the entrenchment of all the initial nanoparticles. Agglomeration (not accompanied by nanopore formation) is characterized by a reduction in the surface densities of nanoparticles and a corresponding increase in height (10% <f_{Pore} and E_{Agg} > 10%) without any apparent entrenchment. This presumably occurs when lateral mobility on the surface is favored over entrenchment within the annealing time (10 min). However, upon longer annealing, both the partially entrenched and agglomerated nanoparticles entrench to a greater extent, resulting in nanopore formation (Figure 5.2). This indicates that nanopore formation in these cases is slower than that observed for distributions that completely entrench within 10 min of rapid thermal processing. However, for some nanoparticle distributions, no nanopore formation or agglomeration is observed. Furthermore, extended heating of the nanoparticles results in no change in the surface features (f_{Pore} < 10% and E_{Agg} < 10%). It was surmised, through several experiments, that the features present on the surface are in fact, not Pd

nanoparticles but SiO_2 encapsulated nanoparticles and thus this behavior is defined as encapsulation. This behavior is discussed in greater detail further in this work.

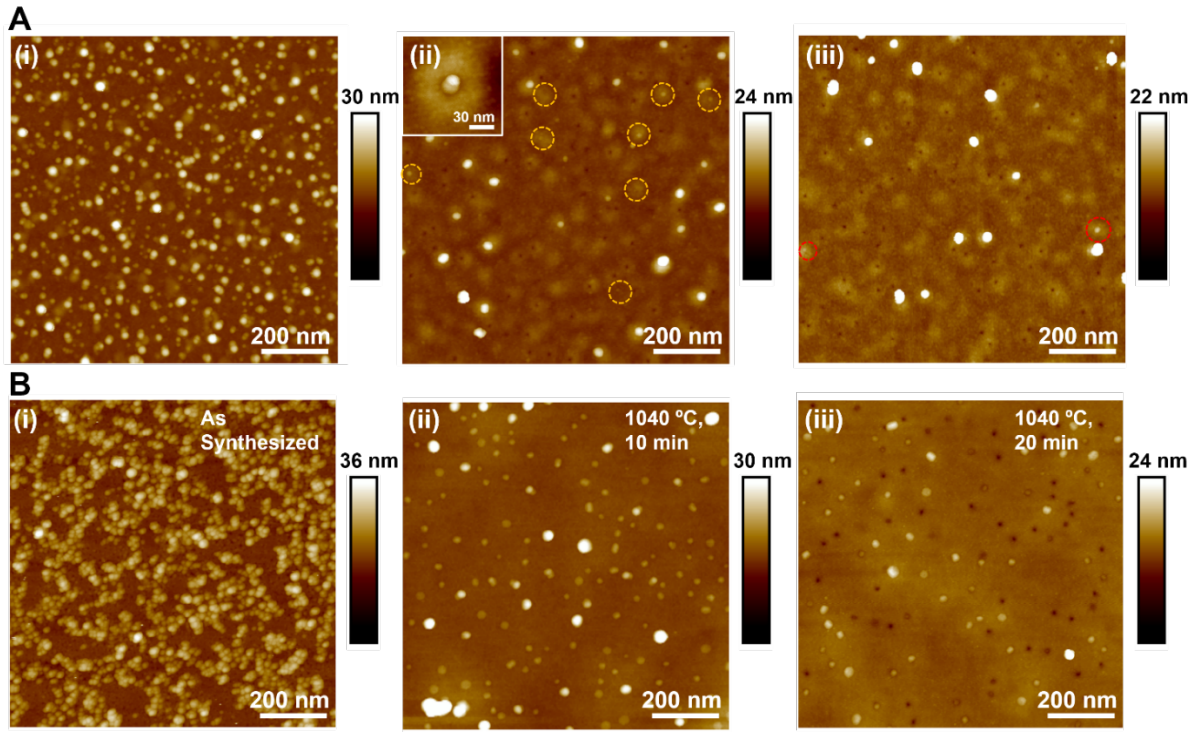

Figure 5.2 A) AFM images of Pd nanoparticles i) as synthesized (size ~ 7 nm, surface density ~ 500 nanoparticles/μm^2), that show ii) partial entrenchment (f_{pore} = 50%) after heating for 10 minutes at 1040 ºC with several *nearly-entrenched* nanoparticles (dotted circles, inset) which iii) entrench almost entirely (f_{pore} = 90%) after extended heating for 20 minutes at 1040 ºC with very few *nearly-entrenched* nanoparticles (dotted circles) B) AFM images of Pd nanoparticles i) as synthesized (size ~ 10 nm, surface density ~ 2500 nanoparticles/μm^2), that exhibit ii) agglomeration without nanopore formation (f_{pore} = 0%) on heating for 10 minutes at 1040 ºC, which iii) on extended heating for 20 minutes at 1040 ºC leads to nanopore formation (f_{pore} = 45%) in the SiO_2 surface.

The heating conditions that were used (1040 ºC for 10 min using a ramp rate of 3.3 ºC/s) have shown nanopore formation for many metal nanoparticles (Au, Ag, Cu, Pt, Pd) in the size range of 5- 15 nm with a surface density of 15- 30 nanoparticles /μm^2.[24] However, in the case of Pd nanoparticles, we have observed that the final fate of the nanoparticles in forming nanopores within 10 min of rapid thermal processing is dependent not only on the heating conditions used but also on the initial size and surface

density of the nanoparticles. The different behaviors previously identified, (complete and partial entrenchment, agglomeration, and encapsulation) are observed across different sizes, distribution, and surface area coverages of Pd nanoparticles. Particularly, we observe that nanopore formation, either with partial or complete entrenchment, occurs almost across the range of nanoparticle sizes and surface densities (Figure S11). At Pd surface coverage above 20%, agglomeration is always observed, with or without nanopore formation (Figure 5.3). In few cases, even with surface area coverages less than 20%, there are some nanoparticle distributions that exhibit agglomeration before entrenchment. The surface area coverage is a function of both the nanoparticle size and surface densities. Large nanoparticles with low surface density (for example, size = 12 nm, surface density = 80 nanoparticles/μm^2) have the same surface area coverage (8.5%) as that of smaller nanoparticles with high surface density (for example, size = 3 nm, surface density = 750 nanoparticles/μm^2). In this situation, the nanoparticle distribution with a higher surface density of nanoparticles will agglomerate before forming nanopores. Thus, surface area coverage alone cannot be used to predict the dominant behavior among the four behaviors defined (complete and partial entrenchment, agglomeration, and encapsulation).

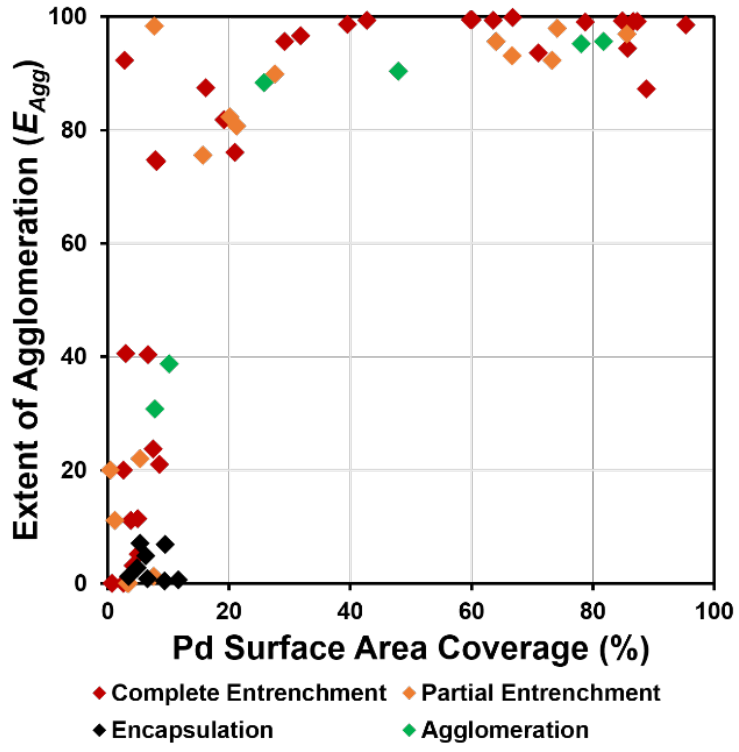

Figure 5.3 Different behaviors (complete and partial entrenchment, encapsulation, and agglomeration) observed as a function of surface area coverages and E_{Agg} of Pd nanoparticles on SiO_2 when heated to 1040 ºC for 10 min using a ramp rate of 3.3 ºC/s.

The key distributions of interest are those where no agglomeration is observed so that entrenchment and encapsulation can be studied in isolation, specifically, when the surface area of Pd

nanoparticles on SiO_2 and the extent of agglomeration is less than 20% (Figure 5.4). Nanoparticle distributions with sizes between 4-25 nm and surface densities between 5- 450 nanoparticles/μm^2) lie in this region. Across this range, Pd nanoparticles, below 5% surface coverage on SiO_2, primarily undergo complete entrenchment or partial entrenchment after heating. In the 5-15% surface coverage range, only nanoparticle encapsulation or partial entrenchment is observed (Figure 5.4 A). As discussed in the previous section, the surface area coverage is a function of both the nanoparticle size and surface density. Entrenchment to form nanopores (complete or partial) occurs when the nanoparticles have sizes between 6-25 nm and surface densities between 5-350 nanoparticles/μm^2 (Figure 5.4 B). Encapsulation occurs when the nanoparticles have sizes between 4-8 nm and surface densities between 250- 450 nanoparticles/μm^2. Thus, in the absence of agglomeration, the two dominant behaviors, entrenchment (complete or partial) and encapsulation are dominant at mutually exclusive ranges of surface area coverages as well as the nanoparticle sizes and surface densities. While it is much more difficult to identify the distributions that favor complete entrenchment over partial, we have shown before that partial entrenchment is indicative of slower nanopore formation.

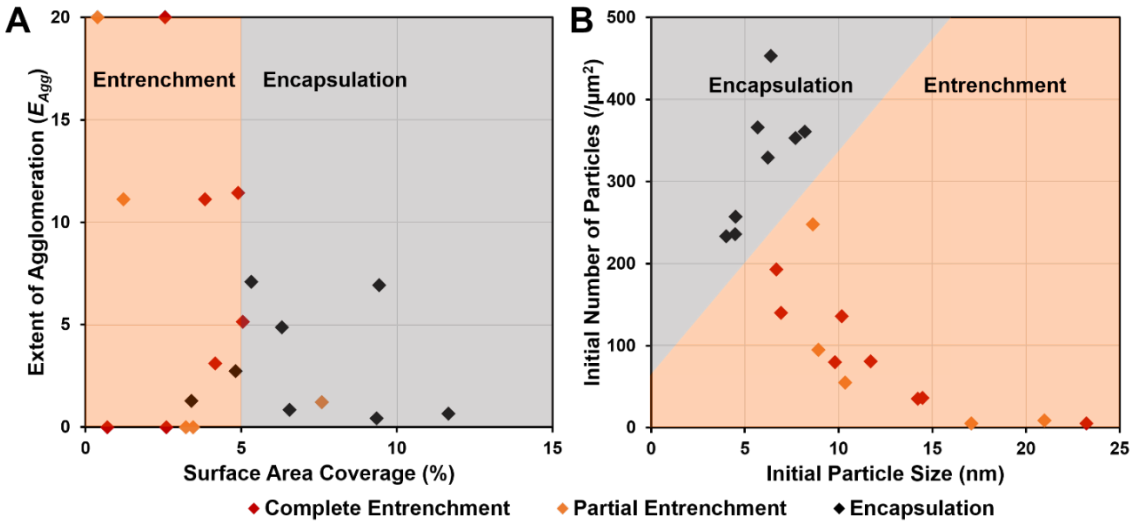

Figure 5.4 Pd/SiO_2 distributions that result in minimal aggregation (E_{Agg} < 20%) have surface area coverages less than 15 %. A) In this range, entrenchment, complete or partial, is dominant up to 5% surface area coverage whereas encapsulation is dominant between 5-15% coverages. B) When plotted as a function of initial nanoparticle size and

density, the observed behavior is segregated where encapsulation is dominant at smaller sizes (4 – 8 nm) and higher surface densities (200 - 500 nanoparticles /μm^2), while entrenchment is dominant at larger sizes (6 – 25 nm) and lower surface densities (10 – 250 nanoparticles /μm^2). All the samples are heated at 1040 ºC for 10 min using a ramp rate of 3.3 ºC/s.

When we expose a wide range of different sizes and surface densities of Pd nanoparticles to a temperature that favors a range of different behaviors, there is possibly competition among the many pathways for dominance. Since agglomeration primarily depends on the proximity of the nanoparticles, we observe that as soon as we reach surface area coverages above 20% or (surface density of above 500 nanoparticles/μm^2), all the nanoparticles exhibit agglomeration, whether they form nanopores or not. In cases where agglomeration is not favored, nanopore formation (complete or partial entrenchment) and encapsulation are dominant. Among these two behaviors, encapsulation is observed for smaller nanoparticles (4-8 nm) with higher surface densities (250-450 /μm^2). At these distributions, the nanoparticles are spaced far apart enough (30-60 nm) that particle mobility to form large aggregates is not favored and the small nanoparticles (4-8 nm) get encapsulated in the support. However, for larger nanoparticles (6-25 nm) that show no tendency to agglomerate and resist complete encapsulation by SiO_2, well-defined nanopores are formed after heating at 1040 ºC for 10 min. These considerations allow us to predict the dominant behavior that could be expected when a certain size and surface density if nanoparticles are subjected to similar heating conditions. Thus, we can expect large nanoparticles (10- 25 nm) with low surface densities (< 200 nanoparticles /μm^2) to form nanopores without agglomeration. Similarly, small (1- 10 nm) nanoparticles with high surface densities (100- 700 nanoparticles /μm^2) are highly mobile and will agglomerate before entrenchment. Nanoparticles with distributions between these two extremes (sizes 4-8 nm and surface densities 250- 450 nanoparticles /μm^2) that have a low mobility will get encapsulated within the SiO_2 support.

5.3.2 Understanding encapsulating behavior

While most the nanoparticle distributions studied here ultimately lead to nanopore formation on rapid thermal processing, we observe that for distributions with nanoparticle sizes and surface densities

range from 4 - 8 nm and 250 - 450 /μm^2, respectively, the surface feature distribution remains unchanged after rapid thermal processing (1040 ºC for 10 min using a ramp rate of 3.3 ºC/s), with no apparent nanopore formation (Figure 5.5 Ai-ii). The surface features do not undergo further transformation on extended heating, unlike the partially entrenched or agglomerated nanoparticles (Figure 5.5 Aiii). We hypothesized that since neither agglomeration nor nanopore formation is observed, there must be SiO_2 encapsulation of the Pd nanoparticles, which acts as barrier to complete entrenchment. It has been reported that strong metal-surface interactions (SMSI) lead to encapsulation of metal nanoparticles in reducible oxides.[8,10,23] To investigate if the Pd nanoparticles, when subjected to entrenchment conditions, become encapsulated with SiO_2, various heated samples were treated with a Pd etchant. For the nanoparticle distributions where no apparent change was observed after heating, the surface topology remained unchanged after the Pd-etch (Figure 5.5 Aiv) indicating that some protective layer, most likely SiO_2, exists over the features. In other cases, when the Pd nanoparticles are only partially embedded in the support, Pd-etching reveals the oxide ridges formed around the nanoparticles (Figure S12).

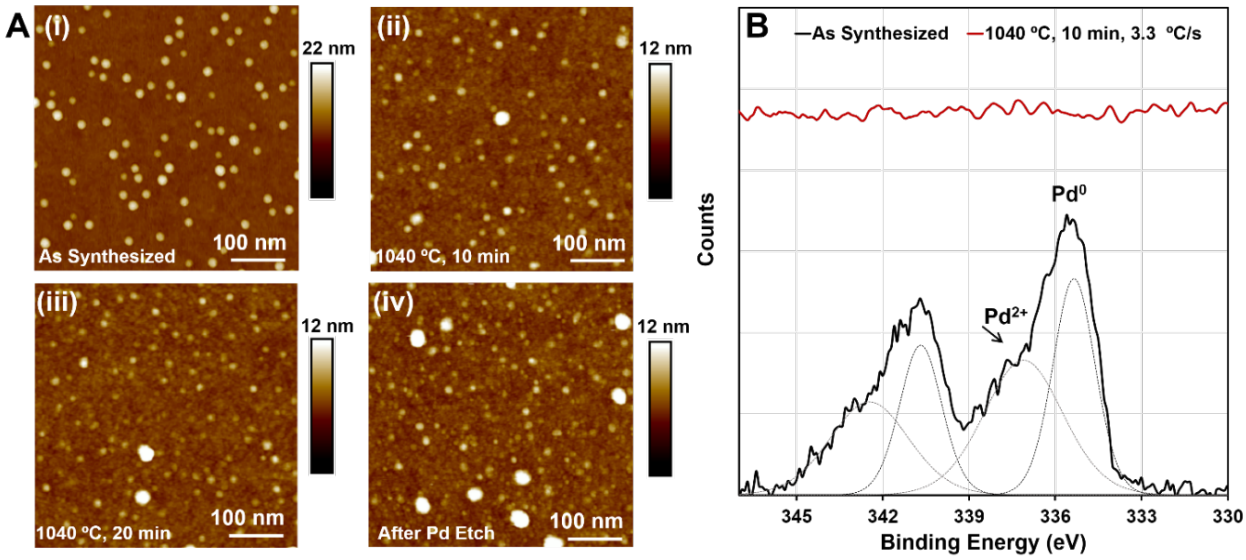

Figure 5.5 A) AFM images of the distribution of features on the SiO_2 surface i) as synthesized, ii) after heating at 1040 ºC for 10 min, iii) after heating at 1040 ºC for 20 min, and iv) after Pd etching (after extended heating). B) For nanoparticles that undergo encapsulation XPS studies show that Pd signal is lost upon heating at 1040 ºC for 10 mins.

The encapsulation of nanoparticles is corroborated by the loss of the Pd XPS signals (Figure 5.5 B) after the rapid thermal treatment. The surface features remaining after heating (that are not Pd nanoparticles) have the same spatial arrangement as the initial Pd nanoparticles. We therefore conclude that the Pd nanoparticles are encapsulated within the SiO_2 support. We observe that the number of features of all the distributions exhibiting encapsulation on rapid thermal processing is unchanged after heating. Moreover, the sizes of the encapsulated features are comparable to that of the initial nanoparticles (Figure 5.6).

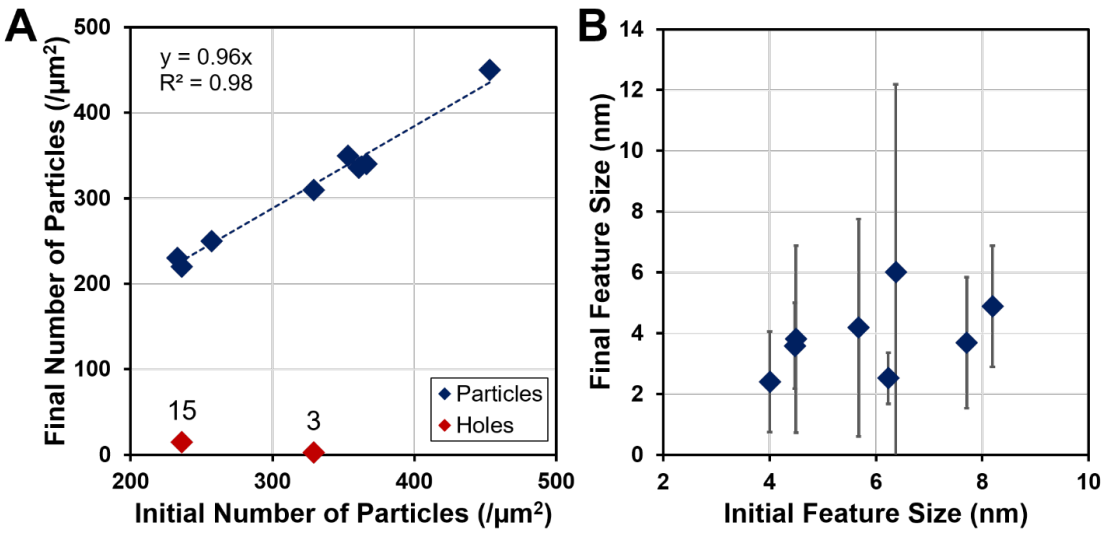

Figure 5.6 A) Feature density and B) feature size of encapsulated nanoparticles before and after rapid thermal processing at 1040 ºC for 10 min using a ramp rate of 3.3 ºC/s

The extent of SMSI effect observed in literature for Pd/SiO_2 is significantly lower than Pd on other reducible oxides (Al_2O_3 or TiO_2) and is almost negligible.[9] However, most of these studies have been done below 1000 ºC. When Pd nanoparticles of certain distributions become encapsulated in the SiO_2 support it is probable that the diffusion of Pd into the SiO_2 causes the support to become viscoelastic[24] and mobile enough to encapsulate the nanoparticles during oxide ridge formation (Scheme 5.1 A). Since these nanoparticles are not mobile enough to agglomerate and form larger nanoparticles that can form distinct

nanopores, it is possible that the nanoparticles do get entrenched, but the oxide ridges are so close together that the nanopore gets closed off (Scheme 5.1 B). In either scenario, neither the nanoparticle nor the nanopore is accessible so it would be safe to assume that it is encapsulated.

Scheme 5.1 Proposed encapsulation mechanism of Pd nanoparticles within the SiO_2 support by A) encapsulation of nanoparticles before nanopore formation by oxide ridges and B) closing of nanopores after entrenchment by large oxide ridges.

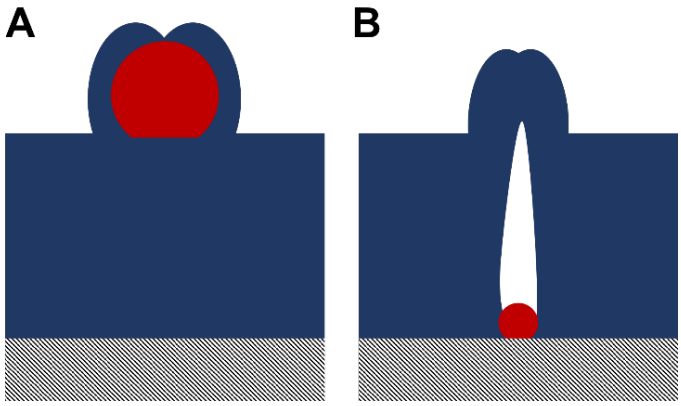

5.3.3 Entrenchment at different heating conditions

Previously, we reported that 10-15 nm Au nanoparticles required a minimum temperature of 1000 ºC and 10 min of heating to form nanopores in SiO_2.[24] We also observed that Ag nanoparticles of the same size entrenched at a much lower temperature of 900 ºC. In the previous sections we saw that the nature of entrenchment depends on initial nanoparticle distributions and the competition of nanopore formation with other surface mobility phenomena. In this section, how the evolution of nanopores under different heating conditions (annealing time, temperature, and ramp-rates) for the Pd/SiO_2 depends on the tendency of nanoparticles to agglomerate. We observed the behavior of Pd nanoparticles with two different distributions, one that exhibited mild/no agglomeration (E_{Agg} < 20 %) and another that favored extreme agglomeration (E_{Agg} > 80 %) at increasing temperatures, heating times, and heating ramp rates. The initial sizes and surface densities for these two distributions are shown in Figure S13.

a) Temperature

The changes in Pd features on SiO_2 at increasing temperatures between 850 ºC -1040 ºC (for 10 minutes of heating at 3.3 ºC/s) are studied at two different surface distributions. For the small size and high surface density nanoparticles (with diameter 3-4 nm and surface densities above 5000 nanoparticles/μm^2),

agglomeration is observed at 850 and 900 ºC where the nanoparticle density decreases from >5000 to 2000 nanoparticles/μm^2 and the nanoparticle diameter increases from approximately 3.5 to 6 nm (Figure 5.7). Rapid thermal processing at 950 ºC shows that further agglomeration occurs, and the surface nanoparticle densities decrease from 2000 to 60 nanoparticles/μm^2 while the nanoparticle diameter increases five times. At 1000 and 1040 ºC, the agglomerated nanoparticles on the surface entrench into the SiO_2 surface resulting in nanopores of the same diameters as the agglomerated nanoparticles (Figure 5.7 B). There are more nanopores observed at 1000 and 1040 ºC than agglomerated nanoparticles at 950 ºC.

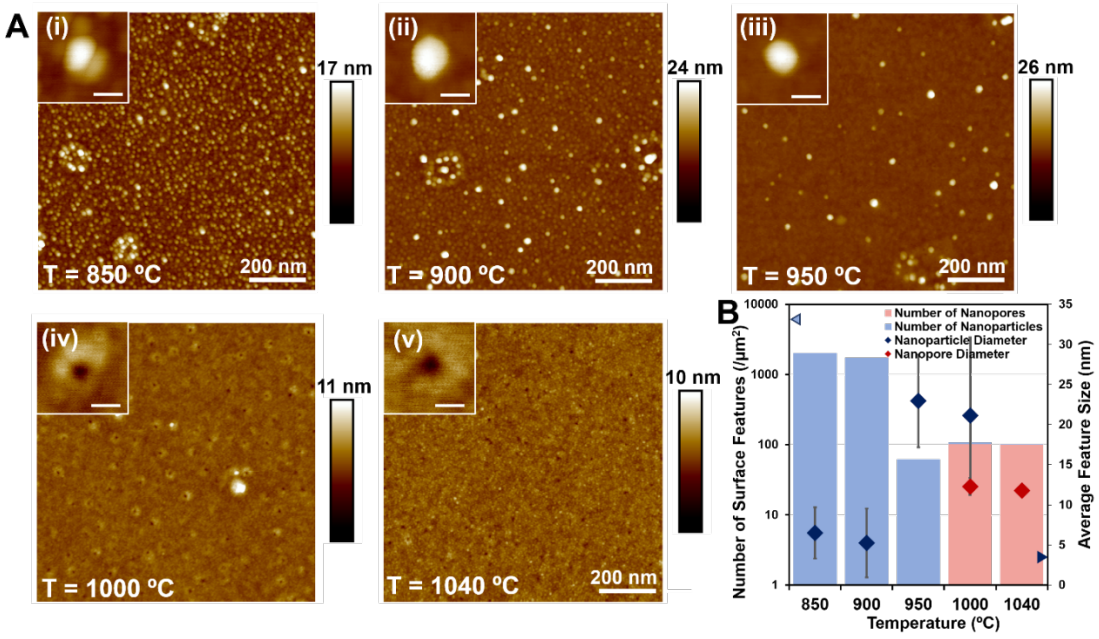

Figure 5.7 A) AFM images of small, high surface density Pd nanoparticles on SiO_2 heated with a ramp rate of 3.3 ºC/s and held for 10 min at i) 850, ii) 900, iii) 950, iv) 1000, and v) 1040 ºC. B) Trends in the nanoparticle and nanopore surface densities and diameters at each temperature. All inset scale bars are 20 nm. The initial nanoparticle surface density and diameter before heating are indicated on each axis.

The behavior of nanoparticles of a larger size and low surface density (with size 6-7 nm and surface densities of around 200 nanoparticles/μm^2) is significantly different (Figure 5.8). Since these nanoparticles are have larger interparticle spacing, agglomeration is not as universally favored. Some nanoparticles that are spaced closed together due to non-uniformity in the surface distribution will agglomerate but eventually

stay immobile. The size and the surface density of these nanoparticles remains steady at 850 ºC and 900 ºC. After 10min at 950 ºC, even though nanoparticle size and density does not significantly change, oxide ridge formation is observed around the Pd nanoparticles without complete entrenchment. This behavior is similar what we have previously reported for Au nanoparticles of similar sizes and surface densities at 900 ºC.[24] For the Pd nanoparticles, nanopore formation begins at 1000 ºC, although < 20% of the nanoparticles entrench. Entrenchment is more pronounced at 1040 ºC where almost all the nanoparticles form nanopores. Moreover, the average diameter of the resulting nanopores are same as that of the initial nanoparticles indicating that nanopore formation is not predicated on growth to a specific size.

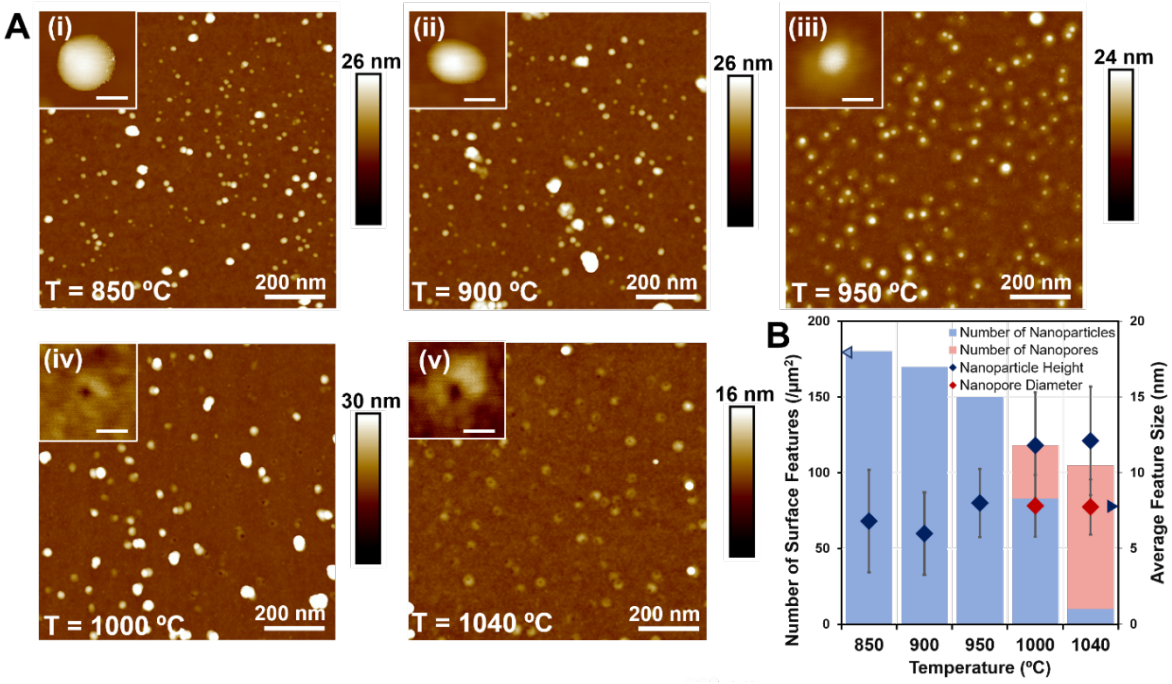

Figure 5.8 A) AFM images of large, low surface density Pd nanoparticles on SiO_2 heated for 10 minutes at 3.3 ºC/s at i) 850, ii) 900, iii) 950, iv) 1000, and v) 1040 ºC. B) Trends in the nanoparticle and nanopore surface densities and diameters at each temperature. All inset scale bars are 20 nm. The initial nanoparticle surface density and size (height) before heating are indicated by the arrowheads on each axis.

These results show that at temperatures below 1000 ºC, small nanoparticles with high surface mobility will agglomerate to form larger nanoparticles, thus reducing their total surface area. Even at temperatures above 1000 ºC, where nanopore formation occurs, these nanoparticles will agglomerate

before forming nanopores (Scheme 5.2A). Large, well-spaced nanoparticles are fairly immobile and do not undergo any transformation until they are subjected to entrenchment temperatures (Scheme 5.2B). For both these distributions, oxide ridge formation is observed at temperatures only slightly below the entrenchment temperature. These behaviors indicate that since agglomeration and oxide ridge formation behaviors have lower energy barriers. The small, high density nanoparticles all agglomerate and entrench at 1000 ºC while the larger, low density nanoparticles entrench only partially at the same temperature, showing that the rate of nanopore formation depends on the nanoparticle size. Additionally, the higher fraction of nanopores at 1040 ºC than at 1000 ºC, suggests that the rate of nanoparticle entrenchment depends on their heating temperature.

Scheme 5.2 Proposed behaviors of A) small, high density, and B) large, low surface density Pd nanoparticles at increasing temperatures at increasing annealing temperatures

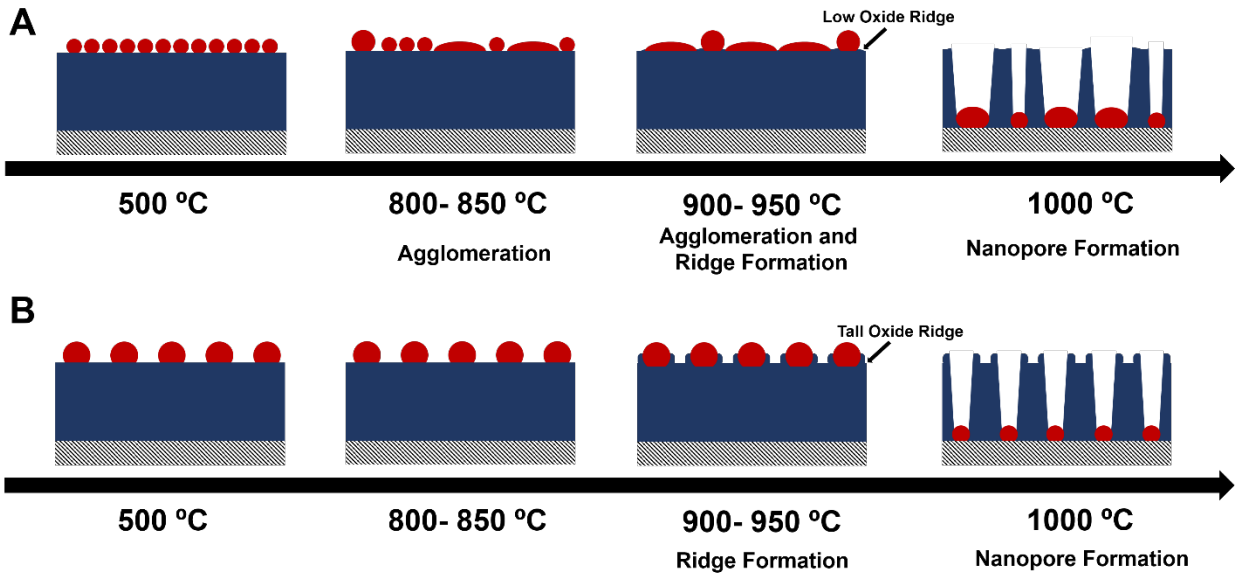

b) Hold Time

The evolution of nanopores with time at entrenchment temperatures (1040 ºC) was studied at two different surface distributions of Pd nanoparticles on SiO_2. For the small size and high surface density nanoparticles (with diameter 3-4 nm and surface densities above 5000 nanoparticles/μm^2) in the first 1.5 min, only agglomeration is observed (Figure 5.9). After 3 min, very few nanopores are formed, but agglomeration is dominant. At this point, we observe oxide ridge formation around the nanoparticles.

However, between 3 and 5 min, all the agglomerated nanoparticles entrench to form nanopores. The diameter and number of the nanopores is similar to those of the agglomerated nanoparticles. The depth of the nanopores for cannot be determined using AFM but we can tell that the nanoparticles have entrenched well below the surface to not be detected by the tip anymore. These observations prove that entrenchment and agglomeration do not occur simultaneously at temperatures that favor them but are sequential. Only when the highly mobile nanoparticles agglomerate to a size that renders them immobile does nanopore formation start. The energy provided to the nanoparticles during the rapid thermal processing is favored to be utilized towards rearrangement to a minimized surface energy configuration (agglomeration) before nanopore formation begins. Thus, we can conclude that nanopore formation pathway has a higher activation barrier than agglomeration.

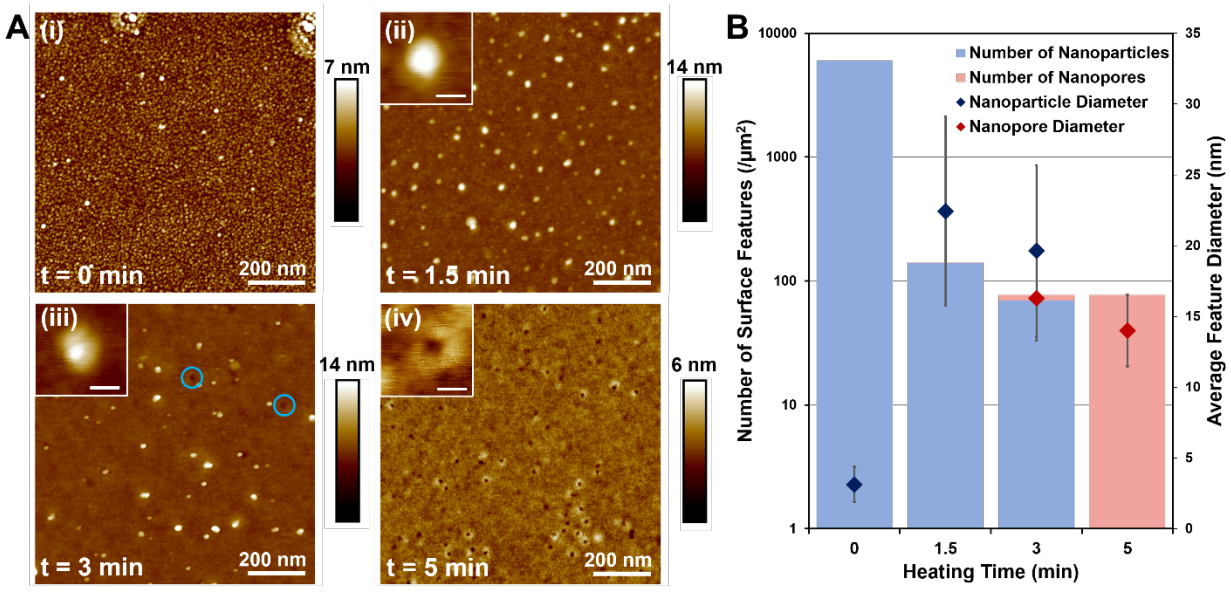

Figure 5.9 A) AFM images of small, high surface density Pd nanoparticles on SiO_2 heated to 1040 ºC at 3.3 ºC/s for i) 0, ii) 1.5, iii) 3, and iv) 5 min. B) Trends in the nanoparticle and nanopore surface densities and diameters at each time point. All inset scale bars are 20 nm.

For larger and low surface density (with size 9-10 nm and surface densities of around 60 nanoparticles/μm^2) where no agglomeration occurs, nanopore formation initiates in the first 1.5 min of heating (Figure 5.10). With increasing hold times, the fraction of nanoparticles that form nanopores

increases until mostly nanopores are observed at 5 min of hold time. In this case, the large, well-spaced nanoparticles are not laterally mobile. With no agglomeration to compete with nanopore formation, the rapid thermal processing causes the nanoparticles to start entrenching almost instantaneously.

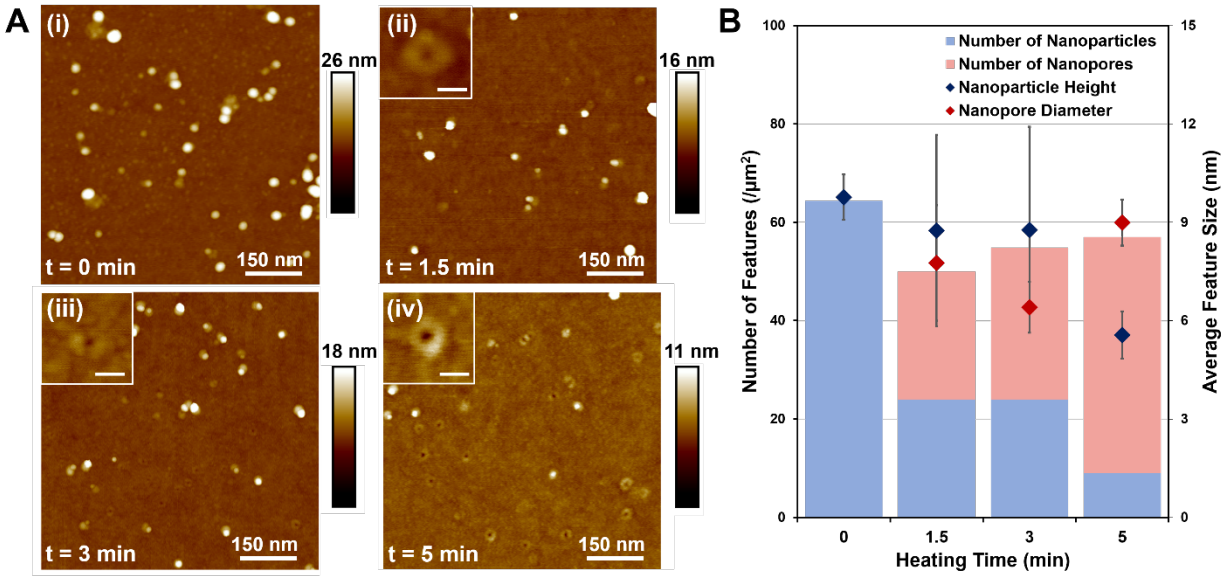

Figure 5.10 A) AFM images of large, low surface density Pd nanoparticles on SiO_2 heated at 3.3 ºC/s to 1040 ºC for i) 0, ii) 1.5, iii) 3, and iv) 5 min. B) Trends in the nanoparticle and nanopore surface densities and diameters at each time point. All inset scale bars are 20 nm.

c) Ramp Rates

In addition to the temperature and time of the heating process, the ramp rate used to heat the nanoparticles is crucial to determining the nature of the resulting surface features. For both the nanoparticle distributions, at a low ramp rate of 0.33 ºC/s (Figure 5.11 A(i) and B(i)), no distinct nanopores are observed, but the surface features are indicative of agglomeration and encapsulation in SiO_2. At a higher ramp rate of 1 ºC/s, complete nanopore formation is observed for the smaller, high density nanoparticles (Figure 5.11 A(ii)) whereas the larger nanoparticles show only partial entrenchment (Figure 5.11 B(ii)). Despite incomplete entrenchment, for the larger, low surface density nanoparticles, the nanoparticle and the oxide ridge surrounding it are distinct. Complete entrenchment is observed for both the nanoparticle distributions at 3.3 ºC/s.

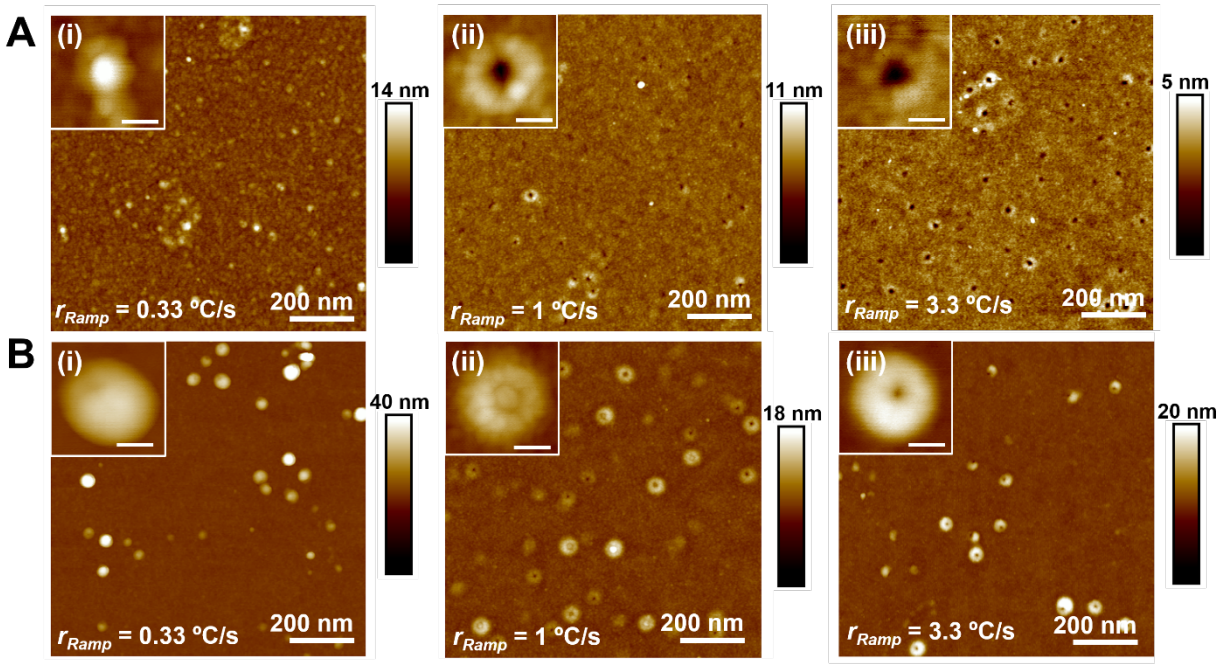

Figure 5.11 AFM images of A) small, high surface density Pd nanoparticles on SiO_2 heated at 1040 ºC and held for 10 min at ramp rates (r_{Ramp}) of i) 0.33, ii) 1, and iii) 3.3 ºC/s and B) large, low surface density Pd nanoparticles on SiO_2 heated at 1040 ºC and held for 10 min at ramp rates of i) 0.33, ii) 1, and iii) 3.3 ºC/s

We have seen previously that agglomeration is dominant till 900 ºC and oxide ridge formation occurs at 950 ºC before nanopore formation starts at 1000 ºC. When low ramp-rates (< 1 ºC/s) are employed, the nanoparticles stay at the temperatures that favor agglomeration and oxide ridge formation for a very long time before they reach entrenchment temperatures. In this situation, they may become partially encapsulated in tall oxide ridges resulting from continuous oxide transport at the interface. Thu by the time they attain entrenchment temperatures, no distinct nanopores can be formed. On the other hand, using higher ramp rates (> 3 ºC/s) we minimize the residence time of the nanoparticles to temperatures below 1000 ºC and ensure distinct pore formation on the surface. When we use even higher ramp-rate of 10 ºC/s, the nature nanopores formed remains the same (Figure S14). It is important to note here that the slowest ramp rate we used (0.33 ºC/s) is much higher than the standard annealing ramp rates used in catalysis (0.16 ºC/s or 10 ºC/min). Although some reports have achieved nanopore formation (100-150 nm) at lower ramp rates, it has primarily been for micron-sized particles.[26] In cases where the height of the oxide

ridge is comparable to the nanopore diameter, as considered in this work, large oxide ridges can close off nanopores or encapsulate the nanoparticles.

5.3.4 Nanopore formation on complete entrenchment

The nanopores formed by the method of high temperature entrenchment could have a wide range of applications depending on their diameters and aspect ratios. The diameter and surface density of the nanopores as well the height of their surrounding oxide ridges depend strongly on the initial size and surface density of the nanoparticles and their tendency to agglomerate before entrenchment (Figure 5.12). Large, low surface density nanoparticles that do not significantly agglomerate before entrenchment (E_{Agg} < 20%) form nanopores with diameters (Figure 5.12 A) and surface densities comparable to their initial distribution (Figure 5.12 C). On the contrary, we observe that small, high density nanoparticles that agglomerate drastically (E_{Agg} > 80%), all have nanopores with diameters of 10- 15 nm and surface densities significantly lower than the initial nanoparticles. This indicates that most nanoparticles agglomerate to a similar size and surface density before nanopore formation starts. This size (15- 20 nm) is likely such that the total surface area is minimized, and the particles become immobile.

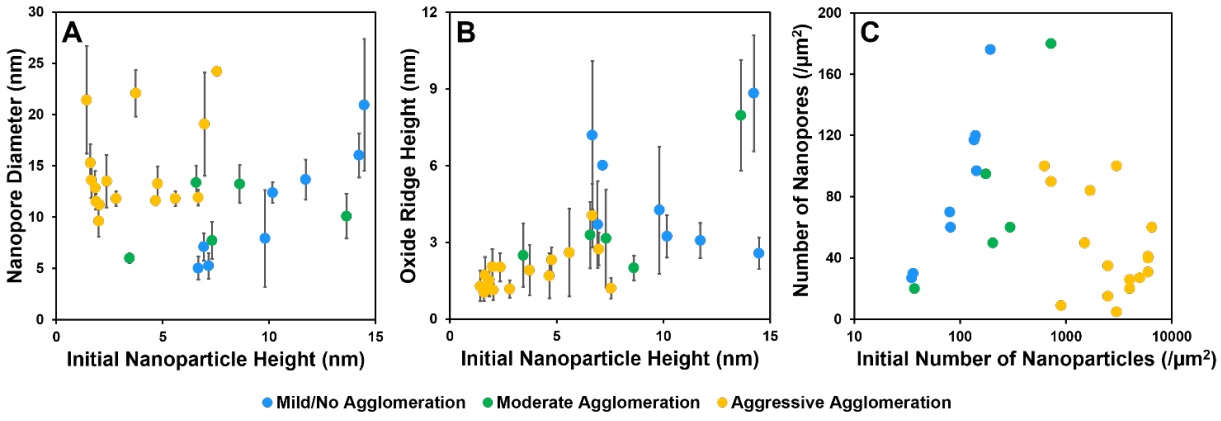

Figure 5.12 A) Average nanopore diameter as a function of initial nanoparticle height, B) average oxide ridge height as a function of initial nanoparticle height, and C) number of nanopores formed as a function of initial number of Pd nanoparticles at different extents of agglomeration- mild/no agglomeration (E_{Agg} < 20 %), moderate agglomeration (20% < E_{Agg} < 80 %), and extreme agglomeration (E_{Agg} > 80 %).

Both, the nanopore diameter and surface density are a function of the initial distribution of the nanoparticles. The number of nanopores formed increases linearly with the initial number of Pd nanoparticles until attaining a maxima at ~200 nanopores /μm^2 (Figure 5.12 C). We have shown in the preceding sections that above these nanoparticle surface densities, nanopore formation occurs after agglomeration. Thus, above the surface densities of 200 nanoparticles/μm^2, agglomeration is dominant and the number of nanopores formed is significantly lower than the initial number of nanoparticles.

Scheme 5.3 Proposed oxide ridge formation mechanisms with time, of A) small, high density, and B) large, low surface density Pd nanoparticles at temperatures above 1000 ºC.

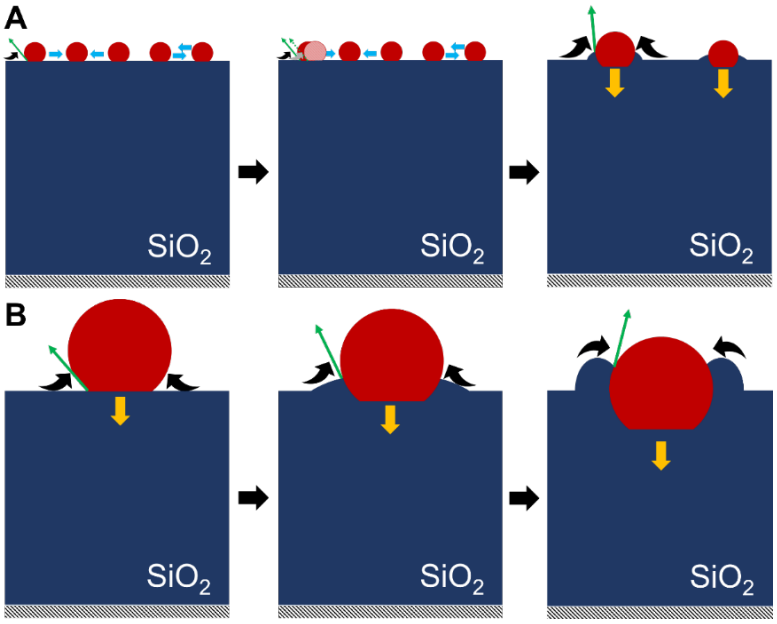

We also observe that the average height of the oxide ridges formed around the particles that do not significantly agglomerate is much larger than those for the nanoparticles that do agglomerate despite having comparable nanopore diameters (Figure 5.12 B). Since the small nanoparticles with high surface densities are very mobile on the surface, the triple-line[39] at which oxide transport that causes ridge formation occurs is also very mobile (Scheme 5.3 A). In this situation, the ridge formation around the nanoparticle in one location is not as significant as it would be if the nanoparticle were immobile and the triple-line remained fixed in one spatial location (Scheme 5.3 B). Thus, if nanopores with minimal oxide ridges were desired, it would be preferable to have the nanoparticles agglomerate before entrenchment. Similarly, different applications of the nanopores, different diameters and surface densities are desired. Table S3 and Figure 5.13 highlights the different nanopore distribution as a function of the synthesis conditions of the nanoparticles.

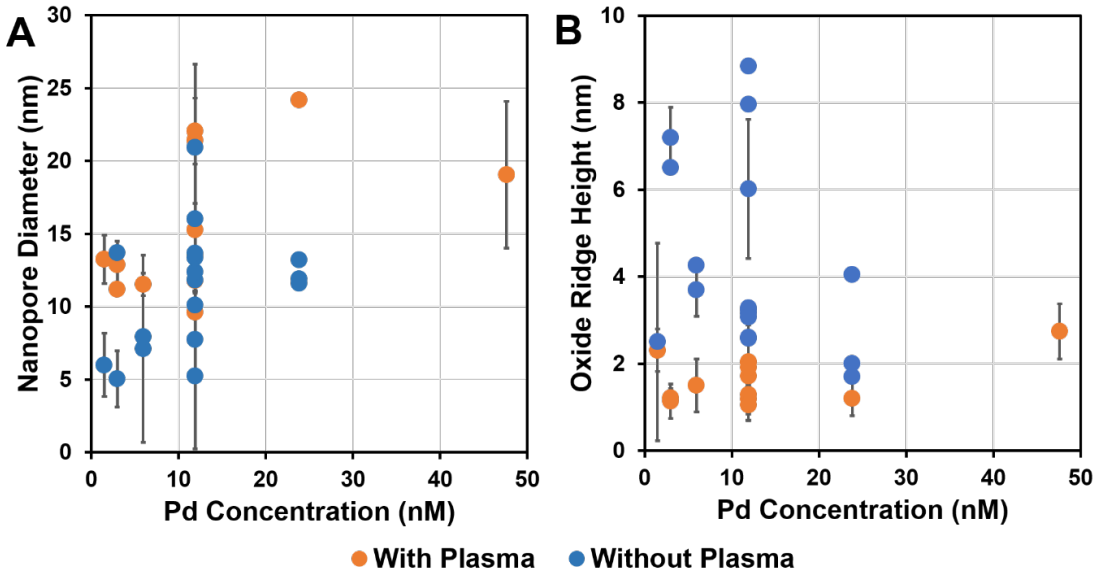

Figure 5.13 A) Diameters of nanopores and B) heights of oxide ridges formed after heating to 1040 ºC for 10 minutes at 3.3 ºC/s as a function of synthesis conditions (concentration of Pd in the block copolymer micelle solution and use of oxygen plasma) of the Pd nanoparticles.

5.4 Conclusions

In this chapter, we have elucidated how nanopore formation on thermal entrenchment of Pd nanoparticles on SiO_2 supports competes with other surface phenomena, especially sintering and encapsulation. We have established the dependence of the nature of entrenchment of nanoparticles as a function of the initial size and surface density of the Pd nanoparticles. We anticipate that this behavior will be different for various metal nanoparticles depending on their sintering tendencies[40] and diffusivities in SiO_2.[21] Previously, we had established that a minimum temperature of 1000 ºC is necessary for Au nanoparticles to form nanopores and had studied the evolution of these pores with time.[24] Here, we have further shown that the nature of nanoparticle entrenchment under different heating conditions (temperature, time, and ramp rates) depends on the initial nanoparticle distribution and its tendency to agglomerate before entrenchment.

Nanopore formation in oxides via rapid thermal processing of metal nanoparticles has applications in sensing[26], separations[28,29], electronics design[30], and catalysis[24,27]. Here we have shown that the diameter

and surface density of the nanopore can be tuned by controlling the size and distribution of the initial metal nanoparticles. Nanopores of the same diameter can be achieved using two distributions of nanoparticles, with or without agglomerations. However, without agglomeration, tall oxide ridges will accompany the nanopores.

For the application of separation, the oxide ridge may hamper flow of the feed in a filtration set-up and it would be desirable to have nanopores with negligible oxide ridges. This can be achieved via thermal processing of high density, small nanoparticles that will agglomerate before entrenchment and still give nanopores 10-15 nm in diameter. The distributions of nanoparticles in which no nanopore formation is observed and the nanoparticles get completely encapsulated in the SiO_2 matrix can be avoided if nanopore formation is desired.

Acknowledgements

This material is based upon work supported by the Sherman Fairchild Foundation, Inc. and the Air Force Office of Scientific Research under Award number FA9550-16-1-0150. This work made use of the EPIC and SPID facilities of Northwestern University's NUANCE Center, which has received support from the Soft and Hybrid Nanotechnology Experimental (SHyNE) Resource (NSF ECCS-1542205); the MRSEC program (NSF DMR-1121262) at the Materials Research Center; the International Institute for Nanotechnology (IIN); the Keck Foundation; and the State of Illinois, through the IIN.

5.5 References

(1) Flynn, P. C. The Sintering of Supported Metal Catalysts. *Catal. Rev.* **1975**, *12* (1), 93–135.

(2) Wynblatt, P. Particle Growth in Model Supported Comparison of Experiment. *Acta Met.* **1976**, *24*, 1175--1182.

(3) Schauermann, S.; Nilius, N.; Shaikhutdinov, S.; Freund, H. J. Nanoparticles for Heterogeneous Catalysis: New Mechanistic Insights. *Acc. Chem. Res.* **2013**, *46* (8), 1673–1681.

(4) Coq, B. Structure – Activity Relationships in Catalysis by Metals : Some Aspects of Particle Size , Bimetallic and Supports Effects. *Coord. Chem. Rev.* **1998**, *180*, 1753–1783.

(5) Zhou, Y.; Ramanathan, S. Correlated Electron Materials and Field Effect Transistors for Logic: A Review. *Crit. Rev. Solid State Mater. Sci.* **2013**, *38* (4), 286–317.

(6) Dieny, B.; Chshiev, M. Perpendicular Magnetic Anisotropy at Transition Metal/Oxide Interfaces and Applications. *Rev. Mod. Phys.* **2017**, *89* (2).

(7) Hansen, T. W.; Delariva, A. T.; Challa, S. R.; Datye, A. K. Sintering of Catalytic Nanoparticles: Particle Migration or Ostwald Ripening? *Acc. Chem. Res.* **2013**, *46* (8), 1720–1730.

(8) Tauster, S. J.; Fung, S. C.; Garten, R. L. Strong Metal-Support Interactions. Group 8 Noble Metals Supported on TiO2. *J. Am. Chem. Soc.* **1978**, *100* (1), 170–175.

(9) Powell, B. R.; Whittington, S. E. Encapsulation: A New Mechanism of Catalyst Deactivation. *J. Catal.* **1983**, *81* (2), 382–393.

(10) Pan, C. J.; Tsai, M. C.; Su, W. N.; Rick, J.; Akalework, N. G.; Agegnehu, A. K.; Cheng, S. Y.; Hwang, B. J. Tuning/Exploiting Strong Metal-Support Interaction (SMSI) in Heterogeneous Catalysis. *J. Taiwan Inst. Chem. Eng.* **2017**, *74*, 154–186.

(11) Panpranot, J.; Phandinthong, K.; Sirikajorn, T.; Arai, M.; Praserthdam, P. Impact of Palladium Silicide Formation on the Catalytic Properties of Pd/SiO2catalysts in Liquid-Phase Semihydrogenation of Phenylacetylene. *J. Mol. Catal. A Chem.* **2007**, *261* (1), 29–35.

(12) Fu, Q.; Wagner, T. Interaction of Nanostructured Metal Overlayers with Oxide Surfaces. *Surf. Sci. Rep.* **2007**, *62* (11), 431–498.

(13) Anton, R. Interaction of Gold, Palladium and Au-Pd Alloy Deposits with Oxidized Si(100) Substrates. *Thin Solid Films* **1984**, *120* (4), 293–311.

(14) Kunwar, S.; Pandey, P.; Sui, M.; Zhang, Q.; Li, M. Y.; Lee, J. Effect of Systematic Control of Pd Thickness and Annealing Temperature on the Fabrication and Evolution of Palladium Nanostructures on Si (111) via the Solid State Dewetting. *Nanoscale Res. Lett.* **2017**, *12* (1), 364–378.

(15) Karakouz, T.; Tesler, A. B.; Sannomiya, T.; Feldman, Y.; Vaskevich, A.; Rubinstein, I. Mechanism of Morphology Transformation during Annealing of Nanostructured Gold Films on Glass. *Phys. Chem. Chem. Phys.* **2013**, *15* (13), 4656–4665.

(16) Harrisp, J. M.; Pretorius, R.; Nicole. Reaction of Thin Metal Films with SiO2 Substrates. *Solid-State Electrotronics* **1978**, *21* (1), 667–675.

(17) Saiz, E.; Tomsia, a. P.; Cannon, R. M. Ridging Effects on Wetting and Spreading of Liquids on Solids. *Acta Mater.* **1998**, *46* (7), 2349–2361.

(18) Goeke, R. S.; Datye, A. K. Model Oxide Supports for Studies of Catalyst Sintering at Elevated Temperatures. *Top. Catal.* **2007**, *46* (1–2), 3–9.

(19) Helveg, S.; Chorkendorff, I.; Skoglundh, M.; Simonsen, S. B.; Dahl, S. Coarsening of Pd Nanoparticles in an Oxidizing Atmosphere Studied by in Situ TEM. *Surf. Sci.* **2015**, *648* (June), 278–283.

(20) Wang, S. Q. Barriers Against Copper Diffusion into Silicon and Drift Through Silicon Dioxide. *MRS Bull.* **1994**, *19* (8), 30–40.

(21) McBrayer, J. D. Diffusion of Metals in Silicon Dioxide. *J. Electrochem. Soc.* **1986**, *133* (6), 1242.

(22) van den Oetelaar, L. C. A.; van den Oetelaar, R. J. A.; Partridge, A.; Flipse, C. F. J.; Brongersma, H. H. Reaction of Nanometer-Sized Cu Particles with a SiO2 Substrate. *Appl. Phys. Lett.* **1999**, *74* (20), 2954–2956.

(23) Pesty, F.; Steinrück, H. P.; Madey, T. E. Thermal Stability of Pt Films on TiO2(110): Evidence for Encapsulation. *Surf. Sci.* **1995**, *339* (1–2), 83–95.

(24) Gosavi, A. A.; Hedrick, J. L.; Chen, P.-C.; Notestein, J. M.; Mirkin, C. A. A Tri-Layer Approach to Controlling Nanopore Formation in Oxide Supports. *Nano Res.* **2019**, *12* (1), 1–6.

(25) de Vreede, L. J.; Schmidt Muniz, M.; Van Den Berg, A.; Eijkel, J. C. T. Nanopore Fabrication in Silicon Oxynitride Membranes by Heating Au-Particles. *J. Micromechanics Microengineering* **2016**, *26*, 37001–37006.

(26) de Vreede, L. J.; Van Den Berg, A.; Eijkel, J. C. T. Nanopore Fabrication by Heating Au Particles on Ceramic Substrates. *Nano Lett.* **2015**, *15*, 727–731.

(27) Ono, L. K.; Behafarid, F.; Cuenya, B. R. Nano-Gold Diggers: Au-Assisted SiO2-Decomposition and Desorption in Supported Nanocatalysts. *ACS Nano* **2013**, *7* (11), 10327–10334.

(28) Park, T.; Lee, S. J.; Cha, J. H.; Choi, W. Scalable Fabrication of Nanopores in Membranes: Via

Thermal Annealing of Au Nanoparticles. *Nanoscale* **2018**, *10* (47), 22623–22634.

(29) Kirchhoff, K.; Odijk, M.; Le-The, H.; van den Berg, A.; Kappl, M.; Müller, M.; Lohse, D.; Eijkel, J. C. T.; Tregouet, C. Engulfment Control of Platinum Nanoparticles into Oxidized Silicon Substrates for Fabrication of Dense Solid-State Nanopore Arrays. *Nanotechnology* **2018**, *30* (6), 065301.

(30) Kwon, S.; Jang, S.; Choi, J. W.; Choi, S.; Jang, S.; Kim, T. W.; Wang, G. Controllable Switching Filaments Prepared via Tunable and Well-Defined Single Truncated Conical Nanopore Structures for Fast and Scalable SiOx Memory. *Nano Lett.* **2017**, *17* (12), 7462–7470.

(31) Min, B. K.; Santra, A. K.; Goodman, D. W. Understanding Silica-Supported Metal Catalysts: Pd/Silica as a Case Study. *Catal. Today* **2003**, *85* (2–4), 113–124.

(32) Juszczyk, W.; Łomot, D.; Pielaszek, J.; Karpi, Z. Transformation of Pd / SiO 2 Catalysts during High Temperature Reduction. **2002**, *78* (March), 95–98.

(33) Juszczyk, W.; Karpiński, Z.; Łomot, D.; Pielaszek, J. Transformation of Pd/SiO2into Palladium Silicide during Reduction at 450 and 500°C. *J. Catal.* **2003**, *220* (2), 299–308.

(34) Min, B. K.; Santra, A. K.; Goodman, D. W. Thermal Stability of Pd Supported on Single Crystalline SiO[Sub 2] Thin Films. *J. Vac. Sci. Technol. B Microelectron. Nanom. Struct.* **2003**, *21* (6), 2319.

(35) Spatz, J. P.; Mößmer, S.; Möller, M. Mineralization of Gold Nanoparticles in a Block Copolymer Microemulsion. *Chem. - A Eur. J.* **1996**, *2* (12), 1552–1555.

(36) Pan, D.; Fu, Q.; Lu, J. Nanolithography through Mixture of Block Copolymer Micelles. *Nanotechnology* **2012**, *23* (30), 305302.

(37) Spatz, J. P.; Roescher, A.; Moller, M. Gold Nanoparticles in Micellar Poly(Styrene)-b-Poly(Ethylene Oxide) Films-Size and Interparticle Distance Control in Monoparticulate Films. *Adv. Mater.* **1996**, *8* (4), 337–340.

(38) Meng, G.; Yanagida, T.; Kanai, M.; Suzuki, M.; Nagashima, K.; Xu, B.; Zhuge, F.; Klamchuen, A.; He, Y.; Rahong, S.; et al. Pressure-Induced Evaporation Dynamics of Gold Nanoparticles on Oxide Substrate. *Phys. Rev. E - Stat. Nonlinear, Soft Matter Phys.* **2013**, *87*.

(39) Saiz, E.; Tomsia, A. P.; Cannon, R. M. Triple Line Ridging and Attachment in High-Temperature Wetting. *Scr. Mater.* **2001**, *44* (1), 159–164.

(40) Liu, G.; Eichelsdoerfer, D. J.; Rasin, B.; Zhou, Y.; Brown, K. A.; Liao, X.; Mirkin, C. A. Delineating the Pathways for the Site-Directed Synthesis of Individual Nanoparticles on Surfaces. *Proc. Natl. Acad. Sci. U. S. A.* **2013**, *110* (3), 887–891.

Chapter Six: Exploring Thermal Entrenchment of Metal Nanoparticles on 3D SiO_2 Supports

Abha Gosavi, Nikhita Ahuja, M. Alexander Ardagh, Justin Notestein and Chad Mirkin

6.1 Introduction

Heterogeneous catalysts provide several advantages over homogenous catalysts. These include easy separation, regeneration and reuse. They can be tuned to afford selectivity and reactivity comparable to their homogeneous counterparts. Metal nanoparticles, supported on oxides have been used as heterogenous catalysts for a wide range of liquid, gas, and mixed phase reactions.[1] The reusability of heterogenous nanoparticles catalysts is often limited by catalyst deactivation *via* poisoning, coking, and sintering. While chemical and thermal methods may be employed to reverse the deactivation *via* poisoning and coking, sintering is irreversible.[1] Nanoparticle sintering occurs *via* two mechanisms- i) Ostwald ripening and ii) particle migration and coalescence.[2–4] Ostwald ripening, which is driven by difference in particle sizes, can be controlled by generating homogenous nanoparticles.[4] Particle migration can be mitigated by immobilizing nanoparticles onto the supporting oxides. Various methods have been explored to immobilize catalytically active nanoparticles onto supports.[5,6] The most popular method is to anchor metal nanoparticles within porous oxide supports.[7] In this chapter, we explore thermal embedding of the nanoparticles within the supporting oxides to generate stable catalysts.

In the recent years, there have been several reports of metal nanoparticles (Au, Ag, Cu, Pd, Pt) forming nanopores on planar SiO_2 supports on being subjected to temperatures above 1000 ºC.[8–12] In the previous chapters, we have studied this phenomenon of nanoparticle entrenchment in detail to establish the scope and limitation of this nanopore formation. It was observed that while Au nanoparticles formed nanopores in amorphous SiO_2, other oxide layers (Al_2O_3, TiO_2, HfO_2, quartz) were impervious to nanopore formation. This selective nanopore formation was utilized to design planar tri-layered supports that consisted of thin SiO_2 layers preceded by Al_2O_3 layers on a Si wafer (that provided structural integrity). These tri-layer structures are effective in controlling the extent of entrenchment of the metal nanoparticles

and prevent complete nanopore formation. Using this technique, nanoparticles, embedded 3-5 nm within the support, are immobilized and can serve as sinter-resistant catalysts.[8]

In this work, we explore the possibility to extending the phenomenon of nanopore formation, hitherto observed only on planar SiO_2 supports, to three-dimensional SiO_2 supports. Our hypothesis is that metal nanoparticles (Au and Pd) will form nanopores on non-porous spherical SiO_2 supports at temperatures above 1000 ºC, analogous to their behavior on planar amorphous SiO_2. The nanopore formation can then be controlled by using composite Al_2O_3-SiO_2 supports synthesized using sol-gel method.[13] The partially embedded nanoparticles would the act as sinter-resistant catalysts for a range of different multi-phase reactions (Scheme 6.1).

Scheme 6.1 A) Hypothesized nanopore formation by rapid thermal processing of Au nanoparticles on spherical SiO_2. B) Proposed Al_2O_3 - SiO_2 composite structures to control the extent of nanopore formation.

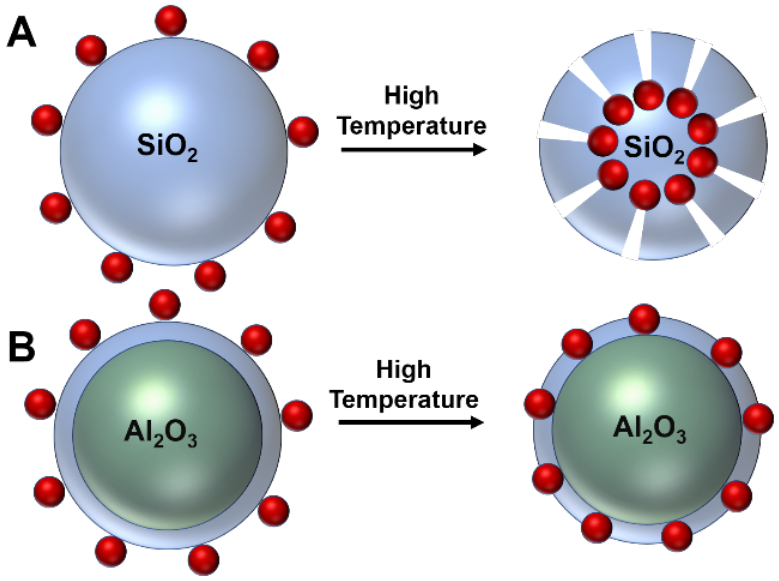

We observed that for both Au and Pd nanoparticles, supported on non-porous spherical SiO_2 of two different sizes (500 and 150 nm), only nanoparticle sintering occurred after annealing at 1020 ºC for 10 minutes. Similar behavior was observed for the nanoparticles on the Al_2O_3-SiO_2 composite supports. While nanopore formation reproducibly occurs for nanoparticles of range of different sizes and spacings on planar SiO_2 supports, no such behavior is observed for spherical supports. We hypothesize that this disparity in behavior occurs due to the difference in the internal stresses of the two types of SiO_2 surfaces. While, the planar structure of Si-SiO_2 wafers has very few internal stresses, the small spherical SiO_2 is highly self-stressed. Under these stressed conditions, the diffusivity of the metals in the spherical SiO_2 may be

significantly lowered, thus preventing glass transition temperature (T_g) depression and the subsequent formation of nanopores.[8,14,15]

6.2 Methods

6.2.1 Synthesis of Stober SiO_2

a) Large SiO_2 spheres (S1, Diameter 500 nm)

A well-established recipe for the synthesis of Stober SiO_2 was used to generate uniform SiO_2 spheres.[16] 60 ml of ammonia solution (7N in Methanol, Sigma Aldrich), 110 ml ethanol (Anhydrous 200 proof, Decon Laboratories), 39 ml methanol (≥99.9% HPLC grade, Sigma Aldrich), and 70 ml Nanopure water were mixed together in a 1000 ml flask at room temperature. To this, a mixture of 17 ml tetraethyl orthosilicate (TEOS, ≥ 99% GC grade, Aldrich) in 200 ml of ethanol was added slowly while stirring at 1000 rpm at room temperature for 24 h. The solution gradually changes from transparent to translucent white and eventually opaque at the end of the 24 h. The solution was then collected and centrifuged at 4750 rpm for 30 mins and washed with ethanol thrice. The yield obtained by draining excess liquid and drying the material at room temperature under vacuum for 48 h is 5-6 g of Stober SiO_2.

b) Small SiO_2 spheres (S2, Diameter 150 nm)

To obtain smaller SiO_2 spheres, 31 ml of TEOS (≥ 99% GC grade, Aldrich) was mixed with 325 ml of methanol (Sigma Aldrich) in a 1000 ml flask. To this, a mixture of 72 ml nanopure water and 71 ml ammonia solution (7N in methanol, Sigma Aldrich) was injected at one time into the beaker ensuring that there was no contact of solution with the flask wall. This step is crucial for getting homogeneous SiO_2 spheres. There can be seeded growth if the phase formed by the alcohol, ester and ammonia is not homogeneous leading to a bimodal distribution in the size of the final spheres. This mixture was stirred at 1100 RPM for 2 min to achieve uniform mixing, after which it was stirred gently at 500 RPM for 18 h at room temperature. The mixture is centrifuged, washed, and dried in the same way as described above.

Modified Al_2O_3-SiO_2 (S3) supports with a 3 nm SiO_2 overcoat were synthesized by sol-gel method as described in our previous work.[13] All the supports (S1, S2, and S3) were calcined in air at 800 ºC for 3

hours at ramp rate 1.5 ºC/min to remove any excess water from SiO_2 surface prior to nanoparticle deposition (Figure 6.1).

6.2.2 Deposition of metal nanoparticles on Stober SiO_2

a) Au/SiO_2

Gold nanoparticles were deposited on the SiO_2 supports (S1, S2, and S3) using a method described in literature.[17] 50 ml volume of 3 M $HAuCl_4$ was mixed with 5 ml PVA (90%) solution (1 wt% in distilled water) stirred in a beaker at 500 RPM for 20 mins, after which 2.5 ml of 10 M $NaBH_4$ (99.99%, Sigma Aldrich) was added under vigorous stirring. The solution changes color to deep red immediately upon addition of $NaBH_4$ indicating the formation of Au nanoparticles. This mixture is further stirred at 300 rpm for 30 mins, and then aged overnight. The Au nanoparticles thus synthesized were deposited onto the SiO_2 using a modified incipient wetness impregnation method. The with the expected gold loading of 1 wt%, 1 gm of the Stober SiO_2 was introduced into the Au nanoparticle solution, using only as much liquid as needed to wet the support and 0.1 M H_2SO_4 was added dropwise to adjust the pH to 1-2. The solution was stirred at 400 rpm for 10 mins to allow mixing. The mixture was then centrifuged at 4750 rpm for 10 mins, and then washed with nanopure water thrice before vacuum drying at room temperature. The material is then calcined in air at 300 ºC for 4 h at a ramp rate of 1 ºC/min.

b) Pd/SiO_2

6.6 mg of Na_2PdCl_4 (Sigma Aldrich, ≥99.99%) was taken and mixed with ~1 ml nanopure water. To this, 500 mg of Stober SiO_2 was added. The volume of liquid was adjusted to just be enough to soak the support. The slurry is mixed/shaken thoroughly, and then 0.5 M H_2SO_4 is added dropwise until the pH is ~1-2. Then the materials were then dried under a steady flow of N_2 at room temperature. The resulting material has a Pd loading of 0.5 wt%. The effect of Na presence in the behavior of the Pd nanoparticles at high temperature was tested by using a Pd precursor without Na, like palladium acetate ($PdAc_2$). 7.4 mg of $PdAc_2$ is mixed in nanopure water with 500 mg of support. 0.5 M H_2SO_4 was added dropwise until the pH is 1-2 and mixed thoroughly for 10 min followed by drying under a steady flow of N_2 at RT.

6.2.3 Rapid thermal processing

Thermal processing to achieve nanopore formation of the metal nanoparticles on Stober SiO_2 samples was performed under steady Ar flow (100 mL/min) in a rapid thermal processing (RTP) furnace (MTI Corporation, OTF-1200X-4-RTP-UL) at 1040 ºC using a ramp rate of 3.3 ºC/sec for 10 minutes. The samples were passively cooled to room temperature under Ar flow (25 ml/min).

6.2.4 Characterization

The surface area and porosity structures were measured with Micrometrics 2010 ASAP by performing N_2 physisorption at liquid N_2 temperature after the sample is outgassed at 190 ºC under vacuum for 4 h. The surface area analyses were carried out after every step of rapid thermal processing. The samples were imaged in a transmission electron microscope (TEM) (Hitachi STEM 2300) using a 300 kV electron beam.

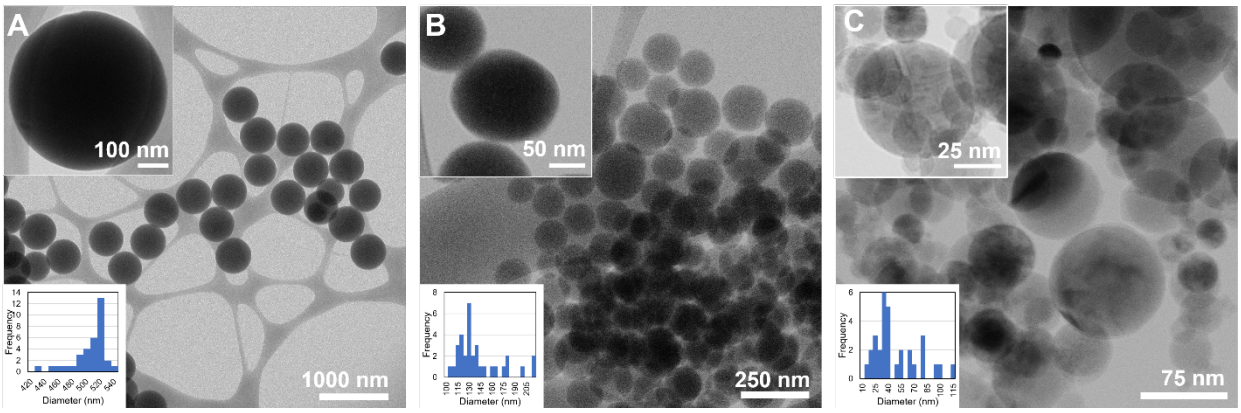

Figure 6.1 ***TEM*** images and particle size distributions of Stober SiO_2 spheres of diameters A) 500 nm (S1) and B) 140 nm (S2) and C) Al_2O_3-SiO_2 composites (S3) of average diameter 50 nm.

6.3 Results and Discussion

6.3.1 Sintering behavior of Au/SiO_2

When uniformly distributed Au nanoparticles (~5 nm) supported on S1 and S2 were heated to 1020 ºC for 10 min under a steady Ar flow, the nanoparticles sintered to form larger nanoparticles. Extended

heating (20 min) resulted in further sintering. Under the same heating conditions, on S1 the average nanoparticle size increases from 6 nm to 18 nm while on S2 the average nanoparticle size increases from 6 nm to 11 nm (Figure 6.2). There is also no significant change (as would be expected with pore formation) in the total surface area as well as the micropore volume which indicates that no pore formation occurs when these nanoparticles are heated (Table 6.1). Similarly sized Au nanoparticles supported on planar SiO_2 synthesized by block copolymer lithography, show nanopore formation when heated under these conditions.[8]

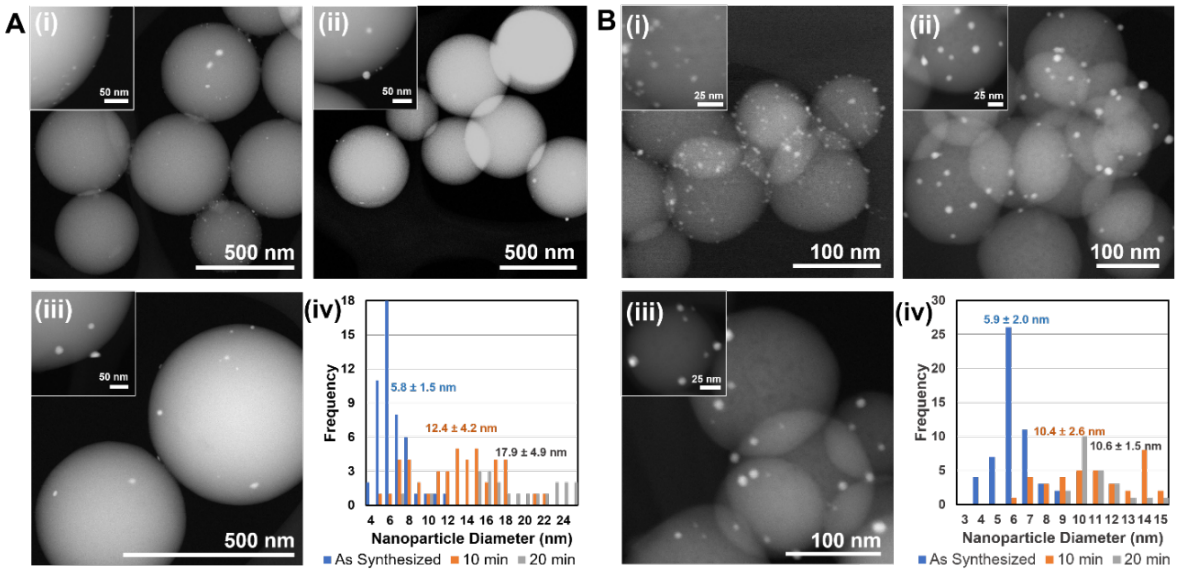

Figure 6.2 TEM images of Au nanoparticles supported on A) S1 and B) S2, i) as synthesized, ii) heated at 1020 ºC for 10 min, iii) heated at 1020 ºC for 20 min and iv) the particle size distributions of the nanoparticles at each step.

6.3.2 Sintering of Au/Al_2O_3-SiO_2

We have previously shown that modified Al_2O_3-SiO_2 planar supports are useful in controlling the extent of nanopore formation when Au nanoparticles are heated for extended times at 1020 ºC.[8] However, on analogous spherical supports, the Au nanoparticles exhibited only sintering (Figure 6.3). The average nanoparticle size increases from 4 nm to 14 nm after 10 min of annealing at 1020 ºC. No significant change is observed in the total surface area of the samples before and after heating.

Table 6.1 Summary of total surface area and total micropore volumes measured after performing N_2 physisorption on S1, S2, S3, and Au nanoparticles deposited on these supports.

Samples	**Total surface area (m^2/g)**			**Total micropore volume (cm^3/g)**		
	As Synthesized	1020 ºC, 10 min	1020 ºC, 20 min	As Synthesized	1020 ºC, 10 min	1020 ºC, 20 min
Calcined S1	9.9			2.7 E-3		
Calcined S2	32.9			4.5 E-3		
Au NP/ S1	11.2	10.9	7.9	3.1 E-3	2.2 E-3	3.1 E -3
Au NP/ S2	31.2	33.3	31.1	5.7 E-3	5.1 E-3	3.1 E-3
Calcined S3	45.1			-		
Au NP/ S3	45.8		42.3	-		-

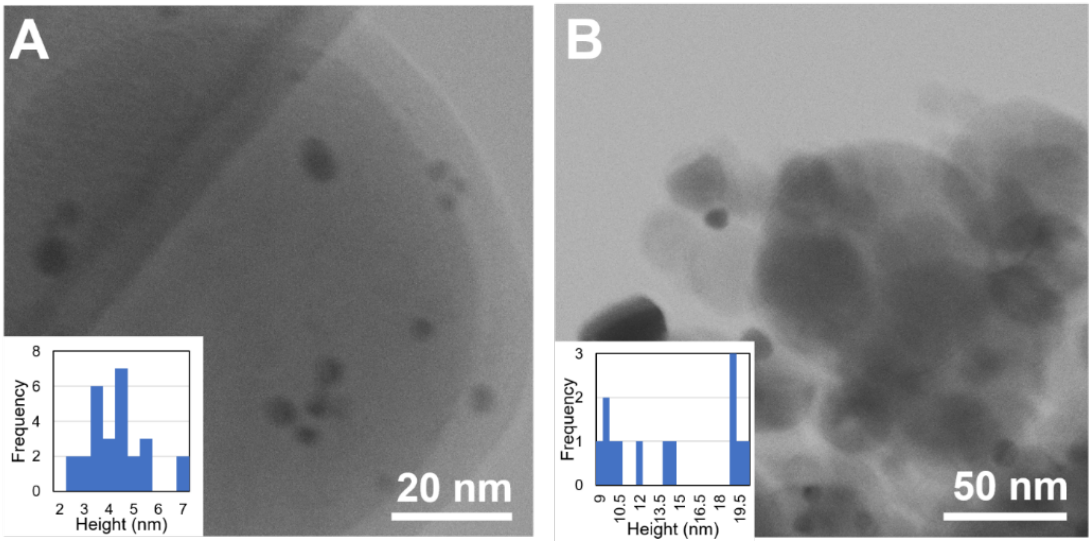

Figure 6.3 ***TEM*** images and particle size distributions of Au nanoparticles supported on S3, A) as synthesized and B) heated at 1020 ºC for 10 min.

6.3.4 Role of Na in the entrenchment of Pd/SiO_2

We have seen that the formation of nanopores on planar SiO_2 by thermal entrenchment of Au nanoparticles is slower than that by Pd nanoparticles.[8,9] Additionally, the surface mobility on SiO_2 for Au is

much higher than that for Pd.[18,19] Thus, while we see only sintering for Au nanoparticles on Stober SiO_2, nanopore formation could be possible by thermal entrenchment of Pd nanoparticles. Thus, we explored Pd a potential candidate to explore nanopore formation on spherical SiO_2 supports. Pd nanoparticles synthesized using Na_2PdCl_4 supported on S1 are uniformly distributed on the surface. On heating to 1020 ºC for 10 min, the observed behavior is strikingly different. The Stober SiO_2 underwent fragmentation and we observed several broken or cracked spheres (Figure 6.4). This behavior could be attributed to two possible causes, 1) Pd nanoparticles form nanopores that go through the entire diameter of the Stober SiO_2 leading it to its fragmentation, or 2) trace Na residue, from the metal precursor used for synthesis, causes a severe depression in the T_g of the SiO_2 causing them to fuse together.[20–22] Handling during sample preparation could cause these to fragment unevenly.

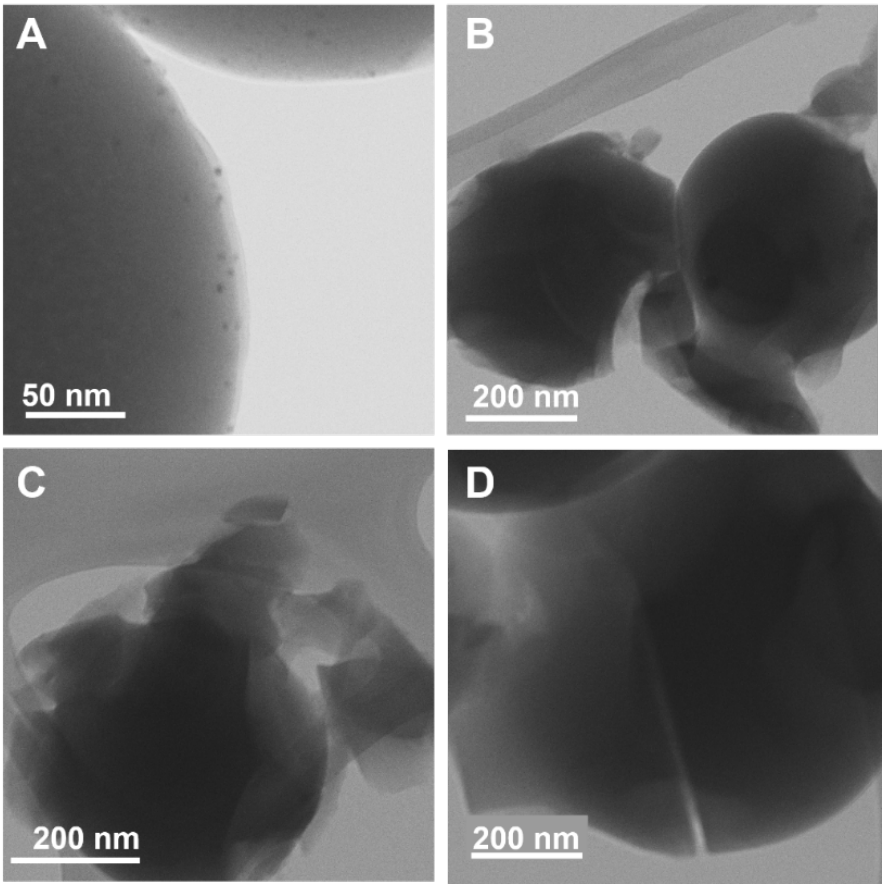

Figure 6.4 TEM images A) of Pd nanoparticles, synthesized using Na_2PdCl_4, supported on S1, as synthesized and B), C) and D) fragments of Stober SiO_2 spheres formed after being heated at 1020 ºC for 10 min.

To understand the reason behind the fragmented SiO_2 spheres, we observed the behavior of Pd nanoparticles synthesized without any trace Na using $PdAc_2$. On heating to 1020 ºC for 10 min, we observed that the nanoparticles sinter under these conditions (particle size increases from 4 nm to 14 nm) and no SiO_2 fragmentation was observed (Figure 6.5). This experiment proved that the Pd nanoparticles, like Au, exhibit only sintering on spherical SiO_2 under conditions that lead to pore formation on planar supports. This also demonstrates that the SiO_2 fragmentation is caused by the lowering of the SiO_2 T_g in the presence of Na.

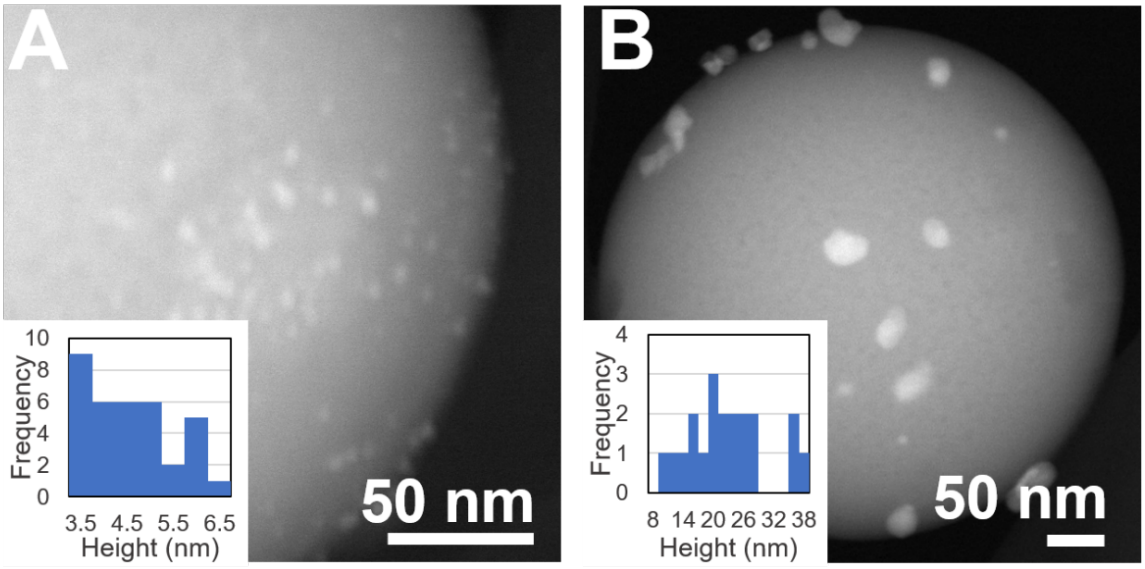

Figure 6.5 TEM images and particle size distributions of Pd nanoparticles, synthesized using $PdAc_2$, supported on S1, A) as synthesized and B) heated at 1020 ºC for 10 min.

6.4 Conclusions

In this chapter, we explored the behavior of metal nanoparticles (Au and Pd) on non-porous SiO_2 supports at high temperatures above 1000 ºC. While the heating conditions used are known to promote nanopore formation in planar SiO_2, only sintering was observed for the spherical supports. These results corroborate the vast that sintering is observed for Pd/SiO_2 at temperatures close to 900 ºC.[2–4,23–27] While the synthesis routes for the metal nanoparticles are different on planar and spherical SiO_2, the metal

nanoparticles are fully reduced. Moreover, there is no source organic residue on Au and Pd nanoparticles on spherical SiO_2 synthesized by incipient wetness impregnation.

While both the SiO_2 supports are amorphous, starkest differences between the two systems are the shape and relative size of the support. The planar Si-SiO_2 wafer is larger the nanoparticles supported on it by seven orders of magnitude and thus acts like an *infinite plane*. The Stober SiO_2 on the other hand is only 2 orders of magnitude larger than the metal nanoparticles. The spherical structure of the Stober SiO_2 is thus highly self-stressed compared to the planar SiO_2. In this case, the diffusivity of materials to and from stressed layers depends not only on the concentrations of the material and the nature of the medium but also on the stresses in the system.[14,15] Thus the diffusion of the metal atoms may be greatly reduced under the highly stressed conditions on the spherical SiO_2[14,15] leading to SiO_2 T_g remaining unaltered. Since the viscoelastic behavior of the support is a crucial stage for nanopore formation, no entrenchment is observed for the self-stressed Stober SiO_2. This reveals that the nature of entrenchment is dependent not only on the size and surface density of the metal nanoparticles, as previously shown, but also on the shape and relative of the amorphous SiO_2 support. It can be inferred that in the case of metal nanoparticles supported on spherical SiO_2, the lateral mobility and sintering of the metal nanoparticles on the curved surface of the support is much stronger than the diffusion of the metal into the surface that leads to nanopore formation.

Acknowledgements

This work made use of the BioCryo facility of Northwestern University's NUANCE Center, which has received support from the Soft and Hybrid Nanotechnology Experimental (SHyNE) Resource (NSF ECCS-1542205); the MRSEC program (NSF DMR-1720139) at the Materials Research Center; the International Institute for Nanotechnology (IIN); and the State of Illinois, through the IIN. It also made use of the CryoCluster equipment, which has received support from the MRI program (NSF DMR-1229693).

6.5 References

(1) Astruc, D. *Transition - Metal Nanoparticles in Catalysis : From Historical Background to the State - of - the Art*; 2008.

(2) Flynn, P. C. The Sintering of Supported Metal Catalysts. *Catal. Rev.* **1975**, *12* (1), 93–135.

(3) Xu, Q.; Kharas, K. C.; Croley, B. J.; Datye, A. K. The Sintering of Supported Pd Automotive Catalysts. *ChemCatChem* **2011**, *3* (6), 1004–1014.

(4) Hansen, T. W.; Delariva, A. T.; Challa, S. R.; Datye, A. K. Sintering of Catalytic Nanoparticles: Particle Migration or Ostwald Ripening? *Acc. Chem. Res.* **2013**, *46* (8), 1720–1730.

(5) Dai, Y.; Lu, P.; Cao, Z.; Campbell, C. T.; Xia, Y. The Physical Chemistry and Materials Science behind Sinter-Resistant Catalysts. *Chem. Soc. Rev.* **2018**, *47* (12), 4314–4331.

(6) Lu, J.; Fu, B.; Kung, M.; Xiao, G.; Elam, J. W.; Kung, H.; Stair, P. C. Coking- and Sintering-Resistant Palladium Catalysts Achieved Through Atomic Layer Deposition. *Science (80-.).* **2012**, *335* (February), 1205–1208.

(7) Zhang, J.; Wang, L.; Zhang, B.; Zhao, H.; Kolb, U.; Zhu, Y.; Liu, L.; Han, Y.; Wang, G.; Wang, C.; et al. Sinter-Resistant Metal Nanoparticle Catalysts Achieved by Immobilization within Zeolite Crystals via Seed-Directed Growth. *Nat. Catal.* **2018**, *1* (7), 540–546.

(8) Gosavi, A. A.; Hedrick, J. L.; Chen, P.-C.; Notestein, J. M.; Mirkin, C. A. A Tri-Layer Approach to Controlling Nanopore Formation in Oxide Supports. *Nano Res.* **2019**, *12* (1), 1–6.

(9) de Vreede, L. J.; Van Den Berg, A.; Eijkel, J. C. T. Nanopore Fabrication by Heating Au Particles on Ceramic Substrates. *Nano Lett.* **2015**, *15*, 727–731.

(10) Ono, L. K.; Behafarid, F.; Cuenya, B. R. Nano-Gold Diggers: Au-Assisted SiO2-Decomposition and Desorption in Supported Nanocatalysts. *ACS Nano* **2013**, *7* (11), 10327–10334.

(11) Ajayan, P. M.; Makrs, L. D. Evidence for Sinking of Small Particles into Substrates and Implications for Heterogeneous Catalysis. *Nature* **1989**, *338*, 139–141.

(12) de Vreede, L. J.; Schmidt Muniz, M.; Van Den Berg, A.; Eijkel, J. C. T. Nanopore Fabrication in Silicon Oxynitride Membranes by Heating Au-Particles. *J. Micromechanics Microengineering* **2016**, *26*, 37001–37006.

(13) Ardagh, M. A.; Bo, Z.; Nauert, S. L.; Notestein, J. M. Depositing SiO2 on Al2O3: A Route to Tunable Bronsted Acid Catalysts. *ACS Catal.* **2016**, *6* (9), 6156–6164.

(14) Larcht'e, F. C.; Cahn, J. l. The Effect of Self-Stress on Diffusion in Solids. *Acta Metall.* **1982**, *30* (10), 1835–1845.

(15) Fischer, F. D.; Svoboda, J. Stress, Deformation and Diffusion Interactions in Solids - A Simulation Study. *J. Mech. Phys. Solids* **2015**, *78*, 427–442.

(16) Stöber, W.; Fink, A.; Bohn, E. Controlled Growth of Monodisperse Silica Spheres in the Micron Size Range. *J. Colloid Interface Sci.* **1968**, *26* (1), 62–69.

(17) Luo, J.; Chu, W.; Sall, S.; Petit, C. Facile Synthesis of Monodispersed Au Nanoparticles-Coated on Stöber Silica. *Colloids Surfaces A Physicochem. Eng. Asp.* **2013**, *425*, 83–91.

(18) Javey, A.; Dai, H. Regular Arrays of 2 Nm Metal Nanoparticles for Deterministic Synthesis of Nanomaterials. *J. Am. Chem. Soc.* **2005**, *127* (34), 11942–11943.

(19) Liu, G.; Eichelsdoerfer, D. J.; Rasin, B.; Zhou, Y.; Brown, K. A.; Liao, X.; Mirkin, C. A. Delineating the Pathways for the Site-Directed Synthesis of Individual Nanoparticles on Surfaces. *Proc. Natl. Acad. Sci. U. S. A.* **2013**, *110* (3), 887–891.

(20) Johnson, L. E.; Sushko, P. V.; Tomota, Y.; Hosono, H. Electron Anions and the Glass Transition Temperature. *Proc. Natl. Acad. Sci.* **2016**, *113* (36), 10007–10012.

(21) Avramov, I.; Vassilev, T.; Penkov, I. The Glass Transition Temperature of Silicate and Borate Glasses. *J. Non. Cryst. Solids* **2005**, *351* (6–7), 472–476.

(22) Anderson, O, H. Glass Transition Temperature of Glasses in the SiO2-Na2O-CaO-P2O5-Al2O3-B2O3 System. *J. Mater. Sci.* **1992**, *3*, 326–328.

(23) Benavidez, A. D.; Kovarik, L.; Genc, A.; Agrawal, N.; Larsson, E. M.; Hansen, T. W.; Karim, A. M.; Datye, A. K. Environmental Transmission Electron Microscopy Study of the Origins of Anomalous Particle Size Distributions in Supported Metal Catalysts. *ACS Catal.* **2012**, *2* (11), 2349–2356.

(24) Delariva, A. T.; Hansen, T. W.; Challa, S. R.; Datye, A. K. In Situ Transmission Electron Microscopy of Catalyst Sintering. *J. Catal.* **2013**, *308*, 291–305.

(25) Baker, R. T. K. The Relationship between Particle Motion on a Graphite Surface and Tammann Temperature. *J. Catal.* **1982**, *78* (2), 473–476.

(26) Helveg, S.; Chorkendorff, I.; Skoglundh, M.; Simonsen, S. B.; Dahl, S. Coarsening of Pd Nanoparticles in an Oxidizing Atmosphere Studied by in Situ TEM. *Surf. Sci.* **2015**, *648* (June), 278–283.

(27) Min, B. K.; Santra, A. K.; Goodman, D. W. Understanding Silica-Supported Metal Catalysts: Pd/Silica as a Case Study. *Catal. Today* **2003**, *85* (2–4), 113–124.

Chapter Seven: Anomalous Thermal Entrenchment of Ni, Co, and Ag Nanoparticles

Abha Gosavi, Justin Notestein, Chad Mirkin

7.1 Introduction

In the previous chapters, we have established that nanopore formation is universal to many metal nanoparticles (Au, Ag, Cu, Pd, and Pt). We have also postulated that this entrenching behavior occurs when metal ions from nanoparticles diffuse into the supporting amorphous SiO_2 at temperatures > 1000 ºC, lowering its glass transition temperature (T_g) and making the SiO_2 viscoelastic enough to allow entrenchment.[1] In principle, all metal nanoparticles should form nanopores in amorphous SiO_2 if they undergo the same transformation that Au nanoparticles do. In this chapter, we explore how metal nanoparticles, like Ni and Co on SiO_2 supports when subjected to the conditions that lead to nanopore formation for other metals. Ni and Co are higher up in the reactivity series than other metals we have studied so far (Au, Ag, Pd, Pt, Cu) and readily form oxides when exposed to air.[2] We observe that these metals do not form nanopores, or even show oxide ridge formation on extended heating at 1040 ºC under inert conditions. Both compositions of metal nanoparticles sinter on the SiO_2 surface. The extremely low diffusivities of these metals compared to others could be the reason behind this outlying behavior.[3–6]

At the other end of the spectrum, we examine the nanopore formation of Ag nanoparticles, which progresses at much lower temperatures than other metals. We have previously seen, in Chapters 4 and 5, that Au and Pd nanoparticles need a minimum of 1000 ºC to undergo nanopore formation. At temperatures below the minimum, we observed only particle agglomeration (if favored by the distribution) and oxide ridge formation at 900 ºC for both Au and Pd nanoparticles.[1] However, we had also seen that Ag nanoparticles entrench at 900 ºC forming much larger oxide ridges than any other metal nanoparticles of comparable sizes. In this work, we study the nanopore formation by Ag nanoparticles at different temperatures, sizes, and heating duration. We observe that while Ag entrenchment starts at 800 ºC, only nanoparticles larger than 10 nm form nanopores. The smaller nanoparticles on these surfaces are either no longer visible on

the surface or remain apparently unaltered (no nanopore formation). We hypothesize that they either diffuse completely into the support or get embedded by the SiO_2. The high solubility of Ag in SiO_2, which is about two orders of magnitude higher than Au or Pd, possibly leads to the anomalous behavior of Ag nanoparticles.[6] This may also explain why the oxide ridges formed around the nanopores are so large and develop facets on extended heating. The significantly lower nanopore formation temperature of Ag makes it an interesting alternative for producing nanopores under milder conditions.

7.2 Methods

7.2.1 Nanoparticle synthesis

All metal nanoparticles were synthesized by block copolymer micelle lithography using aqueous solutions of PEO(2800)-*b*-P2VP(1500) (Polymer Source Inc.) and metal precursors at the metal:P2VP molar ratio of 1:4. $Co(NO_3)_2$, $Ni(NO_3)_2$, and $AgNO_3$ (Sigma Aldrich) were used as precursors for Co, Ni, and Ag nanoparticles respectively. The pH of the inks was maintained between 4-5 by adding dilute HCl and these were shaken for 16 h to allow micelle formation. Thin films of the M-micelle solution were spin-cast on Si wafers (NOVA Electronic Materials, 285 nm thermal oxide) at different rotation speeds of 1000 and 2000 RPM. The $AgNO_3$-laden samples were subjected to O_2 plasma (10W, 2 min). The M-micelles were reduced to nanoparticles by thermal annealing in a tube furnace (ThermoScientific Blue) under flowing Ar (195 mL/min) for 10 hours at 150 ºC and then for 10 hours at 500 ºC under H_2 flow (195 mL/min) to ensure complete thermal degradation of the block copolymer.

7.2.2 Rapid thermal processing

Thermal processing of the metal nanoparticles on SiO_2 was performed under steady Ar flow (100 mL/min) in a rapid thermal processing (RTP) furnace (MTI Corporation, OTF-1200X-4-RTP-UL). The Ni and Co nanoparticles were treated at 1040 ºC using a ramp rate of 3.3 ºC/s for 40 min, in intervals of 10 minutes. For Ag nanoparticles, temperatures between 600- 1000 ºC and hold time between 5- 20 min were used. The samples were passively cooled to room temperature under Ar flow (25 mL/min).

7.2.3 Characterization

Nanoparticle height and spatial distribution was characterized by atomic force microscopy (AFM) (Bruker FastScan using FastScan C probes). AFM image analysis and quantitative measurements were performed using Nanoscope Analysis software (Bruker).

7.3 Results and Discussion

7.3.1 Non-entrenchment of Ni and Co nanoparticles

When Co and Ni nanoparticles, uniformly distributed on the SiO_2 surface are heated to 1040 ºC for 40 minutes, no nanopore formation is observed. Co nanoparticles (Figure 7.1) exhibit aggregation and reduction in the number of features when heated (Figure 7.1F) but the height of the features remains unchanged. While the initial nanoparticles have a circular interface (AFM reveals only the top-view), the nanoparticles develop strong facets after heating. Various anisotropic structures, including cubes, rods, and platelets are observed over 40 minutes of heating.

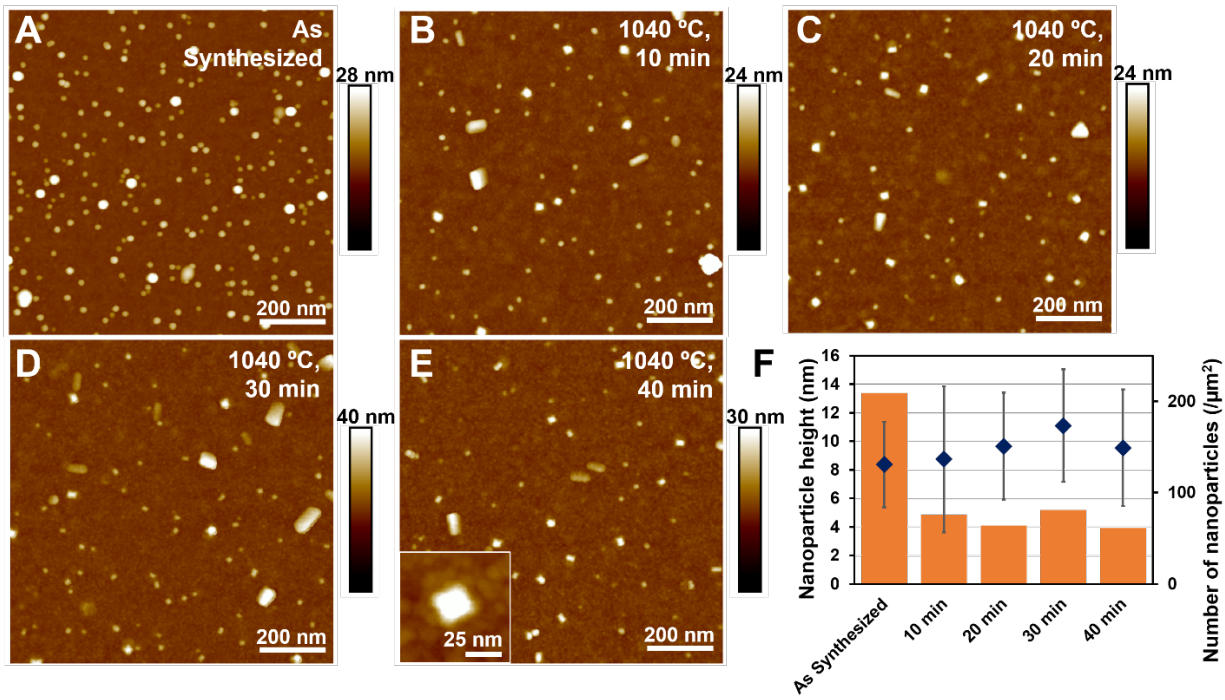

Figure 7.1 AFM images of Co nanoparticles on SiO_2 A) As synthesized and heated to 1040 ºC at 3.3 ºC/s for B) 10 min, C) 20 min, D) 30 min, and E) 40 min. F) Trends in the nanoparticle height and surface density as a function of

heating time. The blue diamonds and error bars indicate the nanoparticle height and standard deviation (left axis) and the orange bars indicate the surface density (right axis).

Ni nanoparticles, on the other hand, showed only nanoparticle sintering after being heated at 1040 ºC over 40 minutes (Figure 7.2). The initial distribution of the nanoparticles is bimodal (Figure 7.2A) and there are nanoparticles of 4 nm and 15 nm. On heating, the smaller nanoparticles are lost, probably by sintering into larger nanoparticles, and the distribution is unimodal. The nanoparticle size and density between 10- 40 min of heating is unchanged and no anisotropic nanostructures, like Co, are observed.

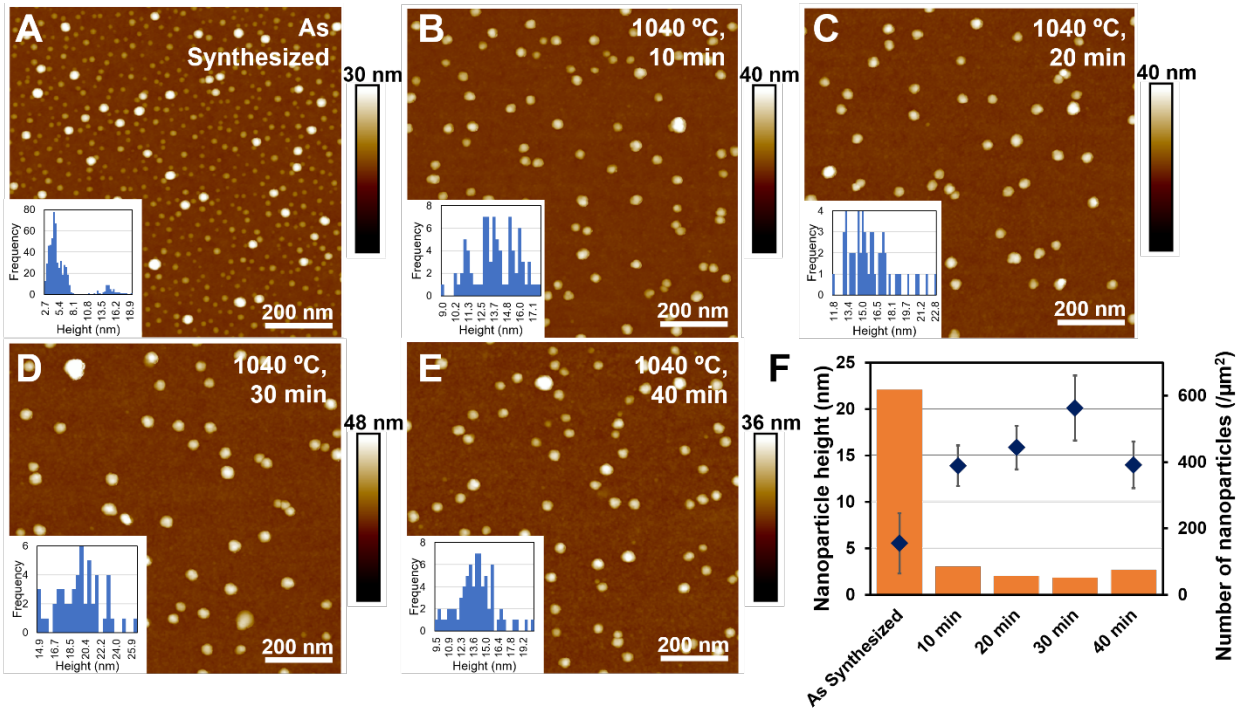

Figure 7.2 AFM images and particle size distributions of Ni nanoparticles on SiO_2 A) as synthesized, and heated to 1040 ºC at 3.3 ºC/s for B) 10 min, C) 20 min, D) 30 min, and E) 40 min. F) Trends in the nanoparticle height and surface density as a function of heating time. The blue diamonds and error bars indicate the nanoparticle height and standard deviation (left axis) and the orange bars indicate the surface density (right axis).

Both Ni and Co nanoparticles show great thermal stability at temperatures that usually lead to nanopore formation or oxide ridge formation for other metal nanoparticles. Even though oxides of Co and Ni are readily formed and thermally stable, they decompose to form metallic nanoparticles at temperatures

between 300-400 ºC.[2,7,8] However, the diffusivity of Co and Ni in SiO_2 is lower than that of Au by almost eight orders of magnitude.[3–6] Similarly, XPS and electron microscopy studies done in literature show that diffusion of these Co through SiO_2 is indeed very slow.[9,10] On the other hand, the development of cubic aggregated Co nanoparticles is a characteristic behavior on annealing and has been reported in literature.[11] Similarly, coarsening of Ni/SiO_2 at these temperatures has been reported.[12]

7.3.2 Anomalous entrenchment of Ag nanoparticles

a. Minimum size needed to observe nanopore formation

We have previously seen that Pd nanoparticles of different sizes and spacings will show different fates upon heating to high temperatures. In Chapter 5, we had seen that small and high surface density nanoparticles tended to agglomerate before nanopore formation, whereas large low surface density nanoparticles formed nanopores with diameters comparable to the initial particle size. For Ag nanoparticles, we observe that nanoparticles smaller than 10-15 nm in height do not form nanopores (Figure 7.3). When we have many small nanoparticles (< 10 nm) but only a few larger nanoparticles (> 10 nm), we observe that the number of nanopores equals the number of large nanoparticles after annealing at 900 ºC for 5 min. When two nanoparticle distributions have the same number of large nanoparticles (Figure 7.3 B and C), but very different particle densities and size distributions for smaller nanoparticles, the number of nanopores seen after heating depend only on the number of nanoparticles larger than 10 nm. There is no apparent trace of the smaller nanoparticles after the rapid thermal processing. It is probable that the smaller nanoparticles may be diffusing into the SiO_2 surface without forming nanopores due to the very high solubility of Ag in SiO_2 at this temperature.[6] Thus, for Ag, a minimum size of 10-15 nm is needed to undergo entrenchment and nanopore formation.

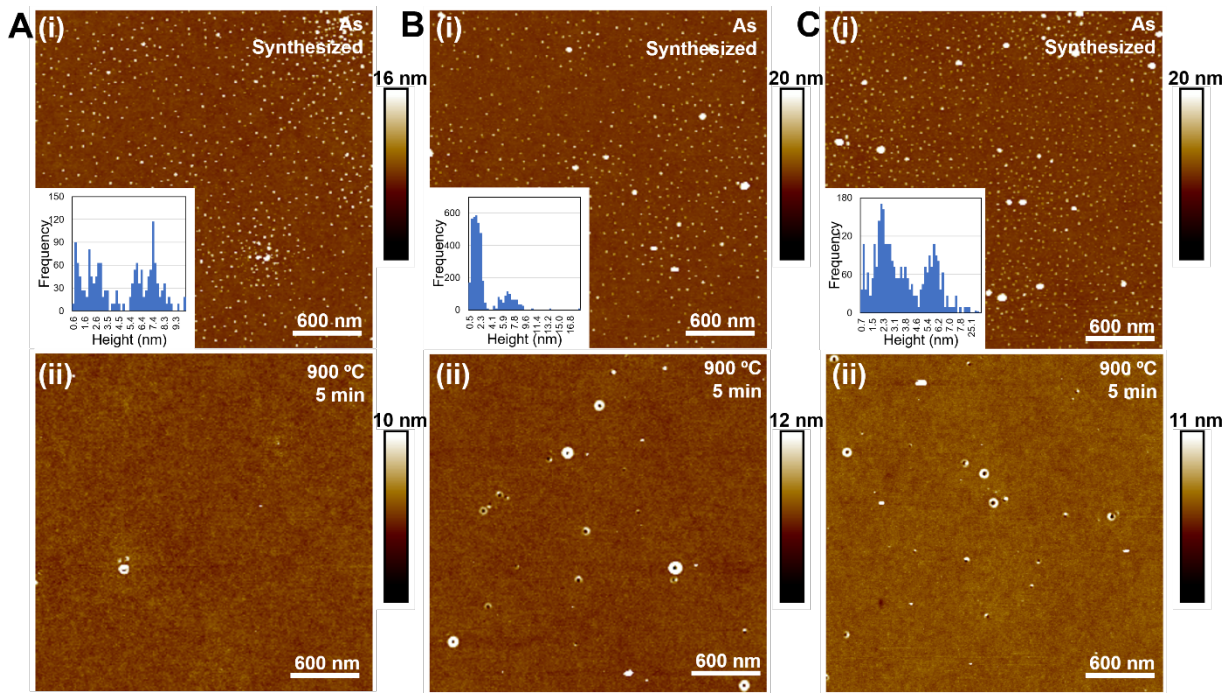

Figure 7.3 AFM images and initial particle size distributions for Ag nanoparticles with surface densities of nanoparticles larger than 10 nm of A) 0.1/ μm^2, B) 1.5 /μm^2 and C) 1.5 /μm^2, (i) As synthesized and (ii) after heating to 900 ºC for 5 min

b. Minimum temperature to observe nanopore formation

Like Au and Pd nanoparticles studied before, Ag nanoparticles also require a minimum temperature above which nanopore formation is observed. Once more, we observe that even though both small (<10 nm) and larger (> 10 nm) Ag nanoparticles are present on the surface (Figure 7.4A), only the larger nanoparticles undergo nanopore formation. When Ag nanoparticles are subjected to increasing temperatures, at 600 ºC the Ag nanoparticles remain unaltered and at 700 ºC, only oxide ridge formation is observed (Figure 7.4 B i, ii). Nanopore formation starts at 800 ºC and similar behavior is observed at 900 and 1000 ºC (Figure 7.4 B iii, iv, v). The diameter and the height of the oxide ridge remains independent of the temperature.

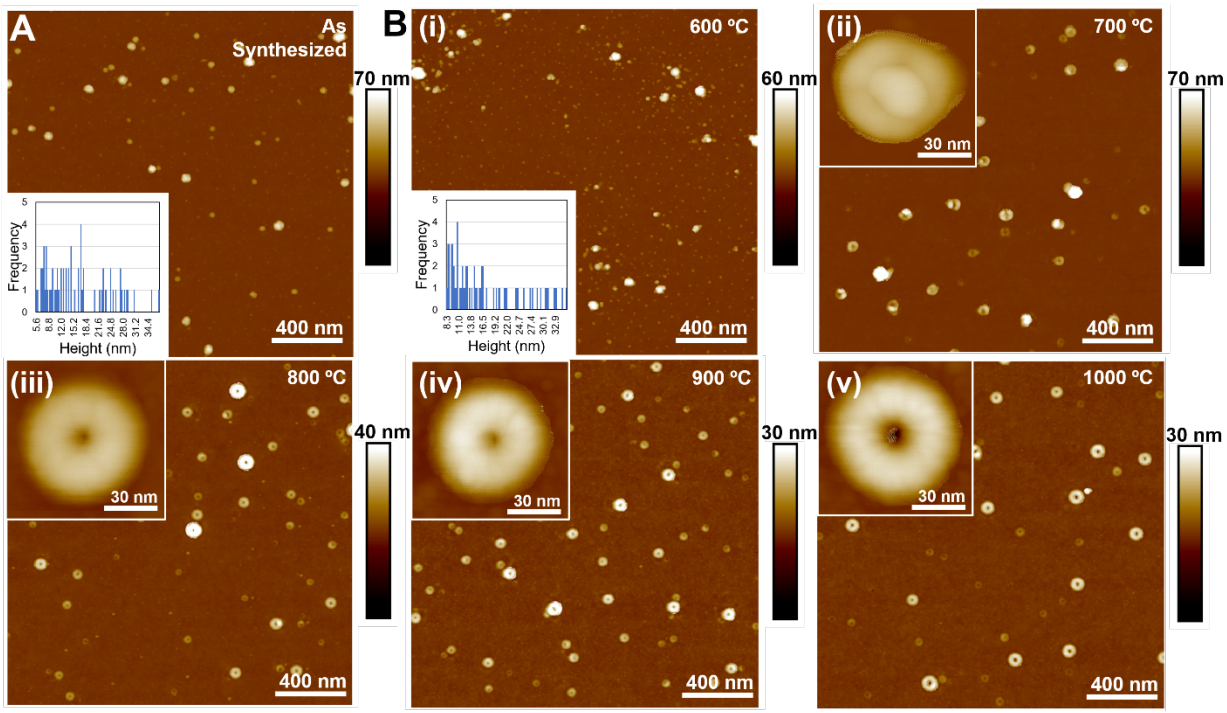

Figure 7.4 AFM images and particle size distributions of Ag nanoparticles A) as synthesized and B) after heating for 10 min at i) 600 ºC, ii) 700 ºC, iii) 800 ºC, iv) 900 ºC, and v) 1000 ºC.

c. Size and shape of oxide ridges formed by Ag nanoparticles

The oxide ridges formed around Ag nanoparticles of heights 15-20 nm are much larger than those observed for Au and Pd nanoparticles of comparable sizes (Figure 7.5 and Table 7.1). The height of the oxide ridges follows the order Au ≈ Pd << Ag which is similar to the order for solubility of the metal ions in solid SiO_2 (Au < Pd << Ag).[6] Higher diffusion of the metal ions into the SiO_2 may increase the oxide mobility at the triple line, causing large oxide ridges to be formed.[13] It is also interesting to note that Au, which has the lowest solubility in SiO_2, takes 40 min to be completely entrenched, and even then, not all nanoparticles form nanopores and further annealing may be required (Figure 7.5B).

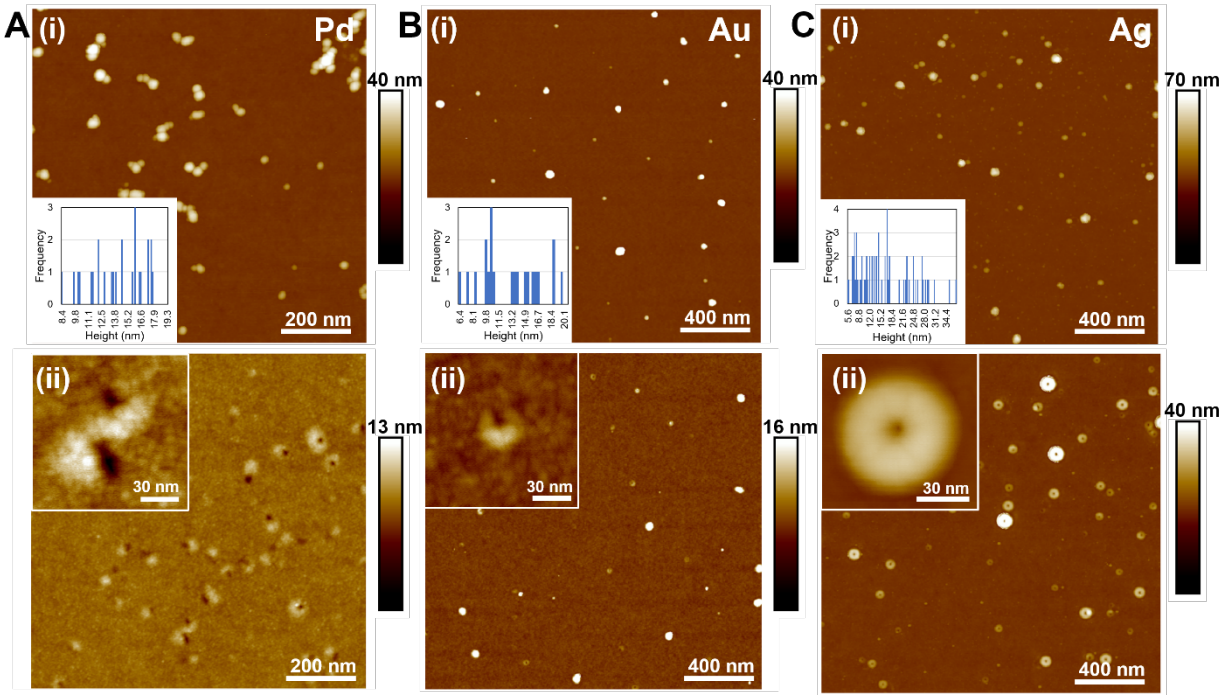

Figure 7.5 AFM images and initial particle size distributions of A) Pd nanoparticles i) as synthesized and ii) heated at 1040 ºC for 10 min, B) Au nanoparticles i) as synthesized and ii) heated at 1020 ºC for 40 min, and C) Ag nanoparticles i) as synthesized and ii) heated at 800 ºC for 10 min

Table 7.3 Summary of initial nanoparticle size and surface density and final oxide ridge height and number of nanopores formed by entrenchment of Au, Pd, and Ag nanoparticles

Metal	Initial nanoparticle height (nm)	Initial number of nanoparticles (/μm^2)	Oxide ridge height after heating (nm)	Number of nanopores after heating (/μm^2)
Au	18.8 ± 8.7	8	3.2 ± 1.2	6
Pd	14.9 ± 3.6	30	2.6 ± 0.6	30
Ag	16.9 ± 7.7	15	9.1 ± 5.7	15

On extended heating of Ag nanoparticles at 700 ºC, a temperature at which no nanopore formation is observed but oxide ridges are formed, we observe that the shape of oxide ridge develops over time. While the oxide ridges formed after 10 min of heating have no donut-like shape, distinctly faceted ridges

are observed after 20 min of heating (Figure 7.6). Additionally, on extended heating, the size (diameter and width) of the oxide ridge increases whereas the size of the Ag nanoparticle decreases.

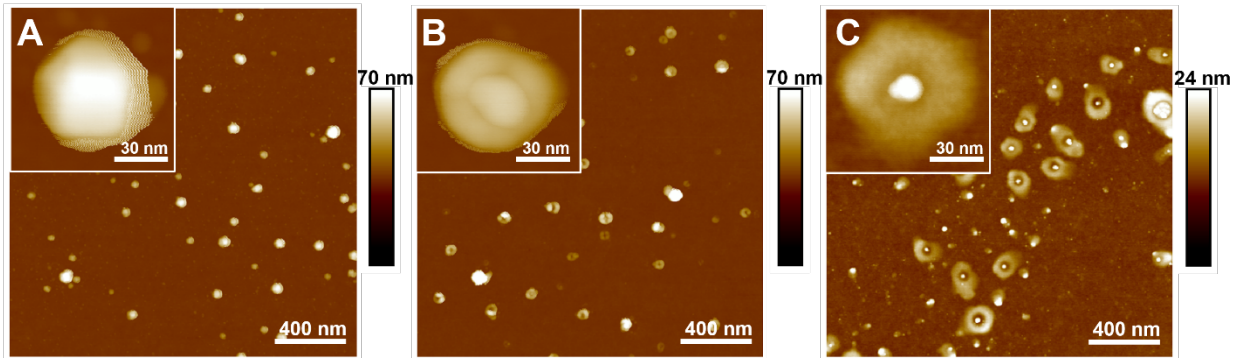

Figure 7.6 AFM images of Ag nanoparticles A) As synthesized and after heating to 700 ºC for B) 10 min and C) 20 min

These faceted oxide ridges are similar to those observed in the literature after extended heating of Cu nanoparticles on crystalline Al_2O_3 wafers over 78 h at 980 ºC.[14–16] Curiotto et al., attribute the faceted oxide ridge to the orientation relationship of the Cu crystals and Al_2O_3 crystalline planes underneath. At high temperatures, the metal and the oxide undergo surface rearrangement to achieve equilibrium. As a result, the Cu crystals sink into the Al_2O_3 layer while the oxide is transported along the triple line at the interface.[14] The authors postulate that the shape of the oxide ridge results from an attempt of the system to reach its equilibrium shape. In the case of Ag/ SiO_2 however, the SiO_2 is amorphous and hence will not undergo the same rearrangements as the crystalline Al_2O_3. The large Ag nanoparticles that undergo this transformation are initially faceted. Since 700 ºC is significantly below the bulk melting point of Ag (961 ºC), it can be hypothesized that the nanoparticles do not undergo surface melting and most of the facets are maintained (Figure 7.6B inset). Thus, the oxide ridge also attains facets as oxide transport continues at the triple line. At higher temperatures however, the oxide ridges have no facets since the Ag nanoparticle may undergo melting and do not retain their facets (Figure 7.4B iii, iv, v). This effect was not observed when we had previously studied the oxide transport for extended heating of Au nanoparticles at 900 ºC.[1] The smaller nanoparticle size, lower solubility in SiO_2, and proximity of the operating temperature to the bulking melting temperature (1060 ºC) of Au could be the possible reasons behind this.[6]

7.4 Conclusions and Scope

In this final chapter, we examined the outliers and exceptional metal nanoparticles in the context of high temperature entrenchment. We observe that no nanopore formation occurs when Ni and Co nanoparticles, which have significantly low diffusivities in SiO_2, are heated at 1040 ºC for extended periods of time. This proves that while nanopore formation by thermal entrenchment of metal nanoparticles can be universal in principle, the diffusion of the metal ions into the SiO_2 a crucial step for nanopore formation.

We also looked at the Ag/SiO_2 system in greater detail. Ag nanoparticles entrench at significantly lower temperatures than Au and Pd nanoparticles and form much larger oxide ridges. Additionally, Ag nanoparticles also formed distinct faceted oxide ridges on extended heating at temperature below the minimum required for nanopore formation. Thus, the Ag/SiO_2 system is an anomaly for high temperature entrenchment in many ways, making it an interesting combination to study. Moreover, Ag nanoparticles forms nanopores at the lowest temperature reported so far, 800 ºC, making it an ideal candidate for a simpler route to nanopore fabrication. Using doped glasses with lower glass transition temperature could further lower the temperature needed for nanopore formation.[17,18] Hence, additional work needs to be done to understand high temperature entrenchment of Ag/SiO_2 better and utilize it to explore scalable synthesis of nanopores.

Acknowledgments

This material is based upon work supported by the Sherman Fairchild Foundation, Inc. and the Air Force Office of Scientific Research under Award number FA9550-16-1-0150. This work made use of the EPIC and SPID facilities of Northwestern University's NUANCE Center, which has received support from the Soft and Hybrid Nanotechnology Experimental (SHyNE) Resource (NSF ECCS-1542205); the MRSEC program (NSF DMR-1121262) at the Materials Research Center; the International Institute for Nanotechnology (IIN); the Keck Foundation; and the State of Illinois, through the IIN.

7.5 References

(1) Gosavi, A. A.; Hedrick, J. L.; Chen, P.-C.; Notestein, J. M.; Mirkin, C. A. A Tri-Layer Approach to

Controlling Nanopore Formation in Oxide Supports. *Nano Res.* **2019**, *12* (1), 1–6.

(2) Clugston, M.; Flemming, R. *Advanced Chemistry*; Oxforf University Press: Oxford, 2000.

(3) Baten, J.; Offenberg, M.; Emmerichs, U.; Balk, P.; Grunthaner, P. J.; Ewert, S. Diffusion of Cobalt and Titanium in SiO2. *Appl. Surf. Sci.* **1989**, *39* (1–4), 266–272.

(4) Atkinson, A.; Gardner, J. W. The Diffusion of Fe3+ in Amorphous SiO2 and the Protective Properties of SiO2 Layers. *Corros. Sci.* **1981**, *21* (1), 49–58.

(5) Ghoshtagore, R. N. Diffusion of Nickel in Amorphous Silicon Dioxide and Silicon Nitride Films. *J. Appl. Phys.* **1969**, *40* (11), 4374–4376.

(6) McBrayer, J. D. Diffusion of Metals in Silicon Dioxide. *J. Electrochem. Soc.* **1986**, *133* (6), 1242.

(7) Jang, W. L.; Lu, Y. M.; Hwang, W. S.; Dong, C. L.; Hsieh, P. H.; Chen, C. L.; Chan, T. S.; Lee, J. F. A Study of Thermal Decomposition of Sputtered NiO Films. *Epl* **2011**, *96* (3).

(8) Kittaka, S.; Uchida, N.; Miyashita, I.; Wakayama, T. Thermal Decomposition and Pore Formation of Cobalt Oxide Hydroxide (HCoO2). *Colloids and Surfaces* **1989**, *37* (C), 39–54.

(9) Čechal, J.; Luksch, J.; Koňáková, K.; Urbánek, M.; Brandejsová, E.; Šikola, T. Morphology of Cobalt Layers on Native SiO2 Surfaces at Elevated Temperatures: Formation of Co Islands. *Surf. Sci.* **2008**, *602* (15), 2693–2698.

(10) Kato, H.; Oizumi, Y.; Umetani, S.; Yamada, K.; Hashimoto, I.; Homma, Y. Thermal Behavior of Metal Layers Sandwiched by Silicon Dioxide Layers. *Jpn. J. Appl. Phys.* **2015**, *54* (8), 2–5.

(11) Yeh, Y.; Liu, I. H.; Shen, P. Onset Coarsening/Coalescence of Cobalt Oxides in the Form of Nanoplates versus Equi-Axed Micron Particles. *J. Eur. Ceram. Soc.* **2010**, *30* (3), 677–688.

(12) Sprouster, D. J.; Giulian, R.; Araujo, L. L.; Kluth, P.; Johannessen, B.; Kirby, N.; Ridgway, M. C. Formation and Structural Characterization of Ni Nanoparticles Embedded in SiO2. *J. Appl. Phys.* **2011**, *109* (11).

(13) Saiz, E.; Tomsia, A. P.; Cannon, R. M. Triple Line Ridging and Attachment in High-Temperature Wetting. *Scr. Mater.* **2001**, *44* (1), 159–164.

(14) Curiotto, S.; Chien, H.; Meltzman, H.; Labat, S.; Wynblatt, P.; Rohrer, G. S.; Kaplan, W. D.; Chatain, D. Copper Crystals on the (1120) Sapphire Plane: Orientation Relationships, Triple Line Ridges and Interface Shape Equilibrium. *J. Mater. Sci.* **2013**, *48* (7), 3013–3026.

(15) Ghetta, V.; Chatain, D. Morphologies Adopted by Al2O3 Single-Crystal Surfaces in Contact with

Cu Droplets. *J. Am. Ceram. Soc.* **2004**, *85* (4), 961–964.

(16) Kaplan, W. D.; Chatain, D.; Wynblatt, P.; Carter, W. C. A Review of Wetting versus Adsorption, Complexions, and Related Phenomena: The Rosetta Stone of Wetting. *J. Mater. Sci.* **2013**, *48* (17), 5681–5717.

(17) Karakouz, T.; Tesler, A. B.; Sannomiya, T.; Feldman, Y.; Vaskevich, A.; Rubinstein, I. Mechanism of Morphology Transformation during Annealing of Nanostructured Gold Films on Glass. *Phys. Chem. Chem. Phys.* **2013**, *15* (13), 4656–4665.

(18) Avramov, I.; Vassilev, T.; Penkov, I. The Glass Transition Temperature of Silicate and Borate Glasses. *J. Non. Cryst. Solids* **2005**, *351* (6–7), 472–476.

Chapter Eight: Summary and Future Directions

8.1 Goals Achieved

Throughout this thesis, we have attempted to address the issue of catalyst stability under reaction conditions- first by understanding the leaching of Pd during Suzuki-Miyaura cross-coupling reaction and later by employing controlled partial entrenchment of metal nanoparticles on novel tri-layer structures to generate potential sinter-resistant catalysts. In exploring the Suzuki-Miyaura cross-coupling reaction as a model reaction for catalyst discovery, we learnt that there is atomic leaching of Pd in the liquid reaction phase. While this loss can be mitigated or recouped by catalyst regeneration, its persistence shows that the reaction is truly homogenous in nature. Thus, it would be unsuitable to use it as a model to study heterogenous catalysts.

Next, we have established the scope and the mechanism of nanopore formation when metal nanoparticles, supported on planar amorphous SiO_2, are subjected to very high temperatures (>1000 ºC) for a short time (10 min). Exploratory work showed that nanopore formation occurs not only for Au but also for Ag, Cu, Pd, and Pt (although not for Ni and Co) and that this behavior selectively occurs on amorphous SiO_2 and not on crystalline oxides.[1] We employed this behavior to design tri-layer substrates consisting of thin layers of SiO_2 on Al_2O_3 that are successful in controlling the depth to which nanopore formation occurs. In the latter part, we focused on how the initial size and surface density of the nanoparticles affects the final fate of the nanopore when subjected to high temperature annealing. We have shown that nanopore formation competes with agglomeration and encapsulation pathways, and the dominant mechanism depends on the distribution of nanoparticles. Furthermore, we have expanded the knowledge in this field by studying nanopore formation at different temperatures and on different surfaces. We have demonstrated that nanopore formation needs a minimum temperature to begin and that this temperature depends on the nature of the nanoparticles and their diffusivity through the SiO_2 matrix. We have also explored thermal entrenchment of Au and Pd nanoparticles on spherical SiO_2 supports and observed no nanopore formation. The highly self-stressed spherical supports, contrary to their planar counterparts, drastically slow down the diffusion of metal ions into the SiO_2,[2] thus leaving the T_g of the material unaltered. The depression of T_g

being a crucial step in the mechanism of nanopore formation, no entrenchment is observed on spherical geometries.

We have also encountered one major limitation to nanopore formation. While nanopore formation occurs readily for nanoparticles synthesized by block copolymer lithography that used PEO-*b*-P2VP, we have observed that it can be poisoned by the presence of organic residue. Nanopore formation is not observed when nanoparticles synthesized using PS-*b*-P2VP as subjected to the same annealing conditions. Similar behavior is seen for nanoparticles synthesized by scanning probe block copolymer lithography (SPBCL), which uses PEO-*b*-P2VP but does leave large carbonaceous residues (Figure S16, S17). Thus, for the purposes of nanopore formation, initial nanoparticles free from organic contaminants would be desired.

The work summarized in this thesis is an attempt at understanding the scope, limitations, and mechanism of nanopore formation by thermal entrenchment of metal nanoparticles. Throughout the manuscript, significant emphasis was placed on understanding the nature of thermal entrenchment and its potential application to generate partially entrenched nanoparticles that could be used as sinter-resistant catalyst. However, there are still several unanswered questions about the details of nanopore formation that beg to be investigated. Besides catalysis, the partially entrenched nanoparticles and nanopores formed during the entrenchment process could have a wide range of functions. We envision that these materials could be especially ideal for applications in separations, sensing, and electronics.[3–5]

8.2 Future Directions

8.2.1 Spectroscopic and *in situ* studies for better understanding of the mechanism

Throughout this work we have endeavored to understand the mechanism of metal-oxide interactions at high temperature and subsequent nanopore formation. We postulate that the diffusion of metal ions into the supporting SiO_2 is crucial to nanopore formation. This would imply that trace amounts of metal would be present in the oxide ridges surrounding the nanopores as well as in the walls of the nanopores. Cross-section electron microscopy done by de Vreede et al., has however shown that the Au

nanoparticles present at the base of the nanopore are crystalline and do not exhibit any apparent dissolution in the surrounding oxide.[6]

Additionally, for some metals like Cu that react with SiO_2 to form silicides, we can expect the presence of metal silicides.[7,8] Our preliminary experiments have shown that Pd nanoparticles form nanopores under reducing conditions (6% H_2) at 1040 ºC (Figure 8.1 A and B). Under these conditions, formation of PdSi is expected.[7,9–11] XPS analysis of these surfaces revealed no PdSi presence in both the Pd 3d and Si 2p spectra (Figure 8.1 C and D). While metallic (335.5 eV) and oxide (337.5 eV) forms of Pd are observed before heating, the XPS signals are lost after heating, possibly due to very deep nanopore formation. The Si 2p spectra only shows the presence of SiO_2 (103.5 eV) and no silicides. Similar observation was made by Ono et al., who demonstrated SiO_2 decomposition in the presence of Au nanoparticles at high temperatures.[12] However, lack of signals is not indicative of absence of metal silicides. XPS may not be sensitive enough to detect the trace presence of silicides, if any. We need more sensitive techniques, like Rutherford backscattering spectroscopy (RBS) to look at the surface in greater detail. RBS has been used to study the compositional changes at the metal-oxide interface in many instances and could be very useful in studying thermal entrenchment of nanoparticles.[11,13,14] This technique could also be useful in determining the composition of the oxide ridges. In the previous chapters we have shown that the diffusivity of the metal plays a big role in the nature and size of the oxide ridges observed. The metal nanoparticles may be removed by gentle etchants or by sonication and the oxide ridges can be studied in greater detail. RBS can reveal if these oxides are pure or are doped with metals.

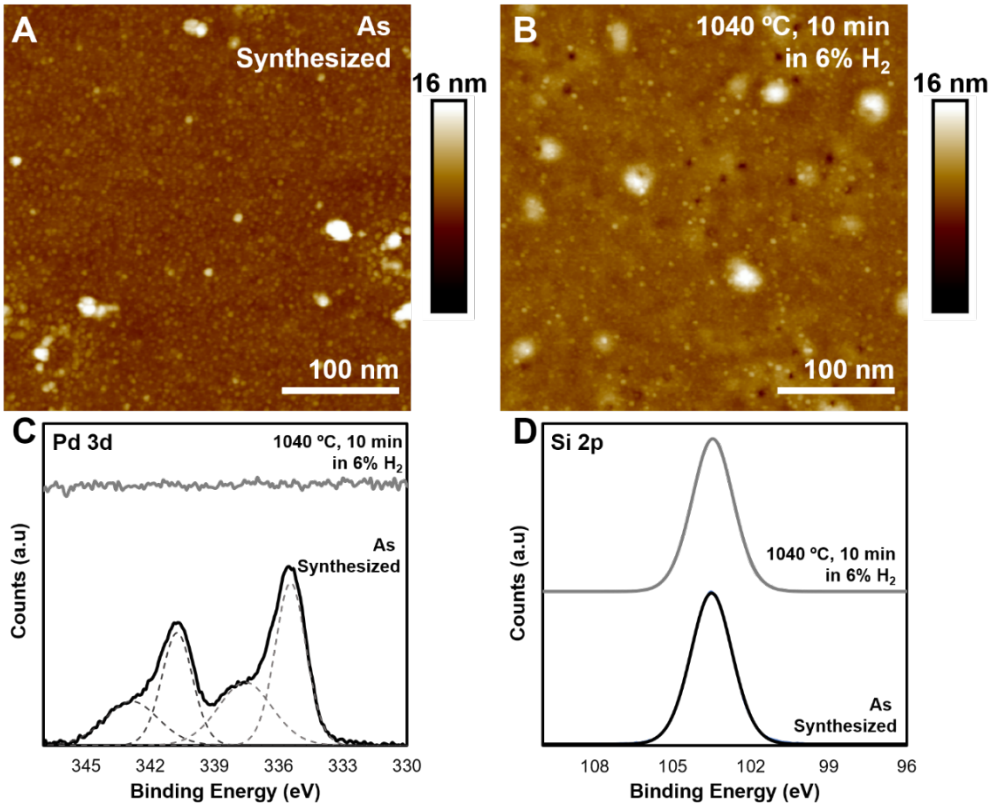

Figure 8.1 AFM images of Pd nanoparticles on SiO_2 surface A) as Synthesized and B) after annealing at 1040 ºC for 10 min in 6% H_2. XPS spectra C) Pd 3d and D) Si 2p for Pd/SiO_2 surface before and after annealing.

In addition to spectroscopic studies, electron microscopy can also be explored as a potential way to observe the nanopore formation *in situ* in real time. Heated stages on some transmission electron microscopes can attain temperatures above 1200 ºC and have been used to study phase transformations at high temperatures.[15,16] While it could be extremely difficult to stabilize the detector while ramping the temperatures rapidly, it would be worthwhile to observe the thermal entrenchment of Ag (which occurs at 800 ºC) as well as the growth of oxide ridges. TEM with energy dispersive X-ray (EDX) detectors can enable us to understand the elemental composition and the structure of the nanoparticle present at the base of the nanopore, the walls of the nanopore, as well as the oxide ridges. Thus, detailed spectroscopic and microscopic investigations will help us better understand the nuances of nanopore formation.

8.2.2 Entrenchment on thin layers of SiO_2 and other amorphous supports

In this work, we have primarily looked at amorphous SiO_2 layers of 300 nm thickness. However, preliminary experiments show that nature of nanoparticle entrenchment depends on the thickness of SiO_2 on a Si wafer. We observed (Figure 8.2) that nanopores formed on 500 nm, 50 nm, and 10 nm of SiO_2 layers are like those seen for 300 nm thick SiO_2. However, on 3 nm SiO_2 layers on Si wafers, created by HF etching of the Si-wafer and allowing a native oxide layer to grow, we observe that while no nanopores are formed, nanoparticles form grooves on the surface (Figure 8.2 A). These may be arising from the particle mobility on the thin viscoelastic layer of SiO_2 under the flow of the Ar gas. Similar directed groove-formation has been observed for Au nanoparticles heated at 400 ºC on InP, InAs, and GaP surfaces under steady H_2O-N_2 gas flow.[17] It is also possible that the metal nanoparticles diffused/ entrenched through the SiO_2 layer and reacted with the underlying Si to form PdSi.[18] Metal silicides have been shown to cause SiO_2 decomposition with could lead to the formation of the grooves on the surface.[19] Further exploration in this direction can lead to a new way of fabrication of ordered grooved on oxide and semiconductor surfaces which can be used as waveguides or in electronic devices.[17]

Additionally, metal nanoparticles can also be used to make nanopores in other amorphous materials at high temperatures. Metallic glasses[20] and oxide semiconductors[21] may be few potential materials that enable nanopore formation and can be explored to expand the library of nanoporous materials.

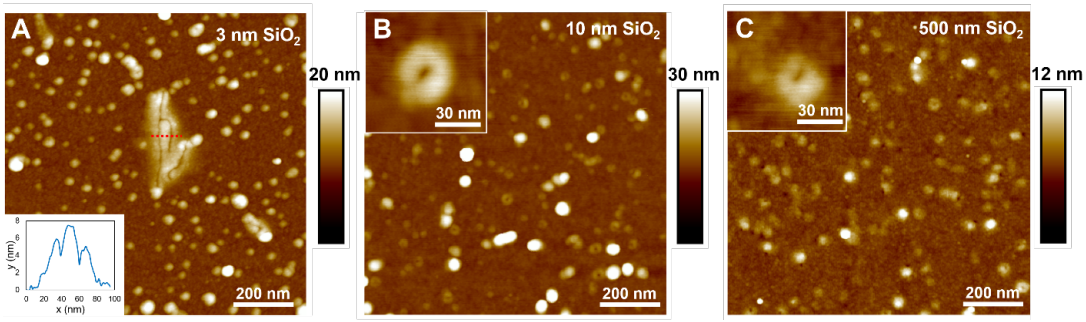

Figure 8.2 AFM images of surface features after uniform Pd nanoparticles were subjected to heating at 1040 C for 10 min on Si wafer with A) 3 nm SiO_2 (Inset shows the profile of the section marked by the red dotted line), B) 10 nm SiO_2, and C) 500 nm SiO_2.

8.2.3 Applications of nanopores in separations and sensing

We have shown that nanoparticles can be controllably entrenched to different depths in tri-layer substrates.[1] However, if total entrenchment is allowed and metal nanoparticles are heated on free-standing SiO_2 layers, nanoporous membranes may be obtained. Synthesis of nanopores by this route for applications in separations has been shown in literature. Eijkel et al., have demonstrated a protocol to achieve ordered arrays of nanopores 30-50 nm in diameter by heating 500 nm Pt discs at 1000 ºC. These ordered nanopores have low surface densities of ~10 nanopores/ μm^2.[5] In this work, we have shown that various arrays of Pd nanoparticles of different sizes and distributions can be easily synthesized with block copolymer lithography. The Pd nanoparticles, when heated, give highly tunable nanopores between 6 to 25 nm in diameter with densities as high as 150 nanopores/ μm^2. Such nanopore dimensions are harder to achieve, though not impossible, on other porous materials like anodic aluminum oxide (AAO) and by precious techniques like focused ion beam (FIB) milling.[22]

We have presented a protocol to develop scaffolded free-standing layers of SiO_2 of tunable thickness that can be then used as substrates for nanoparticle deposition and subsequent nanopore formation after thermal processing (Scheme 8.1). The first step is the fabrication of a stable and robust suspended SiO_2 thin film held up by silicon scaffolding. In order to do so, thin silicon wafers (280 μm thick) that have 300 nm thermal oxides on both sides would be subjected to several photolithography and etching steps as outlined. During the deep reactive ion etching (DRIE) step, extra care must be used to stop the etching process just before the last SiO_2 layer and avoid breakage. At that point, a KOH etching bath can be used to etch any remaining silicon between the scaffolds. This process will give the membranes that be then made porous by thermal entrenchment of nanoparticles. Arrays of different SiO_2 patch diameter and densities (Figure 8.3) can be tested to determine optimal parameters for stable scaffolds for spin-coating and heating. On optimizing the dimensions of the SiO_2 membranes and their stability, Pd nanoparticles could be deposited *via* block copolymer lithography and subsequently entrenched at temperatures above 1000 ºC. The nanoporous membranes can then be tested for applications in separations of biomolecules

and seed nanoparticles from anisotropic nanoparticle growth solutions. These nanopore could also be functionalized with different end groups to enhance their selectivities and sensing capabities.[12]

Scheme 8.1 A protocol to generate nanoporous SiO_2 membranes.

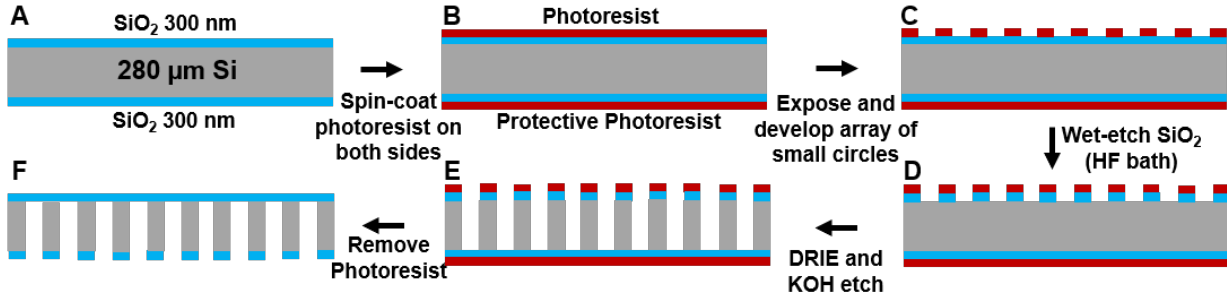

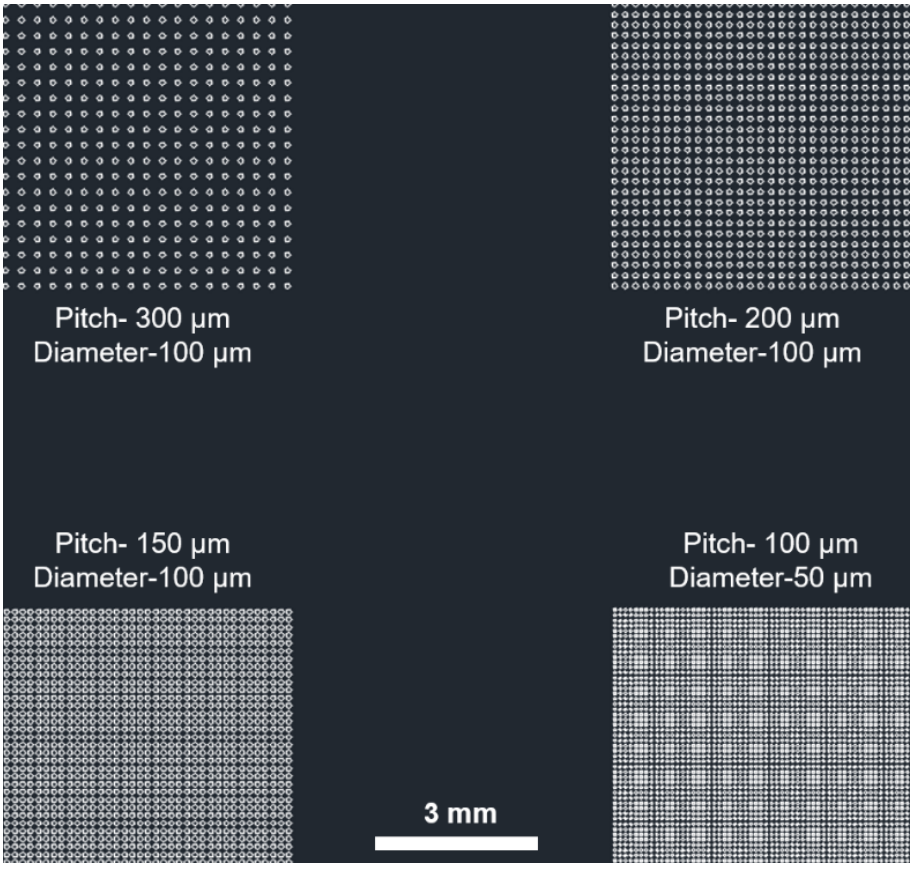

Figure 8.3 Optical microscopy image of Si-wafer with DRIE-etched SiO_2 patches of different pitch and diameters.

8.2.4 Entrenchment of anisotropic nanoparticles

Nanopores of various lengths and diameters have a wide range of applications. It would be even more interesting to obtain nanopores of different shapes. Anisotropic nanopores are usually chemical etching of crystalline materials. Nanopores with a square or triangular cross section have been synthesized in Si supports using strongly acidic or basic etchants.[23,24] These anisotropic through-pores or pits have applications in development of semiconductor and memory devices.[25,26] Formation of anisotropic pores in SiO_2 is more challenging and has not been reported yet. Temperature entrenchment of anisotropic metal nanoparticles may be a potential way to form these nanostructures on oxide supports. Extended heating of Cu crystals on Al_2O_3 supports shows the formation of hexagonal pits on the surface surrounded by hexagonal oxide ridges.[27] We have seen similar behavior for Ag nanoparticles when they were heated at 700 ºC (which is below the nanopore formation temperature of 800 ºC) for 20 min. While the metal nanoparticles are still intact within these anisotropic pits, they can be removed by chemical etchants as we had done for Pd nanoparticles. Another potential way to obtain anisotropic entrenchment is to use anisotropic metal nanoparticles as the precursor. Depending on the shape and size of these nanoparticles, entrenchment may be achieved before the nanoparticles lose their facets at high temperatures. Additionally, partially embedded nanocubes or planar triangles may also have interesting plasmonic properties.[28]

In conclusion, nanopore formation by thermal entrenchment of metal nanoparticles on SiO_2 has a wide range of possible applications. In looking at the scope and mechanism, we have barely scratched the surface of the potential scope of this field.

8.3 References

(1) Gosavi, A. A.; Hedrick, J. L.; Chen, P.-C.; Notestein, J. M.; Mirkin, C. A. A Tri-Layer Approach to Controlling Nanopore Formation in Oxide Supports. *Nano Res.* **2019**, *12* (1), 1–6.

(2) Larcht'e, F. C.; Cahn, J. l. The Effect of Self-Stress on Diffusion in Solids. *Acta Metall.* **1982**, *30* (10), 1835–1845.

(3) Park, T.; Lee, S. J.; Cha, J. H.; Choi, W. Scalable Fabrication of Nanopores in Membranes: Via Thermal Annealing of Au Nanoparticles. *Nanoscale* **2018**, *10* (47), 22623–22634.

(4) Kwon, S.; Jang, S.; Choi, J. W.; Choi, S.; Jang, S.; Kim, T. W.; Wang, G. Controllable Switching Filaments Prepared via Tunable and Well-Defined Single Truncated Conical Nanopore Structures for Fast and Scalable SiOx Memory. *Nano Lett.* **2017**, *17* (12), 7462–7470.

(5) Kirchhoff, K.; Odijk, M.; Le-The, H.; van den Berg, A.; Kappl, M.; Müller, M.; Lohse, D.; Eijkel, J. C. T.; Tregouet, C. Engulfment Control of Platinum Nanoparticles into Oxidized Silicon Substrates for Fabrication of Dense Solid-State Nanopore Arrays. *Nanotechnology* **2018**, *30* (6), 065301.

(6) de Vreede, L. J.; Schmidt Muniz, M.; Van Den Berg, A.; Eijkel, J. C. T. Nanopore Fabrication in Silicon Oxynitride Membranes by Heating Au-Particles. *J. Micromechanics Microengineering* **2016**, *26*, 37001–37006.

(7) van den Oetelaar, L. C. A.; van den Oetelaar, R. J. A.; Partridge, A.; Flipse, C. F. J.; Brongersma, H. H. Reaction of Nanometer-Sized Cu Particles with a SiO2 Substrate. *Appl. Phys. Lett.* **1999**, *74* (20), 2954–2956.

(8) Pretorius, R.; Harris, J. M.; Nicolet, M. A. Reaction of Thin Metal Films with SiO2 Substrates. *Solid State Electron.* **1978**, *21* (4), 667–675.

(9) Juszczyk, W.; Karpiński, Z.; Łomot, D.; Pielaszek, J. Transformation of Pd/SiO2into Palladium Silicide during Reduction at 450 and 500°C. *J. Catal.* **2003**, *220* (2), 299–308.

(10) Juszczyk, W.; Łomot, D.; Pielaszek, J.; Karpi, Z. Transformation of Pd / SiO 2 Catalysts during High Temperature Reduction. **2002**, *78* (March), 95–98.

(11) Min, B. K.; Santra, A. K.; Goodman, D. W. Understanding Silica-Supported Metal Catalysts: Pd/Silica as a Case Study. *Catal. Today* **2003**, *85* (2–4), 113–124.

(12) Ono, L. K.; Behafarid, F.; Cuenya, B. R. Nano-Gold Diggers: Au-Assisted SiO2-Decomposition and Desorption in Supported Nanocatalysts. *ACS Nano* **2013**, *7* (11), 10327–10334.

(13) McBrayer, J. D. Diffusion of Metals in Silicon Dioxide. *J. Electrochem. Soc.* **1986**, *133* (6), 1242.

(14) Fu, Q.; Wagner, T. Interaction of Nanostructured Metal Overlayers with Oxide Surfaces. *Surf. Sci. Rep.* **2007**, *62* (11), 431–498.

(15) Snoeck, E.; Roucau, C.; Baules, P.; Casanove, M. .; Fahot, M.; Astie, B.; Degauque, J. Use of in Situ TEM Experiments for Phase Transition Studies. *Microsc. Microanal. Microstruct* **1993**, *4*, 249–264.

(16) Terasawa, T.-O.; Kikuchi, S.; Manabu, T.; Tokushi, K. Development of 2000 K Class High Temperature In Situ Transmission Electron Microscopy of Nanostructured Materials via Resistive

Heating. *J. Nanosci. Nanotechnol.* **2017**, *17* (4), 2848–2851.

(17) Nikoobakht, B.; Herzing, A.; Muramoto, S.; Tersoff, J. Vapor-Liquid-Solid Etch of Semiconductor Surface Channels by Running Gold Nanodroplets. 2015, pp 8360–8364.

(18) Anton, R. Interaction of Gold, Palladium and Au-Pd Alloy Deposits with Oxidized Si(100) Substrates. *Thin Solid Films* **1984**, *120* (4), 293–311.

(19) Babor, P.; Duda, R.; Polcak, J.; Prusa, S.; Potocek, M.; Varga, P.; Chechal, J.; Sikola, T. Real-Time Observation of Self-Limiting SiO2/Si Decomposition Catalysed by Gold Silicide Droplets. *RSC Adv.* **2015**, *5*, 101726–101731.

(20) Kruzic, J. J. Bulk Metallic Glasses as Structural Materials: A Review. *Adv. Eng. Mater.* **2016**, *18* (8), 1308–1331.

(21) Kanjanachuchai, S.; Wongpinij, T.; Euaruksakul, C.; Photongkam, P. Au-Catalyzed Desorption of GaAs Oxides. *Nanotechnology* **2019**, *30* (21), 215703.

(22) Stroeve, P.; Ileri, N. Biotechnical and Other Applications of Nanoporous Membranes. *Trends Biotechnol.* **2011**, *29* (6), 259–266.

(23) Osaka, Y.; Sugano, S.; Hashimoto, S. Plasmonic-Heating-Induced Nanofabrication on Glass Substrates. *Nanoscale* **2016**, *8*, 18187–18196.

(24) Liu, G.; Young, K. L.; Liao, X.; Personick, M. L.; Mirkin, C. A. Anisotropic Nanoparticles as Shape-Directing Catalysts for the Chemical Etching of Silicon. *J. Am. Chem. Soc.* **2013**, *135* (33), 12196–12199.

(25) Black, C. T.; Ruiz, R.; Breyta, G.; Cheng, J. Y.; Colburn, M. E.; Guarini, K. W.; Zhang, Y.; Heights, Y. Polymer Self Assembly in Semiconductor Microelectronics. *Int. Bus.* **2007**, *51* (5), 605–633.

(26) Albrecht, T. R.; Bedau, D.; Dobisz, E.; Gao, H.; Grobis, M.; Hellwig, O.; Kercher, D.; Lille, J.; Marinero, E.; Patel, K.; et al. Bit Patterned Media at 1 Tdot/in 2 and Beyond. *IEEE Trans. Magn.* **2013**, *49* (2), 773–778.

(27) Curiotto, S.; Chien, H.; Meltzman, H.; Labat, S.; Wynblatt, P.; Rohrer, G. S.; Kaplan, W. D.; Chatain, D. Copper Crystals on the (1120) Sapphire Plane: Orientation Relationships, Triple Line Ridges and Interface Shape Equilibrium. *J. Mater. Sci.* **2013**, *48* (7), 3013–3026.

(28) Karakouz, T.; Tesler, A. B.; Bendikov, T. A.; Vaskevich, A.; Rubinstein, I. Highly Stable Localized Plasmon Transducers Obtained by Thermal Embedding of Gold Island Films on Glass. *Adv. Mater.* **2008**, *20* (20), 3893–3899.

Supplementary Information

1. N 1s XPS spectra for PS-*b*-P2VP-Pd micelles

Pd micelles nanoparticles synthesized using PS(110K)-*b*-P2VP(52K) were observed to have a persistent peak in the N 1s spectra between 339.6-400 corresponding to pyridine. However, after being subjected to annealing at 150 ºC under Ar for 10 h followed by O_2 at 600 ºC for 3h, the peak seems to disappear as the spectra becomes very noisy. A closer examination of the raw counts (Figure S1) shows that small peaks at 399 and 406 eV are present that correspond to pyridine and nitrates respectively. It is possible that oxidation of organic residue in this step causes a thin film to form over the sample reducing the overall signal strength.

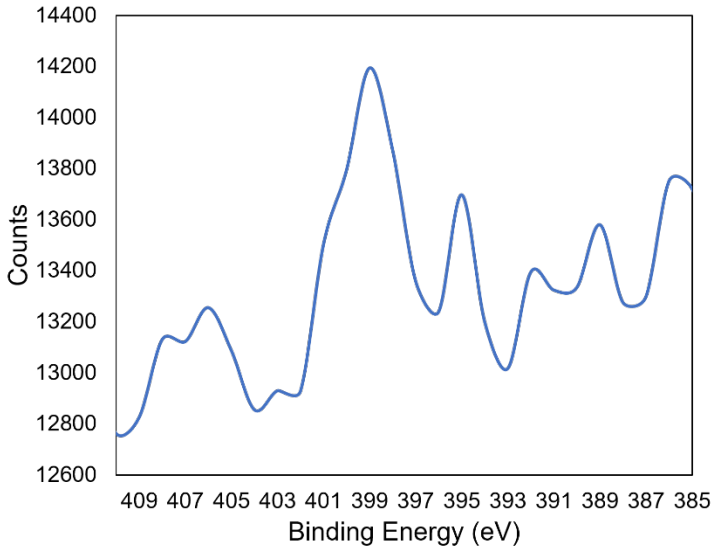

Figure S1 Raw counts from N 1s spectrum obtained from the XPS of PS-b-P2VP-Pd micelles synthesized using PS(110K)-b-P2VP(52K), with initial Pd:P2VP loading of 1:2 after 8 times dilution after annealing at 150 ºC under Ar for 10 h followed by O_2 at 600 ºC for 3h.

2. High temperature annealing of Au and Pd nanoparticles synthesized using PS-*b*-P2VP

Au and Pd nanoparticles synthesized using PS(110K)-*b*-P2VP(52K) and the two-step annealing for polymer removal were heated to 1040 ºC for 40 and 10 min respectively. While we have previously observed nanopore formation for such metal nanoparticles synthesized using PEO-*b*-P2VP, we saw that

Pd nanoparticles lead to the formation of nanowires, possibly carbon, after this thermal processing (Figure S2). Au nanoparticles, however, did not show nanowire growth but did not form nanopore either (Figure S3). The residual organic matter from the P2VP that does not get removed despite severe annealing could be serving as a carbon source for the growth of these nanowires for Pd and increasing the hydrothermal stability of Au nanoparticles.

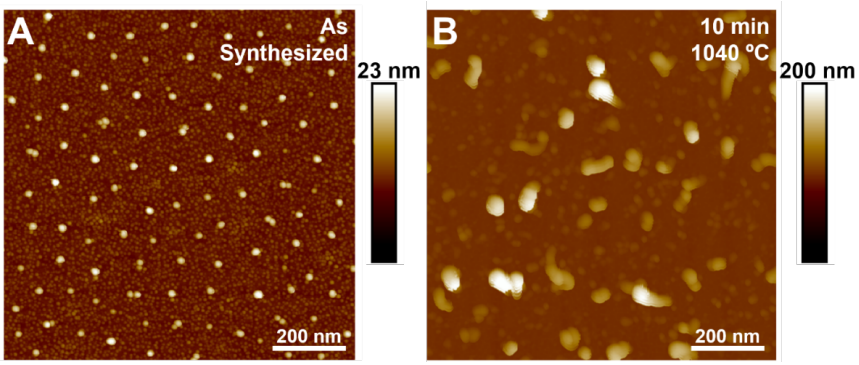

Figure S2 AFM images of Pd nanoparticles synthesized using PS(110K)-*b*-P2VP(52K), with initial Pd:P2VP loading of 1:2 after two-step thermal annealing A) as synthesized and B) after heating to 1040 ºC for 10 min in Ar.

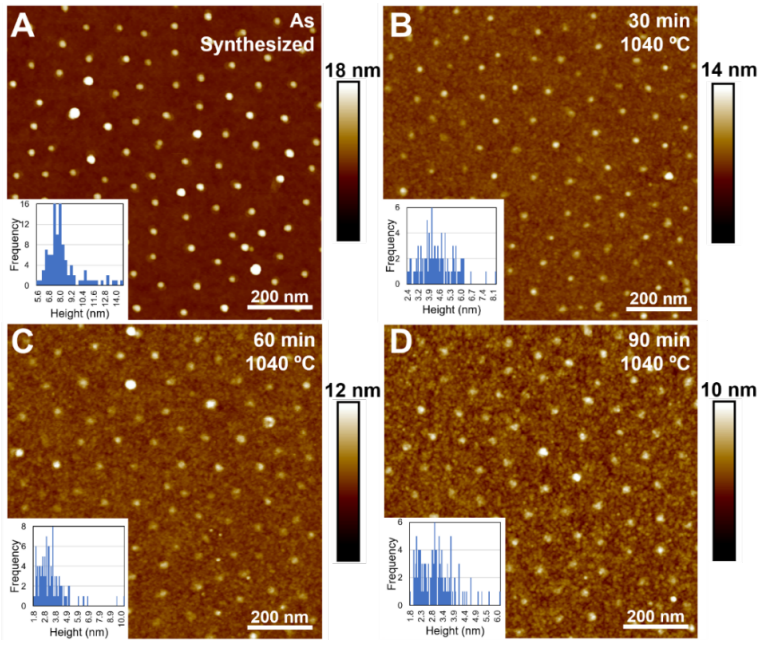

Figure S3 AFM images and particle size distributions of Au nanoparticles synthesized using PS(110K)-*b*-P2VP(52K), with initial Au:P2VP loading of 1:2 after two-step thermal annealing A) as synthesized and after heating to 1040 ºC in Ar for A) 10 min, B) 20 min, C) 30 min, and D) 40 min.

3. A standard GC-MS chromatogram for Suzuki-Miyaura cross-coupling reaction

A typical GC-MS chromatogram for the Suzuki-Miyaura cross-coupling reaction is shown in Figure S4.

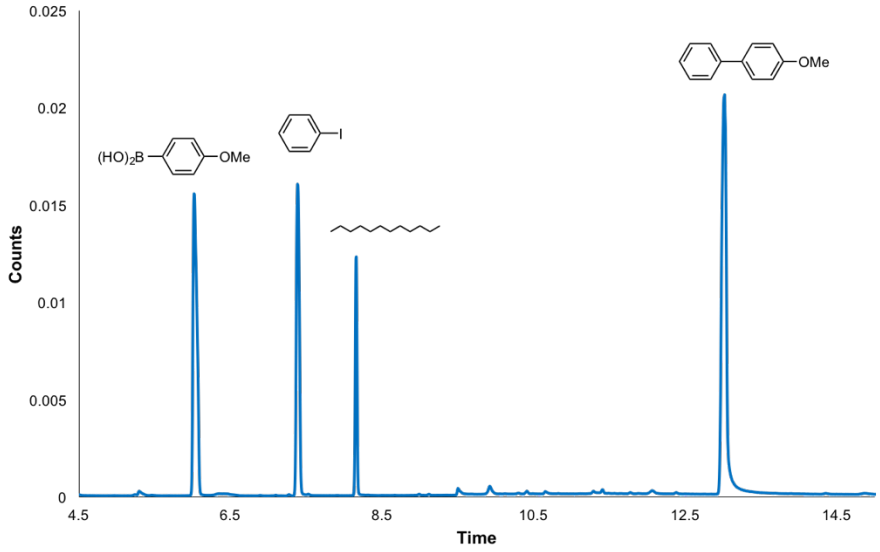

Figure S4 Chromatogram from GC-MS analysis of reaction between iodobenzene and 4-methoxyphenyl boronic acid in 1:1 dioxane-water system using K_3PO_4 as the base. The catalyst used was 1 cm^2 wafer with uniformly dispersed Pd nanoparticles (49 $x10^{-9}$ g/chip). Dodecane is used as the internal standard.

4. Line sections of typical nanoparticle surfaces and nanopores

Line sections of each of the insets in Figures 4.2, 4.3 and 4.5 were examined using Nanoscope Analysis software. These are depicted in Figure S5. These give a clear understanding of the topography of the surfaces, height of ridges, and differences between a nanopore and a partially entrenched nanoparticle.

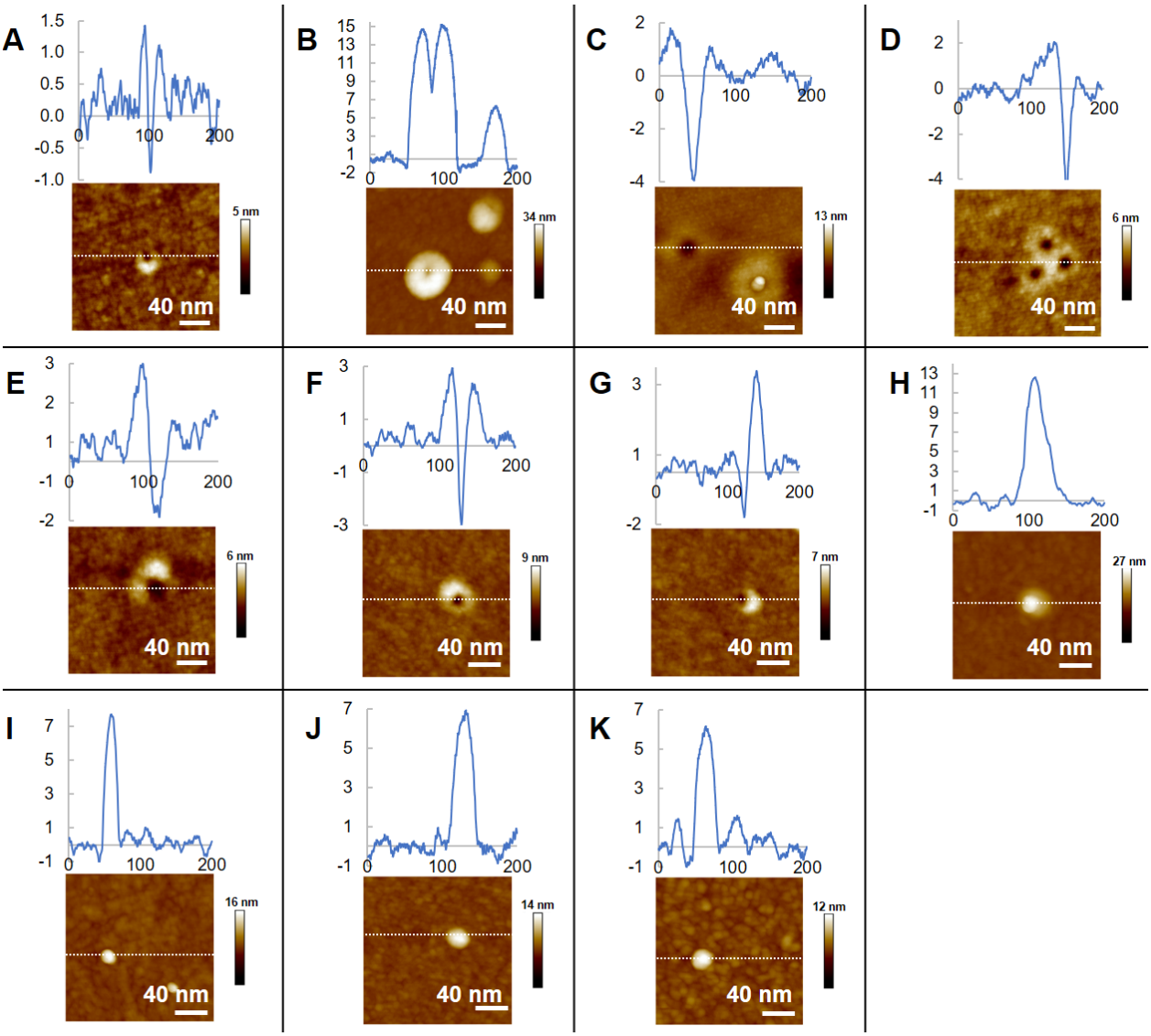

Figure S5 Line sections and AFM images of nanoparticle or nanopore surfaces after being subjected for 40 minutes in four intervals of 10 minutes each at respective temperature. A) Au on Si wafer with 285 nm thermal oxide layer (1020 ºC), B) Ag on Si wafer with 285 nm thermal oxide layer (900 ºC), C) Pt on Si wafer with 285 nm thermal oxide layer (1040 ºC), D) Pd on Si wafer with 285 nm thermal oxide layer (1020 ºC), E) Cu on Si wafer with 285 nm thermal oxide layer (1020 ºC), F) Au on Si wafer with 285 nm thermal oxide layer (1040 ºC), G) Au on Si wafer with 285 nm thermal oxide layer (1000 ºC), H) Au on Si wafer with 285 nm thermal oxide layer (900 ºC), I) Au on 10 nm Al_2O_3 deposited on Si wafer with 285 nm thermal oxide layer (1020 ºC), J) Au on tri-layer support with an entrenchment layer of 3 nm thickness (1020 ºC), and K) Au on tri-layer support with an entrenchment layer of 5 nm thickness (1020 ºC). All axes are in nanometers. The dotted lines across the AFM images indicate the regions the line sections were taken across.

5. Cross sectional imaging of Au nanoparticles on modified silicon wafers

Cross sections of gold nanoparticles supported on Al_2O_3 on Si wafer and tri-layer supports were acquired after coating the fractured samples with a 5 nm layer of gold using a Hitachi SU-8030 Scanning Electron Microscope at an accelerating voltage of 3 kV and 10 μAm current (Figure S6). There is no nanopore formation observed in these cases while the thermal SiO_2 (~300 nm) layer is distinct from the underlying Si and is intact. The partial entrenchment of Au nanoparticles in the tri-layer supports cannot be clearly identified due to the resolution limits of the microscope.

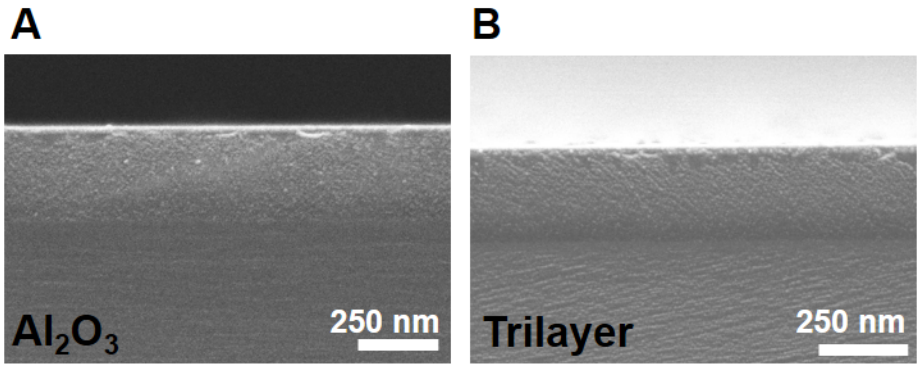

Figure S6 SEM images of cross sections of A) Au on 10 nm Al_2O_3 deposited on Si wafer with 285 nm thermal oxide layer (1020 ºC) and B) Au on tri-layer support with entrenchment layer of 5 nm thickness (1020 ºC) respectively. Each of the samples had been heated to 1020 ºC for 40 minutes in four intervals of 10 minutes each.

6. Behavior of Au nanoparticles on quartz wafers

The proposed mechanism for selective nanopore formation on amorphous SiO_2 (Scheme 4.2) was confirmed by testing the behavior of Au nanoparticles on crystalline SiO_2 (quartz). Uniformly distributed Au nanoparticles supported on quartz, when subjected to the same heat treatment as their amorphous counterparts (1020 ºC, 40 minutes), showed no nanopore formation but only severe agglomeration (Figure S7). When the Au nanoparticles were dissolved in aqua regia, the morphology of the underlying quartz shows that some ridge formation is seen (Figure S7 C, D). This confirms the proposed mechanism that though ridge formation occurs on all oxides, a glass transition (that does not occur on quartz and other crystalline oxides) is required to observe nanopore formation.

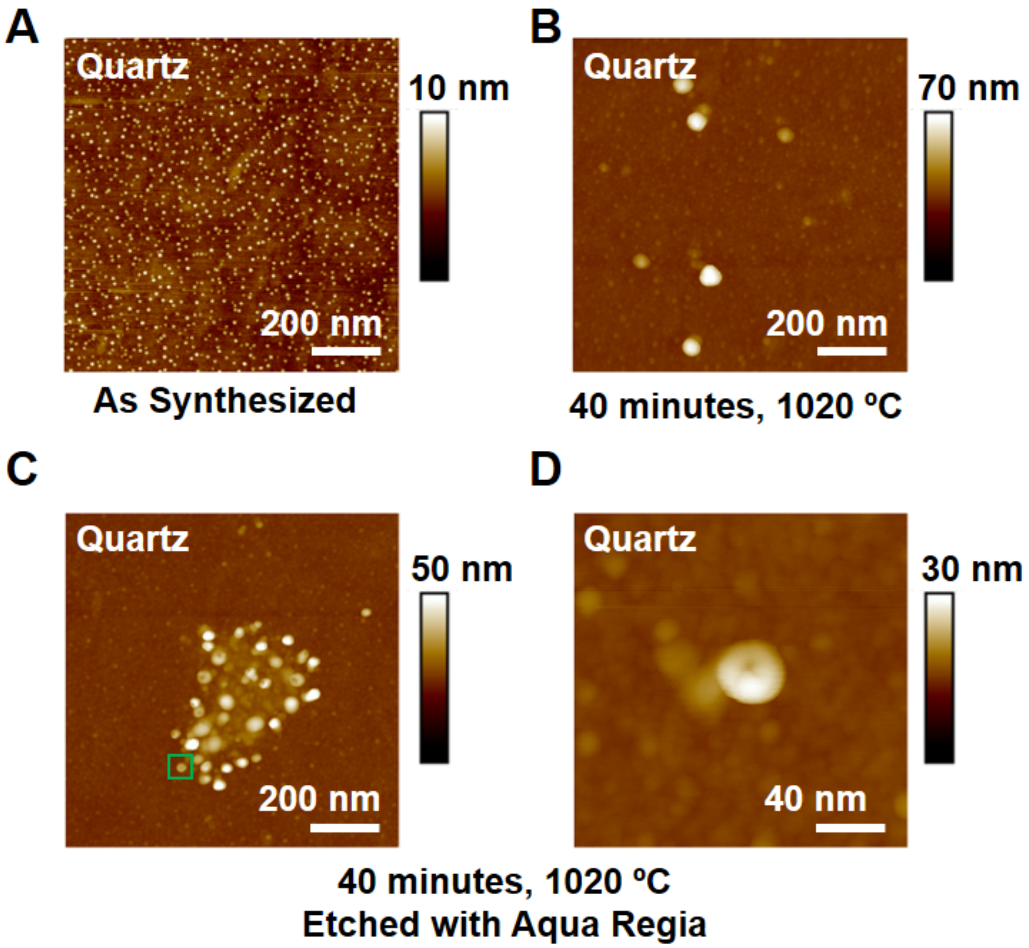

Figure S7 A) AFM image of Au nanoparticles uniformly distributed on quartz B) After heating for 40 minutes at 1020 ºC (in intervals of 10 minutes), agglomeration of Au nanoparticles is observed. C) Surface topology after dissolution of Au with aqua regia indicated ridge formation around the agglomerated nanoparticles. D) Zoomed-in image of the ridge left behind on the quartz surface after removing the nanoparticles.

7. Pd Nanoparticle Synthesis

The various PEO-*b*-P2VP block copolymers used in the synthesis of Pd nanoparticles of different distributions discussed in Chapter 5 are summarized in table S1. Figure S8 shows how the nanoparticle surface density and size changes with different synthesis conditions. It was observed that with oxygen plasma treatment before annealing, a distribution of small (< 5nm), high surface density features were achieved. On the other hand, without plasma, larger (5-20 nm), low surface density nanoparticles were obtained (S8 A). With different block copolymer chain lengths and Pd concentration in the solution, as

shown in S8 B and C, a wide range of different sizes and surface densities were obtained. Figure S8 D shows that using the same concentration of Pd in the aqueous block copolymer solution, different densities can be obtained by changing the other two parameters.

Table S1 Different PEO-*b*-P2VP block copolymer chain lengths used for the synthesis of Pd nanoparticles.

Polymer	Mol. Weight of PEO block	Mol. Weight of P2VP Block
P0	1500	2800
P6	1800	1000
P7	7000	3500
P8	14000	2500
P9	21000	13500

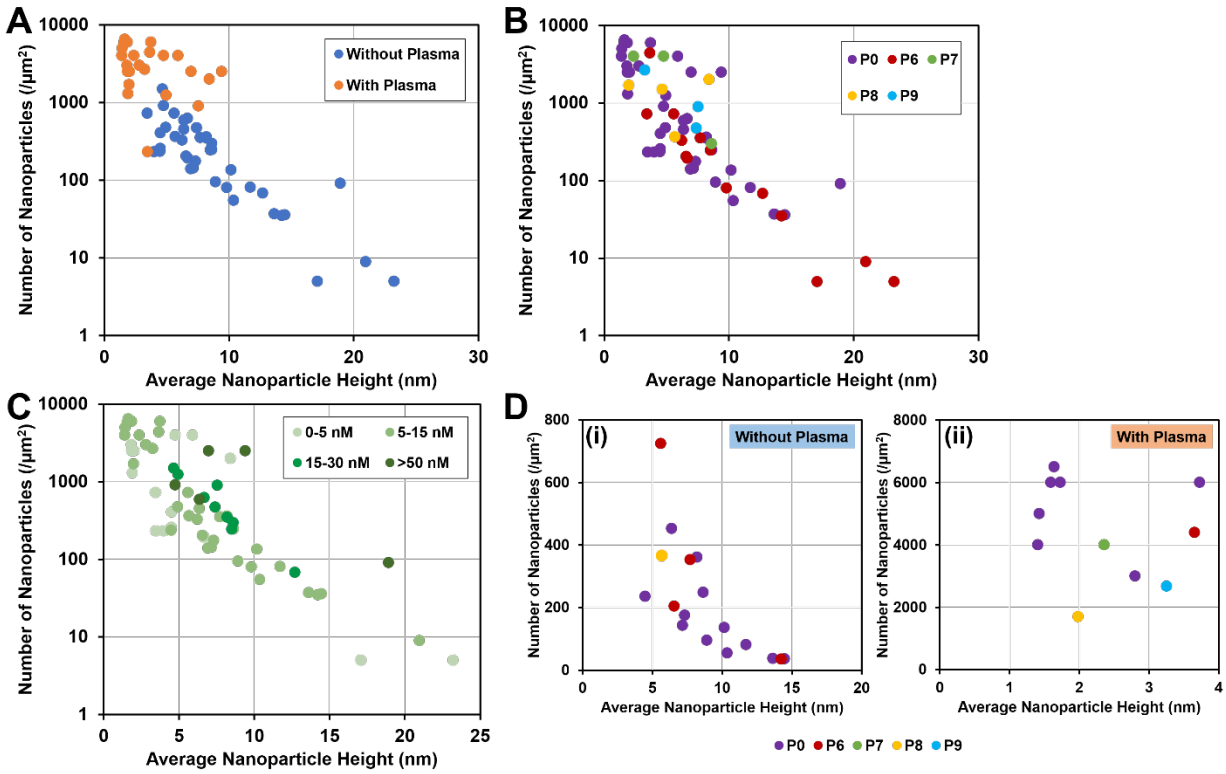

Figure S8 Range of different nanoparticle sizes and surface densities obtained by changing the synthesis conditions like using A) O_2 plasma treatment, B) different block copolymer chain lengths, C) different concentration of Pd precursor

in the solution. D) Using a set concentration of Pd (12 nM) two very different distributions, (i) Large size, low surface density and (ii) Small size, high surface density, can be obtained using different polymers, without and with O_2 plasma treatment, respectively.

8. Outlying distributions

a. Small nanoparticles, low surface densities

Nanoparticles with smaller sizes and low surface densities (size ~ 1.3 nm, surface density ~ 100 nanoparticles/μm^2), as shown in Figure S9, can be synthesized using very dilute Pd-block copolymer solutions. No clear nanopores or encapsulated nanoparticles are seen on the SiO_2 surface after heating (1040 ºC for 10 min using a ramp rate of 3.3 ºC/s) these nanoparticles since the particle size and density roughly matches the surface roughness of the bare SiO_2 surface. Thus, due to near-indistinguishable features from the SiO_2 wafer surface after thermal processing, these are excluded from consideration to avoid ambiguous inferences.

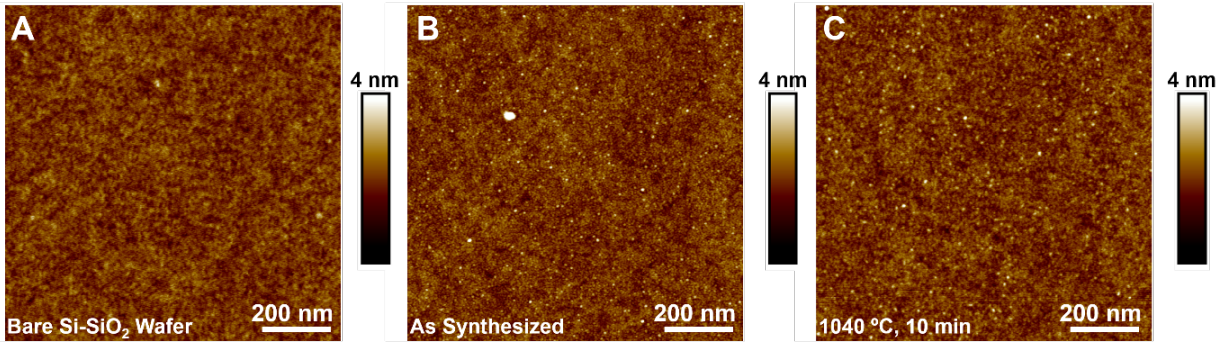

Figure S9 AFM images of A) bare Si-SiO_2 wafer surface, B) small, low surface density Pd nanoparticles as synthesized, and C) sample surface after heating at 1040 ºC for 10 min using a ramp rate of 3.3 ºC/s

b. Large nanoparticles, high surface densities

Pd nanoparticles with large sizes and high surface densities (size ~ 7 nm, surface density ~ 4000 nanoparticles/μm^2) can be synthesized by using low spin coating rates, concentrated Pd solutions, and use of oxygen plasma. At these distributions, the nanoparticles on heating at 1040 ºC for 10 min using a ramp rate of 3.3 ºC/s show complete entrenchment (Figure S9). However, due to the high density of the nanopores and low mobility of the large nanoparticles, minimal agglomeration is observed. Under these

conditions, the nanopores overlap each other and make the SiO_2 surface extremely porous rendering the individual nanopore indistinct. These distributions are also excluded from consideration.

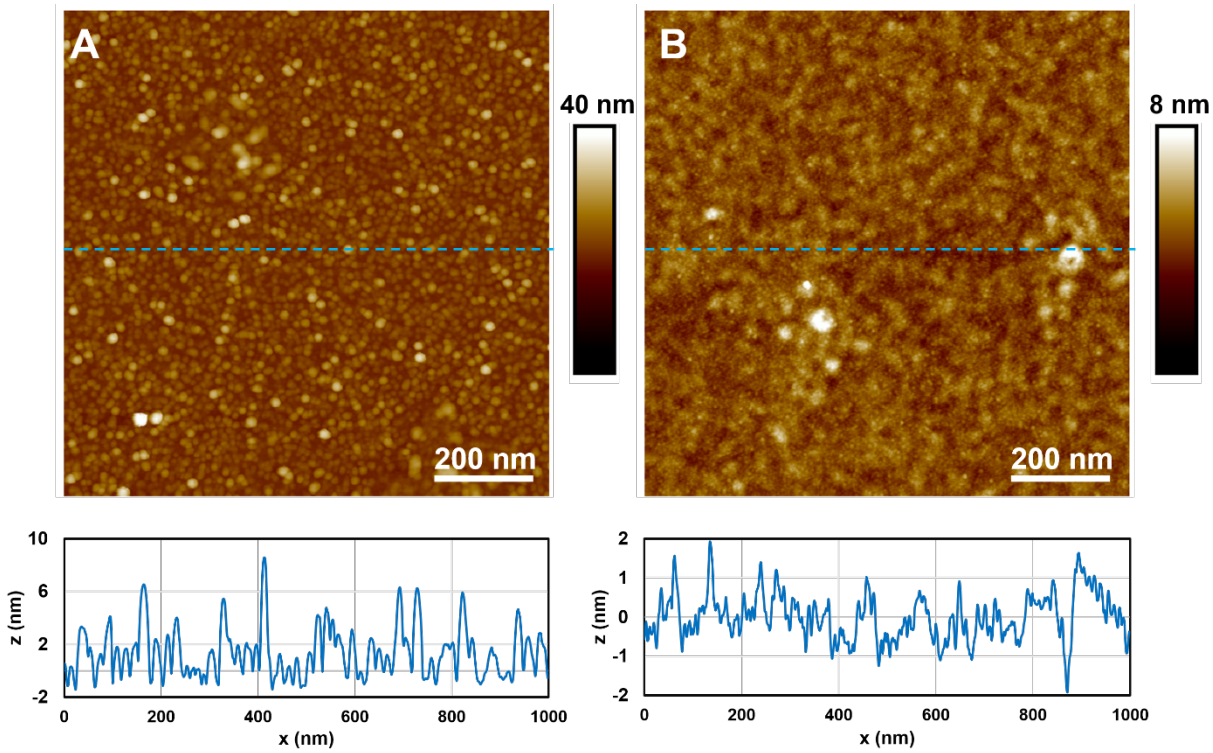

Figure S10 AFM images and line scans of A) large, high density Pd nanoparticles as synthesized and B) highly perforated SiO2 surface after being heated at 1040 ºC for 10 min using a ramp rate of 3.3 ºC/s

9. Change in the volume of surface Pd with time

For small, high surface density nanoparticles, the particle mobility at temperatures above 800 ºC is very high. Thus, these nanoparticles tend to agglomerate with time. There are also mechanisms like evaporation of the surface Pd atoms and diffusion of Pd into the SiO_2 surface that are enhanced at high temperatures. In order to quantify the role of agglomeration and diffusion and evaporation in the changing nanoparticle distribution with time, the apparent volume of the Pd on the surface was calculated and is shown in Scheme S1 and Table S2. Any material loss would be attributed to either diffusion or evaporation since these two cannot be distinguished between. However, within error, no material loss was observed and the amount of Pd present before and after heating can be reconciled. Thus, the change in nanoparticle

size and surface density can be attributed to agglomeration and other surface effects are considered to be negligible.

Scheme S1 For calculating the total volume of the surface Pd with changing sizes and densities the shape of each Pd nanoparticle is assumed to be that of a truncated sphere.

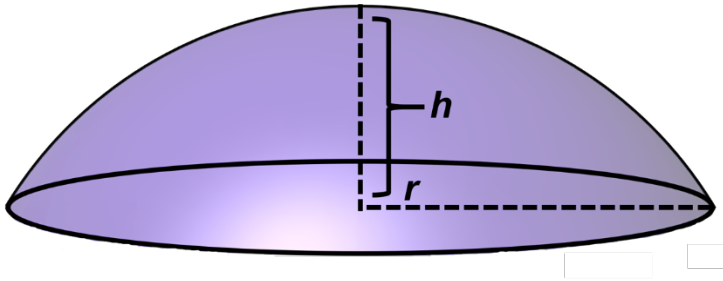

$$Volume = \frac{\pi h^2 (3r - h)}{3}$$

Table S2 Summary of nanoparticle height, radius, surface density, and total calculated volume as a function of time at 1040 ºC (reached using a ramp rate of 3.3 ºC/s)

Time at 1040ºC (min)	**Nanoparticle Height *h* (nm)**	**Nanoparticle Radius *r* (nm)**	**Number of Nanoparticles (/μm^2)**	**Volume of Surface Pd (nm^3/μm$^{2)}$**
0	1.56 ± 0.62	1.51 ± 0.63	6000	45 x10^3
1.5	3.74 ± 1.84	11.21 ± 3.34	140	61 x10^3
3	4.82 ± 1.75	9.81 ± 3.03	70	42 x10^3

10. Fate of Pd nanoparticles of different sizes and surface densities after thermal processing

Different behaviors (total and partial entrenchment, agglomeration, and encapsulation) are observed across different sizes and surface densities of Pd nanoparticles after annealing at 1040 ºC for 10 min using a ramp rate of 3.3 ºC/s. Particularly, we observe that nanopore formation, either with partial or

total entrenchment, occurs almost across the range of nanoparticle sizes and surface densities (Figure S11).

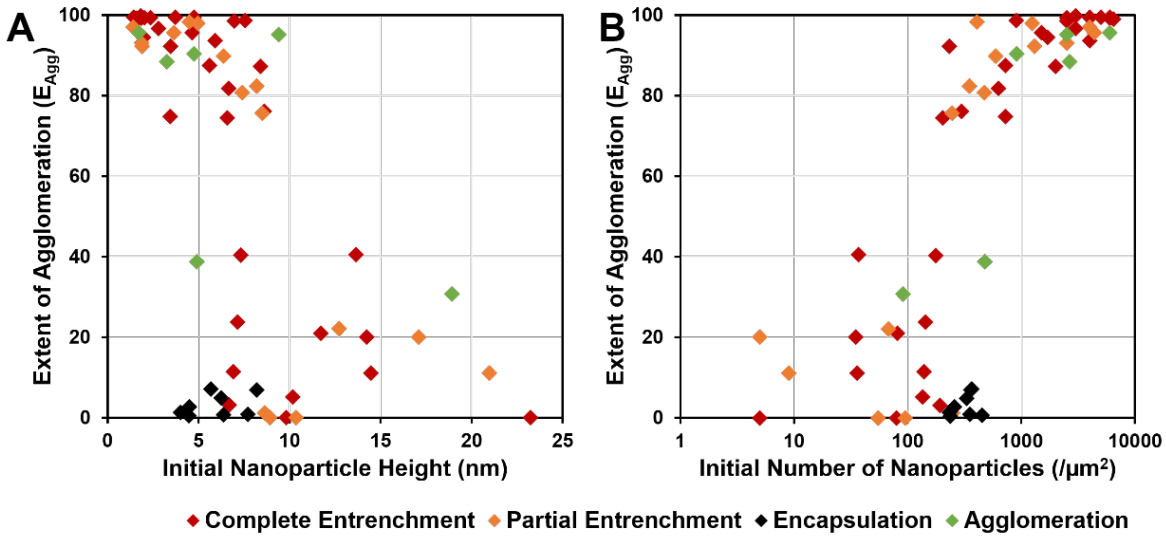

Figure S11 Different behaviors (Complete and partial entrenchment, encapsulation, and agglomeration) and degrees of aggregation preceding nanopore formation (EAgg) observed as a function of A) initial nanoparticle size and b) initial nanoparticle surface density for Pd nanoparticles heated to 1040 ºC for 10 minutes at 3.3 ºC/s.

11. Etching Partially Embedded Pd Nanoparticles

Larger Pd nanoparticles that are spaced far apart, have very low surface mobility and show no agglomeration. These nanoparticles, on heating at 1040 ºC for 10 minutes, do not exhibit nanopore formation but show a reduction in the nanoparticle height due to partial embedding in the SiO_2 surface. On etching the Pd from the surface, the oxide ridges and the trenches left behind by the nanoparticles can be clearly seen thus, demonstrating that the Pd nanoparticles are not encapsulated in SiO_2. (Figure S12).

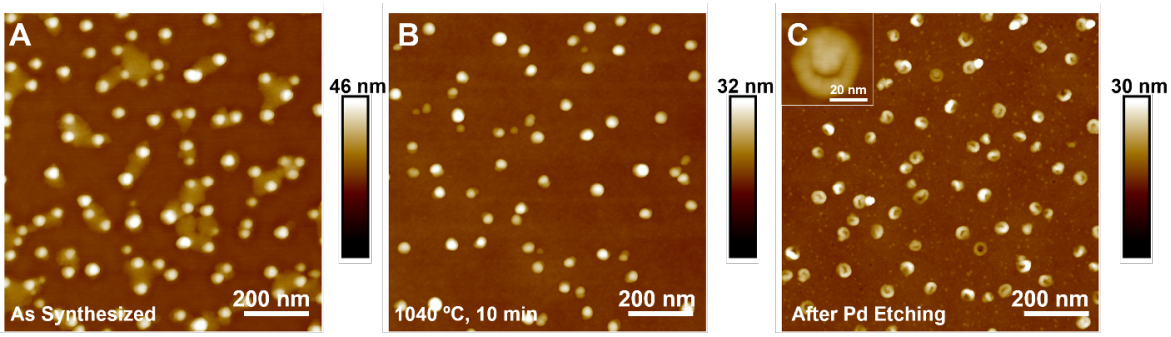

Figure S12 AFM images of A) Pd nanoparticles that show no nanopore formation but only B) partial embedding in the SiO_2 surface on heating at 1040ºC for 10 minutes, can be C) etched away to reveal the oxide ridges and the trenches formed by the partial entrenchment

12. Initial distributions for studying the different heating conditions

The nature of nanopore formation at different heating conditions (temperature, hold time, ramp rate) is studied for two different surface distributions of Pd nanoparticles. These distributions are illustrated in Figure S13. For the smaller, high surface density nanoparticles (Figure S13 A), there is high tendency of the nanoparticles to agglomerate so the effect of both agglomeration and nanopore formation can be studied simultaneously. The larger, low surface density nanoparticles (Figure S13 B) have a low surface mobility and thus do not agglomerate aggressively. For this distribution, nanopore formation without the influence of agglomeration is studied.

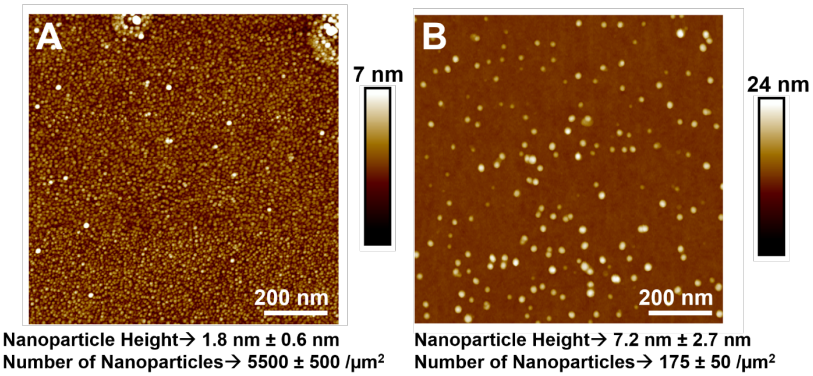

Figure S13 AFM images of initial distributions of Pd nanoparticles on SiO_2 surface used to study the different heating conditions. A) High surface density, small sized nanoparticles that tend to agglomerate, B) low surface density, large nanoparticles that have low surface mobility.

13. Increasing ramp rates above minimum values

We observe that a minimum ramp rate of 3.3 ºC /s is needed to observe clear nanopore formation. However, increasing the ramp rate of heating does not affect the nature of nanopore formation so long as it is above the minimum values (Figure S14).

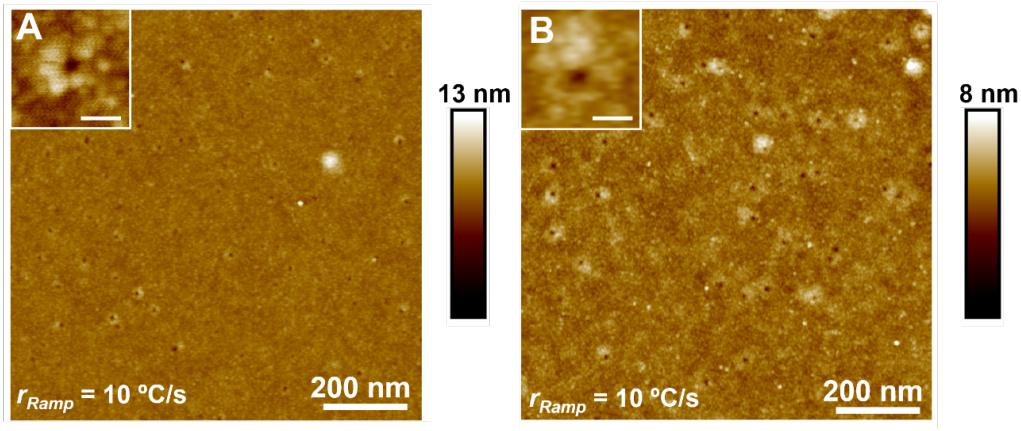

Figure S14 AFM images of A) small, high surface density and B) large, low surface density Pd nanoparticles on SiO_2 heated at 1040 ºC and held for 10 min at ramp rates (r_{Ramp}) 10 ºC/s.

14. Additional trends in total entrenchment

When Pd nanoparticles on SiO_2 surface are heated to 1040 ºC for 10 minutes and only nanopores are obtained on the surface, the behavior is termed as total entrenchment. For nanoparticles with low surface are coverage with no agglomeration (E_{Agg} < 20%), height of the oxide ridge around the nanopores is in the range of 3-10 nm (Figure S15 A) and is much higher than those with a higher tendency to agglomerate (E_{Agg} > 80%) which form oxide ridges less than 5 nm in height (Figure S15 B). For nanoparticles with a high tendency to agglomerate, relative diameter of nanopore, with respect to the height of the starting nanoparticle increases with increasing surface area coverage (Figure S15 C).

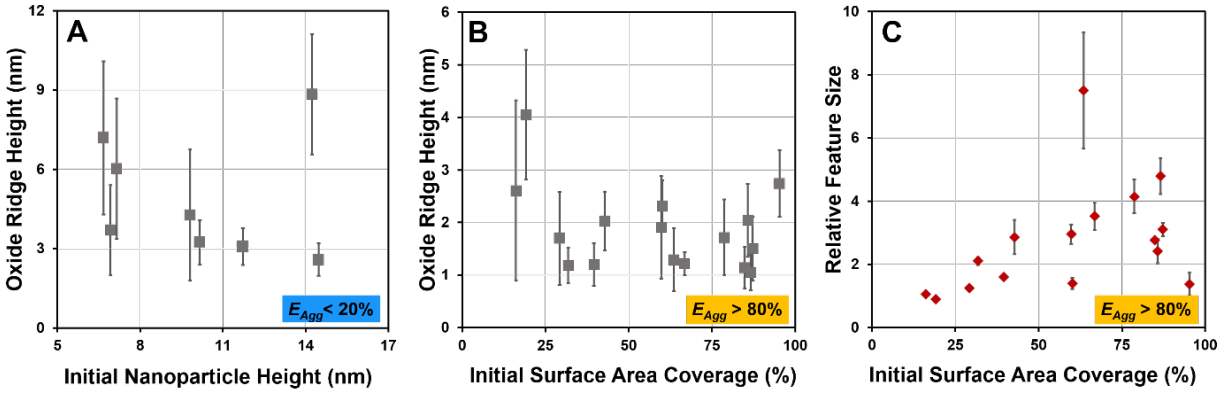

Figure S15 Trends in the oxide ridge height A) with initial height of Pd nanoparticles that show little/no agglomeration (E_{Agg} < 20%) and B) with initial surface area coverage of Pd nanoparticles that exhibit significant agglomeration before nanopore formation (E_{Agg} > 80%). C) The relative nanopore diameter with respect to the initial nanoparticle height as a function of the initial surface area Pd nanoparticles that exhibit significant agglomeration before nanopore formation (E_{Agg} > 80%). All samples are heated to 1040 ºC for 10 minutes at 3.3 ºC/s.

15. Designing Nanopores of Desired Dimensions

The nanopores formed by thermal processing of metal nanoparticles on SiO_2 supports can be tuned to achieve a range of nanopore diameters. The different synthesis conditions (concentration of Pd in block co-polymer micelle solution, chain lengths of block copolymers used, oxygen plasma) that lead to increasing nanopore diameters are summarized in Table S3.

Table S3 A detailed summary of the synthesis conditions used in the block copolymer micelle mediated synthesis of Pd nanoparticles of different distributions that lead to nanopores of different distributions after heating to 1040 ºC for 10 minutes at 3.3 ºC/s with varying extents of agglomeration that precedes the nanopore formation

Pd Concentration (nM)	**Block Co-polymer**	**O_2 Plasma**	**Initial NP Height (nm)**	**Initial Number of NP (/μm²)**	**Nanopore Diameter (nm)**	**Oxide Ridge Height (nm)**	**Number of Nanopores (/μm²)**	**E_{Agg} (%)**
3.0	P6	No Plasma	6.7 ± 1.6	193	5.0 ± 1.2	7.2 ± 2.9	176	<20
11.9	P0	No Plasma	7.2 ± 2.6	143	5.3 ± 1.3	6.0 ± 2.7	97	20-40
1.5	P6	No Plasma	3.4 ± 1.4	725	6.0 ± 0.5	2.5 ± 1.2	180	60-80
6.0	P0	No Plasma	6.9 ± 2.5	140	7.1 ± 1.3	3.7 ± 1.7	120	<20
11.9	P0	No Plasma	7.3 ± 2.1	176	7.7 ± 1.8	3.2 ± 1.9	95	40-60
6.0	P6	No Plasma	9.8 ± 2.0	80	7.9 ± 4.7	4.3 ± 2.5	70	<20
11.9	P8	5min, 15 Watt	2.0 ± 1.0	1700	9.6 ± 1.5	2.0 ± 0.7	84	80-100
11.9	P0	No Plasma	13.6 ± 5.9	37	10.1 ± 2.2	8.0 ± 2.2	20	20-40
3.0	P0	5min, 60 Watt	2.0 ± 1.2	2500	11.2 ± 0.2	1.1 ± 0.4	15	80-100
6.0	P0	5min, 60 Watt	1.9 ± 1.0	6000	11.5 ± 0.8	1.5 ± 0.6	40	80-100
23.8	P8	No Plasma	4.7 ± 2.4	1500	11.6 ± 0.4	1.7 ± 0.9	50	80-100
11.9	P0	5min, 30 Watt	2.8 ± 0.6	3000	11.8 ± 0.7	1.2 ± 0.3	100	80-100

11.9	P6	No Plasma	5.6 ± 1.5	725	11.8 ± 0.7	2.6 ± 1.7	90	80-100
23.8	P0	No Plasma	6.7 ± 1.8	627	11.9 ± 0.8	4.1 ± 1.2	100	80-100
11.9	P0	No Plasma	10.2 ± 2.0	136	12.4 ± 1.0	3.2 ± 0.8	117	<20
3.0	P0	5min, 60 Watt	1.8 ± 0.8	3000	12.9 ± 1.6	1.2 ± 0.2	5	80-100
23.8	P7	No Plasma	8.6 ± 3.4	297	13.2 ± 1.9	2.0 ± 0.5	60	60-80
1.5	P7	5min, 30 Watt	4.8 ± 2.0	4000	13.3 ± 1.7	2.3 ± 0.5	20	80-100
11.9	P6	No Plasma	6.6 ± 4.2	204	13.4 ± 1.6	3.3 ± 1.3	50	60-80
11.9	P7	5min, 60 Watt	2.4 ± 0.9	4000	13.5 ± 2.6	2.0 ± 0.6	26	80-100
11.9	P0	5min, 30 Watt	1.6 ± 0.6	6500	13.6 ± 1.8	1.7 ± 0.7	60	80-100
11.9	P0	No Plasma	11.7 ± 4.6	81	13.7 ± 1.9	3.1 ± 0.7	60	<20
3.0	P6	No Plasma	23.2 ± 2.8	5	13.7 ± 5.0	6.5 ± 1.6	5	<20
11.9	P0	5min, 60 Watt	1.6 ± 0.7	6000	15.3 ± 1.8	1.0 ± 0.3	41	80-100
11.9	P6	No Plasma	14.2 ± 2.5	35	16.0 ± 2.2	8.8 ± 2.3	27	<20
47.6	P0	5min, 60 Watt	7.0 ± 3.1	2500	19.1 ± 5.0	2.7 ± 0.6	35	80-100
11.9	P0	No Plasma	14.5 ± 4.1	36	20.9 ± 6.4	2.6 ± 0.6	30	<20
11.9	P0	5min, 45 Watt	1.4 ± 0.9	5000	21.4 ± 5.2	1.3 ± 0.6	27	80-100
11.9	P0	5min, 60 Watt	3.7 ± 0.8	6000	22.1 ± 2.3	1.9 ± 1.0	31	80-100
23.8	P9	5min, 30 Watt	7.5 ± 2.6	900	24.2 ± 0.3	1.2 ± 0.4	9	80-100

16. Role of organic residue in poisoning nanopore formation

We have seen entrenchment of metal nanoparticles and nanopore formation on various SiO_2-based supports (fused SiO_2, Si wafer, and tri-layer supports) at temperatures above 1000 ºC when nanoparticles synthesized using PEO-P2VP block copolymer micelles. Literature has shown that nanopore formation can be achieved for nanoparticles synthesized using solution-phase methods as well as E-beam lithography. We also explored SPBCL as a synthesis technique to create very ordered arrays of metal nanoparticles. However, when ordered arrays of Ag nanoparticles were subjected to thermal conditions that usually lead to nanopore formation (900 ºC, 10 min), we saw no nanopore formation. Instead we observe growth of nanowires (Figure S16). While we haven't been able to ascertain the composition of the nanowires, the sharp contrast in the SEM image (Figure S16 C) indicates that the nanowires are of conductive material. Carbon nanotubes have been known to grow at these high temperatures. In contrast however, when Pd nanoparticles synthesized using SPBCL were heated to 1040 ºC for 10-40 min we saw that while some parts of the ordered array formed uniform nanopores within 10 min (Figure S17 B) while other parts remained thermally stable showing no nanopore formation or even oxide ridge formation (Figure S17 A).

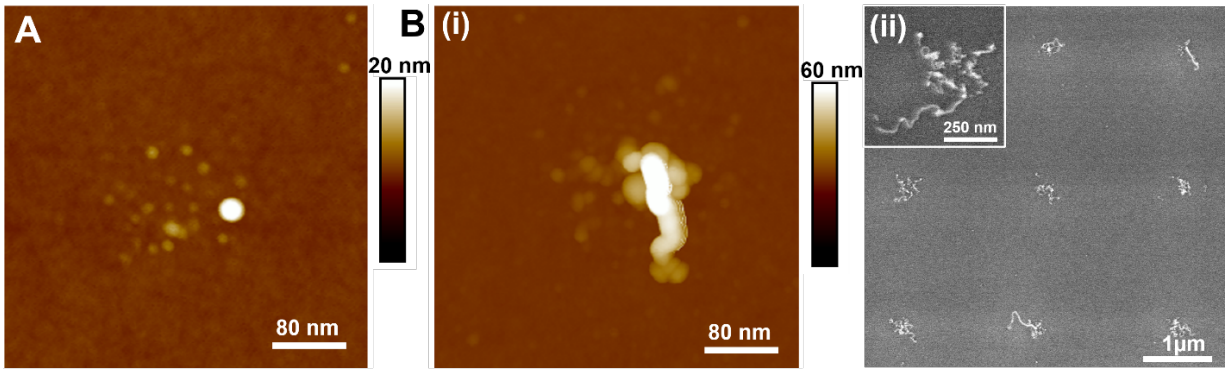

Figure S16 AFM images of SBPCL-synthesized Ag nanoparticles A) as synthesized and B) after rapid thermal processing at 900 ºC for 10 min. C) SEM image of nanowire growth on the Ag nanoparticles after being heated at entrenchment conditions.

It is possible that organic residue from the block copolymer nanoreactors that wasn't removed completely during the annealing steps, could be acting as a carbon source to facilitate the growth of these nanowires. The supporting SiO_2 surface is silanized with hexamethyldisilazane (HMDS) before depositing

the polymer nanoreactors to render it hydrophobic. Residue from incomplete thermal degradation of the HMDS during the annealing could be another source of contamination that promotes nanowire growth. On the other hand, we also see that neither nanopore formation nor nanowire growth occurs in some cases when arrays of metal nanoparticles are subjected to entrenchment conditions (Figure S17 A). These nanoparticles belong to the size (8-9 nm) and surface density (100 nanoparticles /μm^2) that we have previously shown to lead to nanopore formation. It is possible that a thin layer of carbon forms on the nanoparticle when it is heated to the high temperatures above 1000 ºC. Carbon overcoats have been shown to improve thermal stability of metal nanoparticles drastically. This may prevent any diffusion of metal ions into the SiO_2 and consequent nanopore formation.

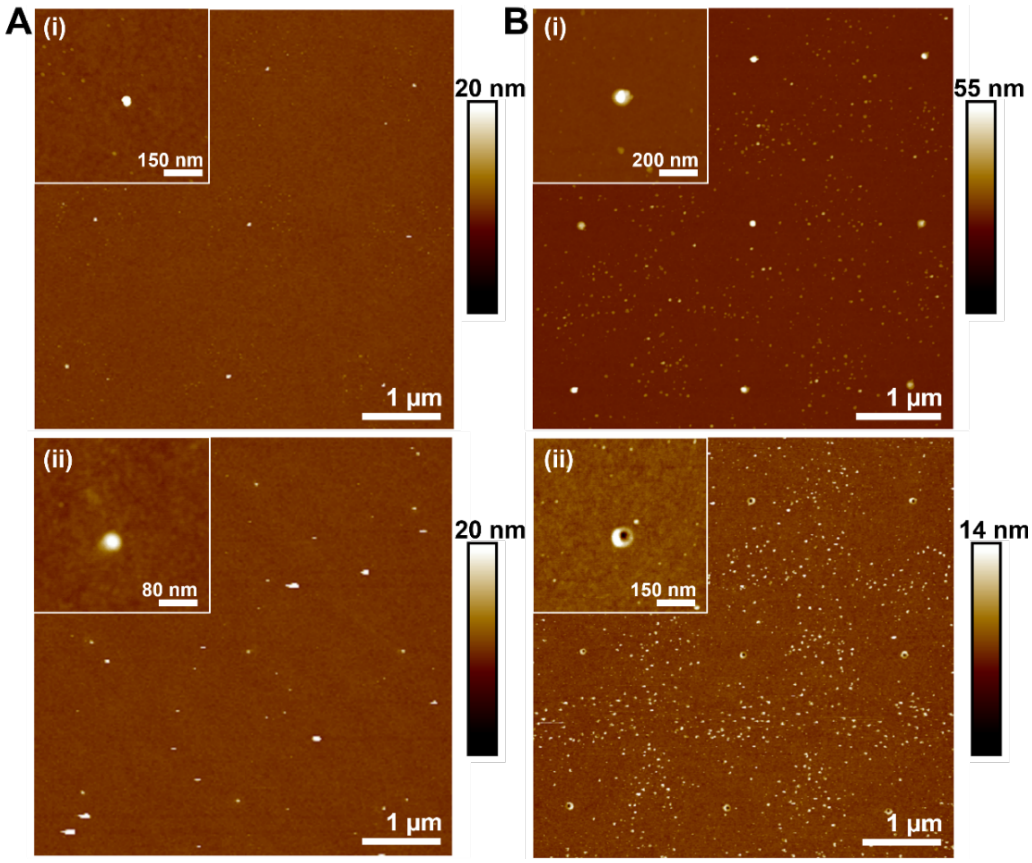

Figure S17 AFM images of SPBCL-synthesized Pd nanoparticles from two different areas (A and B) on the same array, i) as synthesized and ii) after rapid thermal processing at 1040 ºC for A) 40 min and B) 10 min.

While, we have a rough idea of why no nanopore formation is observed in these cases, there is room to explore, in further detail, how nanopore formation is prevented in presence of organic residue. Additionally, this may give us a way to understand the high thermal stability of some nanoparticles.